NOTE TO USERS

10

Geology and lithogeochemistry of the Chester Group and hydrothermal sediments of the Swayze greenstone belt, Superior province, Ontario

Christopher Wright

Department of Earth and Planetary Sciences
McGill University
Montréal, Québec, Canada

March 21, 2002

"A thesis submitted to the Faculty of Graduate Studies and Research in partial fulfillment of the requirements of the degree of Master of Science"

Your file Votre référence
ISBN: 0-612-85836-7
Our file Notre référence
ISBN: 0-612-85836-7

Abstract

Geological and high-field-strength element (HFSE) relationships for Chester Group felsic volcanic rocks and corresponding sub-volcanic intrusives in the south-east Swayze greenstone belt (SESGB) indicate deposition in an dynamic volcanic-arc tectonic setting, from two separate magmas with calc-alkaline and HFSE-depleted trace element signatures respectively. Chester Group, Yeo Formation rocks have undergone a regionally extensive sericite-quartz (type 1) alteration, involving the loss of 3.25 wt.% Na_2O, addition of 12 wt.% SiO_2 and 2.2 wt.% K_2O, and 13% net mass-gain, indicating water/rock ratios of at least 6. Chlorite-sericite±biotite±garnet (type 2) alteration at paleo-hydrothermal vent sites was localized along synvolcanic fault structures. Type 2 alteration was accompanied by a loss of 2.44 wt.% Na_2O and 8.69 wt.% SiO_2, and a gain of 5.90 wt.% Fe_2O_3, requiring water/rock ratios of at least 432.

Hydrothermal sediments or iron formation (IF) within the SGB are composed largely of Si and Fe. Base-metal mineralization in the SESGB and other localities in the SGB is hosted by brecciated hydrothermal sediments, overlain and flanked by, more broadly distributed pelitic IF, enriched in large ion lithophile elements (LILE), Al_2O_3, TiO_2 and HFSE, with distinct Fe_2O_3/TiO_2 versus $Al_2O_3/(Al_2O_3+Fe_2O_3+MnO)$ ratios indicative of mixing with locally derived volcanic material. Well-laminated BIF-type hydrothermal sediments are distributed widely throughout the SGB and are enriched in MnO, depleted in LILE, HFSE and transition elements, and have a wide range of Ce/Ce* values reflecting diverse redox conditions in paleodepositional environments distal to hydrothermal venting. Thermodynamic calculations suggest that hydrothermal fluids responsible for generation of hydrothermal sediments have lower temperatures (250-300 °C) but similar pH (~4) to polymetallic volcanogenic massive-sulphide ore-forming fluids.

Resumé

Les relations entre la géologie et les éléments à fort potentiel d'ionisation (HFSE) des roches volcaniques felsiques et des intrusions sub-volcaniques correspondants du Groupe de Chester et de la partie sud-est de la ceinture de roches vertes de Swayze (SESGB), suggèrent un milieu tectonique de déposition typique d'arc volcanique dynamique, à partir de deux magmas calco-alcalins caracterisés par un appauvrissement en HFSE et en éléments traces respectivement. Les roches de la Formation de Yeo du Groupe de Chester ont subi une altération régionale en séricite-quartz (type 1), impliquant une perte de 3.25 wt.% de Na_2O, une augmentation de 12 wt.% de SiO_2, et de 2.2 wt.% K_2O, accompagnée d'un gain de 13 % de masse nette correspondant à un ratio eau/roche d'au moins 6. L'altération en chlorite+séricite±biotite±grenat (type 2) typique des cheminées volcaniques paléo-hydrothermles était localisée le long d'une structure de faille synvolcanique. L'altération de type 2 est accompagnée par une perte de 2.44 wt.% Na_2O et de 8.69 wt.% SiO_2 et par un gain de 5.90 wt.% Fe_2O_3 indiquant un ratio eau/roche d'au moins 432. Les sédiments hydrothermaux ou les formations de fer contenues au sein de la ceinture de roche vertes de Swayze (SGB) sont largement composées de Si et de Fe.

Les minéralisations hydrothermales reconnues dans la partie sud-est de SGB et ailleurs le long de la SGB, se situent à l'intérieure d'une brèche de sédiments hydrothermaux, recouverte et flanquée par une formation de fer pélitique largement répandue et enrichie par des éléments lithophiles à large rayon ionique (LILE) tel que Al_2O_3, TiO_2 et les HFSE, avec un ratio distinctif Fe_2O_3/TiO_2 versus $Al_2O_3/(Al_2O3+Fe_2O_3+MnO)$ caractéristique d'un mélange contenant une composante volcanique de source locale. Les sédiments hydrothermaux rubannée de type BIF sont largement distribués au sein de la SGB et sont enrichis en MnO, appauvris en LILE, HFSE et en éléments transitionnels, et possèdent un large éventail de valeurs du ratio Ce/Ce*, indicatif des conditions réductrices variables d'un environnement paléo-dépositionnel distal aux cheminées hydrothermales. Des calculs thermodynamiques indiquent que les fluides hydrothermaux responsables de la formation des sédiments, ont une température inférieure (250-300 °C) mais possèdent un pH comparable (pH ~4) aux fluides hydrothermaux polymétalliques source des gisements volcanogénique de sulfures massifs.

Preface

This thesis consists of five chapters. The first chapter is a general introduction to the project, and the second chapter is a review of the geology of the Swayze greenstone belt (SGB). The third chapter is a study of the paleotectonic setting and hydrothermal alteration of the Chester Group volcanics and sub-volcanic equivalents from the south-east SGB (SESGB), based on field relations, petrography and lithogeochemistry. The fourth chapter is an analysis of the geology, petrography and lithogeochemistry of the hydrothermal sediments of the SGB. The fifth chapter is a summary of the thesis' specific contributions to science. A reference list, appendices including cited data, and corresponding figures and tables follow each chapter. Chapters 3 and 4 were prepared in manuscript form and can be read as self-supporting articles.

Contributions of authors

The thesis author, C. Wright, is responsible for all of the new scientific data and interpretations of the geology and lithogeochemistry of the supracrustal rocks of the Swayze greenstone belt. Dr. A.E. Williams-Jones acted as research supervisor and advised the author during the study and preparation of the thesis, and is listed as second-author of chapters prepared in manuscript form.

Outcrop mapping, drill core logging, lithogeochemical sampling, petrography, photography and mass-change calculations were performed by the author of the thesis; the first author of chapters 3 and 4. This author submitted 169 samples to commercial laboratories for lithogeochemical analysis. ICP-AES whole rock analyses were performed by T. Nicholson at TSL Assayers in Vancouver, BC. ICP-MS trace element analyses were performed under the supervision of Dr. E.L. Hoffman at Actlabs,

Ancaster, ON. Flame and standard AA assays as well as sample-loss-on-ignition determinations were overseen by G. LeBel at TSL Assayers in Swastika, ON. Lithogeochemical data for 13 samples used in this study were taken from a lithogeochemical database compiled by J. Harris of the GSC. L. Bonhomme of Explorers Alliance Ltd. contributed 5 sample analyses. Petrographic thin sections were prepared by G. Panagioditis at the McGill University Rock Preparation Lab.

Acknowledgements

Funding for field and analytical work was provided by Falconbridge Ltd., Timmins Exploration Office, Timmins, ON. Study conception and logistics were developed in conjunction with M. Collison, A. Coutts, G. DeSchutter, N. Dupras, and S. McLean of the Falconbridge Ltd. Timmins Exploration Office. T. Maxwell provided assistance in the field. Thesis preparation was influenced greatly by discussions with Drs. W.H. MacLean and D. Francis at McGill University. The mechanics of thesis preparation, scientific methodology and thermodynamic calculations were guided by members of Willy's Group: S. Archibald, K. Ault, A. Chouinard, J. Clark, O. Grondin, Dr. A. Migdisov, and Dr. C. Normand.

Table of contents

List of figures and tables

Introduction to the thesis

The Swayze greenstone belt was recently demonstrated to be a relatively unexplored and poorly understood, contemporaneous extension of the prolific Abitibi subprovince (Ayer *et al.*,1999; Heather and Shore, 1999). The Abitibi subprovince is host to approximately 114 known Archean Cu-Zn deposits (Hannington *et al.*, 1999), but, of these, only five deposits are currently in production and only one represents a new orebody, discovered in the last 10 years. The low level of Cu-Zn production and rate of discovery of new orebodies in the Abitibi subprovince is partly a result of the inability of mineral-exploration geologists to incorporate recent technological innovations into exploration programs. Furthermore, most lithogeochemical and alteration lithogeochemical research has focussed on the geology around the largest ore-deposits, resulting in an inadequate understanding of other parts of the belts and non-traditional styles of base-metal mineralization. The geology of SGB and the abundant hydrothermal sediment-hosted base-metal showings it contains are an excellent example of an inadequately understood metallogenic domain in need of investigation using modern techniques. The Swayze greenstone belt is an excellent place to study Archean hydrothermal sediments and volcanic-exhalative base-metal mineralization.

This thesis attempts to answer questions about the processes leading to the development of regionally-extensive hydrothermal sediments and base-metal mineralization in the SGB, and to assess whether the hydrothermal sediments represent the ore-equivalent horizons of undiscovered VMS deposits or, instead, a separate class of sub-economic base-metal sulphide mineralization. In order to understand the genesis of the hydrothermal sediments in the SGB, the physiochemical nature of the hydrothermal fluids and the architecture of the hydrothermal system, 1 : 50 000 scale

reconnaissance mapping, 1 : 5 000 scale outcrop mapping, drill core logging, lithogeochemical sampling and elemental mass-change calculations were undertaken on variably altered volcanic rocks in the south-east SGB. A suite of IF samples was also collected from drill core and outcrop throughout the SGB to examine petrographic relationships to the compositional variability of the hydrothermal sediments. The geology and lithogeochemistry of variably altered volcanic rock and of mineralized and barren hydrothermal sediments were compared to alteration zones and hydrothermal sediments elsewhere in the Superior province to help evaluate the VMS exploration potential of the SGB.

In the second part of this study, we combine geological mapping, and lithogeochemical methods to interpret paleoenvironmental controls on hydrothermal sediment composition in the SGB. These data are used in conjunction with thermodynamic modelling to evaluate the potential of IF to represent a VMS ore-equivalent horizon in the SGB, and to refine exploration models for polymetallic massive-sulphide deposits in other greenstone belts.

A review of the literature on hydrothermal mineral deposits reveals that studies of volcanic-exhalative mineral deposits of the Abitibi subprovince have focussed on three aspects: (a) descriptive studies of significant ore deposits such as those in the Sturgeon Lake (c.f., Morton *et al.*, 1990), South Bay (c.f., Urabe and Scott, 1983), Timmins (c.f., Hannington, 1999), Noranda (c.f., Barrett *et al.*, 1991), and Matagami (Bonavia and MacLean, 1986) massive sulphide districts, (b) alteration studies around orebodies (c.f., Galley, 1993; Gibson *et al.*, 1983; Koopman *et al.*, 1999; MacLean and Hoy, 1991; MacLean and Kranidiotis, 1997), and (c) high field-strength element (HFSE)

lithogeochemical discrimination of the paleo-tectonic settings of the major VMS ore-deposits (c.f., Barrett and MacLean, 1999; Barrie *et al.*, 1993; Lesher *et al.*, 1986).

Lithogeochemical studies of HFSE have been undertaken by several workers to attempt to classify the tectonic environments in which the massive-sulphide deposits of the Superior province formed. Lesher *et al.* (1986) compiled lithogeochemical data from 28 dacitic and rhyolitic complexes in the Abitibi, Wabigoon and Uchi greenstone belts, and developed a classification scheme for rhyolite types based largely on HFSE content. Type FI of Lesher *et al.,* (1986) consists of rhyolite and dacite with high Zr/Y and chondrite-normalized $(La/Yb)_n$ ratios (9-31 and 6-34 respectively), lacking a negative Eu anomaly and having low abundances of the HFSE. This rhyolite-dacite type corresponds to the so-called calc-alkaline type for Archean greenstone belt volcanic sequences of Barrett and MacLean (1999), and Group IV of Barrie *et al.* (1993). These lavas are thought to be the products of a low degree, high pressure-partial melting of garnet-bearing eclogite, or assimilation of crust during the high-level fractionation of a primary magma, and do not host any known, economically viable volcanogenic massive-sulphide (VMS) deposits in the Superior province (Lesher *et al.,* 1986). FI or Group IV volcanic centres are though to be analogous to volcanic complexes developed in modern arc settings. FIII (Lesher *et al., 1986*) or Group I (Barrie *et al.,* 1993) type felsic volcanics exist in bimodal mafic-felsic suites that undergo tholeiitic fractionation trends featuring the incompatibility of HFSE and low Zr/Y and $(La/Yb)_n$ ratios. These volcanic complexes are known to host most of the VMS orebodies in the Superior province.

The lithogeochemistry and mineralogy of hydrothermal alteration stratigraphically below Archean VMS deposits of the Abitibi subprovince has been studied by a number of workers and is summarized in a review by Franklin (1996). Quantitive procedures for

the definition of alteration trends and intensity based on a mass-balance approach were developed by Gresens (1967) and modified by Grant (1986) and MacLean and Barrett (1993) for widespread application in ore-deposit-related alteration studies. The application of such studies has led to the consensus that although there is some variety in the alteration mineral-assemblages and the geometry of alteration zones associated with the volcanic exhalative ore bodies, two salient features persist among deposits. Hydrothermal alteration zones can be broadly subdivided into a distal, semiconformable alteration zone of quartz + sericite with, or without substantial epidote, Mg-rich chlorite or andalusite, that typically grades into a discordant, Fe-rich chlorite, Fe-sulphide-bearing alteration zone which may also contain secondary quartz (Franklin, 1996; Gibson *et al.*, 1983; and MacLean and Hoy, 1991). There is agreement among researchers that these alteration zones were developed during the circulation of metal-charged hydrothermal fluids within submarine, volcano-sedimentary complexes, that lead to the deposition of volcanic-exhalative mineral deposits.

A review of the literature on individual VMS deposits reveals that VMS deposits are commonly associated with an ore-equivalent horizon consisting of hydrothermal sediments that are the distal products of seafloor hydrothermal systems responsible for the production of the massive-sulphide deposits (e.g., Davidson, 1977; Large, 1992; Kalogeropoulos and Scott, 1989; Liaghat and MacLean, 1992; Peter and Goodfellow, 1996, 2000). This horizon is typically an Algoma-type iron formation (IF) from the point of view of its geological setting and its interpreted genesis. Iron formations are conspicuous in greenstone belts because they weather dominantly compared to their host volcanic rocks, frequently forming large, gossanous outcrops along ridge crests

and lake shores, and because they produce extremely well-defined magnetic and electro-magnetic anomalies detectable by airborne and ground geophysical surveys.

Kimberly (1989) summarized genetic models for many types of IF, and for the cherty Algoma-type IF, favours the exhalation of hydrothermal fluids that, upon mixing with seawater in the ocean water column, deposit a combination of fine, iron oxyhydroxide particles including glacuonite, greenalite and silica-gel. The precipitation of hydrous solid phases is interpreted to result from mixing between hydrothermal fluids and seawater. Klein (1973) demonstrated that diagenetic and later greenschist facies metamorphic processes transform various primary precipitates into chert, magnetite, grunerite, stilpnomelane, siderite, garnet, pyrite, pyrrhotite and chlorite. In addition, contamination of Algoma-type metalliferous sediments is common, and microscopic-, metre- or even hundred metre-thick intercalations of volcaniclastic or epiclastic detritus greatly affect bulk compositions (Liaghat and MacLean, 1992; Peter and Goodfellow, 1996, 2000).

IF was first identified in the Swayze greenstone belt (SGB) in 1906 when prospectors in search of iron-ore were drawn to the area by the expansion of railways westward from Sudbury, Ontario (Fulmerton *et al.*, 1993). Unfortunately exploration for iron-ore has been fruitless to date because the iron ranges identified by early prospecting have proven to be too low in grade, high in sulphur content, and too narrow to be economic. However, during the late 1920s base-metal occurrences associated with iron formation were discovered at the Shunsby and Jefferson properties in Cunningham and Marion townships (Fulmerton *et al.*, 1993), and Algoma-type IF in the SGB became an important target for base-metal sulphide exploration. No base-metal production has come from the SGB despite over 70 years of exploration of these targets.

This study comprises a two-part investigation into the genesis of Archean hydrothermal sediments in the Swayze greenstone belt (SGB) and links between volcanic-exhalative activity and base-metal sulphide mineralization, undertaken as a partial fulfillment of a MSc. thesis project by the author. The research project was carried out at McGill University in Montréal, Québec, under the supervision of Prof. A. E. Williams-Jones, and with the support of the Falconbridge Ltd Timmins Exploration Office, in Timmins, Ontario.

References

Ayer, J.A., Trowell, N.F., Amelin, Y. and Corfu, F., 1999. Geological compilation of the Abitibi greenstone belt in Ontario: Toward a revised stratigraphy based on compilation and new geochronology results. Summary of field work and other activities. Ontario Geological Survey Miscellaneous Paper 169, 14-24.

Barrett, T.J., MacLean, W.H.J., Cattalani, S., Hoy, L., and Riverin, G., 1991, Massive sulphide deposits of the Noranda area, Quebec: III; The Ansil Mine. Canadian Journal of Earth Sciences, 28, p. 1699-1730.

Barrett, T.J. and MacLean, W.H., 1999. Volcanic sequences, lithogeochemistry and hydrothermal alteration in some bimodal volcanic-associated massive sulfide systems. Reviews in Economic Geology, 8, p. 101-131.

Barrie, C.T., Ludden, J.N. and Green, T.H., 1993. Geochemistry of volcanic rocks associated with Cu-Zn and Ni-Cu deposits in the Abitibi subprovince. Economic Geology, 88, p. 1341-1358.

Bonavia, F.F., and MacLean, W.H., Geology and ore enrichment factors at Radiore mine, Quebec. Mineralium Deposita, 27, p. 137-146.

Davidson, A.J., 1977. Petrography and chemistry of the Key Tuffite at Bell Allard, Matagami, Quebec. M.Sc. thesis, McGill University, Montreal, Québec, 131 p.

Galley, A.G., 1993. Characteristics of semi conformable alteration zones associated with volcanogenic massive sulphide deposits. Journal of Geochemical Exploration, 48, p. 175-200.

Gibson, H.L., Watkinson, D.H., and Comba, C.D.A., 1983. Silicification: Hydrothermal alteration in an Archean geothermal system within the Amulet Rhyolite formation, Noranda, Quebec. Economic Geology, 78, p. 954-971.

Grant, J.A., 1996. The isocon diagram – A simple solution to Gresen's equation for metasomatic alteration. Economic Geology, 81, p. 47-65.

Gresens, R.L., 1967. Composition-volume relationships of metasomatism; Chemical Geology, 2, p. 47-65.

Hannington, M.D., Barrie, C.D., and Bleeker, W., 1999. The giant Kidd Creek volcanogenic massive sulfide deposit, western Abitibi subprovince, Canada: Preface and introduction. Economic Geology Monograph 10, p. 1-30.

Heather, K.B. and Shore, G.T., 1999. Geology, Swayze greenstone belt, Ontario. Geological Survey of Canada Open File, 3384a-i.

Large, R.C., 1992. Australian volcanic-hosted massive sulfide deposits: Features, styles, and genetic models. Economic Geology, 87, p. 471-510.

Lesher, C.M., Goodwin, I.H., Campbell, I.H. and Gorton, M.P., 1986. Trace element geochemistry of ore-associated and barren felsic metavolcanic rocks in the

Superior Province, Canada. Canadian Journal of Earth Sciences, 23, p. 222-237.

Liaghat, S. and MacLean, W.H., 1992. The Key Tuffite, Matagami mining district: Origin of the tuff components and mass-changes. Exploration and Mining Geology, 1, 2, p.197-207.

Kalogeropoulos, S.I., and Scott, S.D., 1983. Mineralogy and geochemistry of tuffaceous exhalites (tetsusekiei) of the Fukazawa Mine, Hokuroku district, Japan. Economic Geology Monograph 5, p. 412-432.

Kimberly, M.M., 1989. Exhalative origins of iron formations. Ore Geology Reviews, 5, p. 13-145.

Klein, C.K., Jr., 1973. Changes in mineral assemblages with metamorphism of some banded Precambrian iron-formations. Economic Geology. 68, p. 1075-1088.

Koopman, E.R., Hannington, M.D., Santaguida, F., and Cameron, B.I., 1999. Petrology and geochemistry of proximal hydrothermal alteration in the Mine Rhyolite at Kidd Creek. Economic Geology, Monograph 10, p. 267-296.

MacLean, W.H. and Barrett, T.J., 1993. Lithogeochemical techniques using immobile elements. Journal of Geochemical Exploration, 48, p. 109-133.

MacLean, W.H. and Hoy, L.D., 1991. Geochemistry of hydrothermally altered rocks at the Horne Mine, Noranda, Quebec. Economic Geology, 86, p.506-528.

MacLean, W.H., and Kranidiotis, P., 1987. Immobile elements as monitors of mass transfer in hydrothermal alteration: Phelps Dodge massive-sulphide deposit, Matagami, Quebec. Economic Geology, 82, p. 951-962.

Morton R.L., Hudak, G.J., Walker, J.S., and Franklin, J.M., 1990. Physical volcano logy and hydrothermal alteration of the Sturgeon Lake caldera complex. *In* J.M. Franklin, B.R. Schnieders and E.R. Koopman (eds.), Mineral Deposits in the Western Superior Province, Ontario, Geological Survey of Canada, Open File 2164, p. 74-94.

Peter, J.M., and Goodfellow, W.D., 1996. Mineralogy, bulk and rare-earth element geochemistry of massive-sulphide associated hydrothermal sediments of the Brunswick Horizon, Bathurst Mining Camp, New Brunswick. Canadian Journal of Earth Sciences, 33, 2, p.252-283.

Peter, J.M. and Goodfellow, W.D., 2000. Hydrothermal sedimentary rocks of the Heath Steele Belt, Bathurst mining camp, New Brunswick-3: Application of mineralogy, and mineral and bulk compositions to massive-sulphide exploration. *In* Economic Geology Monograph 11: Massive Sulfide Deposits of the Bathurst Mining Camp and Northern Maine. *Edited by* W.D. Goodfellow, S.R. McCutcheon and Jan M. Peter, *in press.*

Urabe, T. and Scott, S.D., 1983. Geology and footwall alteration of the South Bay massive sulphide deposits, northwestern Ontario, Canada. Canadian Journal of Earth Sciences, 20, p. 1862-1879.

Geology of the Swayze greenstone belt

The SGB is considered to be the western-most extension of the Abitibi subprovince of the Superior province in northern Ontario (c.f., Ayer *et al.,* 1999; and Heather and Shore, 1999). The belt is connected to the rest of the Abitibi subprovince by a thin band of supracrustal rocks in the north-east and to the Shining Tree greenstone belt by a sinew of volcanic and sedimentary rocks in the south-east. The Ramsey-Algoma batholith and the Chester Granitoid Complex abut the SGB to the south. The eastern margin of the belt is bound by the Kenogamissi batholith, the north by the Biggs pluton, and the west by the Kapuskasing structure (Figure 2.1). The study area was originally mapped by the Ontario Department of Mines in the 1930s (Furse, 1932; Laird, 1936), and subdivided into east-south-east striking, steeply dipping, foliated Kewatin mafic to felsic volcanics, Timiskaming clastic sediments, and massive and sheeted Algoman granite-diorite intrusive suites, all cut by north-north-west striking, sub-vertical dipping diabase dykes of the Matachewan swarm. At the time of the first provincial survey, gold mineralization had been discovered in Chester and Osway townships in the south-east Swayze greenstone belt (SESGB) and further exploration and minor production was in progress. The area was re-mapped several times by government geological surveys and mining companies, the most recent effort being a seven-year joint Northern Ontario Development Agency-Geological Survey of Canada (NODA-GSC) project completed in 1999 (Heather and Shore, 1999). Access to the study area from the city of Timmins, Ontario, is by Highway 101, the all-weather Sultan Industrial Road, and by gravel logging roads, trails, lakes and rivers. The field area has been extensively logged for the past 30 years, resulting in improvements to access and to outcrop exposure. Relief in the SGB is less than 50 m and a veneer of Quaternary till, sand and clay deposits fills

depressions in bedrock topography. Quaternary deposits are overlain by muskeg, alder swamp, and black spruce and poplar fores. The SGB lies on the northern flank of the Arctic – Atlantic (James Bay – Great Lakes and St. Lawrence) watershed, and drainage is dendritic in form and flow is roughly northward.

2.1 Geology of the SGB supracrustal stratigraphy

On the basis of field observations and regional geological mapping, radiometric age determinations, and compilation of previous work, Heather *et al.* (1995) defined a stratigraphic type-section through the relatively undeformed Woman River anticline (Figure 2.1). The type-section correlates well with stratigraphic relationships throughout the SGB. Four cycles of mafic to felsic volcanic rocks (Chester, Marion, Trailbreaker and Swayze groups), each with minor intercalations of clastic sediment, occur at the base of the SGB stratigraphic section and correspond to the Kewatin volcanic rocks described by previous workers (cf. Laird, 1936; Thurston *et al.*, 1977). All, except the Swayze Group, are capped by regionally extensive iron formation. The uppermost group in the type-section is the Ridout Group, which unconformably overlies the Trailbreaker and Swayze groups in various parts of the SGB. The Ridout Group consists of clastic sediments and quartz pebble conglomerates, with minor quartz- and feldspar-porphyritic felsic dykes (QFP), felsic volcaniclastics and tuffaceous beds. These rocks correspond to the Timiskaming assemblage sediments described by previous workers (cf. Ayer *et al.*, 1999; Thurston *et al.*, 1977) and exhibit stratigraphic, temporal, textural and petrographic similarities to other Timiskaming sequences in the Abitibi subprovince. Heather and Shore (1999) further sub-divided the five supracrustal groups into formations on the basis of dominant lithology and geographic location within the SGB.

U-Pb age determinations of zircons from a felsic lapilli-tuff of the Yeo Formation (CYf), the uppermost unit of the Chester Group, indicate that CYf volcanic activity occurred at 2739 (± 2) Ma. The upper limit of volcanic activity of the Strata Lake Formation, at the top of the Marion Group (MSf) has been similarly dated at 2731 to 2724 (± 2) Ma (Heather and van Breeman, 1994; Heather *et al.,* 1995, 1996; and Heather and Shore, 1999). Zircons from an outcrop of volcanic rock of intermediate composition assigned to the Trailbreaker Group in Huffman Township yielded ages of 2707 (± 2) Ma (Heather *et al.*, 1995,1996). Work by Ayer *et al.* (1999), suggests that the ages published by Heather *et al.* (1995, 1996) and Heather and Shore (1999), are correlative with those of other volcanic assemblages elsewhere in the western Abitibi subprovince, such as the ca. 2745-2740 Ma Pacaud assemblage south of Kirkland Lake, and the ca. 2730-2725 Ma Deloro and 2710-2702 Ma Tisdale assemblages in the Timmins area.

2.2 Chester Granitoid Complex geology

The Chester Granitoid Complex (CGC) underlies Chester Group volcanic rocks in the south-east sector of the SGB, and has been interpreted by Heather and Shore (1999) as being the sub-volcanic equivalent of CYf rocks on the basis of stratigraphic evidence, geochronology and rare-earth element (REE) geochemistry. The CGC is composed of a northern leuco- and melano- hornblende-trondhjemite phase and a southern diorite phase, both overlain by CYf rocks. The CGC is host to numerous Au-Cu showings and extensive epidote-quartz alteration and pyritic vein mineralization.

2.3 SGB structural geology

Heather *et al.* (1995) and Heather and Shore (1999) have described a complex metamorphic and structural history for the SGB. Primary sedimentary and volcanic

textures (D_0) and synvolcanic faults have a sub-parallel, penetrative schistosity (S_1) and are deformed locally into isoclinal, intrafolial folds (FI) (Heather and Shore, 1999). D_0 and D_1 features of the supracrustal rocks are re-folded about east-west trending axes (F_2), forming broad, doubly plunging anticlinoria and tight, steeply plunging synclinoria (Heather and Shore, 1999), resulting in a cuspate-lobate map pattern (Figure 2.1). High strain zones in the cores of cuspate F_2 synclinoria resulted in a well-developed axial planar cleavage and intense flattening, constrictional elongation with some component of simple shear (Heather and Shore, 1999). Heather *et al.* (1995) suggested that the Ridout high strain zone, which runs through the southern portion of the SGB, may be an extension of the Larder Lake-Kirkland Lake-Matachewan structure to the east in the southern Abitibi subprovince. Late north-north-west striking brittle faults have a spacing of 5-10 km, and are parallel to, and thought to be associated with the emplacement of diabase dykes of the Matachewan dyke swarm.

All supracrustal rocks in the SGB have been metamorphosed to at least greenschist facies. Amphibolite to pyroxene hornfels facies contact-metamorphism has affected rafts of supracrustal material within encompassing batholiths and is also manifested by narrow (~1 km) aureoles around syn- to post-tectonic batholiths. Contact-metamorphic aureoles are folded about F_2 axes.

2.4 SGB base-metal mineralization

Four major base-metal occurrences occur in the SGB, but there has been no significant production from the belt to date (Figure 2.1). An exhaustive list of mineral showings from the SGB has been compiled by Fulmerton *et al.* (1993) and Fulmerton (1995).

The Jefferson Zn-Pb deposit (Figure 2.1) was discovered in the 1930s and underwent extensive, though sporadic exploration until the 1990s. Mineralization occurs as several small lenses of semi-massive- and stringer-type pyrite-sphalerite-galena with very minor chalcopyrite. The mineralization is hosted by brecciated IF above the Marion Formation, Strata Lake Group felsic volcanics (MSf) and below mafic flows of the Trailbreaker Group, October Lake Formation (TOm). A resource of 100 200 metric tonnes (t) grading 4.6 % Zn and 3.3 % Pb has been calculated for the deposit (Fulmerton, 1995).

Mineralization at the Shunsby Zn-Cu deposits (Figure 2.1) occurs at the same stratigraphic level as the Jefferson deposit; however, at the Shunsby deposits it comprises stringers of pyrite-chalcopyrite mineralization in a muddy rhyolite breccia below a discontinuous horizon of brecciated, laminated hydrothermal sediments (pyrite-sphalerite-chert) below the base of the TOm. Five separate deposits have been outlined on the Shunsby property, with higher Zn and lower Cu grades in the larger lenses. A total resource of 3.98 Mt grading 2.51% Zn and 0.61% Cu has been calculated for the Shunsby deposits (Fulmerton, 1995).

The Peter Lake Zn-Pb showing has been intersected in three drill holes and lies along the same stratigraphic horizon as the Shunsby and Jefferson deposits, about 3 km west-north-west of the Shunsby property (Figure 2.1). This prospect consists of a brecciated, discontinuous 5-10 m thick, laminated pyrite-sphalerite-chert horizon containing minor amounts of galena.

Base-metal mineralization at the Huffman Township Zn-Pb showing has been exposed over a strike length of 250 m in three small pits at surface and was intersected in three drill holes. Mineralization consists of a single, 2 m thick pod of massive pyrite, pyrrhotite

and sphalerite, and several discontinuous 5-10 m thick pyrite-chert-sphalerite-chlorite-argillite horizons with thin laminations and cross-cutting veinlets of sphalerite and galena. The mineralized horizon occurs at the top of the Yeo Formation felsic volcanic pile within hydrothermal sediments overlain by Trailbreaker Group mafic volcanics. The most economically important drill hole intersection cut 12.3 m of argillaceous breccia-type IF with 1.5% Zn, 0.65% Pb and 1.5 ppm Ag, and 4 m of breccia-type IF with 2.8% Zn, 0.85 % Pb and 3.6 ppm Ag (calculated from data supplied by L. Bonhomme).

2.5 References

Ayer, J.A., Trowell, N.F., Amelin, Y. and Corfu, F., 1999. Geological compilation of the Abitibi greenstone belt in Ontario: Toward a revised stratigraphy based on compilation and new geochronology results. Summary of Field Work and Other Activities. Ontario Geological Survey Miscellaneous Paper 169, 14-24.

Fulmerton, S., Houle, K., and Archibald, G., 1993. Mineral showings, occurrences, deposits and mines of the Swayze greenstone belt, interim report, 1 and 2. Ontario Geological Survey Open File Report 5871, p. 1-763.

Fulmerton, S., 1995. Summary tables on mineral prospects in the Swayze greenstone belt. Ontario Geological Survey Open File Report 5913. p. 1-105.

Furse, G.D., 1932. Geology of the Swayze area. Ontario Department of Mines, Annual Report, 41, Pt. 3, p. 35-53.

Heather, K.B. and Shore, G.T., 1999. Geology, Swayze greenstone belt, Ontario. Geological Survey of Canada Open File, 3384a-i.

Heather, K.B. and van Breeman, O., 1994. An interim report on geological, structural and geochronological investigations of granitoid rocks in the vicinity of the

Swayze greenstone belt, southern Superior province, Ontario. Current Research 1994-C; Geological Survey of Canada, p. 259-268.

Heather, K.B., Shore, G.T. and van Breeman, O., 1995. The convoluted "layer-cake": An old recipe with new ingredients for the Swayze greenstone belt, southern Superior province, Ontario. Current Research 1995-C, Geological Survey of Canada, p. 125-136.

Heather, K.B., Shore, G.T. and van Breeman, O., 1996. Geological investigations in the Swayze greenstone belt, southern Superior province, Ontario. Current Research 1996-C, Geological Survey of Canada, p. 125-136.

Laird, H.C., 1936. Geology of Opeepeesway Lake area, District of Sudbury. Ontario Department of Mines, Annual Report, 44, p. 31-37, accompanying 1 : 63 360 scale map.

Thurston, P.C., Siragusa, G.M., and Sage, R.P., 1977. Geology of the Chapleau area, Districts of Algoma, Sudbury, and Cochrane. Ontario Division of Mines Geoscience Report 157, 293 p.

Figure 2.1: A geological map of the Swayze greenstone belt. (Compiled by the author after Heather and Shore (1999) and unpublished Falconbridge Limited data.)

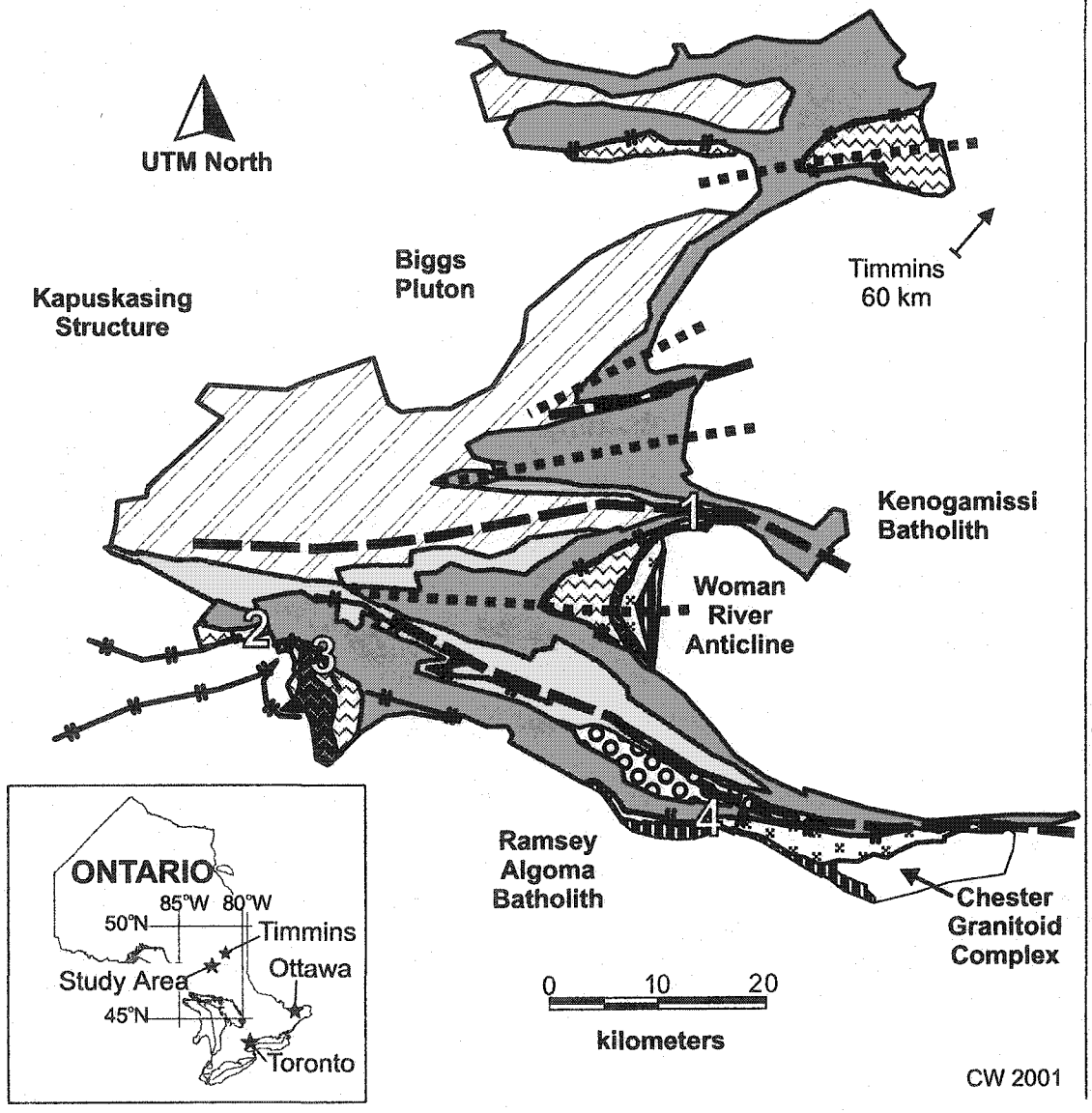

Swayze greenstone belt supracrustal stratigraphy

- Ridout Group sediment
- Swayze Group volcanic and sediment
- iron formation
- THi/THf (intermediate and felsic volcanic)
- TOm (mafic volcanic)
- iron formation
- MSf (felsic volcanic)
- MRm (mafic volcanic)
- iron formation
- CYf (dacite, rhyolite and low-Ti rhyolite)
- CAm (basalt)
- igneous / metamorphic complexes and undivided supracrustal rocks

Regional structural geology

- F_2 anticline axial-trace
- F_2 syncline axial-trace

Base-metal mineralization

1. Jefferson Zn-Pb deposit
2. Shunsby Zn-Cu deposits
3. Peter Lake Zn-Pb showing
4. Huffman Township Zn-Pb showing

Geology and lithogeochemistry of the Chester Group, Swayze greenstone belt, Ontario

Christopher Wright[1] and A.E. Williams-Jones[2]

[1]Falconbridge Ltd., Timmins Exploration
P.O. Box 1140, Timmins, Ontario, Canada
P4N 7H9

[2]Department of Earth and Planetary Sciences
McGill University
3450 University St., Montréal, Québec, Canada
H3A 2A7

March 21, 2002

3.1 Abstract

Exposures of Chester Group volcanic rocks within the south-east Swayze greenstone belt (SESGB) consist of pillowed, amygdaloidal and variolitic basalt of the Arbutus Formation, and quartz and feldspar-phyric dacite, rhyolite and low-Ti rhyolite with massive, laminated pyroclastic, and fragmental textures belonging to the Yeo Formation. The Chester Group volcanic rocks are overlain by a horizon of hydrothermal sediments 5-20 m thick, containing sub-economic Zn-Pb-sulphide mineralization. Macro-scale textural characteristics combined with high-field-strength element analyses indicates that dacite and rhyolite were deposited in a submarine volcanic-arc setting in which calc-alkaline magmas and lavas were emplaced, followed the emplacement of a second magma, which through crustal assimilation and fractionation lead to the extrusion of low-Ti rhyolite. Yeo Formation rocks have undergone a regionally extensive sericite-quartz (type 1) alteration, involving loss of 3.25 wt.% Na_2O, addition of 12 wt.% SiO_2, and 2.2 wt.% K_2O, and 13% net mass-gain, indicating water/rock ratios of at least 6. Chlorite-sericite±biotite±garnet (type 2) alteration at paleo-hydrothermal vent sites was localized along syn-volcanic fault structures. Alteration was accompanied by a loss of 2.44 wt.% Na_2O, and 8.69 wt.% SiO_2, and a gain of 5.90 wt.% Fe_2O_3, requiring water/rock ratios of at least 432. Type 2 alteration is best developed in volcanic rocks in contact with Zn-Pb mineralized hydrothermal sediments.

3.2 Introduction

The Canadian Shield is known to host 115 Archean Cu-Zn deposits, representing approximately 80% of the occurrences of this class of deposit in the world (Hannington *et al.*, 1999). The richly endowed Abitibi subprovince of the Superior province is host to 84% of these deposits; the majority of them being discovered in the period from 1950 to 1970 as a result of dramatic improvements in mineral exploration techniques, including the refinement of geological models, modern diamond-drilling equipment, and geophysical and geochemical prospecting. However, only five of these deposits, Kidd Creek, Bouchard-Hébert, Louvicourt, Dumagami-Laronde and Bell Allard are currently in production, and despite recent innovations in exploration techniques such as precise and inexpensive whole-rock lithogeochemical techniques, global position satellite (GPS) networks, geographic information system (GIS) database management, further refinement of geophysical and geochemical prospecting methods and their contribution to the enhancement of geological models, only one of these orebodies was discovered in the last 10 years.

This study was undertaken with the purpose of using modern mineral-exploration techniques to improve our understanding of the submarine volcanic-exhalative processes that lead to the development of regionally extensive hydrothermal sediments and base-metal mineralization. The first objective was to characterize the paleo-tectonic setting of volcanic rocks of the Chester Group and synvolcanic intrusives of the Chester Granitoid Complex (CGC) of the south-east Swayze greenstone belt (SESGB) on the basis of field observations and high-field-strength element (HFSE) lithogeochemistry. The second objective of the study was to understand the chemical changes of supracrustal rocks during hydrothermal alteration accompanying the volcanic exhalation

of fluids responsible for overlying hydrothermal sediments. The hydrothermal alteration of the volcanic strata is defined in terms of mass and elemental fluxes, mineralogical changes, alteration fluid-type and the spatial distribution of the alteration zones. The synthesis of the lithogeochemical and alteration geochemical investigations resulted in a genetic model of hydrothermal alteration during the production of SGB volcanic-exhalative hydrothermal sediments.

Lesher *et al.* (1986) compiled lithogeochemical data from 28 dacitic and rhyolitic complexes in the Abitibi, Wabigoon and Uchi greenstone belts, and developed a classification scheme for rhyolite types based largely on HFSE content. Type FI of Lesher *et al.*, (1986) consists of rhyolite and dacite with high Zr/Y and chondrite-normalized $(La/Yb)_n$ ratios (9-31 and 6-34 respectively), lacking a negative Eu anomaly and having low abundances of the HFSE. This rhyolite-dacite type corresponds to the so-called calc-alkaline affinity type for Archean greenstone belt volcanic sequences of Barrett and MacLean (1999), and the Group IV type of Barrie *et al.* (1993). These lavas are thought to be the products of a low degree of partial melting of garnet-bearing eclogite. They do not host any known, economically viable volcanogenic massive-sulphide (VMS) deposits in the Superior province (Lesher *et al.*, 1986). FI or Group IV volcanic centres are thought to be analogous to volcanic complexes developed in modern arc settings. FIII (Lesher *et al., 1986*) or Group I (Barrie *et al.*, 1993) type felsic volcanics exist in bimodal mafic-felsic suites that undergo tholeiitic fractionation trends featuring the incompatibility of HFSE and low Zr/Y and $(La/Yb)_n$ ratios. These volcanic complexes are known to host most of the VMS orebodies in the Superior province.

The lithogeochemistry and mineralogy of hydrothermal alteration stratigraphically below typical Archean VMS deposits has been studied by a number of workers (c.f., Franklin *et*

al., 1981; Gibson and Watkinson, 1999; Koopman *et al.,* 1999; and MacLean and Hoy, 1991) and is summarized by Franklin (1996). The Helen Mine, a volcanic-exhalative siderite deposit in the Wawa greenstone belt is also characterized by a broad footwall alteration zone (Morton and Nebel, 1984), and is unique among volcanic-exhalative ore-deposits in the Superior province because of its base-metal poor mineralogy (Goodwin *et al.*, 1985). Although there is some variability in the nature of the alteration facies and their geometry below the ore bodies, they can be broadly subdivided into a distal, semiconformable alteration zone of sericite, Mg-rich chlorite and andalusite (Franklin, 1996; and MacLean and Hoy, 1994), and a discordant, proximal, chlorite-rich, quartz and Fe-sulphide-bearing alteration zone. There is agreement among workers that these alteration zones were developed during the circulation of metal-charged hydrothermal fluids within submarine, volcano-sedimentary complexes, that lead to the deposition of volcanic-exhalative mineral deposits.

3.3 Field and analytical methodology

The SESGB study area is centred on the Huffman Township base-metal sulphide occurrence, about 100 km south-west of the city of Timmins in northern Ontario (Figure 3.1). Data were collected from 1 : 50 000 scale and 1 : 5 000 scale geological mapping, whole-rock lithogeochemical analysis and petrographic analysis of thin sections prepared from outcrop exposures and diamond drill core. Additional samples were collected from correlative strata underlying eight townships east of the map area of Figure 3.2 and supplement those taken from the study area. The field area has been extensively logged for the past 30 years, resulting in improvements to access and enhancing outcrop exposure to approximately 1-2% of the study area (Heather and Shore, 1999).

Lithogeochemical data has been compiled from analysis of 42 samples of volcanic rock collected by the first author from outcrop and diamond drill core in the SESGB, and from 8 sample compositions from an unpublished database compiled by J. Harris and cited in Harris *et al.* (1999).

A 2 to 4 kilogram sample was taken from each outcrop, and a 1 kg portion was removed from the original sample block for analyses. Drill core samples are composites reflecting entire IF intersections, with two 2 cm-long pieces taken from each metre of IF.

Samples were sent to TSL Assayers in Swastika, Ontario where they were crushed to a minus 10 mesh and a 200 g split was taken. The 200 g sample was then pulverized to 70-90% minus 150 mesh with a ring pulverizer. To measure the loss on ignition a 1 g split was roasted for 2 hours at 1000 ° C, weighed, and the LOI was calculated by dividing this weight by the original weight of the sample. A 5 g split was taken and analysed for Au using standard fire assay procedures. An additional 5 g split was taken and analyzed for Zn, Pb and Cu, by flame atomic absorption (FAA) spectroscopy. The remaining pulverized sample was then sent to the TSL Assayers laboratory in Vancouver where C and S were determined by infrared methods and the left-over pulverized sample was roasted for 2 hours at 1000 ° C to oxidize the sulphide component of the sample. A 5 g split of the roasted, pulverized sample was fused with a lithium metaborate flux, dissolved in HNO_3 and analyzed for major elements and Cr, Zr, Y, Cu, Zn, Ni, Co, Nb, V, Sc, Be, Ba and Sr by ion-coupled plasma atomic emission spectroscopy (ICP-AES). The total concentration of iron (Fe^{2+} and Fe^{3+}) is expressed as Fe_2O_3 and all sample compositions listed in this paper have been normalized on a volatile free basis such that major element concentrations (expressed as oxides) total to 100 wt.%.

Zinc and Cu values used in this study are from analysis by ICP-AES unless > 500 ppm, in which case FAA analyses are reported. Selected pulps were also analyzed for trace elements and REE by ion-coupled plasma mass spectroscopy (ICP-MS) at ActLabs in Ancaster, Ontario, from a solution derived from a fused sample.

All samples from outcrop and archived drill core were examined macroscopically to estimate modal mineralogy. A representative suite of polished thin sections was prepared by G. Panagioditis at the McGill University Rock Preparation Lab, and examined under a petrographic microscope by the first author. Least-altered samples of each rock type discussed in this paper were chosen based on the near absence of the secondary minerals sericite and chlorite present in hand specimens and thin sections and relatively low LOI.

3.4 Geology of the Chester Group and Chester Granitoid Complex

The 8 km^2 area considered in this study is underlain by volcanic rocks belonging to the Chester and Trailbreaker groups, and was mapped at a scale of 1 : 5 000 (Figure 3.2). The southern edge of the supracrustal stratigraphy abuts against the foliated biotite (± hornblende) tonalite rocks of the Ramsey-Algoma Batholith. The lower 1.2 km of volcanic stratigraphy is assigned to the Chester Group and has been dated at 2739 (±2) Ma (Heather *et al.*, 1995); the upper mafic rocks, stratigraphically above the hydrothermal sedimentary horizon, are assigned to the October Lake Formation of the Trailbreaker Group (TOm) of Heather and Shore (1999), and have been dated at 2707 (±2) Ma (Heather *et al.*, 1995).

The southernmost rocks of the Chester Group consist of a 1 000 m thick sequence of basaltic flows with well-developed pillow forms and inter-pillow hyaloclastite. The rocks

have been assigned to the lowest unit of the Chester Group, the Arbutus Formation (CAm) of Heather and Shore (1999). A 25 m thick by 750 m long horizon of variolitic mafic flows occurs conformably within the upper quarter of the CAm basalt flows (Figure 3.2), and is composed of 0.2 to 5 cm diameter, popcorn-shaped, leucocratic variolites within a fine grained, melanocratic matrix (Figure 3.3a). The variolites become smaller toward the upper and lower contacts of the unit, but individual pillow-forms and extrusive textures are not well developed. The CAm sequence is weakly schistose and both schistosity and primary, planar volcanic features strike east-south-east and dip subvertically. Pillow facing directions consistently indicate that stratigraphy youngs to the north.

A 100-300 m thick sequence of felsic volcanic rocks and their epiclastic equivalents overlies the CAm in the study area. The felsic volcanic rocks have been assigned to the Chester Group, Yeo Formation (CYf) of Heather and Shore (1999), and are subdivided into dacite, rhyolite and low-Ti rhyolite on the basis of their major element geochemistry (Figure 3.4; see below). Dacitic rocks are compositionally homogeneous but display two distinct textures at the Huffman Township property. In the centre of the map area, very finely laminated, quartz-feldspar-phyric dacite is exposed north of the hydrothermal sediments. Dacite south and east of the IF consists of quartz and feldspar phenocrystic fragmental rocks, and dacite in the east-central part of the map area is characterized by laminated, quartz- and feldspar-phyric ash tuff and fragmental textures (Figure 3.3b,c). Because massive and flow textured dacite is absent from the map area, we suggest that the vent for the dacite lies outside map area of Figure 3.2.

Massive and locally flow-banded rhyolite occurs in a 100 m thick dome in contact with basalt of the CAm in the centre of the map area (Figure 3.5a), while ash tuff and lapilli

tuff occur in the upper rhyolite, in contact with hydrothermal sediments (Figure 3.3d). In thicker portions of the CYf to the east of the Huffman Township Zn-Pb showing, nearly all felsic volcanic material sampled is of rhyolite composition. U-Pb age determinations of zircons from a lapilli tuff of rhyolitic composition in the SESGB place felsic volcanic activity in the CYf at the top of the Chester Group at 2739 (± 2) Ma (Heather *et al.*, 1995, 1996).

A second sequence of aphyric to quartz-phyric massive, flow-banded rhyolite and rhyolitic ash tuff, having a composition consistent with more evolved or more highly fractionated rhyolite referred to herein as low-Ti rhyolite (Figure 3.4, Table 3.1), is exposed stratigraphically above and to the west of the rhyolite dome. The low-Ti rhyolite varies from weakly foliated and massive at the base to fragmental and volcaniclastic both northward and laterally across the map area (Figure 3.5b).

Hydrothermal sediments occur within the map area of Figure 3.3 both at and near the top of the CYf. Well-banded, chert and magnetite bearing iron formation (IF) is exposed at the western end of the study area in a sequence up to 25 m thick (Figure 3.5d). At the west end of the study area, IF is in contact with low-Ti rhyolite to the south and mafic volcanics of the Trailbreaker Group, October Lake Formation (TOm) to the north. To the west, iron- and silica-rich hydrothermal sediments are generally poorly laminated, brecciated, thinner and occur along less continuous horizons. At the centre of the study area, hydrothermal sediments containing sub-economic quantities of Zn and Pb sulphides overlie both low-Ti rhyolite and a second, upper horizon of rhyolite ash tuff. At the western end of the alteration study area, a lack of outcrop and diamond-drill holes along the CYf—TOm contact, precludes exposure of the hydrothermal sedimentary horizon, however, airborne geophysical survey data (Ontario Geological Survey, 1993)

and horizontal-loop electromagnetic (HLEM) survey data (L. Bonhomme *personal communication,* 2000) suggest that the hydrothermal sediments extend westward along the contact, beyond the edge of the study area.

Well-pillowed basalt and massive gabbro of the TOm formation outcrops across the map area to the north of the hydrothermal sediments, and pillow facings consistently indicate that top is to the north. Narrow, highly strained, strongly schistose domains striking east south-east run through the basalt 100 m north of its lower contact. The basalt sequence is intercalated with discontinuous horizons of well-laminated, interflow sediment. Numerous fine-to medium-grained mafic dykes with sharp, relatively unaltered contacts cross-cut Chester Group stratigraphy in the centre of the map area. These dykes are interpreted to have fed the Trailbreaker group magmatism and do not appear on Figure 3.4.

The Chester Granitoid Complex (CGC) truncates the CAm volcanic stratigraphy and is stratigraphically (and structurally) overlain by the CYf and Trailbreaker Group volcanics. The CGC comprises a northern trondhjemite phase and a southern diorite phase (Heather and Shore, 1999). The trondhjemitic phase is composed of biotite trondhjemite, tonalite, quartz-rich tonalite and feldspar porphyritic tonalite with sub-metre wide pyrite veins enveloped by planar, magnetite-chlorite-epidote altered selvages (Heather and Shore, 1999) locally containing up to 2 wt.% Cu and anomalous concentrations of gold (Fulmerton *et al.,* 1993). The southern dioritic portion of the CGC is composed of hornblende diorite, hornblende quartz diorite and leuco-diorite and has been observed to both cross cut the trondhjemitic intrusives and occur as inclusions within the trondhjemite phase (Heather and Shore, 1999). Both phases of intrusive contain up to 1% disseminated magnetite. U-Pb ages of 2740 (±2) Ma have been

determined by Heather and van Breeman (1994) from zircon crystals obtained from the CGC trondhjemite.

3.5 High field-strength element geochemistry of SESGB rocks

Lithogeochemical studies of metamorphosed and hydrothermally altered rock are often hampered by element mobility, especially the alkali and alkali-earth elements or large ion lithophile elements (LILE), and transition elements. In the case of alteration associated with VMS deposits, immobility of high field-strength elements (HFSE) and rare-earth elements (REE) is well-established (c.f., Barrett and MacLean 1994; Finlow-Bates and Stumpfl, 1981; MacLean and Barrett, 1993; MacLean and Kranidiotis, 1987) and the interpretation of chondrite-normalized REE patterns and HFSE concentration ratios such as Zr/Y has consequently become widespread as a means of classifying altered and metamorphosed volcanic rocks in greenstone belts (Lesher *et al.*, 1986, Barrett and MacLean,1999, Prior *et al.*, 1999).

Average bulk rock major- and trace element compositions of Chester Group basalts (CAm) and felsic volcanics (CYf) are listed in Table 3.1 and REE concentrations for individual analyses appear in Appendix 3.1. CAm basalts have low concentrations of Zr, and Y, a low Zr/Y ratio, and relatively high concentrations of Ti (Figure 3.6; Table 3.1). A plot of REE concentrations of CAm basalt normalized to C1 chondrite (cf. Boynton, 1984) yields a flat pattern (La/Yb_n = 1.2) with only minor enrichment of all REE over chondrite (Figure 3.7a).

CYf rhyolites and dacites have similar Zr/Y ratios, that are considerably higher (>5) than those of low-Ti rhyolite and CAm basalt. CYf rhyolite and dacite have fractionated REE patterns, and are more enriched in the LREE La, Ce, Pr, Nd and Sm than CAm and

chondrites (Figure 3.7). Chondrite-normalized $(La/Yb)_n$ ratios are 6.7 and 6.0, respectively, for dacite and rhyolite, and REE patterns for CYf rhyolite show a negative Eu anomaly (Figure 3.7b). The CYf rhyolite and dacite have similar HFSE ratios and overall abundances to the CHC trondhjemite (Figure 3.6, Figure 3.7).

CYf low-Ti rhyolite has the highest Al/Ti ratio of Chester Group volcanics (160; Table 3.1), and a lower Zr/Y ratio than the CYf rhyolite and dacite (Table 3.1; Figure 3.6). Low-Ti rhyolite also has a lower $(La/Yb)_n$ and lower REE abundances than the CYf dacite and rhyolite (Figure 3.7). Overall REE abundances and HFSE ratios are similar between CYf low-Ti rhyolite and CGC diorite (Figure 3.6, Figure 3.7).

3.6 Alteration of volcanic stratigraphy underlying SESGB hydrothermal sediments

3.6.1 Petrography of altered felsic volcanic stratigraphy associated with hydrothermal sediments

Outcrop and drill core mapping of SESGB stratigraphy indicates two distinct hydrothermal alteration mineral assemblages. The most common alteration facies (type 1), consists of finely disseminated sericite within milky white felsic volcanic and volcaniclastic rocks. Within hyaloclastic, volcanic breccia and fragmental rocks, matrices consist of fine-grained quartz and sericite, locally resulting in a characteristic matrix-recessive weathering pattern (Figure 3.3d). Sericite occurs as individual, pristine grains 5-20 µm long and 1-5 µm wide in tuffaceous rocks (Figure 3.8a). Sericitic alteration is associated with quartz-filled veinlets and primary breccia matrices (Figure 3.8b).

Petrographic studies indicate that chlorite-rich alteration occurs in breccia and hyaloclastic matrices, in which cases, fragments are altered to quartz and sericite

(Figure 3.8c). In areas of stronger alteration, fine-grained chlorite and sericite are overprinted by coarser muscovite, biotite and garnet porphyroblasts (Figure 3.8d). Biotite and muscovite porphyroblasts have cleavages oblique to those in sericite and chlorite indicating later formation and mineralogical re-equilibration during regional-metamorphism (Figure 3.8d). The assemblage characterized by chlorite-sericite ± muscovite ± biotite ± garnet defines type 2 alteration in the SESGB area.

3.6.2 Mass-changes accompanying hydrothermal alteration

Net mass-changes and individual elemental fluxes caused by hydrothermal alteration were calculated for CYf samples by the single precursor technique outlined in MacLean and Kranidiotis (1987) and MacLean and Barrett (1993). The principle of the single-precursor method is that inter-element ratios of immobile elements are maintained during addition or subtraction of mobile elements.

Precursor compositions for dacite, rhyolite and low-Ti rhyolite were compiled from whole-rock analyses of least-altered samples and are listed in Table 3.1. The immobility of Al and Ti during hydrothermal alteration in the SESGB can be demonstrated with a bivariate plot of Al_2O_3 versus TiO_2, in which altered samples of similar initial composition plot along lines trending through the origin thus maintaining constant inter-element ratios despite addition or subtraction of mobile elements (Figure 3.9).

Calculation of net mass-change or mass factor (MF) for altered CYf rocks is based on the ratio of Al in the appropriate precursor to Al in each altered sample (e.g., $Al_2O_{3\ precursor}$ / $Al_2O_{3\ altered\ sample}$). The calculation of pre-alteration compositions was accomplished by multiplying the concentrations of each by the MF. The appropriate precursor composition was then subtracted from the resulting reconstituted composition to arrive

at calculated elemental mass-changes. Altered rock compositions, mass-factors, reconstituted compositions and mass-changes are reported in Appendix 3.2.

Hydrothermal alteration involving both mass-gains and mass-losses has affected CYf rocks underlying the Huffman Zn-Pb occurrence. Samples from across the SESGB showing predominantly type 1 sericitic alteration underwent net mass-gains of Si, and K; K was gained in roughly similar proportions to losses of Na (Table 3.2). CYf samples with type 2 alteration assemblages underwent loss of Si and Na, and enrichment of Fe, Mg, Mn, S, Zn and Cu compared to the precursor, however, some rocks with relatively weak type 2 alteration overprinting type 1 alteration experienced minor net mass-gains. Petrographic analyses of sericite-quartz altered samples indicate that much of the silica added during type 1 alteration takes the form of quartz in-fillings of fractures and primary pore spaces. Type 1 and type 2 alteration facies can be distinguished on the basis of alteration mineral assemblages and mass-changes, which are summarized in Table 3.2.

Field relations of types 1 and 2 alteration are illustrated in Figure 3.10. The only exposures of type 2 alteration found during mapping of the SESGB for study were observed in drill core and outcrop in the map area of Figure 3.2. This is also the only area where flow-facies or (magmatic) vent-proximal felsic volcanic material was observed in the SESGB. Furthermore, examples of strong type 2 alteration of volcaniclastic material were restricted to rocks within 250 m of Zn-Pb sulphide mineralization and proximal to synvolcanic faults, traceable by north-south displacement of volcanic contacts during detailed mapping (Figure 3.10). Examples of type 1 alteration were found in the westernmost exposures of CYf low-Ti rhyolite in the SESGB, in one low-Ti rhyolite sample from the Huffman Township showing (Figure 3.10), and in locations up to 25 km east of the showing.

3.7 Discussion

3.7.1 Paleo-tectonic setting of the Chester Group felsic volcanics

The high Zr/Y and $(La/Yb)_n$ ratios of the Yeo Formation dacite and rhyolite are similar to those of the CGC trondhjemite, and are consistent with the HFSE concentrations of Archean calc-alkaline volcanic centres elsewhere in the Superior province (Barrett and MacLean, 1999; Barrie *et al.,* 1993; and Lesher *et al.,* 1986). Petrogenetic models for the formation of these calc-alkaline magmas require the presence of garnet either as a crystallizing phase during fractionation, or as a stable phase in the residua during partial melting (Lesher *et al.,* 1986). Partition coefficients (C_f) for La and Zr between garnet and a coexisting felsic melt are low (C_f = 0.39 and 1.2 respectively) compared to those for Yb and Y (C_f = 43.475 and 35 respectively), giving rise to a HREE and Y-depleted melt (Rollinson, 1993, Table 4.3, p. 110-111).

Low-Ti rhyolite has Zr/Y and chondrite-normalized La/Yb ratios (4.0 and 5.7 respectively) within the range of the FII or FIII rhyolite types of Lesher *et al.* (1986) and the tholeiitic category of Barrett and MacLean (1999); however, low-Ti rhyolite lacks the elevated concentrations of HFSE of these rhyolite types. Therefore, we propose that the CYf low-Ti rhyolite represents a distinct type of HFSE-depleted tholeiitic rhyolite not yet documented in the Superior Province. We reason that the low Zr/Y and La/Yb ratios of the CYf low-Ti rhyolite and CGC diorite are a result of a second magma batch that underwent high-level fractionation within a near-surface magma chamber, similar to that proposed for FIII type felsic volcanics (Lesher *et al.,* 1986). Unlike FIII type magmas, this magma assimilated large quantities of HFSE-depleted mafic crust (e.g., CAm basalt), and gave rise to a magma that was relatively depleted in the HFSE.

A four-step petrogenetic model is proposed for the CGC and CYf volcanic rocks. Partial fusion of garnet peridotite in the mantle produced a LREE- and Zr-enriched magma that was emplaced into oceanic crust (CAm basalt). CYf dacite and rhyolite were extruded onto the CAm basalt from the trondhjemitic portion of the CGC in a volcanic-arc setting. A second batch of magma collected within the CGC and, during fractionation to felsic composition, assimilated large quantities of HFSE-depleted CAm basalt resulting in a less LREE-enriched, and overall HFSE-depleted felsic magma. This sub-volcanic magma-chamber is preserved as the diorite phase of the CGC. High-level plagioclase-dominated fractionation of the relatively HFSE-depleted magma led to a second extrusive phase within the volcanic-arc, and resulted in the emplacement of the CYf low-Ti rhyolite flows and pyroclastics on top of the CYf volcanic arc. Following extrusion of the CYf submarine volcanic-arc, hydrothermal sediments were deposited within the volcanic-arc basin during the approximately 15-26 Ma interval that preceeded extrusion of the TOm basalt.

3.7.2 Quantitive comparison of alteration in the SESGB, and at the Horne and Helen mines

The Horne and Helen mines are both well-studied and economic mineral deposits in the Superior Province, that, like the Huffman Township Zn-Pb showing, are hosted by variably-altered felsic volcanic complexes. A quantitive comparison of the alteration zone mass-changes and geometries of these formerly-producing deposits with that of the Huffman Township showing is helpful in evaluating whether the hydrothermal sediments of the SGB represent an intermediate member of a continuum of polymetallic massive-sulphide mineralization (pyrite-chalcopyrite-sphalerite-gold), and volcanic-exhalative Fe mineralization (siderite-pyrite).

Calculations of average percent-change compared to precursor compositions indicate that there were additions of 28% SiO_2 and 862% K_2O and a loss of 51% Na_2O in quartz-sericite altered rocks stratigraphically below and distal to the Horne mine (calculated from data in MacLean and Hoy, 1994). By contrast, the type 1 alteration of CYf volcanic rocks distal to base-metal mineralization in the SESGB was characterized by the relative addition of an average of 16% SiO_2, and 149% K_2O, and a loss of 66% Na_2O (Figure 3.11a). Although the trends of silicification and Na/K exchange are common to distal alteration zones at the Horne Mine and the Huffman Township Zn-Pb showing, the magnitudes of such changes are considerably greater in the vicinity of the Horne orebody.

Mass-changes associated with type 2 alteration in the SESGB proximal to the Huffman Township showing were also similar in nature, but smaller in magnitude than those calculated for the proximal, discordant, chlorite-stringer networks stratigraphically below the Horne orebody. The relative mass-gains in the Horne, chlorite alteration-pipe were 220% Fe_2O_3 and 432% MgO, whereas the mass-losses were 72% SiO_2, 100% Na_2O, and the net mass-loss was 33% (calculated from data in MacLean and Hoy, 1994). At the Huffman Township showing there were mass-gains of 349% Fe_2O_3, and 174% MgO, losses of 19% SiO_2 and 57% Na_2O, and a net mass-loss of 1% for type 2 alteration. These calculations reveal that the hydrothermal system at the Huffman Township Zn-Pb showing was significantly richer in Fe (and poorer in Mg), but less effective in leaching silica and alkali-elements than the system associated with the Horne massive sulphide deposit.

Hydrothermally altered felsic volcanic rocks in the stratigraphic footwall of the Helen siderite mine in the Wawa greenstone belt, Ontario (Morton and Nebel, 1984), consist

mainly of rhyolite with dome, block and ash flow morphologies and subordinate massive mafic to felsic intrusives. A very broad, semi-conformable sericite and pyrophyllite alteration zone (6 X 2 km) is overprinted by a diffuse (1 X 2 km) discordant Al-silicate (Mn-chloritoid and andalusite) and chlorite alteration zone (Morton and Nebel, 1984). Similar to type 1 alteration in the SESGB, sericitic alteration below the Helen mine is distal to exhalative mineralization and is characterized by the addition of K, Mg and Fe and a loss of Na (Morton and Nebel, 1984). Morton and Nebel (1984) concluded that proximal chlorite alteration at the Helen Mine occurred through replacement of sericite and/or primary albite and that this is reflected in the addition of Fe, Mg and Mn, and loss of Na, K and Si, like that of type 2 alteration at the Huffman Township showing. Morton and Nebel (1984) and Goodwin *et al.* (1985) have proposed that the relatively diffuse nature of the alteration and the base-metal poor composition of the ore at the Helen Mine were a result of low-temperature hydrothermal circulation, with a high water/rock ratio and poorly focussed hydrothermal venting onto the seafloor.

The Horne polymetallic massive sulphide deposit, Helen siderite deposit, and the Huffman Township Zn-Pb showing can be placed in a continuum of volcanic-exhalative mineral deposits that have regionally extensive sericite-quartz alteration zones and proximal chloritic alteration zones. The exhalative products of each of the systems define a continuum between Fe-rich, base- and precious-metal poor (e.g. Helen mine), and Cu, Zn, and Au rich deposits (e.g. Horne mine). The intensity, focus, and distribution of alteration zones and corresponding mass changes also form a continuum between the roughly 1 km wide proximal chloritic alteration zone at the Helen mine, the 500 m wide, fault controlled zone of type 2 alteration at the Huffman Township showing,

and the networks of intense, sub-meter wide chlorite stringer systems at the Horne mine (McLean and Hoy, 1991).

3.7.3 Constraints on hydrothermal fluid composition and water/rock ratio of alteration for SESGB

The results of the mass-change calculations presented above and the nature of the volcanic-exhalative rocks indicate that fluids responsible for the alteration of the volcanics and the deposition of hydrothermal sediments in the SESGB transported large amounts of Fe and K, with lesser quantities of Mg, Mn, S, Zn, Pb, and CO_2. Seawater and unaltered dacite, rhyolite and low-Ti rhyolite are relatively poor in Fe, K, Zn, Cu and S, and are unlikely sources for these components in SESGB altered rocks and hydrothermal sediments (Table 3.1 and Table 3.3). Although altered dacite and rhyolite are in direct contact with hydrothermal sediments in the SESGB, young CAm basalt may have acted as a large reservoir for heated, Fe and base-metal-bearing, acidic fluid prior to the extrusion of the CYf volcanics. Warm, basalt-equilibrated hydrothermal vent fluids such as those sampled in modern back-arc and mid-ocean ridge hydrothermal fields (Scott, 1997), and those generated experimentally (Seyfried and Bischoff, 1981; Shiraki *et al.,* 1987) indicate that seafloor basalt is a reasonable source of Fe, K, Zn and S (Table 3.3).

The potential of CAm basalt to have been the source of Fe for SESGB hydrothermal sediments can be tested by a simple mass-balance calculation. Hydrothermal sediments at the top of the Chester Group in the SESGB have an average thickness of 5 m, and contain ~ 30 wt.% Fe_2O_3. The CAm basalt contains an average of 11.53 wt.% Fe_2O_3, and has a thickness of over 1 000 m. Mass-balance requires the remobilization of just 0.15 wt.% Fe_2O_3 from the CAm basalt to account for the 30 wt.% Fe_2O_3 in the IF.

The minimum water/rock ratios required to alter dacite, rhyolite, and low-Ti rhyolite can be calculated using mass-changes of Fe and K for type 1 and type 2 alteration facies. Compositional data from hydrothermal vent-fluids in modern back-arc basins, interpreted here to be analogous to the paleo-tectonic environment of the Chester Group volcanics, can be used to estimate the Fe and K concentrations of volcanic-exhalative fluids in the SESGB. Hydrothermal fluids from modern back-arc basins are heated, acidic solutions that are considerably enriched in Si, K, Fe, Zn and Pb compared to seawater and mid-ocean ridge fluids, and have compositions similar to those obtained from fluid-inclusions in Kuroko District ores (Table 3.3). The minimum water/rock ratio required to produce the enrichment 467 mmol/kg K typical of type 1 altered Chester Group felsic volcanics (2.1 wt.% K_2O; Table 3.2) is 6, assuming a fluid with a K content of 73.7 mmole/kg, the most K-rich fluids yet sampled from back-arc basin vents (Table 3.3). The minimum water/rock ratios for type 2 alteration of CYf volcanic rocks can be estimated by considering the mass-gain of Fe_2O_3 (Table 3.2), and the Fe content of back-arc basin fluids (Table 3.3). To achieve the 739 mmol/kg Fe-enrichment (5.9 wt.% Fe2O3, Table 3.2) via interaction with a back-arc basin fluid containing 1.71 mmol/kg Fe, a minimum water/rock ratio of 432 is required.

The estimates of the water/rock ratios associated with types 1 and 2 alteration are consistent with a model in which hydrothermal fluids are dispersed through a large volume of volcanic rock (type 1) or focussed along narrow conduits (type 2).

3.7.4 Alteration model for Chester Group felsic volcanics

The depletion of type 1 quartz-sericite altered rocks in Na_2O and their enrichment in K_2O (Figure 3.12a) is interpreted to have occurred because of the reaction of primary plagioclase to secondary sericite:

[3.1] $3NaAlSi_3O_8 + K^+ + 2H^+ \Rightarrow KAl_3Si_3O_{10}(OH)_2 + 6SiO_2 + 3Na^+$

Similarly, the systematic loss of Na_2O and gains in Fe, Mg and Mn (Figure 3.12b) that accompanied type 2 (chlorite-sericite±biotite±garnet) alteration can be explained either by transformation of primary plagioclase to chlorite by the reaction:

[3.2] $2NaAlSi_3O_8 + 5(Fe,Mg,Mn)^{2+} + 8H_2O \Rightarrow (Fe,Mg,Mn)_5Al_2Si_3O_{10}(OH)_8 + 3SiO_2 + 2Na^+ + 8H^+$,

or by overprinting of sericite by chlorite through the reaction:

[3.3] $2KAl_3Si_3O_{10}(OH)_2 + 15(Fe,Mg,Mn)^{2+} + 3SiO_2 + 24H_2O \Rightarrow 3(Fe,Mg,Mn)_5Al_2Si_3O_{10}(OH)_8 + 2K^+ + 28H^+$

Rocks undergoing type 1 alteration were enriched in Si (Figure 3.12c,d), as a result of the reaction:

[3.4] $H_4SiO_4(aq) \Rightarrow SiO_2 + H_2O$

while many rocks exhibiting type 2 alteration underwent depletion of Si (Figure 3.12c,d) by the reverse reaction.

Experimental and theoretical studies show that silica solubility in hydrothermal fluids is strongly temperature dependent and effectively independent of pH (Rimstidt and Barnes, 1980). Thus a warm, basalt-equilibrated, quartz undersaturated fluid interacting with large volumes of Chester Group volcaniclastics would initially dissolve quartz but would soon cool, depositing quartz and occluding the primary porosity of CYf rocks on a regional scale. This hypothesis is validated for type 1 altered rocks, by the calculation of Si mass-gain and net mass-gain, which is consistent with a loss of porosity. As porosity was occluded, fluid-flow was focussed along active syn-volcanic faults where type 2 alteration occurred at higher water/rock ratios. Because of the relatively high flow rates, and high water/rock ratio of alteration, these later hydrothermal fluids would have transferred relatively little of their heat to the surrounding rocks and consequently, their

capacity to carry silica would not have diminished significantly. They would therefore have remained undersaturated with respect to silica and dissolved quartz from the CYf volcanics by the reverse of reaction [3.4], thereby explaining the calculated loss of SiO_2 and overall net mass-loss that accompanied type 2 alteration.

Mass-gains in K, Fe, Mg and Mn (Figure 3.12e) are consistent with the occurrence of sericite in altered volcanic fragments and with chlorite in the matrices of type 2 altered rocks. Figure 3.12f shows the strong correlation between the changes in SiO_2 concentrations for type 1 and type 2 altered samples and net mass-changes.

A five-step model is proposed for type 1 and type 2 alteration facies developed within CYf volcanic rocks in the SESGB. (1) Seawater is circulated through and reached equilibrium with warm CAm basalt (Figure 3.13a); (2) emplacement of the CGC at 2740 (±2) Ma and the extrusion of the CYf-CYf volcanic-arc complex (ca. 2739 Ma) develops thermal and pressure gradients that facilitate circulation of basalt-equilibrated hydrothermal fluids (Figure 3.13b); (3) cooling fluids upwelling from CAm basalts interacted with porous CYf volcaniclastics, causing alteration of primary plagioclase to sericite and deposition of quartz, leading to decreases in permeability (Figure 3.13c); (4) flow of hydrothermal fluid is focussed by reduced permeability to zones near active synvolcanic structures, enabling type 2 alteration to overprint type 1 alteration at higher water/rock ratios (Figure 3.13d) and; (5) hydrothermal vents develop on the seafloor at the margins of the CYf arc-complex and lead to localized base-metal sulphide deposition and voluminous metalliferous sediment precipitation from a hydrothermal plume (Figure 3.13e). Hydrothermal sedimentation may have continued for 36-28 Ma until the eruption of the 2707 (±2) Ma Trailbreaker Group volcanics.

3.8 Conclusions

The principal conclusions of this study are:

1. Chester Group volcanic rocks within the SESGB comprise pillowed amygdaloidal and variolitic basalt of the Chester Group Arbutus Formation (CAm), and quartz- and feldspar-phyric dacite and rhyolite with massive, laminated pyroclastic, and fragmental textures of the Yeo Formation (CYf). The Chester Group volcanic rocks are overlain by 5-20 m of hydrothermal sediments, containing sub-economic Zn-Pb-sulphide mineralization. These geological features are indicative of submarine volcanism and volcanic-exhalative activity.

2. Macro-scale textural characteristics combined with HFSE analyses of CYf dacite, rhyolite and low-Ti rhyolite indicate deposition in a submarine volcanic-arc setting.

3. A magma of calc-alkaline affinity produced the CYf dacite and rhyolite, and the CGC trondhjemite. The CYf dacite and rhyolite are geochemically similar to the FI-type of Lesher *et al.* (1986), the group IV type of Barrie *et al.* (1993) and the calc-alkaline-type of Barrett and MacLean (1999). These felsic volcanic types are not known to be associated with economic VMS deposits in the Superior province.

4. A second batch of magma assimilated large quantities of HFSE-depleted mafic crust (CAm) during fractionation to felsic composition in a shallow sub-volcanic magma chamber. This magma was the source of the CYf low-Ti rhyolite, which has low overall abundances of HFSE and low Zr/Y and $(La/Yb)_n$ ratios. Such

uniformly HFSE depleted rhyolite magmas have not been documented in other parts of the Superior Province.

5. CYf volcanics underwent regionally extensive, porosity-occluding, sericite-quartz (type 1) alteration, characterized by loss of Na, addition of Si and K, and net mass-gain, with a minimum estimated water/rock ratio of 6.

6. Chlorite-sericite±biotite±garnet (type 2) alteration occurred at paleo-hydrothermal vent sites localized along synvolcanic fault structures. Alteration was associated with loss of Na, addition of Si, and K, and minor net mass-loss, requiring water/rock ratios in excess of 400.

7. The fluids responsible for Type 1 and type 2 alteration were both quartz-undersaturated and initially equilibrated with basalt. During type 1 alteration, fluids became saturated in quartz through a combination of extensive interaction with felsic volcaniclastics and cooling, while fluids became quartz-undersaturated during type 2 alteration because interaction with the volcaniclastics was localized and cooling was minimal.

8. From the perspective of alteration mass changes, alteration intensity, alteration zone architecture and hydrothermal products, hydrothermal sediments and base-metal sulphide mineralization from the SESGB can be placed in a continuum between polymetallic massive-sulphide deposit such as the Horne Mine, and siderite-pyrite iron deposits such as the Helen Mine.

3.9 References

Barrett, T.J. and MacLean, W.H., 1999. Volcanic sequences, lithogeochemistry and hydrothermal alteration in some bimodal volcanic-associated massive sulfide systems. Reviews in Economic Geology, 8, p. 101-131.

Barrett, T.J. and MacLean, W.H., 1994. Chemostratigraphy and hydrothermal alteration in exploration for VHMS deposits in greenstones and younger volcanic rocks. *In,* D.R. Lentz (ed.), Geological Association of Canada, Short Course Notes Volume 11: Alteration and Alteration Processes Associated with Ore-Forming Systems, p. 433-467.

Barrie, C.T., Ludden, J.N. and Green, T.H., 1993. Geochemistry of volcanic rocks associated with Cu-Zn and Ni-Cu deposits in the Abitibi subprovince. Economic Geology, 88, p. 1341-1358.

Boynton, W.V., 1984. Geochemistry of the rare-earth elements: Meteorite studies. *In,* P. Henderson (ed.), Rare-earth element geochemistry., Elsevier, New York, p. 63-114.

Finlow-Bates, T. and Stumpfl, E.F., 1981. The behavior of the so-called immobile elements in hydrothermally altered rocks associated with volcanogenic submarine exhalative ore deposits. Mineralium Deposita, 16, p. 319-328.

Franklin, J.M., 1996. Volcanic-associated massive-sulphide base-metals. *In,* O.R. Eckstrand, W.D. Sinclair, and R.I. Thorpe (eds.), Geology of Canadian Mineral Deposit Types. Geological Survey of Canada, Geology of Canada, 8, p. 158-183.

Franklin, J.M., Lydon J.W. and Sangster, D.F., 1981. Volcanic-associated massive sulfide deposits. Economic Geology 75th Anniversary Volume, p. 485-627.

Fulmerton, S., Houle, K., and Archibald, G., 1993. Mineral showings, occurrences, deposits and mines of the Swayze greenstone belt, interim report, 1 and 2. Ontario Geological Survey Open File Report 5871, p. 1-763.

Gibson, H.L., and Watkinson, D.H. An Archean subseafloor hydrothermal system, regional semiconformable alteration, and massive-sulphide deposits, Noranda, Quebec, Canada. *in preparation.*

Goodwin, A.M., Thode, H.G., Chou, C.-L., and Kharkansis, S.N., 1985. Chemostratigraphy and origin of the late Archean siderite-pyrite-rich Helen iron formation, Michipicoten belt, Canada. Canadian Journal of Earth Sciences, 22, p. 72-84.

Hannington, M.D., Barrie, C.D., and Bleeker, W., 1999. The giant Kidd Creek volcanogenic massive sulfide deposit, western Abitibi subprovince, Canada: Preface and introduction. Economic Geology Monograph 10, p. 1-30.

Harris, J.R., Wilkinson, L., Grunsky, E., Heather, K., and Ayer, J., 1999. Techniques for analysis and visualization of lithogeochemical data with applications to the Swayze greenstone belt, Ontario. Journal of Geochemical Exploration, 67, p. 301-334.

Heather, K.B. and Shore, G.T., 1999. Geology, Swayze greenstone belt, Ontario. Geological Survey of Canada, Open File 3384a-i.

Heather, K.B. and van Breeman, O., 1994. An interim report on geological, structural and geochronological investigations of granitoid rocks in the vicinity of the

Swayze greenstone belt, southern Superior province, Ontario. Current Research 1994-C, Geological Survey of Canada, p. 259-268.

Heather, K.B., Shore, G.T. and van Breeman, O., 1995. The convoluted "layer-cake": an old recipe with new ingredients for the Swayze greenstone belt, southern Superior province, Ontario. Current Research 1995-C, Geological Survey of Canada, p. 125-136.

Heather, K.B., Shore, G.T. and van Breeman, O., 1996. Geological investigations in the Swayze greenstone belt, southern Superior province, Ontario. Current Research 1996-C, Geological Survey of Canada, p. 125-136.

Koopman, E.R., Hannington, M.D., Santaguida, F., and Cameron, B.I., 1999. Petrology and geochemistry of proximal hydrothermal alteration in the Mine Rhyolite at Kidd Creek. Economic Geology Monograph 10, p. 267-296.

Lesher, C.M., Goodwin, I.H., Campbell, I.H. and Gorton, M.P., 1986. Trace element geochemistry of ore-associated and barren felsic metavolcanic rocks in the Superior province, Canada. Canadian Journal of Earth Sciences, 23, p. 222-237.

MacLean, W.H. and Barrett, T.J., 1993. Lithogeochemical techniques using immobile elements. Journal of Geochemical Exploration, 48, p. 109-133.

MacLean, W.H. and Hoy, L.D., 1991. Geochemistry of hydrothermally altered rocks at the Horne Mine, Noranda, Quebec. Economic Geology, 86, p.506-528.

MacLean, W.H., and Kranidiotis, P., 1987. Immobile elements as monitors of mass-transfer in hydrothermal alteration: Phelps-Dodge massive-sulphide deposit, Matagami, Quebec. Economic Geology, 82, p. 951-962.

Morton, R.L. and Nebel, M.L., 1984. Hydrothermal alteration of felsic volcanic rocks at the Helen siderite deposit, Wawa, Ontario. Economic Geology, 79, p. 1319-1333.

Ontario Geological Survey, 1993. Ontario airborne magnetic and electromagnetic surveys: Archean and Proterozoic greenstone belts, Swayze area. ERLIS dataset 1015 (CD-ROM).

Pisutha-Arnond, V. and Ohmoto, H., 1985. Thermal history and chemical and isotopic compositions of the ore-forming fluids responsible for the Kuroko massive sulfide deposits in the Hokuroku district of Japan. Economic Geology Monograph 5, p. 523-558.

Prior, G. J., Gibson, H.L., Watkinson, D.H., Cook, R.E., and Hannington, M.D., 1999. Rare-earth and high field strength element geochemistry of the Kidd Creek rhyolites, Abitibi greenstone belt, Canada: Evidence for Archean felsic volcanism and massive sulfide ore formation in an Iceland-style rift environment. Economic Geology Monograph 10, p. 457-484.

Rimstidt, J.D. and Barnes, H.L., 1980. The kinetics of silica-water reactions. Geochimica Cosmochimica acta, 44, p.1683-1699.

Rollinson, H., 1993. Using Geochemical Data: Evaluation, Presentation, Interpretation. Longman, New York, 352 p.

Scott, S.D., 1997. Submarine hydrothermal systems and deposits. *In*, H.L. Barnes (ed.), Geochemistry of Hydrothermal Ore Deposits, 3rd Edition. John Wiley & Sons, New York, NY, p. 798-876.

Seyfried Jr., W.E. and Bischoff, J.C., 1981. Experimental seawater-basalt interaction at 300 °C, 500 bars, chemical exchange, secondary mineral formation and implications for the transport of heavy metals, Geochimica et Cosmochimica Acta, 45, p. 135-147.

Shiraki, R., Sakai, H., Endoh, M., and Kishima, N., 1987. Experimental studies on rhyolite- and andesite-seawater interactions at 300 °C and 1000 bars. Geochemical Journal, 21, p. 139-148.

Appendix 3.1: Lithogeochemical data

Appendix 3.1: Lithogeochemical data

sample	8474	8476	8478	8479	8480	AU01753	AU04212	AU04219	AU04234	AU04236
flag	IBH	IBH	IBH	IBH	IBH	IBH	IBH	IBH	IBH	IBH
SiO_2	74.64	49.78	59.89	71.21	73.53	56.46	64.36	83.41	81.07	61.12
Al_2O_3	0.54	1.03	0.55	0.60	0.25	0.46	0.89	0.21	0.05	0.25
Fe_2O_3	14.84	42.08	26.13	15.94	15.66	41.31	31.27	14.22	17.65	34.29
CaO	6.75	2.38	7.14	7.65	8.26	0.22	1.64	0.20	0.07	0.24
MgO	2.66	4.29	5.55	3.77	1.85	1.23	1.38	0.70	0.91	3.80
Na_2O	0.01	0.02	0.01	0.01	0.01	0.01	0.06	0.01	0.01	0.01
K_2O	0.02	0.05	0.01	0.01	0.01	0.02	0.12	1.04	0.02	0.03
TiO_2	0.02	0.04	0.01	0.02	0.01	0.03	0.03	0.02	0.01	0.02
MnO	0.45	0.19	0.75	0.41	0.38	0.03	0.23	0.11	0.10	0.06
P_2O_5	0.06	0.14	0.17	0.37	0.04	0.23	0.20	0.08	0.11	0.17
TIC	3.38	0.88	3.52	3.62	1.98	0.15	0.03	0.57	0.01	0.14
S	1.62	0.87	4.81	0.90	3.63	0.14	0.14	0.51	0.03	0.29
LOI	7.74	2.30	5.03	9.10	3.55	1.30	1.45	3.53	0.41	0.98
V*	44.1	82.3	73.9	55.1	52.1	81.4	61.3	36.4	40.4	66.0
Cr*	297.5	98.2	253.3	468.6	369.9	67.8	93.2	104.2	131.1	65.5
Co*	5.5	10.3	52.8	5.5	15.6	10.2	2.9	8.6	2.5	20.3
Ni*	41.9	26.8	61.2	32.0	26.0	16.3	2.6	2.6	2.5	2.5
Cu*	16.5	10.3	168.9	33.1	198.0	117.0	153.1	36.4	5.0	121.9
Zn*	2.8	406.4	221.7	55.1	104.2	2.5	2.6	2.6	33.3	35.6
Ga^3	1.9	4.3	2.6	1.7	1.3	2.8	5.3	1.4	1.3	2.6
Ge^3	3.80	3.92	2.57	3.24	3.06	12.45	4.58	4.21	4.01	8.56
As^3	51.6	2.6	2.6	2.8	2.6	2.5	2.6	7.5	2.5	2.5
Mo^3	2.9	4.6	1.1	2.8	1.0	1.0	1.0	2.2	1.0	2.7
Ag^2	0.3	0.1	0.7	0.1	0.5	0.1	0.1	0.1	0.1	0.1
In^3	0.055	0.206	0.053	0.055	0.052	0.103	0.256	0.052	0.050	0.111
Sn^3	0.6	0.5	0.5	0.6	0.5	0.5	3.9	0.5	0.5	0.5
Sb^3	0.110	0.103	0.106	0.250	0.104	0.684	0.102	0.104	0.101	0.751
W^3	0.3	1.1	0.3	0.3	0.3	0.3	0.3	1.4	0.3	0.3
Au^2	1.1	212.0	43.3	18.7	7.3	34.6	17.4	7.3	7.1	3.0
Tl^3	0.028	0.026	0.026	0.028	0.026	0.025	0.026	0.026	0.025	0.025
Pb^2	1.1	1.0	61.2	259.1	8.3	1.0	1.0	1.0	1.0	1.0
Bi^3	0.06	0.05	0.05	0.06	0.18	1.05	1.03	0.29	0.05	0.20
Be	2.8	2.6	2.6	2.8	2.6	2.5	2.6	2.6	2.5	2.5
Rb^3	0.6	0.5	0.5	0.6	0.5	0.5	0.5	0.5	0.5	0.5
Sr*	33.1	61.7	137.2	44.1	41.7	20.3	10.2	5.2	7.8	10.2
Cs^3	0.1	0.1	0.1	0.1	0.1	0.1	0.1	0.1	0.1	0.1
Ba*	19.4	15.2	1.6	1.7	10.3	5.5	114.5	7.0	16.7	22.8
Sc	2.8	2.6	5.3	2.8	2.6	2.5	2.6	2.6	2.5	2.5
Y*	6.6	6.9	7.6	17.7	5.9	7.2	7.5	2.6	3.6	6.6
Zr*	9.9	9.1	7.8	9.2	6.2	6.8	11.7	4.3	5.6	7.2
Nb*	0.1	0.1	0.1	0.1	0.1	0.1	0.1	0.1	0.1	0.1
Hf^3	0.23	0.33	0.16	0.26	0.15	0.20	0.30	0.05	0.05	0.18
Ta^3	0.01	0.02	0.01	0.01	0.01	0.01	0.11	0.01	0.01	0.01
Th^3	0.2	0.4	0.1	0.1	0.1	0.2	0.2	0.1	0.0	0.2
U^3	0.1	0.1	0.0	0.1	0.0	0.1	0.0	0.0	0.0	0.1
La^3	3.2	4.1	1.5	3.4	3.0	4.2	4.0	1.2	2.0	4.3
Ce^3	6.1	8.5	3.1	6.4	5.6	8.7	7.4	2.4	3.7	10.3
Pr^3	0.7	1.0	0.4	0.8	0.7	1.0	0.8	0.3	0.4	1.3
Nd^3	3.158	4.066	1.770	3.997	2.963	4.297	3.279	1.120	1.808	5.064
Sm^3	0.717	0.865	0.500	1.117	0.748	0.916	0.720	0.250	0.351	1.113
Eu^3	0.690	0.746	0.447	0.964	0.609	0.569	0.611	0.228	0.370	0.757
Gd^3	0.773	0.815	0.682	1.651	0.807	0.907	0.770	0.283	0.356	1.028
Tb^3	0.142	0.161	0.154	0.323	0.144	0.165	0.139	0.054	0.071	0.183
Dy^3	0.862	0.993	1.019	2.056	0.839	1.019	0.938	0.366	0.442	1.102
Ho^3	0.192	0.220	0.222	0.426	0.181	0.226	0.223	0.087	0.109	0.235
Er^3	0.587	0.706	0.662	1.150	0.550	0.723	0.729	0.264	0.337	0.744
Tm^3	0.082	0.108	0.088	0.136	0.081	0.106	0.110	0.040	0.051	0.111
Yb^3	0.515	0.727	0.568	0.700	0.525	0.694	0.682	0.270	0.323	0.750
Lu^3	0.081	0.111	0.086	0.104	0.078	0.106	0.103	0.040	0.046	0.117
UTM E	410563	410173	410401	410401	410401	415325	416170	411060	411769	412147
UTM N	5270758	5270756	5270735	5270759	5270771	5271245	5270340	5270668	5271443	5271340

-All data have been normalised to a volatile free basis such that major oxides total 100%.
-Major oxides, S, total inorganic carbon (TIC) and loss on ignition (LOI) are expressed as weight percent, Au is expressed in parts per billion, and all other trace elements as parts per million. The letters ND indicate that no data are available.

-analysis key ^{3} indicates analysis by ICP-MS
* indicates analysis by ICP-AES or AA

-flag key *first letter: sample type:* V=volcanic sample, C=Chester Granitoid Complex
second letter: lithology type: VB= basalt, VD=dacite, VR=rhyolite, VL=low-Ti rhyolite, CD=diorite, CT=trondhjemite
third letter: -alteration type: F=least altered, A=altered, S=type 1, C=type 2, E=epidote-quartz

-sample locations are given in NAD83 projection for UTM zone 17

Appendix 3.1: Lithogeochemical data

sample	AU04240	AU04242	AU04245	AU06673	AU06680	AU06684	AU06685	AU06542	AU06544	AU06545
flag	IBH	IBH	IBH	IBH	IBH	IBH	IBH	IBN	IBN	IBN
SiO_2	68.10	69.29	87.05	57.26	56.49	20.49	65.34	69.65	73.03	55.80
Al_2O_3	0.07	0.04	0.24	0.59	0.82	0.61	1.59	0.18	0.30	0.09
Fe_2O_3	27.37	24.72	12.20	41.24	41.45	75.46	30.43	27.09	22.99	37.32
CaO	1.59	1.49	0.03	0.14	0.43	0.30	0.54	0.21	0.49	1.80
MgO	2.67	3.91	0.18	0.29	0.30	2.45	1.75	2.59	2.22	3.37
Na_2O	0.01	0.01	0.05	0.04	0.17	0.01	0.01	0.01	0.01	0.01
K_2O	0.01	0.01	0.02	0.06	0.04	0.09	0.01	0.08	0.04	0.01
TiO_2	0.01	0.01	0.01	0.02	0.02	0.02	0.06	0.01	0.01	0.01
MnO	0.06	0.41	0.17	0.08	0.05	0.40	0.10	0.05	0.85	1.69
P_2O_5	0.12	0.11	0.04	0.27	0.23	0.17	0.18	0.12	0.06	0.10
TIC	3.57	0.47	0.06	0.05	0.06	0.05	2.48	0.11	0.06	0.24
S	0.56	0.17	0.21	0.14	0.11	20.60	1.05	0.41	0.20	0.11
LOI	11.08	1.26	2.14	3.75	0.08	19.49	10.15	1.24	0.37	0.01
V*	56.3	50.9	30.8	23.0	32.0	31.2	43.9	15.2	15.1	15.1
Cr*	111.4	295.4	126.7	130.3	175.3	87.3	172.9	137.1	267.3	135.5
Co*	5.6	10.2	2.7	8.8	5.0	25.0	15.7	5.1	5.0	5.0
Ni*	2.8	56.0	2.6	26.1	45.1	56.1	39.0	20.3	40.3	25.1
Cu*	56.3	2.5	2.6	344.0	50.1	243.3	334.6	5.1	45.4	30.1
Zn*	185.9	2.5	57.5	78.2	20.0	143.5	524.2	2.5	2.5	2.5
Ga[3]	1.5	1.8	1.1	3.3	2.8	ND	5.1	1.4	ND	2.6
Ge[3]	6.22	6.55	5.17	6.89	14.52	ND	3.11	1.92	ND	1.38
As[3]	14.9	2.5	8.0	14.3	2.5	ND	52.2	15.5	ND	2.5
Mo[3]	1.1	1.0	1.0	1.0	1.0	ND	1.1	1.0	ND	1.0
Ag[2]	0.1	0.1	0.1	0.5	0.4	1.9	1.0	0.1	0.1	0.2
In[3]	0.056	0.051	0.051	0.052	0.050	ND	0.146	0.051	ND	0.050
Sn[3]	0.6	0.5	0.5	0.5	1.2	ND	0.6	0.5	ND	0.5
Sb[3]	0.113	0.245	0.103	0.528	1.592	ND	1.031	0.587	ND	0.374
W[3]	0.3	0.3	0.3	1.7	1.4	ND	1.7	0.9	ND	1.0
Au[2]	7.9	7.1	17.5	7.3	1.0	183.4	23.4	1.0	1.0	1.0
Tl[3]	0.028	0.025	0.026	0.026	0.025	ND	0.028	0.025	ND	0.025
Pb[2]	1.1	1.0	1.0	1.0	8.0	143.5	7.8	1.0	1.0	1.0
Bi[3]	0.06	0.05	0.05	0.15	0.12	ND	0.13	0.13	ND	0.14
Be	2.8	2.5	2.6	2.6	2.5	3.1	2.8	2.5	2.5	2.5
Rb[3]	0.6	0.5	0.5	4.5	4.6	ND	1.7	3.7	ND	4.7
Sr*	56.3	8.5	5.1	10.4	30.0	12.5	22.3	20.3	20.2	30.1
Cs[3]	0.1	0.1	0.1	0.2	0.3	ND	0.2	0.2	ND	0.4
Ba*	4.4	22.0	17.7	165.8	38.7	74.9	11.2	4.2	30.3	12.2
Sc	2.8	2.5	2.6	2.6	2.5	3.1	2.8	2.5	2.5	2.5
Y*	4.8	4.0	4.0	6.0	6.7	3.1	7.4	6.2	2.5	4.4
Zr*	6.3	5.1	4.6	8.4	7.1	37.4	14.8	6.1	20.2	6.9
Nb*	0.1	0.1	0.1	0.1	0.2	6.2	0.5	0.1	5.0	0.1
Hf[3]	0.16	0.05	0.05	0.19	0.20	ND	0.40	0.11	ND	0.21
Ta[3]	0.02	0.01	0.01	0.02	0.03	ND	0.05	0.01	ND	0.01
Th[3]	0.2	0.1	0.1	0.3	0.3	ND	0.6	0.3	ND	0.4
U[3]	0.1	0.0	0.0	0.1	0.2	ND	0.2	0.2	ND	0.1
La[3]	1.9	2.1	2.1	3.1	7.8	ND	6.1	1.9	ND	1.0
Ce[3]	3.3	4.0	3.5	6.4	14.7	ND	13.4	3.6	ND	1.6
Pr[3]	0.4	0.5	0.4	0.7	1.5	ND	1.5	0.4	ND	0.2
Nd[3]	1.664	1.996	1.555	2.890	6.293	ND	6.143	2.099	ND	0.799
Sm[3]	0.342	0.413	0.307	0.656	1.284	ND	1.358	0.566	ND	0.214
Eu[3]	0.384	0.321	0.272	0.750	0.956	ND	0.917	0.588	ND	0.187
Gd[3]	0.406	0.465	0.321	0.729	1.157	ND	1.256	0.750	ND	0.292
Tb[3]	0.082	0.086	0.055	0.121	0.178	ND	0.198	0.127	ND	0.060
Dy[3]	0.550	0.548	0.381	0.764	1.037	ND	1.198	0.767	ND	0.396
Ho[3]	0.124	0.114	0.093	0.172	0.202	ND	0.252	0.163	ND	0.102
Er[3]	0.422	0.366	0.313	0.512	0.581	ND	0.748	0.480	ND	0.354
Tm[3]	0.062	0.053	0.047	0.071	0.077	ND	0.101	0.069	ND	0.055
Yb[3]	0.392	0.345	0.304	0.533	0.548	ND	0.684	0.446	ND	0.341
Lu[3]	0.055	0.054	0.049	0.083	0.080	ND	0.106	0.066	ND	0.060
UTM E	412292	410667	412925	415784	417093	419150	419150	412600	426175	428283
UTM N	5271327	5270771	5271486	5271121	5270699	5269575	5269570	5334210	5335790	5336075

Appendix 3.1: Lithogeochemical data

sample	AU06547	AU06550	AU06747	AU06748	AU06750	AU06503	AU06709	AU06535	AU06669	AU06671
flag	IBN	IBN	IBN	IBN	IBN	IBS	IBS	IBT	IBT	IBT
SiO_2	64.76	75.19	36.51	50.43	45.25	82.46	82.40	44.08	75.33	50.59
Al_2O_3	0.12	0.14	0.01	0.01	0.01	0.22	0.14	1.99	0.28	0.64
Fe_2O_3	29.31	19.34	62.34	45.17	48.32	12.69	14.85	51.30	19.94	41.85
CaO	1.46	2.02	0.31	1.09	1.53	3.31	0.36	0.44	1.92	4.51
MgO	2.83	2.53	0.43	2.95	4.49	1.01	1.85	1.54	1.92	2.01
Na_2O	0.01	0.01	0.03	0.06	0.06	0.04	0.01	0.01	0.02	0.01
K_2O	0.01	0.01	0.11	0.05	0.06	0.07	0.09	0.13	0.02	0.01
TiO_2	0.01	0.01	0.01	0.01	0.01	0.01	0.01	0.08	0.01	0.02
MnO	1.42	0.65	0.04	0.05	0.11	0.13	0.24	0.10	0.41	0.08
P_2O_5	0.08	0.08	0.22	0.16	0.14	0.05	0.05	0.32	0.14	0.27
TIC	0.03	0.04	0.02	5.33	8.55	0.59	0.05	0.43	0.05	4.53
S	0.08	1.69	0.13	0.24	0.04	1.43	0.33	2.76	1.99	0.23
LOI	0.01	1.83	0.01	16.32	20.79	2.76	2.47	3.37	0.63	11.25
V*	15.1	5.1	44.6	60.0	63.2	36.1	25.7	26.0	20.2	28.2
Cr*	185.7	265.4	87.4	162.0	164.4	299.5	215.7	124.6	232.4	214.6
Co*	2.5	5.1	3.5	6.0	3.2	5.2	15.4	15.6	2.5	2.8
Ni*	15.1	25.5	14.9	18.0	12.6	15.5	41.1	26.0	25.3	33.9
Cu*	15.1	97.0	129.0	102.0	82.2	2.6	113.0	207.6	108.1	33.9
Zn*	2.5	25.5	34.7	78.0	69.6	2.6	82.2	26.0	2.5	2.8
Ga[3]	ND	ND	1.9	ND	ND	1.8	ND	ND	ND	ND
Ge[3]	ND	ND	5.61	ND	ND	0.26	ND	ND	ND	ND
As[3]	ND	ND	2.5	ND	ND	2.6	ND	ND	ND	ND
Mo[3]	ND	ND	1.0	ND	ND	2.9	ND	ND	ND	ND
Ag[2]	0.1	0.3	0.1	0.1	0.1	0.9	0.2	0.4	0.4	0.2
In[3]	ND	ND	0.050	ND	ND	0.052	ND	ND	ND	ND
Sn[3]	ND	ND	0.5	ND	ND	0.5	ND	ND	ND	ND
Sb[3]	ND	ND	0.099	ND	ND	0.411	ND	ND	ND	ND
W[3]	ND	ND	0.6	ND	ND	3.1	ND	ND	ND	ND
Au[2]	1.0	1.0	20.8	1.2	8.9	10.3	7.2	1.0	1.0	1.1
Tl[3]	ND	ND	0.025	ND	ND	0.026	ND	ND	ND	ND
Pb[2]	1.0	1.0	1.0	1.2	1.3	3.1	1.0	1.0	1.0	1.1
Bi[3]	ND	ND	0.10	ND	ND	0.11	ND	ND	ND	ND
Be	2.5	2.6	2.5	3.0	3.2	2.6	2.6	2.6	2.5	2.8
Rb[3]	ND	ND	3.2	ND	ND	3.4	ND	ND	ND	ND
Sr*	10.0	20.4	69.4	96.0	88.5	16.7	71.9	20.8	20.2	90.4
Cs[3]	ND	ND	0.2	ND	ND	0.3	ND	ND	ND	ND
Ba*	10.0	10.2	6.4	12.0	12.6	5.8	10.3	10.4	10.1	22.6
Sc	2.5	2.6	2.5	3.0	3.2	2.6	2.6	2.6	2.5	2.8
Y*	2.5	2.6	6.0	3.0	3.2	5.1	2.6	5.2	5.1	2.8
Zr*	10.0	10.2	5.7	24.0	25.3	7.7	10.3	41.5	10.1	22.6
Nb*	5.0	5.1	0.1	6.0	6.3	0.1	5.1	5.2	5.1	5.6
Hf[3]	ND	ND	0.10	ND	ND	0.17	ND	ND	ND	ND
Ta[3]	ND	ND	0.00	ND	ND	0.01	ND	ND	ND	ND
Th[3]	ND	ND	0.1	ND	ND	0.2	ND	ND	ND	ND
U[3]	ND	ND	0.1	ND	ND	0.2	ND	ND	ND	ND
La[3]	ND	ND	4.3	ND	ND	2.2	ND	ND	ND	ND
Ce[3]	ND	ND	8.5	ND	ND	5.2	ND	ND	ND	ND
Pr[3]	ND	ND	0.8	ND	ND	0.6	ND	ND	ND	ND
Nd[3]	ND	ND	3.455	ND	ND	2.687	ND	ND	ND	ND
Sm[3]	ND	ND	0.652	ND	ND	0.684	ND	ND	ND	ND
Eu[3]	ND	ND	0.377	ND	ND	0.545	ND	ND	ND	ND
Gd[3]	ND	ND	0.628	ND	ND	0.794	ND	ND	ND	ND
Tb[3]	ND	ND	0.101	ND	ND	0.139	ND	ND	ND	ND
Dy[3]	ND	ND	0.676	ND	ND	0.790	ND	ND	ND	ND
Ho[3]	ND	ND	0.155	ND	ND	0.162	ND	ND	ND	ND
Er[3]	ND	ND	0.523	ND	ND	0.488	ND	ND	ND	ND
Tm[3]	ND	ND	0.079	ND	ND	0.065	ND	ND	ND	ND
Yb[3]	ND	ND	0.562	ND	ND	0.423	ND	ND	ND	ND
Lu[3]	ND	ND	0.088	ND	ND	0.063	ND	ND	ND	ND
UTM E	429423	431750	401780	404166	407070	371200	374495	383242	352502	377415
UTM N	5335940	5337083	5333620	5333753	5333760	5285560	5285600	5288732	5278888	5291475

Appendix 3.1: Lithogeochemical data

sample	AU06672	AU06687	AU06690	AU06691	AU06704	AU06705	AU06710	AU06736	AU06737	AU06740
flag	IBT	IBT	IBT	IBT	IBT	IBT	IBT	IBT	IBT	IBT
SiO_2	53.02	64.33	71.05	66.24	59.79	69.83	57.13	55.61	74.56	70.35
Al_2O_3	0.65	0.17	0.76	0.18	0.01	0.01	1.09	0.35	0.01	0.19
Fe_2O_3	41.45	31.38	19.32	19.95	38.09	28.13	35.80	39.86	23.00	24.54
CaO	2.05	1.05	6.16	8.72	1.49	0.15	4.76	2.65	0.35	1.66
MgO	2.29	2.09	2.16	4.12	0.36	1.61	0.88	0.88	1.26	1.84
Na_2O	0.01	0.01	0.01	0.02	0.01	0.01	0.01	0.13	0.10	0.11
K_2O	0.01	0.01	0.02	0.03	0.08	0.14	0.12	0.12	0.16	0.08
TiO_2	0.02	0.01	0.02	0.01	0.01	0.01	0.03	0.02	0.01	0.02
MnO	0.23	0.74	0.42	0.61	0.07	0.05	0.13	0.19	0.43	1.10
P_2O_5	0.28	0.21	0.09	0.11	0.09	0.05	0.05	0.19	0.11	0.11
TIC	5.10	4.44	1.40	5.14	0.35	0.02	2.91	0.02	0.04	2.24
S	3.88	0.06	2.36	0.51	0.12	0.18	1.13	0.28	0.01	0.50
LOI	16.42	13.19	5.78	11.41	0.38	0.40	6.00	0.01	0.47	7.15
V*	36.0	17.3	21.3	11.3	55.3	35.3	48.1	70.0	30.2	54.0
Cr*	197.8	201.8	234.4	186.4	221.0	141.1	224.3	149.9	131.0	275.6
Co*	3.0	2.9	21.3	2.8	30.1	10.1	26.7	5.0	2.5	2.7
Ni*	18.0	26.8	42.6	22.6	35.2	20.2	42.7	10.0	25.2	21.6
Cu*	125.9	51.9	1395.8	56.5	2.5	40.3	170.9	104.9	125.9	145.9
Zn*	113.9	161.4	175.8	2.8	20.1	146.1	240.3	70.0	45.3	108.1
Ga[3]	ND	ND	ND	1.5	3.9	1.1	4.3	2.9	ND	2.7
Ge[3]	ND	ND	ND	0.28	7.28	2.59	0.27	5.77	ND	0.27
As[3]	ND	ND	ND	2.8	33.3	2.5	7.2	2.5	1.0	22.1
Mo[3]	ND	ND	ND	1.1	2.7	1.0	2.6	2.3	ND	1.1
Ag[2]	0.5	0.3	1.1	0.5	0.1	0.1	0.1	0.2	0.1	0.1
In[3]	ND	ND	ND	0.056	0.050	0.050	0.053	0.050	ND	0.054
Sn[3]	ND	ND	ND	0.6	1.8	0.5	0.5	0.5	ND	0.5
Sb[3]	ND	ND	ND	2.480	1.562	0.326	0.583	0.577	ND	1.108
W[3]	ND	ND	ND	0.6	1.8	0.6	2.4	1.2	ND	1.4
Au[2]	1.2	16.1	1.1	1.1	3.0	10.1	1.1	10.0	10.1	3.2
Tl[3]	ND	ND	ND	0.028	0.025	0.025	0.027	0.025	ND	0.027
Pb[2]	7.2	1.2	25.6	4.5	1.0	1.0	1.1	1.0	1.0	1.1
Bi[3]	ND	ND	ND	0.12	0.11	0.05	0.05	0.10	ND	0.05
Be	3.0	2.9	2.7	2.8	5.0	2.5	2.7	2.5	2.5	2.7
Rb[3]	ND	ND	ND	1.4	7.5	1.2	1.5	4.8	ND	5.0
Sr*	24.0	11.5	32.0	45.2	50.2	60.5	117.5	70.0	ND	118.9
Cs[3]	ND	ND	ND	0.1	1.6	0.1	0.1	3.3	ND	0.1
Ba*	12.0	23.1	10.7	3.4	15.3	4.4	5.9	15.0	10.1	9.7
Sc	3.0	2.9	2.7	2.8	2.5	2.5	2.7	2.5		2.7
Y*	6.0	5.8	5.3	2.8	5.7	3.6	4.0	5.2	2.5	4.5
Zr*	24.0	23.1	21.3	6.3	5.6	5.1	14.8	8.6	10.1	6.7
Nb*	6.0	5.8	5.3	0.1	1.8	0.1	0.4	0.2	ND	0.1
Hf[3]	ND	ND	ND	0.12	0.17	0.10	0.30	0.21	ND	0.16
Ta[3]	ND	ND	ND	0.01	0.02	0.01	0.03	0.02	ND	0.01
Th[3]	ND	ND	ND	0.1	0.5	0.1	0.2	0.3	ND	0.2
U[3]	ND	ND	ND	0.0	0.4	0.0	0.1	0.2	ND	0.1
La[3]	ND	ND	ND	1.3	7.0	2.2	1.6	2.7	ND	2.5
Ce[3]	ND	ND	ND	2.3	16.6	4.8	3.6	5.5	ND	4.7
Pr[3]	ND	ND	ND	0.2	1.7	0.5	0.4	0.6	ND	0.5
Nd[3]	ND	ND	ND	1.008	7.135	2.109	2.002	2.639	ND	2.013
Sm[3]	ND	ND	ND	0.250	1.184	0.453	0.502	0.575	ND	0.432
Eu[3]	ND	ND	ND	0.378	0.451	0.416	0.265	0.351	ND	0.479
Gd[3]	ND	ND	ND	0.302	0.920	0.448	0.547	0.609	ND	0.444
Tb[3]	ND	ND	ND	0.052	0.129	0.081	0.105	0.103	ND	0.076
Dy[3]	ND	ND	ND	0.343	0.774	0.508	0.627	0.655	ND	0.537
Ho[3]	ND	ND	ND	0.074	0.157	0.108	0.133	0.144	ND	0.121
Er[3]	ND	ND	ND	0.232	0.456	0.350	0.436	0.432	ND	0.386
Tm[3]	ND	ND	ND	0.034	0.062	0.051	0.068	0.057	ND	0.055
Yb[3]	ND	ND	ND	0.239	0.406	0.347	0.437	0.394	ND	0.381
Lu[3]	ND	ND	ND	0.039	0.054	0.053	0.069	0.061	ND	0.062
UTM E	377415	377665	378113	378113	387050	386190	375539	379267	379600	390130
UTM N	5291475	5283230	5282872	5282872	5287075	5281720	5291515	5288757	5289215	5284580

Appendix 3.1: Lithogeochemical data

sample	AU06741	AU06744	AU06504	AU06507	AU06509	AU06514	AU06516	AU06517	AU06519	AU06522
flag	IBT	IBT	IBW	IBW	IBW	IBW	IBW	IBW	IBW	IBW
SiO_2	69.95	56.01	45.33	19.04	13.93	6.66	23.19	69.56	8.76	55.51
Al_2O_3	0.07	0.45	0.81	0.50	0.71	0.32	0.34	0.70	1.72	0.29
Fe_2O_3	25.44	36.15	45.41	69.51	77.33	76.07	64.64	21.29	78.89	35.52
CaO	2.37	2.94	0.57	0.63	0.19	5.64	3.39	3.65	0.49	2.56
MgO	1.17	3.69	4.94	7.02	6.16	8.34	6.23	3.69	7.75	4.33
Na_2O	0.09	0.22	0.12	0.21	0.27	0.14	0.18	0.16	0.10	0.18
K_2O	0.02	0.13	0.07	0.06	0.12	0.04	0.09	0.15	0.09	0.14
TiO_2	0.01	0.03	0.05	0.02	0.04	0.01	0.03	0.02	0.08	0.01
MnO	0.75	0.26	2.57	2.85	1.09	2.59	1.78	0.62	1.87	1.33
P_2O_5	0.13	0.12	0.13	0.17	0.16	0.17	0.14	0.15	0.25	0.13
TIC	2.60	0.02	1.33	4.16	4.10	6.67	6.69	3.00	2.71	0.68
S	2.81	0.14	10.60	18.70	20.50	18.90	18.10	3.46	17.80	2.12
LOI	9.22	0.01	5.35	9.67	10.61	21.25	20.54	8.80	11.26	2.81
V*	33.2	55.2	42.5	27.7	45.0	57.2	58.3	16.5	50.8	22.6
Cr*	254.2	90.3	207.1	88.7	73.1	139.8	189.1	247.3	129.9	405.2
Co*	2.8	5.0	31.9	38.8	33.7	50.8	50.4	27.5	33.9	10.3
Ni*	22.1	75.3	74.3	85.4	106.8	95.3	107.1	44.0	107.3	31.0
Cu*	77.4	165.6	21.2	11.1	56.2	76.2	37.8	567.0	118.6	113.6
Zn*	171.3	80.3	276.1	419.1	472.1	165.2	499.2	307.7	480.0	353.2
Ga[3]	ND	ND	ND	ND	ND	3.4	3.2	ND	ND	2.6
Ge[3]	ND	ND	ND	ND	ND	0.32	0.32	ND	ND	0.79
As[3]	ND	ND	ND	ND	ND	3.2	18.2	ND	ND	6.7
Mo[3]	ND	ND	ND	ND	ND	1.3	1.3	ND	ND	4.1
Ag[2]	0.4	0.1	0.4	0.1	0.6	0.9	0.6	0.4	0.5	0.5
In[3]	ND	ND	ND	ND	ND	0.064	0.063	ND	ND	0.135
Sn[3]	ND	ND	ND	ND	ND	0.6	0.6	ND	ND	0.5
Sb[3]	ND	ND	ND	ND	ND	0.127	0.126	ND	ND	0.881
W[3]	ND	ND	ND	ND	ND	2.0	2.1	ND	ND	10.4
Au[2]	34.3	7.0	40.3	61.0	1.1	125.8	30.3	3.3	62.1	1.0
Tl[3]	ND	ND	ND	ND	ND	0.032	0.032	ND	ND	0.026
Pb[2]	1.1	1.0	1.1	37.7	1.1	6.4	6.3	1.1	1.1	96.0
Bi[3]	ND	ND	ND	ND	ND	0.21	0.17	ND	ND	1.41
Be	2.8	2.5	2.7	2.8	2.8	3.2	3.2	2.7	2.8	2.6
Rb[3]	ND	ND	ND	ND	ND	0.6	2.8	ND	ND	5.9
Sr*	132.6	110.4	10.6	11.1	5.6	25.4	37.8	33.0	11.3	31.0
Cs[3]	ND	ND	ND	ND	ND	0.1	0.2	ND	ND	2.0
Ba*	11.1	10.0	10.6	11.1	22.5	5.9	6.4	11.0	11.3	113.2
Sc	2.8	2.5	5.3	2.8	2.8	6.4	6.3	2.7	5.6	2.6
Y*	2.8	2.5	5.3	5.5	2.8	15.2	9.4	11.0	16.9	6.4
Zr*	11.1	20.1	31.9	44.4	45.0	13.6	14.0	22.0	79.1	9.4
Nb*	5.5	5.0	5.3	5.5	5.6	0.1	0.3	5.5	5.6	0.3
Hf[3]	ND	ND	ND	ND	ND	0.28	0.33	ND	ND	0.19
Ta[3]	ND	ND	ND	ND	ND	0.01	0.03	ND	ND	0.01
Th[3]	ND	ND	ND	ND	ND	0.3	0.4	ND	ND	0.2
U[3]	ND	ND	ND	ND	ND	0.5	0.6	ND	ND	0.3
La[3]	ND	ND	ND	ND	ND	5.8	4.6	ND	ND	2.7
Ce[3]	ND	ND	ND	ND	ND	8.6	7.5	ND	ND	7.0
Pr[3]	ND	ND	ND	ND	ND	0.9	0.7	ND	ND	0.5
Nd[3]	ND	ND	ND	ND	ND	3.859	3.087	ND	ND	2.274
Sm[3]	ND	ND	ND	ND	ND	0.883	0.785	ND	ND	0.529
Eu[3]	ND	ND	ND	ND	ND	0.698	0.494	ND	ND	0.505
Gd[3]	ND	ND	ND	ND	ND	1.201	0.890	ND	ND	0.623
Tb[3]	ND	ND	ND	ND	ND	0.229	0.170	ND	ND	0.114
Dy[3]	ND	ND	ND	ND	ND	1.531	1.243	ND	ND	0.680
Ho[3]	ND	ND	ND	ND	ND	0.361	0.281	ND	ND	0.147
Er[3]	ND	ND	ND	ND	ND	1.232	0.901	ND	ND	0.464
Tm[3]	ND	ND	ND	ND	ND	0.195	0.154	ND	ND	0.067
Yb[3]	ND	ND	ND	ND	ND	1.269	1.056	ND	ND	0.437
Lu[3]	ND	ND	ND	ND	ND	0.230	0.181	ND	ND	0.067
UTM E	390130	378956	409830	409980	410186	408565	408015	408015	410470	398528
UTM N	5284580	5289200	5298432	5298487	5298460	5298227	5297925	5297925	5298576	5293083

Appendix 3.1: Lithogeochemical data

sample	AU06523	AU06524	AU06526	AU06527	AU06528	AU06529	AU06532	AU06533	AU06534	AU06715
flag	IBW	IBW	IBW	IBW	IBW	IBW	IBW	IBW	IBW	IBW
SiO_2	52.09	51.63	70.38	74.02	71.65	54.96	66.66	46.95	60.36	64.24
Al_2O_3	2.48	0.17	0.16	0.20	0.24	0.38	0.20	0.20	0.14	0.01
Fe_2O_3	38.29	39.22	21.92	24.26	23.23	35.21	29.08	44.10	32.38	31.16
CaO	0.38	2.42	3.09	0.11	0.75	4.17	0.92	2.89	2.05	0.54
MgO	4.60	5.42	3.73	0.93	3.02	3.99	1.97	3.82	3.32	3.27
Na_2O	0.09	0.08	0.01	0.01	0.04	0.01	0.01	0.01	0.04	0.01
K_2O	0.54	0.16	0.03	0.01	0.05	0.07	0.02	0.01	0.06	0.03
TiO_2	0.07	0.01	0.01	0.01	0.02	0.02	0.01	0.01	0.01	0.01
MnO	1.31	0.77	0.60	0.39	0.94	1.07	1.04	1.90	1.55	0.68
P_2O_5	0.13	0.12	0.07	0.06	0.08	0.10	0.08	0.11	0.09	0.05
TIC	0.48	1.03	1.20	0.90	0.63	4.25	2.22	6.20	4.67	0.02
S	4.83	3.96	1.83	9.89	2.42	2.76	6.89	3.86	2.82	0.18
LOI	6.19	5.22	4.44	9.78	3.76	13.62	11.14	18.57	14.90	0.82
V*	42.7	21.2	31.5	11.1	15.6	29.1	28.2	37.0	29.4	45.4
Cr*	261.8	253.9	336.3	510.7	359.6	168.6	315.7	185.0	294.3	80.8
Co*	10.7	5.3	5.3	22.2	5.2	5.8	11.3	12.3	5.9	10.1
Ni*	42.7	26.4	31.5	61.1	31.3	40.7	50.7	37.0	35.3	20.2
Cu*	149.6	42.3	189.2	161.0	140.7	104.6	67.7	67.8	70.6	50.5
Zn*	154.9	2.6	157.7	5.6	2.6	139.5	2.8	3.1	2.9	141.3
Ga^3	ND	ND	ND	ND	ND	ND	ND	ND	ND	ND
Ge^3	ND	ND	ND	ND	ND	ND	ND	ND	ND	ND
As^3	ND	ND	ND	ND	ND	ND	ND	ND	ND	ND
Mo^3	ND	ND	ND	ND	ND	ND	ND	ND	ND	ND
Ag^2	1.0	0.5	1.1	0.7	0.5	0.6	0.8	0.6	0.6	0.1
In^3	ND	ND	ND	ND	ND	ND	ND	ND	ND	ND
Sn^3	ND	ND	ND	ND	ND	ND	ND	ND	ND	ND
Sb^3	ND	ND	ND	ND	ND	ND	ND	ND	ND	ND
W^3	ND	ND	ND	ND	ND	ND	ND	ND	ND	ND
Au^2	28.8	32.8	35.7	53.3	7.3	1.2	343.9	55.5	153.0	128.2
Tl^3	ND	ND	ND	ND	ND	ND	ND	ND	ND	ND
Pb^2	27.8	11.6	22.1	21.1	8.3	8.1	11.3	7.4	2.4	1.0
Bi^3	ND	ND	ND	ND	ND	ND	ND	ND	ND	ND
Be	2.7	2.6	2.6	2.8	2.6	2.9	2.8	3.1	2.9	2.5
Rb^3	ND	ND	ND	ND	ND	ND	ND	ND	ND	ND
Sr*	10.7	31.7	84.1	22.2	62.5	93.0	33.8	74.0	82.4	70.7
Cs^3	ND	ND	ND	ND	ND	ND	ND	ND	ND	ND
Ba*	21.4	31.7	21.0	11.1	41.7	34.9	11.3	12.3	11.8	10.1
Sc	2.7	2.6	2.6	2.8	2.6	2.9	2.8	3.1	2.9	2.5
Y*	5.3	2.6	5.3	5.6	5.2	5.8	5.6	12.3	11.8	2.5
Zr*	32.1	21.2	10.5	11.1	10.4	23.3	11.3	24.7	11.8	10.1
Nb*	5.3	5.3	5.3	5.6	5.2	5.8	5.6	6.2	5.9	5.0
Hf^5	ND	ND	ND	ND	ND	ND	ND	ND	ND	ND
Ta^3	ND	ND	ND	ND	ND	ND	ND	ND	ND	ND
Th^3	ND	ND	ND	ND	ND	ND	ND	ND	ND	ND
U^3	ND	ND	ND	ND	ND	ND	ND	ND	ND	ND
La^3	ND	ND	ND	ND	ND	ND	ND	ND	ND	ND
Ce^3	ND	ND	ND	ND	ND	ND	ND	ND	ND	ND
Pr^3	ND	ND	ND	ND	ND	ND	ND	ND	ND	ND
Nd^5	ND	ND	ND	ND	ND	ND	ND	ND	ND	ND
Sm^3	ND	ND	ND	ND	ND	ND	ND	ND	ND	ND
Eu^3	ND	ND	ND	ND	ND	ND	ND	ND	ND	ND
Gd^3	ND	ND	ND	ND	ND	ND	ND	ND	ND	ND
Tb^3	ND	ND	ND	ND	ND	ND	ND	ND	ND	ND
Dy^3	ND	ND	ND	ND	ND	ND	ND	ND	ND	ND
Ho^3	ND	ND	ND	ND	ND	ND	ND	ND	ND	ND
Er^3	ND	ND	ND	ND	ND	ND	ND	ND	ND	ND
Tm^3	ND	ND	ND	ND	ND	ND	ND	ND	ND	ND
Yb^3	ND	ND	ND	ND	ND	ND	ND	ND	ND	ND
Lu^3	ND	ND	ND	ND	ND	ND	ND	ND	ND	ND
UTM E	398766	398737	398822	399140	399140	400953	399631	399502	399502	398220
UTM N	5293301	5293330	5293722	5294206	5294173	5294070	5294101	5294122	5294131	5291822

Appendix 3.1: Lithogeochemical data

sample	AU06717	AU06718	AU06719	AU06731	AU06732	AU06733	AU06745	8470	8481	AU04221
flag	IBW	IBW	IBW	IBW	IBW	IBW	IBW	ISH	ISH	ISH
SiO_2	41.65	73.11	70.03	88.44	90.27	68.27	16.08	52.48	72.83	51.91
Al_2O_3	0.01	0.01	0.70	0.39	0.03	0.01	0.01	3.19	6.44	13.90
Fe_2O_3	51.33	23.26	25.14	10.12	9.28	29.74	75.45	37.68	13.41	22.87
CaO	1.25	0.31	1.84	0.26	0.03	0.37	0.51	2.21	1.81	3.42
MgO	4.31	2.35	0.89	0.21	0.03	0.89	4.58	3.53	2.90	3.01
Na_2O	0.01	0.16	0.12	0.19	0.18	0.14	0.09	0.06	1.90	2.27
K_2O	0.01	0.08	0.81	0.20	0.11	0.14	0.05	0.32	0.27	0.70
TiO_2	0.01	0.01	0.05	0.01	0.01	0.01	0.01	0.11	0.43	1.04
MnO	1.36	0.64	0.32	0.12	0.03	0.32	3.13	0.18	0.13	0.76
P_2O_5	0.05	0.07	0.11	0.05	0.03	0.13	0.09	0.24	0.08	0.11
TIC	0.18	0.06	0.43	0.06	0.01	0.53	0.77	0.37	0.31	2.04
S	0.13	0.18	11.80	1.56	0.32	1.24	25.50	0.46	4.06	0.16
LOI	1.14	0.51	10.78	1.80	0.63	3.86	17.75	2.24	4.62	1.71
V*	76.1	25.2	56.3	35.7	30.2	62.7	110.0	82.0	136.9	173.6
Cr*	20.3	272.5	315.2	464.7	528.8	298.0	85.5	51.1	315.9	66.8
Co*	10.2	2.5	11.3	2.6	2.5	2.6	42.8	10.2	36.8	30.6
Ni*	15.2	15.1	16.9	35.7	20.1	15.7	97.8	22.5	64.2	15.3
Cu*	2.5	80.7	202.7	188.9	141.0	130.7	128.3	30.7	184.2	20.4
Zn*	137.1	60.5	90.1	148.1	85.6	449.6	305.5	2.6	352.7	108.3
Ga^3	1.4	ND	ND	ND	1.4	2.2	3.8	7.7	7.8	20.0
Ge^3	0.25	ND	ND	ND	0.25	2.37	0.31	4.16	1.57	1.71
As^3	2.5	ND	ND	ND	16.3	20.7	3.1	2.6	2.6	2.6
Mo^3	1.0	ND	ND	ND	4.0	4.6	1.2	1.0	1.1	2.5
Ag^2	0.1	0.1	3.3	0.5	0.2	0.2	0.2	0.2	0.4	0.1
In^3	0.051	ND	ND	ND	0.050	0.052	0.061	0.103	0.053	0.051
Sn^3	0.5	ND	ND	ND	0.5	0.5	0.6	2.7	0.5	1.8
Sb^3	0.102	ND	ND	ND	0.523	1.222	0.122	0.879	0.105	0.102
W^3	0.7	ND	ND	ND	3.7	13.4	3.0	0.7	0.8	0.5
Au^2	177.7	21.2	1548.1	178.7	3.0	286.5	29.3	76.9	22.1	31.7
Tl^3	0.025	ND	ND	ND	0.025	0.026	0.031	0.026	0.026	0.026
Pb^2	1.0	1.0	10.1	94.0	10.1	32.4	1.2	22.5	47.4	1.0
Bi^3	0.05	ND	ND	ND	0.15	0.05	0.16	0.05	0.05	0.28
Be	2.5	2.5	2.8	2.6	2.5	2.6	3.1	2.6	2.6	5.1
Rb^3	6.6	ND	ND	ND	1.3	4.4	5.0	0.5	0.5	9.3
Sr*	60.9	80.7	90.1	91.9	100.7	115.0	134.4	30.7	84.2	367.7
Cs^3	1.1	ND	ND	ND	0.1	0.2	0.1	2.2	0.1	0.1
Ba*	15.8	20.2	45.0	40.9	4.7	11.0	10.4	45.2	109.4	259.7
Sc	2.5	2.5	2.8	2.6	2.5	2.6	3.1	2.6	15.8	15.3
Y*	8.2	2.5	2.8	2.6	1.9	6.4	9.5	9.3	8.0	32.2
Zr*	5.1	10.1	11.3	10.2	7.7	3.7	9.7	27.8	39.6	165.0
Nb*	0.1	5.0	5.6	5.1	0.1	0.1	0.1	0.4	0.5	6.9
Hf^5	0.12	ND	ND	ND	0.16	0.05	0.20	0.90	1.09	5.37
Ta^3	0.01	ND	ND	ND	0.01	0.01	0.01	0.09	0.17	0.70
Th^3	0.1	ND	ND	ND	0.2	0.2	0.1	0.8	0.6	3.8
U^3	0.1	ND	ND	ND	0.0	0.1	0.2	0.2	0.2	0.8
La^3	2.6	ND	ND	ND	1.2	3.4	1.6	8.2	4.2	19.8
Ce^3	5.7	ND	ND	ND	2.5	6.7	2.6	15.8	9.5	42.9
Pr^3	0.6	ND	ND	ND	0.3	0.7	0.3	1.8	1.2	5.1
Nd^3	3.000	ND	ND	ND	1.016	3.208	1.228	6.924	5.131	20.369
Sm^3	0.807	ND	ND	ND	0.214	0.798	0.346	1.371	1.259	4.545
Eu^3	0.704	ND	ND	ND	0.173	0.816	0.228	0.927	0.445	1.172
Gd^3	0.936	ND	ND	ND	0.234	0.885	0.559	1.243	1.201	4.429
Tb^3	0.171	ND	ND	ND	0.038	0.151	0.143	0.215	0.229	0.840
Dy^3	1.056	ND	ND	ND	0.231	0.880	1.064	1.337	1.408	5.287
Ho^3	0.233	ND	ND	ND	0.051	0.188	0.270	0.288	0.286	1.131
Er^3	0.729	ND	ND	ND	0.166	0.556	0.908	0.907	0.883	3.708
Tm^3	0.104	ND	ND	ND	0.023	0.076	0.150	0.126	0.133	0.610
Yb^3	0.684	ND	ND	ND	0.157	0.470	1.006	0.832	0.850	3.897
Lu^3	0.104	ND	ND	ND	0.027	0.069	0.177	0.128	0.122	0.581
UTM E	397650	397948	398180	395612	395510	395700	410170	410563	410401	410959
UTM N	5291950	5292360	5292954	5290828	5290925	5290550	5298640	5270720	5270775	5270696

Appendix 3.1: Lithogeochemical data

sample	AU04238	AU06679	AU06683	AU06703	AU06725	AU06727	AU06543	AU06549	AU06502	AU06521
flag	ISH	ISH	ISH	ISH	ISH	ISH	ISN	ISN	ISS	ISS
SiO_2	51.37	82.21	59.24	28.49	89.36	89.75	51.06	36.23	65.99	65.89
Al_2O_3	12.05	1.48	4.51	1.13	2.08	0.29	12.91	8.13	2.89	5.34
Fe_2O_3	32.10	14.86	33.80	68.97	6.56	3.20	24.73	49.02	24.67	23.00
CaO	0.12	0.10	0.11	0.11	0.35	5.70	4.97	1.33	2.48	2.22
MgO	3.52	1.00	0.95	0.87	0.95	0.70	2.35	2.26	2.82	2.12
Na_2O	0.01	0.01	0.17	0.01	0.23	0.19	1.54	0.04	0.02	0.16
K_2O	0.09	0.01	0.78	0.12	0.18	0.05	0.61	1.92	0.07	0.79
TiO_2	0.44	0.05	0.29	0.16	0.07	0.01	0.43	0.45	0.09	0.14
MnO	0.03	0.18	0.06	0.07	0.04	0.09	1.19	0.31	0.90	0.17
P_2O_5	0.27	0.09	0.10	0.05	0.18	0.02	0.22	0.30	0.07	0.18
TIC	ND	0.66	0.02	0.01	0.26	1.11	0.07	0.01	0.60	0.66
S	0.18	1.74	19.60	34.80	3.55	0.25	2.75	0.77	1.84	6.27
LOI	9.25	4.47	16.50	26.36	3.36	2.34	2.48	10.45	2.96	6.20
V*	155.1	15.7	60.3	102.5	26.2	10.3	87.3	118.0	31.0	38.9
Cr*	51.8	199.5	283.3	239.1	374.6	350.3	159.8	191.0	154.8	183.2
Co*	22.2	21.0	114.5	61.5	16.8	2.6	17.4	5.6	10.3	44.4
Ni*	16.6	31.5	108.5	82.0	39.1	30.9	98.0	33.7	15.5	72.2
Cu*	2.8	189.0	444.9	321.1	2806.4	231.8	98.0	174.1	2.6	589.7
Zn*	2.8	503.9	577.5	82.0	50648.5	1050.9	2.6	390.9	2.6	17879.0
Ga[3]	25.6	ND	ND	ND	3.4	ND	16.4	18.8	ND	ND
Ge[3]	10.27	ND	ND	ND	0.28	ND	0.26	1.32	ND	ND
As[3]	123.0	ND	ND	ND	6.7	ND	2.6	2.8	ND	ND
Mo[3]	4.6	ND	ND	ND	2.6	ND	1.0	1.1	ND	ND
Ag[2]	0.1	0.4	2.4	2.6	4.1	0.2	0.6	0.4	0.3	5.8
In[3]	0.280	ND	ND	ND	0.056	ND	0.052	0.056	ND	ND
Sn[3]	3.7	ND	ND	ND	0.6	ND	0.5	0.6	ND	ND
Sb[3]	0.263	ND	ND	ND	0.056	ND	0.103	0.601	ND	ND
W[3]	0.8	ND	ND	ND	1.0	ND	1.9	0.3	ND	ND
Au[2]	1.1	3.1	41.0	154.4	7.8	10.3	7.2	165.1	27.9	30.0
Tl[3]	0.028	ND	ND	ND	0.031	ND	0.176	0.028	ND	ND
Pb[2]	ND	1.0	130.2	266.5	17330.1	323.5	1.0	1.1	1.0	3842.3
Bi[3]	0.06	ND	ND	ND	0.06	ND	0.11	0.06	ND	ND
Be	5.5	2.6	3.0	3.4	2.8	2.6	2.6	5.6	2.6	2.8
Rb[3]	0.6	ND	ND	ND	3.1	ND	20.8	35.3	ND	ND
Sr*	15.5	21.0	36.2	54.7	111.8	123.6	381.6	150.5	10.3	22.2
Cs[3]	0.1	ND	ND	ND	0.1	ND	2.5	0.1	ND	ND
Ba*	14.5	5.2	132.6	41.0	26.9	5.2	123.2	386.8	10.3	33.3
Sc	10.0	2.6	12.1	3.4	2.8	2.6	5.2	11.2	2.6	5.6
Y*	24.4	5.2	6.0	3.4	2.7	2.6	11.2	27.5	5.2	11.1
Zr*	122.5	21.0	72.3	82.0	22.5	10.3	70.0	174.9	31.0	55.5
Nb*	4.9	5.2	6.0	6.8	0.5	5.2	3.5	10.9	5.2	5.6
Hf[3]	3.92	ND	ND	ND	0.48	ND	2.42	5.35	ND	ND
Ta[3]	0.55	ND	ND	ND	0.06	ND	0.28	1.00	ND	ND
Th[3]	4.2	ND	ND	ND	0.6	ND	1.6	8.9	ND	ND
U[3]	1.0	ND	ND	ND	0.2	ND	0.5	1.1	ND	ND
La[3]	15.9	ND	ND	ND	4.2	ND	13.0	70.6	ND	ND
Ce[3]	33.5	ND	ND	ND	9.4	ND	28.4	152.4	ND	ND
Pr[3]	4.0	ND	ND	ND	1.0	ND	3.0	17.6	ND	ND
Nd[3]	16.314	ND	ND	ND	4.180	ND	12.955	65.194	ND	ND
Sm[3]	3.577	ND	ND	ND	0.769	ND	2.553	9.771	ND	ND
Eu[3]	2.130	ND	ND	ND	0.305	ND	0.967	2.035	ND	ND
Gd[3]	3.143	ND	ND	ND	0.582	ND	2.192	6.966	ND	ND
Tb[3]	0.604	ND	ND	ND	0.091	ND	0.327	0.971	ND	ND
Dy[3]	3.884	ND	ND	ND	0.509	ND	1.753	4.978	ND	ND
Ho[3]	0.824	ND	ND	ND	0.097	ND	0.345	0.941	ND	ND
Er[3]	2.567	ND	ND	ND	0.295	ND	0.975	2.813	ND	ND
Tm[3]	0.370	ND	ND	ND	0.047	ND	0.129	0.415	ND	ND
Yb[3]	2.377	ND	ND	ND	0.338	ND	0.809	2.667	ND	ND
Lu[3]	0.358	ND	ND	ND	0.053	ND	0.112	0.369	ND	ND
UTM E	412143	416558	413800	419150	410572	410572	425320	429640	371400	372950
UTM N	5271338	5270993	5271450	5269570	5270770	5270772	5335690	5336065	5285180	5287314

Appendix 3.1: Lithogeochemical data

sample	AU06699	AU06536	AU06537	AU06538	AU06539	AU06540	AU06670	AU06735	AU06743	AU06505
flag	ISS	IST	IST	IST	IST	IST	IST	IST	IST	ISW
SiO_2	97.32	56.49	46.74	64.29	58.35	45.75	55.89	45.24	44.11	62.39
Al_2O_3	0.34	4.71	5.92	1.87	3.48	3.05	13.28	2.08	2.05	1.84
Fe_2O_3	1.30	30.14	37.88	28.47	31.05	46.32	17.46	42.44	40.84	31.49
CaO	0.77	3.84	1.57	3.06	3.33	0.90	7.08	4.72	6.06	0.90
MgO	0.15	2.91	4.88	1.81	2.24	2.90	2.16	3.52	5.34	2.39
Na_2O	0.01	0.15	0.09	0.01	0.01	0.24	1.95	0.32	0.22	0.15
K_2O	0.02	1.23	0.40	0.06	1.00	0.33	0.85	0.18	0.87	0.14
TiO_2	0.01	0.18	0.21	0.09	0.18	0.15	0.29	0.11	0.12	0.07
MnO	0.03	0.12	0.13	0.20	0.17	0.12	0.91	1.30	0.24	0.49
P_2O_5	0.05	0.23	0.19	0.16	0.20	0.25	0.12	0.09	0.15	0.12
TIC	0.06	0.32	0.22	2.71	2.03	4.63	0.10	0.01	0.53	0.12
S	0.07	1.65	8.71	1.27	3.41	6.76	0.97	3.70	3.64	6.37
LOI	0.30	3.02	8.98	9.02	10.27	16.79	0.94	2.60	5.35	2.61
V*	5.0	36.3	38.5	27.7	39.2	48.5	50.6	82.6	65.0	41.2
Cr*	396.9	119.2	93.5	210.4	185.0	418.1	197.2	98.1	63.8	200.7
Co*	35.2	20.7	22.0	11.1	16.8	54.5	10.1	15.5	159.5	56.6
Ni*	40.2	41.5	55.0	38.8	39.2	54.5	30.3	56.8	31.9	94.7
Cu*	361.7	171.0	544.4	177.2	140.2	513.8	75.9	129.1	895.1	733.0
Zn*	361.7	10.4	110.0	1882.6	2.8	649.5	2.5	77.4	95.7	238.8
Ga[3]	ND	ND	ND	ND	ND	ND	ND	7.0	ND	ND
Ge[3]	ND	ND	ND	ND	ND	ND	ND	0.26	ND	ND
As[3]	ND	ND	ND	ND	ND	ND	ND	2.6	ND	ND
Mo[3]	ND	ND	ND	ND	ND	ND	ND	1.0	ND	ND
Ag[2]	0.3	0.1	0.3	0.9	0.4	0.5	0.3	0.2	0.2	1.2
In[3]	ND	ND	ND	ND	ND	ND	ND	0.052	ND	ND
Sn[3]	ND	ND	ND	ND	ND	ND	ND	0.5	ND	ND
Sb[3]	ND	ND	ND	ND	ND	ND	ND	0.103	ND	ND
W[3]	ND	ND	ND	ND	ND	ND	ND	1.1	ND	ND
Au[2]	1.0	10.4	1.1	1.1	1.1	1.2	1.0	7.2	1.1	42.2
Tl[3]	ND	ND	ND	ND	ND	ND	ND	0.026	ND	ND
Pb[2]	63.3	5.2	1.1	2.2	1.1	1.2	3.0	1.0	2.1	1.0
Bi[3]	ND	ND	ND	ND	ND	ND	ND	0.12	ND	ND
Be	2.5	2.6	2.7	2.8	2.8	3.0	2.5	2.6	5.3	2.6
Rb[3]	ND	ND	ND	ND	ND	ND	ND	4.8	ND	ND
Sr*	100.5	31.1	11.0	33.2	44.8	24.2	131.5	82.6	138.2	10.3
Cs[3]	ND	ND	ND	ND	ND	ND	ND	3.6	ND	ND
Ba*	5.0	238.4	55.0	11.1	100.9	48.5	80.9	18.0	21.3	10.3
Sc	2.5	5.2	5.5	2.8	5.6	6.1	5.1	5.2	2.7	5.1
Y*	2.5	10.4	11.0	5.5	5.6	6.1	10.1	7.9	2.7	5.1
Zr*	10.0	51.8	77.0	33.2	44.8	48.5	91.0	23.9	42.5	30.9
Nb*	10.0	5.2	5.5	5.5	5.6	6.1	5.1	0.7	5.3	5.1
Hf[3]	ND	ND	ND	ND	ND	ND	ND	0.58	ND	ND
Ta[3]	ND	ND	ND	ND	ND	ND	ND	0.08	ND	ND
Th[3]	ND	ND	ND	ND	ND	ND	ND	0.4	ND	ND
U[3]	ND	ND	ND	ND	ND	ND	ND	0.3	ND	ND
La[3]	ND	ND	ND	ND	ND	ND	ND	4.0	ND	ND
Ce[3]	ND	ND	ND	ND	ND	ND	ND	7.9	ND	ND
Pr[3]	ND	ND	ND	ND	ND	ND	ND	0.8	ND	ND
Nd[3]	ND	ND	ND	ND	ND	ND	ND	3.420	ND	ND
Sm[3]	ND	ND	ND	ND	ND	ND	ND	0.744	ND	ND
Eu[3]	ND	ND	ND	ND	ND	ND	ND	0.312	ND	ND
Gd[3]	ND	ND	ND	ND	ND	ND	ND	0.820	ND	ND
Tb[3]	ND	ND	ND	ND	ND	ND	ND	0.157	ND	ND
Dy[3]	ND	ND	ND	ND	ND	ND	ND	1.016	ND	ND
Ho[3]	ND	ND	ND	ND	ND	ND	ND	0.224	ND	ND
Er[3]	ND	ND	ND	ND	ND	ND	ND	0.691	ND	ND
Tm[3]	ND	ND	ND	ND	ND	ND	ND	0.106	ND	ND
Yb[3]	ND	ND	ND	ND	ND	ND	ND	0.675	ND	ND
Lu[3]	ND	ND	ND	ND	ND	ND	ND	0.104	ND	ND
UTM E	375835	384271	383796	388075	388784	362821	354825	379362	386576	409830
UTM N	5286172	5288044	5288187	5286394	5286188	5288110	5279629	5288857	5287350	5298432

Appendix 3.1: Lithogeochemical data

sample	AU06508	AU06515	AU06518	AU06525	AU06530	AU06531	AU06720	AU06722	AU06734	8471
flag	ISW	ISW	ISW	ISW	ISW	ISW	ISW	ISW	ISW	IXH
SiO_2	60.08	53.44	43.55	63.97	64.82	36.81	69.12	73.24	91.75	36.96
Al_2O_3	6.67	1.66	6.84	3.72	2.45	2.59	5.09	1.24	1.38	1.05
Fe_2O_3	26.65	34.64	35.23	24.52	25.20	50.02	23.08	22.03	5.27	38.75
CaO	0.56	4.73	5.61	1.16	1.86	3.23	0.06	1.09	0.23	12.62
MgO	2.96	4.38	5.86	2.90	4.62	4.41	1.82	0.89	0.83	9.71
Na_2O	0.60	0.16	0.88	0.61	0.09	0.05	0.13	0.16	0.22	0.01
K_2O	1.50	0.08	0.19	2.07	0.09	0.85	0.13	0.54	0.17	0.03
TiO_2	0.17	0.07	0.74	0.11	0.13	0.16	0.19	0.14	0.04	0.05
MnO	0.72	0.63	0.81	0.84	0.57	1.72	0.29	0.58	0.05	0.70
P_2O_5	0.08	0.21	0.28	0.09	0.16	0.16	0.09	0.10	0.05	0.10
TIC	0.05	1.20	0.09	0.03	0.26	1.56	0.02	0.76	0.02	5.43
S	2.42	2.89	1.35	9.04	0.63	5.11	6.40	2.32	0.76	1.75
LOI	1.69	3.13	1.34	8.49	1.43	2.88	6.30	5.96	0.91	11.99
V*	25.5	93.4	193.8	112.3	45.8	77.7	48.2	64.2	20.2	85.7
Cr*	183.7	129.7	321.2	329.1	320.4	82.9	267.8	406.8	454.8	2.9
Co*	5.1	36.3	45.9	11.0	10.8	25.9	16.1	21.4	10.1	11.4
Ni*	40.8	72.6	111.2	38.4	76.3	62.2	32.1	107.0	30.3	34.3
Cu*	107.2	531.1	326.3	197.5	117.0	243.5	85.7	224.8	313.3	22.9
Zn*	698.0	513.5	398.7	87.8	213.6	350.2	176.7	460.3	121.3	479.9
Ga[3]	ND	ND	ND	9.1	5.8	ND	ND	ND	ND	3.0
Ge[3]	ND	ND	ND	0.27	0.89	ND	ND	ND	ND	4.91
As[3]	ND	ND	ND	2.7	2.5	ND	ND	ND	ND	7.2
Mo[3]	ND	ND	ND	1.1	1.0	ND	ND	ND	ND	1.1
Ag[2]	0.2	0.5	0.3	4.4	0.3	1.0	0.9	0.2	0.1	0.2
In[3]	ND	ND	ND	0.055	0.051	ND	ND	ND	ND	0.057
Sn[3]	ND	ND	ND	0.5	0.5	ND	ND	ND	ND	0.6
Sb[3]	ND	ND	ND	0.110	0.259	ND	ND	ND	ND	0.114
W[3]	ND	ND	ND	8.1	1.3	ND	ND	ND	ND	0.3
Au[2]	17.3	1.0	1.0	1226.5	3.1	14.5	28.9	18.2	1.0	85.7
Tl[3]	ND	ND	ND	0.085	0.025	ND	ND	ND	ND	0.029
Pb[2]	68.4	1.0	1.0	19.7	1.0	6.2	9.6	1.1	3.0	1.1
Bi[3]	ND	ND	ND	0.13	0.22	ND	ND	ND	ND	0.06
Be	2.6	2.6	2.5	2.7	2.5	2.6	2.7	2.7	2.5	2.9
Rb[3]	ND	ND	ND	73.4	5.8	ND	ND	ND	ND	0.6
Sr*	61.2	20.7	132.6	32.9	50.9	93.3	53.6	85.6	121.3	34.3
Cs[3]	ND	ND	ND	12.9	1.7	ND	ND	ND	ND	0.1
Ba*	265.3	10.4	40.8	208.8	21.8	124.3	53.6	64.2	10.1	7.9
Sc	5.1	15.6	25.5	2.7	5.1	5.2	2.7	2.7	2.5	5.7
Y*	5.1	15.6	20.4	5.2	9.2	10.4	2.7	2.7	2.5	11.7
Zr*	51.0	31.1	40.8	49.2	34.3	31.1	64.3	21.4	30.3	6.9
Nb*	5.1	5.2	5.1	1.1	1.0	5.2	5.4	5.4	5.1	3.5
Hf[3]	ND	ND	ND	1.20	0.82	ND	ND	ND	ND	0.25
Ta[3]	ND	ND	ND	0.09	0.07	ND	ND	ND	ND	0.01
Th[3]	ND	ND	ND	0.7	1.1	ND	ND	ND	ND	0.3
U[3]	ND	ND	ND	0.3	0.3	ND	ND	ND	ND	0.2
La[3]	ND	ND	ND	4.9	7.4	ND	ND	ND	ND	5.5
Ce[3]	ND	ND	ND	10.0	16.1	ND	ND	ND	ND	11.9
Pr[3]	ND	ND	ND	1.0	1.7	ND	ND	ND	ND	1.5
Nd[3]	ND	ND	ND	4.040	8.030	ND	ND	ND	ND	6.441
Sm[3]	ND	ND	ND	0.884	1.871	ND	ND	ND	ND	1.440
Eu[2]	ND	ND	ND	0.374	0.864	ND	ND	ND	ND	0.866
Gd[3]	ND	ND	ND	0.805	1.679	ND	ND	ND	ND	1.422
Tb[3]	ND	ND	ND	0.122	0.265	ND	ND	ND	ND	0.270
Dy[3]	ND	ND	ND	0.752	1.498	ND	ND	ND	ND	1.728
Ho[3]	ND	ND	ND	0.149	0.296	ND	ND	ND	ND	0.389
Er[3]	ND	ND	ND	0.460	0.871	ND	ND	ND	ND	1.188
Tm[3]	ND	ND	ND	0.066	0.119	ND	ND	ND	ND	0.171
Yb[3]	ND	ND	ND	0.472	0.806	ND	ND	ND	ND	1.108
Lu[3]	ND	ND	ND	0.080	0.119	ND	ND	ND	ND	0.173
UTM E	410186	408565	410470	398699	402127	402127	398180	396280	396094	410563
UTM N	5298460	5298227	5298576	5293683	5295330	5295405	5292935	5290991	5290446	5270739

Appendix 3.1: Lithogeochemical data

sample	8472	8473	AU04225	AU04226	AU06681	AU06726	AU06541	AU06546	AU06510	AU06511
flag	IXH	IXH	IXH	IXH	IXH	IXH	IXN	IXN	IXS	IXS
SiO_2	79.32	67.16	74.18	92.85	53.50	57.28	47.39	6.30	64.90	58.89
Al_2O_3	0.08	0.03	1.11	0.24	0.82	3.40	13.55	0.73	5.98	6.62
Fe_2O_3	14.23	24.98	23.84	3.36	41.69	34.48	19.74	80.57	20.01	29.75
CaO	3.44	3.99	0.05	2.68	0.42	2.22	7.65	5.03	5.15	1.10
MgO	2.64	3.28	0.52	0.76	2.80	2.06	4.64	4.39	2.48	1.94
Na_2O	0.01	0.01	0.01	0.01	0.01	0.12	4.92	0.01	0.22	0.31
K_2O	0.01	0.01	0.04	0.01	0.23	0.07	0.14	0.02	0.46	0.80
TiO_2	0.01	0.01	0.06	0.01	0.02	0.12	1.44	0.05	0.19	0.37
MnO	0.22	0.37	0.06	0.06	0.16	0.09	0.35	2.73	0.52	0.13
P_2O_5	0.04	0.16	0.13	0.02	0.34	0.15	0.16	0.17	0.08	0.09
TIC	1.43	4.77	0.01	0.63	2.86	0.66	3.13	2.15	0.62	0.25
S	0.50	0.21	0.48	0.20	9.50	18.10	5.17	9.89	3.76	14.00
LOI	4.32	12.88	4.32	2.14	16.67	14.07	13.63	18.48	4.15	11.92
V*	37.0	46.2	63.2	15.6	24.2	73.7	344.3	36.9	41.9	97.5
Cr*	322.5	90.3	147.2	187.4	163.0	276.3	180.4	18.4	199.1	699.6
Co*	2.6	5.8	10.5	2.6	12.1	116.7	75.7	12.3	26.2	126.2
Ni*	39.1	43.9	2.6	2.6	48.3	132.6	146.7	66.1	36.7	211.0
Cu*	15.9	5.8	347.8	26.1	690.8	798.1	157.2	129.1	172.9	498.9
Zn*	2.6	43.9	2.6	570.7	6.0	41748.5	5.8	3.1	397.1	3016.4
Ga^3	-1.1	-1.2	4.8	1.4	ND	6.5	20.4	ND	ND	ND
Ge^3	6.03	4.03	4.36	4.81	ND	0.31	0.29	ND	ND	ND
As^3	2.6	2.9	2.6	2.6	ND	23.1	14.8	ND	ND	ND
Mo^3	3.5	1.2	3.0	2.6	ND	1.2	1.2	ND	ND	ND
Ag^2	0.1	0.1	0.1	0.1	1.1	3.9	2.0	0.9	0.4	3.2
In^3	0.053	0.058	0.053	0.052	ND	0.061	0.058	ND	ND	ND
Sn^3	0.5	0.6	0.5	0.5	ND	0.6	0.6	ND	ND	ND
Sb^3	0.106	0.116	0.105	0.104	ND	0.485	0.472	ND	ND	ND
W^3	0.3	0.3	0.3	0.3	ND	1.9	41.1	ND	ND	ND
Au^2	18.0	31.2	7.4	3.1	443.2	17.2	12832.4	130.4	5.2	1.1
Tl^3	0.026	0.029	0.026	0.026	ND	0.031	0.029	ND	ND	ND
Pb^2	4.2	1.2	1.1	214.9	12.1	10633.6	1.2	1.2	3.1	141.1
Bi^3	0.05	0.06	0.36	0.05	ND	0.18	0.15	ND	ND	ND
Be	2.6	2.9	2.6	2.6	3.0	3.1	2.9	3.1	2.6	2.9
Rb^3	0.5	0.6	0.5	0.5	ND	3.6	3.7	ND	ND	ND
Sr*	21.1	23.1	5.3	9.1	24.2	73.7	151.3	61.5	10.5	11.5
Cs^3	0.1	0.1	0.1	0.1	ND	0.2	0.1	ND	ND	ND
Ba*	3.5	7.4	40.4	1.6	72.5	36.7	62.0	12.3	41.9	57.3
Sc	2.6	2.9	2.6	2.6	3.0	3.1	40.7	3.1	5.2	17.2
Y*	3.5	5.4	7.0	2.7	6.0	8.1	46.6	3.1	5.2	5.7
Zr*	10.3	7.5	28.2	15.1	24.2	35.4	103.7	36.9	62.9	57.3
Nb*	0.1	0.1	0.1	0.1	6.0	1.2	3.3	6.1	5.2	5.7
Hf^2	0.16	0.14	0.53	0.24	ND	0.78	2.87	ND	ND	ND
Ta^3	0.01	0.01	0.04	0.01	ND	0.14	0.19	ND	ND	ND
Th^3	0.0	0.0	0.5	0.1	ND	0.9	0.5	ND	ND	ND
U^3	0.0	0.0	0.1	0.0	ND	0.3	0.2	ND	ND	ND
La^3	1.1	2.0	5.3	1.6	ND	9.6	6.1	ND	ND	ND
Ce^3	2.3	3.9	10.8	3.3	ND	21.0	16.0	ND	ND	ND
Pr^3	0.3	0.5	1.3	0.4	ND	2.3	2.1	ND	ND	ND
Nd^3	1.280	2.087	5.226	1.727	ND	9.706	11.357	ND	ND	ND
Sm^3	0.335	0.475	1.032	0.363	ND	1.867	3.823	ND	ND	ND
Eu^3	0.357	0.471	0.617	0.211	ND	0.779	1.345	ND	ND	ND
Gd^3	0.380	0.517	1.014	0.371	ND	1.588	5.182	ND	ND	ND
Tb^3	0.080	0.100	0.172	0.064	ND	0.248	1.080	ND	ND	ND
Dy^3	0.528	0.655	1.022	0.372	ND	1.391	7.400	ND	ND	ND
Ho^3	0.125	0.144	0.225	0.079	ND	0.254	1.644	ND	ND	ND
Er^3	0.389	0.433	0.710	0.245	ND	0.777	5.117	ND	ND	ND
Tm^3	0.059	0.063	0.100	0.035	ND	0.110	0.768	ND	ND	ND
Yb^3	0.395	0.381	0.633	0.239	ND	0.736	4.749	ND	ND	ND
Lu^3	0.065	0.057	0.093	0.036	ND	0.111	0.712	ND	ND	ND
UTM E	410563	410563	410586	410606	414250	410572	406680	428283	373056	373056
UTM N	5270742	5270754	5270782	5270770	5271650	5270767	5333880	5336055	5287166	5287166

Appendix 3.1: Lithogeochemical data

sample	AU06512	AU06513	AU06520	AU06692	AU06693	AU06694	AU06695	AU06697	AU06700	AU06706
flag	IXS	IXS	IXS	IXS	IXS	IXS	IXS	IXS	IXS	IXS
SiO_2	62.08	45.77	63.58	50.79	60.81	95.59	35.22	84.04	58.18	62.40
Al_2O_3	3.48	5.85	5.60	6.18	6.95	0.48	15.59	0.55	0.01	12.29
Fe_2O_3	25.35	34.92	21.80	40.67	27.26	1.65	42.41	15.00	36.00	16.32
CaO	4.66	7.71	5.03	0.22	3.03	1.90	0.33	0.10	2.20	3.43
MgO	3.36	4.77	2.83	1.59	1.37	0.20	4.53	0.16	2.20	1.56
Na_2O	0.13	0.10	0.13	0.01	0.01	0.01	0.01	0.01	0.01	1.26
K_2O	0.25	0.12	0.37	0.01	0.01	0.07	0.62	0.05	0.07	2.15
TiO_2	0.24	0.44	0.30	0.19	0.25	0.01	0.49	0.02	0.01	0.33
MnO	0.32	0.20	0.18	0.07	0.13	0.03	0.12	0.02	1.30	0.21
P_2O_5	0.12	0.13	0.17	0.27	0.17	0.05	0.67	0.05	0.01	0.05
TIC	0.75	3.13	1.15	0.02	0.64	0.23	0.02	0.01	2.76	0.11
S	5.74	11.70	7.97	17.50	7.10	0.06	9.11	6.61	7.50	5.06
LOI	8.08	14.72	9.72	12.28	6.47	0.62	10.01	4.50	11.27	5.05
V*	78.8	136.8	78.0	61.0	44.2	2.5	136.0	31.4	79.1	63.5
Cr*	567.8	1201.2	726.0	186.8	221.1	425.4	79.3	492.7	175.2	174.6
Co*	32.8	101.1	66.0	590.6	121.6	10.1	453.3	21.0	79.1	52.9
Ni*	148.5	331.8	90.0	203.7	60.8	20.3	222.1	73.4	28.3	79.3
Cu*	196.5	2021.9	1476.1	50379.7	3747.9	335.3	12577.9	508.4	322.1	645.4
Zn*	1212.1	3270.7	38401.5	1687.4	16915.4	317.1	2017.0	199.2	67.8	1311.9
Ga^3	7.4	ND	ND	15.4	ND	ND	ND	1.9	16.8	ND
Ge^3	1.88	ND	ND	0.30	ND	ND	ND	4.60	4.72	ND
As^3	6.7	ND	ND	19.2	ND	ND	ND	22.3	12.5	ND
Mo^3	1.1	ND	ND	1.2	ND	ND	ND	1.0	3.9	ND
Ag^2	1.0	5.1	5.2	29.3	4.5	0.3	9.6	0.5	1.2	0.6
In^3	0.055	ND	ND	0.060	ND	ND	ND	0.052	0.057	ND
Sn^3	0.5	ND	ND	0.6	ND	ND	ND	0.5	1.2	ND
Sb^3	0.055	ND	ND	0.121	ND	ND	ND	0.462	0.938	ND
W^3	1.1	ND	ND	10.3	ND	ND	ND	0.6	1.9	ND
Au^2	5.5	3.6	20.4	78.3	1.1	1.0	57.8	1.0	159.3	1.1
Tl^3	0.142	ND	ND	0.030	ND	ND	ND	0.026	0.259	ND
Pb^2	115.7	113.0	13920.6	272.4	3040.4	12.2	192.6	145.7	27.1	1.1
Bi^3	0.05	ND	ND	0.13	ND	ND	ND	0.05	0.14	ND
Be	2.7	3.0	3.0	3.0	2.8	2.5	5.7	2.6	2.8	2.6
Rb^3	8.5	ND	ND	0.6	ND	ND	ND	1.2	27.7	ND
Sr*	25.7	23.8	24.0	12.1	22.1	60.8	56.7	73.4	67.8	243.3
Cs^3	1.5	ND	ND	0.1	ND	ND	ND	0.1	0.4	ND
Ba*	29.7	11.9	36.0	3.7	5.5	10.1	79.3	4.4	54.3	412.6
Sc	10.9	23.8	12.0	6.0	5.5	2.5	11.3	2.6	2.8	10.6
Y*	9.3	11.9	6.0	8.0	11.1	2.5	5.7	3.6	10.3	2.6
Zr*	28.9	47.6	48.0	62.3	66.3	10.1	158.6	11.1	111.0	116.4
Nb*	1.0	5.9	6.0	2.0	5.5	30.4	5.7	0.1	4.0	5.3
Hf^3	0.75	ND	ND	1.54	ND	ND	ND	0.19	2.91	ND
Ta^3	0.06	ND	ND	0.17	ND	ND	ND	0.01	0.39	ND
Th^3	0.6	ND	ND	1.6	ND	ND	ND	0.2	3.7	ND
U^3	0.1	ND	ND	0.9	ND	ND	ND	0.1	0.9	ND
La^3	4.1	ND	ND	3.4	ND	ND	ND	2.0	6.0	ND
Ce^3	9.1	ND	ND	7.2	ND	ND	ND	4.5	14.3	ND
Pr^3	1.0	ND	ND	0.8	ND	ND	ND	0.5	1.4	ND
Nd^3	4.573	ND	ND	3.580	ND	ND	ND	1.993	5.975	ND
Sm^3	1.315	ND	ND	0.946	ND	ND	ND	0.493	1.567	ND
Eu^3	0.788	ND	ND	0.433	ND	ND	ND	0.323	0.734	ND
Gd^3	1.416	ND	ND	1.066	ND	ND	ND	0.529	1.431	ND
Tb^3	0.258	ND	ND	0.187	ND	ND	ND	0.096	0.273	ND
Dy^3	1.465	ND	ND	1.089	ND	ND	ND	0.543	1.747	ND
Ho^3	0.298	ND	ND	0.241	ND	ND	ND	0.120	0.359	ND
Er^3	0.870	ND	ND	0.805	ND	ND	ND	0.363	1.080	ND
Tm^3	0.115	ND	ND	0.132	ND	ND	ND	0.055	0.155	ND
Yb^3	0.725	ND	ND	0.957	ND	ND	ND	0.359	1.082	ND
Lu^3	0.104	ND	ND	0.174	ND	ND	ND	0.060	0.171	ND
UTM E	372911	372911	372950	375650	375640	375660	375650	375880	375807	373713
UTM N	5287296	5287296	5287307	5286115	5286115	5286115	5286120	5286145	5285957	5286245

Appendix 3.1: Lithogeochemical data

sample	AU06708	AU06738	AU06712	AU06506	AU06716	AU06721	AU06746	4377	4415
flag	IXS	IXS	IXT	IXW	IXW	IXW	IXW	VBF	VBF
SiO_2	64.69	85.27	72.06	50.50	52.07	55.85	78.77	50.99	52.32
Al_2O_3	0.50	1.92	0.53	9.66	0.01	0.01	0.03	16.13	16.01
Fe_2O_3	30.81	11.35	26.19	32.37	40.83	37.15	18.42	12.22	10.84
CaO	0.31	0.15	0.10	0.31	0.82	0.40	0.28	9.29	8.52
MgO	2.39	0.87	0.78	5.25	4.44	3.69	1.76	6.50	5.90
Na_2O	0.01	0.14	0.01	0.19	0.01	2.03	0.09	2.98	2.41
K_2O	0.10	0.04	0.09	0.08	0.08	0.20	0.04	0.32	0.21
TiO_2	0.02	0.10	0.03	0.19	0.01	0.01	0.01	1.34	1.10
MnO	1.11	0.08	0.15	1.29	1.68	0.59	0.58	0.23	0.18
P_2O_5	0.05	0.06	0.06	0.18	0.05	0.07	0.02	0.01	0.10
TIC	0.03	0.14	1.66	0.03	0.14	0.01	0.20	0.19	2.41
S	3.06	1.83	9.34	6.45	0.03	0.17	4.15	0.01	ND
LOI	3.96	2.29	11.04	6.43	0.23	0.58	2.52	2.00	6.400
V*	41.7	36.0	33.8	49.3	45.3	50.5	46.3	ND	260
Cr*	135.6	575.7	445.5	136.8	30.2	111.2	318.6	ND	180
Co*	20.9	15.4	39.5	54.7	10.1	5.1	5.1	47.6	51.0
Ni*	36.5	72.0	67.7	49.3	20.1	10.1	46.3	41.1	110
Cu*	229.5	349.5	124.1	186.1	2.5	126.3	169.6	40.1	220
Zn*	240.0	107.9	107.2	10268.2	85.6	288.0	257.0	124.5	66
Ga^3	ND	3.8	ND	12.0	ND	ND	ND	ND	ND
Ge^3	ND	0.26	ND	0.55	ND	ND	ND	ND	ND
As^3	ND	2.6	ND	2.7	ND	ND	ND	ND	ND
Mo^3	ND	1.0	ND	1.1	ND	ND	ND	ND	1.1
Ag^2	0.2	0.3	0.1	0.9	0.1	0.2	0.1	ND	ND
In^3	ND	0.051	ND	0.055	ND	ND	ND	ND	ND
Sn^3	ND	0.5	ND	0.5	ND	ND	ND	ND	ND
Sb^3	ND	0.412	ND	0.109	ND	ND	ND	ND	ND
W^3	ND	0.8	ND	0.7	ND	ND	ND	ND	ND
Au^2	7.3	7.2	84.6	15.3	7.0	3.0	34.9	ND	ND
Tl^3	ND	0.026	ND	0.027	ND	ND	ND	ND	ND
Pb^2	1.0	1.0	1.1	4663.4	1.0	1.0	1.0	ND	ND
Bi^3	ND	0.17	ND	0.05	ND	ND	ND	ND	ND
Be	2.6	2.6	2.8	2.7	2.5	2.5	2.6	ND	0.5
Rb^3	ND	2.8	ND	2.4	ND	ND	ND	ND	14.0
Sr*	62.6	113.1	79.0	12.1	60.4	60.6	102.8	ND	170
Cs^3	ND	0.2	ND	0.3	ND	ND	ND	ND	0.58
Ba*	20.9	16.2	11.3	1.6	20.1	20.2	10.3	ND	130.0
Sc	2.6	5.1	2.8	5.5	2.5	2.5	2.6	ND	34.0
Y*	2.6	2.7	2.8	11.8	2.5	2.5	2.6	ND	25.0
Zr*	20.9	10.6	22.6	123.0	20.1	20.2	10.3	ND	66
Nb*	5.2	0.3	5.6	3.6	5.0	5.1	5.1	ND	3.4
Hf^3	ND	0.26	ND	3.11	ND	ND	ND	ND	1.700
Ta^3	ND	0.02	ND	0.39	ND	ND	ND	ND	0.050
Th^3	ND	0.1	ND	3.0	ND	ND	ND	ND	0.590
U^3	ND	0.0	ND	1.0	ND	ND	ND	ND	0.160
La^3	ND	1.4	ND	22.3	ND	ND	ND	ND	5.00
Ce^3	ND	3.1	ND	41.6	ND	ND	ND	ND	13.00
Pr^3	ND	0.3	ND	4.0	ND	ND	ND	ND	1.80
Nd^3	ND	1.433	ND	15.864	ND	ND	ND	ND	9.000
Sm^3	ND	0.369	ND	3.089	ND	ND	ND	ND	2.800
Eu^3	ND	0.205	ND	1.066	ND	ND	ND	ND	1.0000
Gd^3	ND	0.389	ND	2.560	ND	ND	ND	ND	3.000
Tb^3	ND	0.070	ND	0.339	ND	ND	ND	ND	0.640
Dy^3	ND	0.435	ND	1.796	ND	ND	ND	ND	4.000
Ho^3	ND	0.096	ND	0.354	ND	ND	ND	ND	0.880
Er^3	ND	0.297	ND	1.023	ND	ND	ND	ND	2.000
Tm^3	ND	0.043	ND	0.144	ND	ND	ND	ND	0.4200
Yb^3	ND	0.283	ND	1.003	ND	ND	ND	ND	2.500
Lu^3	ND	0.044	ND	0.152	ND	ND	ND	ND	0.3500
UTM E	374820	370775	375422	409980	397450	396899	410350	411693	421129
UTM N	5286890	5283850	5291580	5298487	5292050	5291466	5298700	5270872	5269286

Appendix 3.1: Lithogeochemical data

sample	4389	AU04232	AU04233	AU04237	23564	23568	AU04205	AU04209	AU04218
flag	VBE	VBE	VBE	VDF	VDA	VDA	VDA	VDA	VDA
SiO_2	57.23	51.37	52.75	69.84	63.47	61.02	70.28	62.09	62.47
Al_2O_3	18.03	14.90	13.48	14.32	17.08	15.69	14.21	14.25	14.46
Fe_2O_3	8.67	11.69	14.37	4.56	7.81	8.05	7.10	8.46	8.14
CaO	6.91	10.44	9.79	3.35	4.28	7.39	1.79	4.27	6.32
MgO	3.36	6.76	5.55	1.78	2.23	2.93	2.23	5.38	2.57
Na_2O	3.61	3.09	2.45	3.89	2.14	2.13	1.79	4.23	3.52
K_2O	0.76	0.30	0.17	1.30	1.85	1.52	1.67	0.25	1.40
TiO_2	1.27	1.13	1.13	0.73	0.89	0.82	0.75	0.72	0.77
MnO	0.17	0.18	0.21	0.07	0.11	0.21	0.08	0.20	0.14
P_2O_5	ND	0.12	0.09	0.17	0.14	0.22	0.10	0.17	0.23
TIC	4.04	ND	ND	ND	ND	ND	ND	ND	ND
S	0.04	0.04	0.01	0.01	ND	ND	0.12	0.01	0.03
LOI	6.00	0.95	1.74	2.65	2.29	5.98	4.86	2.84	3.72
V*	ND	339.2	403.5	155.5	138.6	127.8	185.1	191.7	135.6
Cr*	ND	207.6	81.7	108.9	313.2	245.0	227.5	290.2	104.3
Co*	53.8	50.6	61.3	25.9	20.5	21.3	26.4	31.1	26.1
Ni*	ND	75.9	46.0	36.3	25.7	21.3	68.8	ND	52.2
Cu*	103.0	30.4	107.3	25.9	10.0	2.5	37.0	15.5	15.6
Zn*	103.0	2.5	2.6	10.4	46.2	58.6	2.6	2.6	2.6
Ga^3	ND	ND	17.1	ND	ND	ND	ND	ND	ND
Ge^3	ND	ND	2.13	ND	ND	ND	ND	ND	ND
As^3	ND	ND	2.6	ND	ND	ND	ND	ND	ND
Mo^3	ND	ND	1.0	ND	ND	ND	ND	ND	ND
Ag^2	ND	ND	ND	ND	ND	ND	ND	ND	ND
In^3	ND	ND	0.051	ND	ND	ND	ND	ND	ND
Sn^3	ND	ND	0.5	ND	ND	ND	ND	ND	ND
Sb^3	ND	ND	0.102	ND	ND	ND	ND	ND	ND
W^3	ND	ND	0.3	ND	ND	ND	ND	ND	ND
Au^2	ND	ND	ND	ND	ND	ND	ND	ND	ND
Tl^3	ND	ND	0.026	ND	ND	ND	ND	ND	ND
Pb^2	ND	ND	ND	ND	ND	ND	ND	ND	ND
Bi^3	ND	ND	0.05	ND	ND	ND	ND	ND	ND
Be	ND	10.1	10.2	10.4	5.1	5.3	10.6	5.2	10.4
Rb^3	ND	ND	0.5	ND	ND	ND	ND	ND	ND
Sr*	ND	ND	104.8	ND	ND	ND	ND	ND	ND
Cs^3	ND	ND	0.1	ND	ND	ND	ND	ND	ND
Ba*	ND	ND	46.6	ND	ND	ND	ND	ND	ND
Sc	ND	38.5	44.9	10.4	15.4	10.7	19.0	20.7	12.5
Y*	ND	20.2	19.9	10.4	20.5	21.3	10.6	10.4	10.4
Zr*	ND	60.7	46.7	114.0	164.3	149.2	95.2	103.6	166.9
Nb*	ND	5.1	0.8	41.5	5.0	5.0	5.3	5.2	5.2
Hf^3	ND	ND	1.60	ND	ND	ND	ND	ND	ND
Ta^3	ND	ND	0.10	ND	ND	ND	ND	ND	ND
Th^3	ND	ND	0.5	ND	ND	ND	ND	ND	ND
U^3	ND	ND	0.1	ND	ND	ND	ND	ND	ND
La^3	ND	ND	3.5	ND	ND	ND	ND	ND	ND
Ce^3	ND	ND	8.6	ND	ND	ND	ND	ND	ND
Pr^3	ND	ND	1.2	ND	ND	ND	ND	ND	ND
Nd^3	ND	ND	6.083	ND	ND	ND	ND	ND	ND
Sm^3	ND	ND	1.882	ND	ND	ND	ND	ND	ND
Eu^3	ND	ND	0.724	ND	ND	ND	ND	ND	ND
Gd^3	ND	ND	2.098	ND	ND	ND	ND	ND	ND
Tb^3	ND	ND	0.494	ND	ND	ND	ND	ND	ND
Dy^3	ND	ND	3.394	ND	ND	ND	ND	ND	ND
Ho^3	ND	ND	0.754	ND	ND	ND	ND	ND	ND
Er^3	ND	ND	2.421	ND	ND	ND	ND	ND	ND
Tm^3	ND	ND	0.372	ND	ND	ND	ND	ND	ND
Yb^3	ND	ND	2.261	ND	ND	ND	ND	ND	ND
Lu^3	ND	ND	0.338	ND	ND	ND	ND	ND	ND
UTM E	410330	409892	410529	412116	410968	410401	421085	424540	411560
UTM N	5270554	5270533	5270549	5271293	5270720	5270776	5270291	5269722	5271280

Appendix 3.1: Lithogeochemical data

sample	AU04216	AU06728	23557	AU04215	AU04222	3469	3473	AU01757	AU01764	AU04186
flag	VDC	VDC	VDS	VRF	VRF	VRA	VRA	VRA	VRA	VRA
SiO_2	60.26	59.97	68.63	76.32	74.96	82.28	70.44	68.01	71.35	80.59
Al_2O_3	14.52	16.89	13.88	12.15	12.40	10.75	14.65	17.23	14.20	11.40
Fe_2O_3	12.09	11.55	6.03	3.09	4.40	2.86	3.89	3.94	3.44	2.58
CaO	2.84	2.30	3.63	1.37	1.42	0.07	0.79	2.76	4.33	0.53
MgO	5.79	3.36	1.87	0.86	0.98	0.93	1.47	1.59	1.57	0.21
Na_2O	2.43	2.57	0.21	3.61	4.26	0.61	6.48	4.55	2.81	2.91
K_2O	0.92	2.06	4.75	2.19	1.18	1.27	0.43	1.38	1.86	1.41
TiO_2	0.78	0.93	0.76	0.30	0.31	0.22	0.34	0.43	0.31	0.28
MnO	0.17	0.24	0.07	0.05	0.05	0.90	1.43	0.05	0.08	0.03
P_2O_5	0.19	0.14	0.16	0.05	0.04	0.10	0.10	0.06	0.05	0.06
TIC	ND	0.41	ND	ND	ND	0.05	0.05	ND	ND	ND
S	0.02	0.04	ND	0.01	0.01	ND	ND	0.01	0.07	0.01
LOI	5.60	3.54	5.72	0.90	0.87	1.80	1.50	1.78	4.70	1.56
V*	186.7	151.1	117.2	51.2	97.0	ND	ND	87.0	78.9	71.3
Cr*	357.4	119.8	373.0	92.2	142.9	5.1	5.0	87.0	78.9	117.2
Co*	53.4	26.0	16.0	10.2	5.1	2.5	7.0	15.4	10.5	5.1
Ni*	ND	20.8	26.6	2.6	5.1	5.1	5.0	10.2	10.5	5.1
Cu*	32.0	125.0	11.0	2.6	20.4	10.1	14.9	10.2	2.6	2.5
Zn*	2.7	239.7	37.3	2.6	2.6	ND	19.9	41.0	147.3	2.5
Ga[3]	17.9	ND	ND	ND	ND	ND	ND	ND	ND	ND
Ge[3]	1.89	ND	ND	ND	ND	ND	ND	ND	ND	ND
As[3]	2.7	ND	ND	ND	ND	ND	ND	ND	ND	ND
Mo[3]	1.1	ND	ND	ND	ND	2.4	0.1	ND	ND	ND
Ag[2]	ND	0.2	ND	ND	ND	ND	ND	ND	ND	ND
In[3]	0.053	ND	ND	ND	ND	ND	ND	ND	ND	ND
Sn[3]	0.5	ND	ND	ND	ND	ND	ND	ND	ND	ND
Sb[3]	0.107	ND	ND	ND	ND	ND	ND	ND	ND	ND
W[3]	0.3	ND	ND	ND	ND	ND	ND	ND	ND	ND
Au[2]	ND	10.4	ND	ND	ND	ND	ND	ND	ND	ND
Tl[3]	0.027	ND	ND	ND	ND	ND	ND	ND	ND	ND
Pb[2]	ND	22.9	ND	ND	ND	ND	ND	ND	ND	ND
Bi[3]	0.05	ND	ND	ND	ND	ND	ND	ND	ND	ND
Be	10.7	5.2	5.3	5.1	5.1	1.2	0.9	5.1	5.3	5.1
Rb[3]	21.3	ND	ND	ND	ND	29.4	9.0	ND	ND	ND
Sr*	189.2	177.1	ND	ND	ND	85.2	139.5	ND	ND	ND
Cs[3]	0.1	ND	ND	ND	ND	0.8	0.1	ND	ND	ND
Ba*	137.9	312.6	ND	ND	ND	263.8	119.6	ND	ND	ND
Sc	17.1	15.6	10.7	5.1	7.1	4.1	5.0	6.1	4.2	4.1
Y*	20.7	10.4	16.0	20.5	30.6	38.6	16.9	5.1	5.3	5.1
Zr*	149.6	177.1	127.9	174.2	255.2	304.4	173.4	122.9	94.7	101.9
Nb*	6.3	10.4	5.0	5.1	20.4	10.0	8.2	5.1	5.3	5.1
Hf[3]	4.03	ND	ND	ND	ND	7.20	4.28	ND	ND	ND
Ta[3]	0.56	ND	ND	ND	ND	0.78	0.59	ND	ND	ND
Th[3]	2.8	ND	ND	ND	ND	7.2	4.0	ND	ND	ND
U[3]	0.6	ND	ND	ND	ND	1.6	1.1	ND	ND	ND
La[3]	20.3	ND	ND	ND	ND	31.5	18.9	ND	ND	ND
Ce[3]	45.8	ND	ND	ND	ND	70.0	40.8	ND	ND	ND
Pr[3]	5.2	ND	ND	ND	ND	8.4	4.7	ND	ND	ND
Nd[3]	21.213	ND	ND	ND	ND	34.496	18.929	ND	ND	ND
Sm[3]	4.039	ND	ND	ND	ND	7.609	4.085	ND	ND	ND
Eu[3]	1.142	ND	ND	ND	ND	1.015	0.946	ND	ND	ND
Gd[3]	3.532	ND	ND	ND	ND	6.088	2.989	ND	ND	ND
Tb[3]	0.571	ND	ND	ND	ND	1.015	0.548	ND	ND	ND
Dy[3]	3.354	ND	ND	ND	ND	6.088	3.088	ND	ND	ND
Ho[3]	0.698	ND	ND	ND	ND	1.218	0.628	ND	ND	ND
Er[3]	2.167	ND	ND	ND	ND	3.044	0.996	ND	ND	ND
Tm[3]	0.328	ND	ND	ND	ND	0.629	0.289	ND	ND	ND
Yb[3]	2.052	ND	ND	ND	ND	3.653	1.893	ND	ND	ND
Lu[3]	0.308	ND	ND	ND	ND	0.548	0.269	ND	ND	ND
UTM E	411560	410567	411560	414545	411000	427873	421725	415330	435483	428219
UTM N	5271305	5270788	5271380	5270111	5270534	5268914	5267233	5270631	5270295	5269455

Appendix 3.1: Lithogeochemical data

sample	AU04214	AU04220	AU04249	8477	23558	AU06724	AU04217	AU04227	8469	8475
flag	VRA	VRA	VRA	VRC	VRC	VRC	VLF	VLF	VLC	VLC
SiO_2	73.54	74.95	77.58	63.51	71.46	69.48	79.03	78.03	59.62	73.93
Al_2O_3	13.73	14.07	12.69	10.67	12.03	12.64	13.08	13.16	13.47	14.53
Fe_2O_3	3.30	2.81	2.22	8.37	10.01	9.42	0.81	1.06	17.83	1.48
CaO	3.10	1.87	2.19	13.89	3.07	0.74	0.08	0.49	2.25	2.60
MgO	0.99	1.70	1.53	2.38	2.22	2.07	0.34	0.38	2.04	0.98
Na_2O	2.85	2.21	1.39	0.50	0.42	2.23	4.65	5.60	1.10	2.83
K_2O	2.04	2.00	2.03	0.21	0.40	2.68	1.87	1.18	2.81	3.53
TiO_2	0.32	0.28	0.26	0.23	0.24	0.35	0.10	0.06	0.05	0.06
MnO	0.07	0.04	0.08	0.18	0.07	0.07	0.01	0.02	0.75	0.06
P_2O_5	0.06	0.07	0.03	0.05	0.08	0.11	0.02	0.03	0.06	0.01
TIC	ND	ND	ND	2.94	ND	0.04	ND	ND	0.10	0.46
S	0.04	0.03	ND	2.23	ND	2.30	0.01	0.01	1.06	0.02
LOI	1.70	1.79	2.41	8.31	12.49	3.46	1.11	0.61	2.11	2.48
V*	51.1	56.2	42.0	183.3	92.0	67.7	61.6	20.3	39.8	10.3
Cr*	137.9	107.4	104.0	452.4	1056.0	208.3	77.1	131.7	88.8	70.1
Co*	5.1	5.1	5.0	34.4	46.0	26.0	2.6	2.5	5.0	2.6
Ni*	5.1	2.6	5.0	76.7	ND	26.0	5.1	15.2	34.8	17.5
Cu*	2.6	2.6	2.5	1248.4	ND	255.1	2.6	177.3	10.0	25.8
Zn*	2.6	2.6	5.0	21876.1	40.0	633.1	2.6	2.5	2.5	46.4
Ga^3	ND	ND	ND	11.3	ND	15.1	ND	ND	13.7	18.3
Ge^3	ND	ND	ND	1.05	ND	0.26	ND	ND	1.62	1.60
As^3	ND	ND	ND	2.9	ND	2.6	ND	ND	2.5	2.6
Mo^3	ND	ND	ND	3.5	ND	1.0	ND	ND	1.0	2.7
Ag^2	ND	ND	ND	3.0	ND	0.4	ND	ND	0.1	0.1
In^3	ND	ND	ND	0.057	ND	0.052	ND	ND	0.050	0.052
Sn^3	ND	ND	ND	0.6	ND	0.7	ND	ND	4.3	0.5
Sb^3	ND	ND	ND	0.358	ND	0.607	ND	ND	0.100	0.253
W^3	ND	ND	ND	0.3	ND	0.4	ND	ND	10.4	0.3
Au^2	ND	ND	ND	3.4	ND	1.0	ND	ND	7.0	10.3
Tl^3	ND	ND	ND	0.029	ND	0.229	ND	ND	0.085	0.026
Pb^2	ND	ND	ND	30466.2	ND	13.5	ND	ND	20.9	3.1
Bi^3	ND	ND	ND	0.06	ND	0.13	ND	ND	0.14	0.05
Be	5.1	5.1	ND	2.9	2.5	5.2	5.1	2.5	2.5	5.2
Rb^3	ND	ND	ND	0.6	ND	64.8	ND	ND	53.8	43.9
Sr*	ND	ND	ND	183.3	ND	177.0	ND	ND	69.7	51.6
Cs^3	ND	ND	ND	0.1	ND	0.9	ND	ND	7.5	0.1
Ba*	ND	ND	5.0	75.1	ND	309.3	ND	ND	511.7	541.2
Sc	6.1	4.1	5.0	17.2	23.0	5.2	5.1	3.0	5.0	5.2
Y*	20.4	5.1	21.0	15.1	29.0	11.0	15.4	10.1	25.9	33.9
Zr*	153.3	112.5	125.0	11.1	ND	115.0	51.4	50.6	48.9	56.8
Nb*	5.1	5.1	ND	22.9	6.0	2.8	5.1	5.1	8.3	11.5
Hf^3	ND	ND	ND	0.35	ND	3.05	ND	ND	2.40	2.79
Ta^3	ND	ND	ND	0.01	ND	0.41	ND	ND	0.99	1.39
Th^3	ND	ND	ND	0.2	ND	2.7	ND	ND	2.2	3.0
U^3	ND	ND	ND	0.1	ND	0.7	ND	ND	1.2	1.5
La^3	ND	ND	ND	8.6	ND	11.5	ND	ND	13.3	14.3
Ce^3	ND	ND	ND	18.1	ND	23.6	ND	ND	32.5	36.6
Pr^3	ND	ND	ND	2.4	ND	2.3	ND	ND	4.1	4.7
Nd^3	ND	ND	ND	10.865	ND	8.943	ND	ND	16.024	18.092
Sm^3	ND	ND	ND	2.854	ND	1.792	ND	ND	3.887	4.581
Eu^3	ND	ND	ND	0.810	ND	0.677	ND	ND	1.170	0.927
Gd^3	ND	ND	ND	2.725	ND	1.584	ND	ND	3.294	4.090
Tb^3	ND	ND	ND	0.455	ND	0.300	ND	ND	0.689	0.862
Dy^3	ND	ND	ND	2.425	ND	1.867	ND	ND	4.161	5.418
Ho^3	ND	ND	ND	0.434	ND	0.380	ND	ND	0.865	1.111
Er^3	ND	ND	ND	1.143	ND	1.215	ND	ND	2.634	3.406
Tm^3	ND	ND	ND	0.155	ND	0.188	ND	ND	0.389	0.522
Yb^3	ND	ND	ND	0.946	ND	1.262	ND	ND	2.341	3.044
Lu^3	ND	ND	ND	0.130	ND	0.188	ND	ND	0.332	0.425
UTM E	416169	410978	409194	410399	411560	413725	411560	410525	410563	410173
UTM N	5270217	5270596	5270859	5270761	5271395	5271007	5271320	5270742	5270696	5270741

Appendix 3.1: Lithogeochemical data

sample	23554	AU04223	AU01752	AU04181	AU04185	AU04235	AU04241	AU04243	AU04247	AU04248
flag	VLC	VLC	VLS	VLS	VLS	VLS	VLS	VLS	VLS	VLS
SiO_2	74.41	75.44	80.33	82.63	80.85	79.15	79.97	79.51	78.17	81.18
Al_2O_3	14.22	11.62	11.67	10.33	11.73	12.34	11.66	12.72	12.70	12.94
Fe_2O_3	0.89	8.07	2.02	2.29	0.87	0.70	2.15	0.72	1.77	0.94
CaO	1.38	0.32	0.79	0.65	0.94	0.20	0.04	0.22	2.45	0.03
MgO	0.31	1.06	0.64	1.45	0.14	0.29	0.48	0.42	0.76	0.84
Na_2O	4.04	0.25	1.16	0.50	3.32	2.84	2.13	1.05	0.43	0.22
K_2O	4.60	2.85	3.20	2.02	2.03	4.39	3.43	5.27	3.55	3.77
TiO_2	0.10	0.06	0.12	0.08	0.07	0.06	0.07	0.06	0.12	0.06
MnO	0.05	0.29	0.05	0.02	0.02	0.02	0.04	0.01	0.04	0.01
P_2O_5	0.01	0.04	0.01	0.02	0.02	0.02	0.02	0.01	0.01	0.01
TIC	ND	ND	ND	ND	ND	ND	ND	ND	ND	ND
S	ND	0.02	0.01	0.01	0.02	0.01	0.01	0.01	0.01	0.01
LOI	1.65	2.62	2.28	2.59	1.67	1.25	1.45	1.41	3.13	2.08
V*	41.0	67.0	31.1	57.4	41.1	20.4	35.6	30.9	62.8	41.5
Cr*	618.8	123.7	77.8	119.9	61.6	86.9	81.3	103.0	99.4	57.0
Co*	5.0	2.6	5.2	2.6	2.6	2.6	2.5	2.6	5.2	2.6
Ni*	26.0	2.6	5.2	2.6	2.6	2.6	5.1	2.6	5.2	2.6
Cu*	5.0	2.6	2.6	2.6	2.6	2.6	2.5	2.6	2.6	2.6
Zn*	5.0	2.6	124.5	2.6	2.6	2.6	25.4	15.5	20.9	46.6
Ga[3]	ND	ND	ND	ND	ND	ND	17.4	18.8	ND	ND
Ge[3]	ND	ND	ND	ND	ND	ND	1.37	1.43	ND	ND
As[3]	ND	ND	ND	ND	ND	ND	2.5	2.6	ND	ND
Mo[3]	ND	ND	ND	ND	ND	ND	1.0	1.0	ND	ND
Ag[2]	ND	ND	ND	ND	ND	ND	ND	ND	ND	ND
In[3]	ND	ND	ND	ND	ND	ND	0.051	0.052	ND	ND
Sn[3]	ND	ND	ND	ND	ND	ND	0.5	1.1	ND	ND
Sb[3]	ND	ND	ND	ND	ND	ND	0.102	0.103	ND	ND
W[3]	ND	ND	ND	ND	ND	ND	0.3	1.6	ND	ND
Au[2]	ND	ND	ND	ND	ND	ND	ND	ND	ND	ND
Tl[3]	ND	ND	ND	ND	ND	ND	0.025	1.894	ND	ND
Pb[2]	ND	ND	ND	ND	ND	ND	ND	ND	ND	ND
Bi[3]	ND	ND	ND	ND	ND	ND	0.05	0.05	ND	ND
Be	5.0	2.6	5.2	2.6	2.6	2.6	2.5	2.6	5.2	5.2
Rb[3]	ND	ND	ND	ND	ND	ND	59.6	72.2	ND	ND
Sr*	ND	ND	ND	ND	ND	ND	51.5	49.3	ND	ND
Cs[3]	ND	ND	ND	ND	ND	ND	0.1	0.1	ND	ND
Ba*	ND	ND	ND	ND	ND	ND	753.6	900.2	ND	ND
Sc	5.0	4.1	5.2	2.1	2.1	3.1	3.0	2.6	3.1	3.1
Y*	25.6	15.5	46.7	26.1	5.1	20.4	23.5	14.4	26.2	15.5
Zr*	51.1	61.9	155.6	52.1	30.8	51.1	66.6	65.0	62.8	31.1
Nb*	20.0	5.2	10.4	20.9	5.1	5.1	10.3	11.5	31.4	51.8
Hf[3]	ND	ND	ND	ND	ND	ND	2.75	2.88	ND	ND
Ta[3]	ND	ND	ND	ND	ND	ND	1.31	1.30	ND	ND
Th[3]	ND	ND	ND	ND	ND	ND	2.4	0.9	ND	ND
U[3]	ND	ND	ND	ND	ND	ND	1.3	0.8	ND	ND
La[3]	ND	ND	ND	ND	ND	ND	4.4	13.6	ND	ND
Ce[3]	ND	ND	ND	ND	ND	ND	19.6	33.6	ND	ND
Pr[3]	ND	ND	ND	ND	ND	ND	1.5	4.1	ND	ND
Nd[3]	ND	ND	ND	ND	ND	ND	5.921	14.698	ND	ND
Sm[3]	ND	ND	ND	ND	ND	ND	1.736	2.880	ND	ND
Eu[3]	ND	ND	ND	ND	ND	ND	0.433	0.928	ND	ND
Gd[3]	ND	ND	ND	ND	ND	ND	1.913	2.180	ND	ND
Tb[3]	ND	ND	ND	ND	ND	ND	0.533	0.390	ND	ND
Dy[3]	ND	ND	ND	ND	ND	ND	3.647	2.313	ND	ND
Ho[3]	ND	ND	ND	ND	ND	ND	0.786	0.484	ND	ND
Er[3]	ND	ND	ND	ND	ND	ND	2.516	1.533	ND	ND
Tm[3]	ND	ND	ND	ND	ND	ND	0.402	0.233	ND	ND
Yb[3]	ND	ND	ND	ND	ND	ND	2.264	1.544	ND	ND
Lu[3]	ND	ND	ND	ND	ND	ND	0.330	0.227	ND	ND
UTM E	411560	410750	416361	429355	428260	411929	412255	410401	408637	408749
UTM N	5271317	5270709	5270891	5269289	5269500	5271339	5271307	5270721	5270936	5270928

Appendix 3.1: Lithogeochemical data

sample	AU04203	92-0066a	92-0072a	92-0151a1	93-0091b	92-0068a1	92-0070a1	92-0068a2	92-0070a2
flag	VRS	CD	CD	CD	CD	CTL	CTL	CTM	CTM
SiO_2	84.20	53.54	50.37	50.67	51.35	73.12	74.43	57.33	51.72
Al_2O_3	8.41	18.28	16.52	13.96	14.49	13.26	14.18	13.54	14.67
Fe_2O_3	1.65	10.55	10.34	14.91	14.41	4.08	2.28	14.19	11.21
CaO	1.30	8.07	10.98	6.49	8.54	2.95	2.49	4.99	8.75
MgO	0.40	3.21	7.63	7.17	7.13	0.60	0.69	2.90	5.70
Na_2O	2.23	3.92	1.85	3.84	2.69	5.02	4.05	2.55	2.01
K_2O	1.59	0.64	1.24	0.84	0.12	0.32	1.52	2.17	4.12
TiO_2	0.18	1.35	0.73	1.79	0.94	0.49	0.24	1.68	0.94
MnO	0.02	0.15	0.14	0.23	0.21	0.04	0.02	0.14	0.15
P_2O_5	0.01	0.30	0.21	0.10	0.10	0.10	0.10	0.51	0.74
TIC	ND	0.05	1.13	0.05	0.21	0.20	0.20	1.12	4.22
S	0.03	ND	ND	ND	0.13	ND	ND	ND	ND
LOI	2.71	1.56	3.59	2.78	3.97	1.10	1.32	3.56	6.76
V*	41.3	99.4	194.9	192.1	ND	-5.0	14.2	65.5	158.3
Cr*	103.3	27.1	143.6	90.0	ND	5.0	5.1	19.3	34.8
Co*	5.2	33.1	56.4	57.6	ND	9.0	9.1	38.7	36.9
Ni*	2.6	41.2	174.4	161.8	ND	11.0	5.1	23.4	30.6
Cu*	2.6	13.1	44.1	62.7	ND	10.0	10.1	36.7	87.6
Zn*	2.6	92.4	71.8	151.7	ND	33.1	24.3	88.6	116.1
Ga^3	ND	ND	ND	ND	16.6	ND	ND	ND	ND
Ge^3	ND	ND	ND	ND	ND	ND	ND	ND	ND
As^3	ND	ND	ND	ND	ND	ND	ND	ND	ND
Mo^3	ND	2.1	16.4	0.1	0.6	1.1	0.4	3.0	0.1
Ag^2	ND	ND	ND	ND	ND	ND	ND	ND	ND
In^3	ND	ND	ND	ND	ND	ND	ND	ND	ND
Sn^3	ND	ND	ND	ND	ND	ND	ND	ND	ND
Sb^3	ND	ND	ND	ND	ND	ND	ND	ND	ND
W^3	ND	ND	ND	ND	ND	ND	ND	ND	ND
Au^2	ND	ND	ND	ND	ND	ND	ND	ND	ND
Tl^3	ND	ND	ND	ND	0.010	ND	ND	ND	ND
Pb^2	ND	ND	ND	ND	ND	ND	ND	ND	ND
Bi^3	ND	ND	ND	ND	ND	ND	ND	ND	ND
Be	2.6	0.9	0.6	0.9	ND	1.2	0.9	0.9	1.5
Rb^3	ND	25.1	52.3	31.3	11.4	19.1	47.6	92.7	168.9
Sr*	ND	301.3	318.0	121.4	ND	160.7	263.3	173.1	559.4
Cs^3	ND	0.4	1.9	0.2	0.2	0.1	0.6	2.0	7.3
Ba*	ND	251.1	277.0	222.5	72.5	130.6	486.0	387.0	781.1
Sc	3.1	18.1	24.6	22.2	ND	7.0	3.0	21.4	19.0
Y*	31.0	22.1	14.4	31.3	19.7	51.2	8.1	47.9	27.4
Zr*	165.4	67.3	58.5	111.2	52.8	361.6	141.8	234.2	200.5
Nb*	10.3	7.9	2.8	6.1	2.7	15.1	5.9	10.2	7.5
Hf^3	ND	1.91	1.95	3.03	1.55	8.04	3.75	5.70	4.01
Ta^3	ND	0.57	0.29	0.50	0.25	0.83	0.55	0.52	0.49
Th^3	ND	1.1	1.8	1.1	0.4	5.2	5.0	5.0	7.3
U^3	ND	0.3	0.5	0.3	0.1	1.5	0.3	1.3	1.8
La^3	ND	13.1	14.4	9.1	3.1	46.2	19.2	23.4	53.8
Ce^3	ND	29.1	32.8	23.3	8.3	92.4	35.4	55.0	116.1
Pr^3	ND	3.7	4.2	3.3	1.2	11.0	3.6	7.3	15.8
Nd^3	ND	17.075	18.466	16.181	6.212	42.187	14.176	31.567	66.496
Sm^3	ND	4.018	3.693	4.551	2.071	8.638	2.228	7.434	12.666
Eu^2	ND	1.607	1.231	1.315	0.952	1.306	0.648	2.037	3.378
Gd^3	ND	4.018	3.078	5.056	3.106	8.036	1.013	8.146	8.444
Tb^3	ND	0.653	0.492	0.930	0.569	1.406	0.223	1.324	1.161
Dy^3	ND	3.817	2.565	5.360	3.313	8.739	1.215	8.248	5.489
Ho^3	ND	0.763	0.523	1.112	0.735	1.808	0.243	1.629	0.929
Er^3	ND	2.009	1.026	3.034	2.071	5.022	ND	4.073	2.111
Tm^3	ND	0.301	0.236	0.445	0.342	0.773	0.111	0.784	0.359
Yb^3	ND	1.908	1.334	2.933	2.174	5.123	0.719	4.480	2.111
Lu^3	ND	0.271	0.215	0.405	0.331	0.703	0.122	0.682	0.296
UTM E	432950	422729	431852	436675	427389	427659	428930	427659	428930
UTM N	5269550	5264677	5262446	5261684	5258077	5266549	5265106	5266549	5265106

Appendix 3.2: Mass-change calculations

Appendix 3.2: Mass change data

sample	8469	8475	23554	AU04223	AU01752	AU04181	AU04185	AU04235	AU04241	AU04243	AU04247	AU04248
flag	VLC	VLC	VLC	VLC	VLS	VLS	VLS	VLS	VLS	VLS	VLS	VLS
SiO_2	59.62	73.93	74.41	75.44	80.33	82.63	80.85	79.15	79.97	79.51	78.17	81.18
Al_2O_3	13.47	14.53	14.22	11.62	11.67	10.33	11.73	12.34	11.66	12.72	12.70	12.94
Fe_2O_3	17.83	1.48	0.89	8.07	2.02	2.29	0.87	0.70	2.15	0.72	1.77	0.94
CaO	2.25	2.60	1.38	0.32	0.79	0.65	0.94	0.20	0.04	0.22	2.45	0.03
MgO	2.04	0.98	0.31	1.06	0.64	1.45	0.14	0.29	0.48	0.42	0.76	0.84
Na_2O	1.10	2.83	4.04	0.25	1.16	0.50	3.32	2.84	2.13	1.05	0.43	0.22
K_2O	2.81	3.53	4.60	2.85	3.20	2.02	2.03	4.39	3.43	5.27	3.55	3.77
TiO_2	0.06	0.06	0.10	0.06	0.12	0.08	0.07	0.06	0.07	0.06	0.12	0.06
MnO	0.75	0.06	0.05	0.29	0.05	0.02	0.02	0.02	0.04	0.01	0.04	0.01
P_2O_6	0.08	0.01	0.01	0.04	0.01	0.02	0.02	0.02	0.02	0.01	0.01	0.01
CO2	0.10	0.46	ND	ND	ND	ND	ND	ND	ND	ND	ND	ND
S	1.00	0.02	ND	0.02	0.01	0.01	0.02	0.01	0.01	0.01	0.01	0.01
loi	2.11	2.48	1.65	2.62	2.28	2.59	1.67	1.25	1.45	1.41	3.13	2.08
Cr	89	70	619	124	78	120	62	87	81	103	99	57
Zr	49	57	51	62	156	52	31	51	67	65	63	31
Y	26	34	26	15	47	26	ND	20	23	14	26	16
Cu	10	26	5	3	3	3	3	3	3	3	3	3
Zn	2	46	5	ND	125	ND	ND	ND	25	15	21	47
Ni	35	18	26	ND	5	ND	ND	ND	5	ND	5	ND
Co	5	ND	5	ND	5	ND	ND	ND	ND	ND	5	ND
Nb	8	11	20	ND	10	21	ND	ND	10	11	31	52
V	40	10	41	67	31	57	41	20	36	31	63	41
Sc	5	5	5	4	5	ND	ND	ND	ND	ND	ND	ND
Be	ND	5	5	ND	5	ND	ND	ND	ND	ND	5	5
mf (p/a)	0.97	0.90	0.92	1.13	1.12	1.27	1.12	1.06	1.12	1.03	1.03	1.01
Reconstituted Composition												
$rSiO_2$	58.06	66.76	68.66	85.17	90.28	104.98	90.44	84.14	89.96	81.98	80.72	82.32
rAl_2O_3	13.12	13.12	13.12	13.12	13.12	13.12	13.12	13.12	13.12	13.12	13.12	13.12
rFe_2O_3	17.36	1.33	0.82	9.11	2.27	2.92	0.98	0.74	2.42	0.74	1.83	0.96
rCaO	2.19	2.35	1.27	0.36	0.89	0.82	1.06	0.22	0.05	0.22	2.53	0.03
rMgO	1.99	0.89	0.28	1.20	0.72	1.84	0.16	0.30	0.54	0.44	0.79	0.85
rNa_2O	1.07	2.55	3.73	0.28	1.31	0.64	3.71	3.02	2.40	1.08	0.44	0.22
rK_2O	2.73	3.19	4.25	3.21	3.59	2.57	2.27	4.66	3.86	5.44	3.66	3.83
$rTiO_2$	0.06	0.06	0.09	0.07	0.14	0.11	0.08	0.07	0.08	0.06	0.12	0.06
rMnO	0.73	0.06	0.05	0.33	0.06	0.03	0.02	0.02	0.05	0.01	0.04	0.01
rP_2O_5	0.08	0.01	0.00	0.05	0.01	0.03	0.02	0.02	0.02	0.01	0.01	0.01
rCr	86	63	571	140	87	152	69	92	91	106	103	58
rZr	48	51	47	70	175	66	34	54	75	67	65	32
rY	25	31	24	17	52	33	ND	22	26	15	27	16
rCu	10	23	5	3	3	3	3	3	3	3	3	3
rZn	2	42	5	ND	140	ND	ND	ND	29	16	22	47
rNi	34	16	24	ND	6	ND	ND	ND	6	ND	5	ND
rCo	5	ND	5	ND	6	ND	ND	ND	ND	ND	5	ND
rNb	8	10	18	ND	12	27	ND	ND	12	12	32	53
rV	39	9	38	76	35	73	46	22	40	32	65	42
rSc	5	5	5	5	6	ND	ND	ND	ND	ND	ND	ND
rBe	ND	5	5	ND	6	ND	ND	ND	ND	ND	5	5
rCO2	0.10	0.42	ND	ND	ND	ND	ND	ND	ND	ND	ND	ND
rS	0.97	0.02	ND	0.02	0.01	0.01	0.02	0.01	0.01	0.01	0.01	0.01
Absolute Mass Change												
$dSiO_2$	-20.47	-11.77	-9.87	6.64	11.75	26.45	11.91	5.61	11.43	3.45	2.19	3.79
dAl_2O_3	ND	ND	ND	ND	ND	ND	ND	ND	ND	ND	ND	ND
dFe_2O_3	16.43	0.39	-0.12	8.18	1.34	1.98	0.04	-0.20	1.48	-0.19	0.89	0.02
dCaO	1.91	2.06	0.99	0.08	0.60	0.54	0.77	-0.07	-0.24	-0.06	2.24	-0.25
dMgO	1.63	0.52	-0.08	0.84	0.36	1.48	-0.20	-0.06	0.18	0.07	0.43	0.49
dNa_2O	-4.06	-2.57	-1.40	-4.85	-3.82	-4.49	-1.42	-2.11	-2.73	-4.04	-4.68	-4.91
dK_2O	1.22	1.67	2.73	1.70	2.07	1.05	0.76	3.15	2.34	3.92	2.15	2.31
$dTiO_2$	-0.02	-0.03	0.01	-0.01	0.06	0.02	0.00	-0.02	0.00	-0.02	0.04	-0.02
dMnO	0.71	0.04	0.03	0.31	0.04	0.01	0.01	0.01	0.03	0.00	0.03	0.00
dP_2O_5	0.05	-0.02	-0.02	0.02	-0.01	0.00	0.00	0.00	0.00	-0.02	-0.01	-0.01
dCr	-18	-41	467	35	-17	48	-35	-12	-13	2	-2	-47
dZr	-3	0	-4	19	124	15	-17	3	24	16	14	-19
dY	12	18	11	5	40	20	-13	9	14	2	14	3
dCu	-80	-67	-85	-87	-87	-87	-87	-87	-87	-87	-87	-87
dZn	2	42	5	ND	140	ND	ND	ND	29	16	22	47
dNi	22	3	10	-18	-9	-16	-17	-19	-14	-21	-17	-23
dCo	5	ND	5	ND	6	ND	ND	ND	ND	ND	5	ND
dNb	8	10	18	ND	12	27	ND	ND	12	12	32	53
dV	-2	-32	-3	35	-6	32	5	-19	-1	-9	24	1
dSc	0	0	-1	0	1	-5	-5	-5	-5	-5	-5	-5
dBe	-5	0	-1	-5	1	-5	-5	-5	-5	-5	0	0
dCO2	0	0	ND	ND	ND	ND	ND	ND	ND	ND	ND	ND
dS	1	0	0	0	0	0	0	0	0	0	0	0

Appendix 3.2: Mass change data

sample	AU04215	AU04222	3469	3473	AU01757	AU01764	AU04186	AU04214	AU04220	AU04249	8477	23558
flag	VRF	VRF	VRA	VRA	VRA	VRA	VRA	VRA	VRA	VRA	VRC	VRC
SiO_2	76.32	74.96	82.28	70.44	68.01	71.35	80.59	73.54	74.95	77.58	63.51	71.46
Al_2O_3	12.15	12.40	10.75	14.65	17.23	14.20	11.40	13.73	14.07	12.69	10.67	12.03
Fe_2O_3	3.09	4.40	2.86	3.89	3.94	3.44	2.58	3.30	2.81	2.22	8.37	10.01
CaO	1.37	1.42	0.07	0.79	2.76	4.33	0.53	3.10	1.87	2.19	13.89	3.07
MgO	0.86	0.98	0.93	1.47	1.59	1.57	0.21	0.99	1.70	1.53	2.38	2.22
Na_2O	3.61	4.26	0.61	6.48	4.55	2.81	2.91	2.85	2.21	1.39	0.50	0.42
K_2O	2.19	1.18	1.27	0.43	1.38	1.86	1.41	2.04	2.00	2.03	0.21	0.40
TiO_2	0.30	0.31	0.22	0.34	0.43	0.31	0.28	0.32	0.28	0.26	0.23	0.24
MnO	0.05	0.05	0.90	1.43	0.05	0.08	0.03	0.07	0.04	0.08	0.18	0.07
P_2O_5	0.05	0.04	0.10	0.10	0.06	0.05	0.06	0.06	0.07	0.03	0.05	0.08
CO2	ND	ND	0.05	0.05	ND	ND	ND	ND	ND	ND	2.94	ND
S	0.01	0.01	ND	ND	0.01	0.07	0.01	0.04	0.03	ND	2.23	ND
loi	0.90	0.87	1.80	1.50	1.78	4.70	1.56	1.70	1.79	2.41	8.31	12.49
Cr	92	143	ND	ND	87	79	117	138	107	104	452	1056
Zr	174	255	304	173	123	95	102	153	112	125	11	ND
Y	20	31	39	17	ND	ND	ND	20	ND	21	15	29
Cu	3	20	10	15	10	3	3	3	3	3	1248	ND
Zn	ND	ND	ND	20	41	147	ND	ND	ND	5	21876	40
Ni	ND	5	5	ND	10	11	5	5	ND	5	77	ND
Co	10	5	ND	7	15	11	5	5	5	5	34	46
Nb	ND	20	10	8	ND	ND	ND	ND	ND	ND	23	6
V	51	97	ND	ND	87	79	71	51	56	42	183	92
Sc	5	7	4	5	6	4	4	6	4	5	17	23
Be	5	5	1	1	5	5	5	5	5	ND	ND	ND
mf (p/a)	1.01	0.99	1.14	0.84	0.71	0.86	1.08	0.89	0.87	0.97	1.15	1.02
Reconstituted Composition												
$rSiO_2$	77.11	74.21	93.93	59.05	48.46	61.70	86.76	65.74	65.39	75.06	73.04	72.91
rAl_2O_3	12.28	12.28	12.28	12.28	12.28	12.28	12.28	12.28	12.28	12.28	12.28	12.28
rFe_2O_3	3.13	4.35	3.27	3.26	2.81	2.98	2.78	2.95	2.45	2.15	9.63	10.21
rCaO	1.39	1.40	0.08	0.66	1.97	3.74	0.57	2.77	1.63	2.11	15.98	3.13
rMgO	0.87	0.97	1.06	1.23	1.13	1.36	0.23	0.89	1.48	1.48	2.74	2.26
rNa_2O	3.64	4.21	0.69	5.43	3.24	2.43	3.14	2.55	1.93	1.35	0.58	0.43
rK_2O	2.22	1.17	1.45	0.36	0.98	1.61	1.51	1.83	1.75	1.96	0.24	0.41
$rTiO_2$	0.30	0.30	0.25	0.28	0.31	0.26	0.30	0.28	0.24	0.25	0.26	0.25
rMnO	0.05	0.05	1.03	1.20	0.04	0.07	0.03	0.06	0.04	0.08	0.21	0.07
rP_2O_5	0.05	0.04	0.12	0.09	0.04	0.05	0.07	0.05	0.06	0.03	0.05	0.08
rCr	93	141	ND	ND	62	68	126	123	94	101	520	1077
rZr	176	253	347	145	88	82	110	137	98	121	13	ND
rY	21	30	44	14	ND	ND	ND	18	ND	20	17	30
rCu	3	20	12	13	7	2	3	2	2	2	1436	ND
rZn	ND	ND	ND	17	29	127	ND	ND	ND	5	25159	41
rNi	ND	5	6	ND	7	9	5	5	ND	5	88	ND
rCo	10	5	ND	6	11	9	5	5	4	5	40	47
rNb	ND	20	11	7	ND	ND	ND	ND	ND	ND	26	6
rV	52	96	ND	ND	62	68	77	46	49	41	211	94
rSc	5	7	5	4	4	4	4	5	4	5	20	23
rBe	5	5	1	1	4	5	5	5	4	ND	ND	ND
rCO2	ND	ND	0.06	0.04	ND	ND	ND	ND	ND	ND	3.39	ND
rS	0.01	0.00	ND	ND	0.00	0.06	0.01	0.04	0.03	ND	2.56	ND
Absolute Mass Change												
$dSiO_2$	1.47	-1.44	18.29	-16.60	-27.18	-13.94	11.12	-9.90	-10.25	-0.58	-2.60	-2.73
dAl_2O_3	ND	ND	ND	ND	ND	ND	ND	ND	ND	ND	ND	ND
dFe_2O_3	-0.62	0.61	-0.48	-0.49	-0.94	-0.77	-0.97	-0.80	-1.29	-1.60	5.88	6.47
dCaO	-0.01	0.01	-1.31	-0.74	0.57	2.34	-0.83	1.37	0.24	0.72	14.58	1.73
dMgO	-0.05	0.05	0.14	0.31	0.21	0.44	-0.69	-0.03	0.56	0.56	1.82	1.34
dNa_2O	-0.29	0.28	-3.24	1.50	-0.69	-1.50	-0.79	-1.38	-2.00	-2.58	-3.35	-3.50
dK_2O	0.53	-0.52	-0.24	-1.33	-0.70	-0.08	-0.17	0.14	0.06	0.28	-1.45	-1.28
$dTiO_2$	0.00	0.00	-0.05	-0.02	0.00	-0.04	-0.01	-0.02	-0.06	-0.05	-0.04	-0.06
dMnO	0.00	0.00	0.98	1.15	-0.01	0.02	-0.02	0.01	-0.02	0.03	0.16	0.02
dP_2O_5	0.01	-0.01	0.07	0.04	0.00	0.00	0.02	0.01	0.02	-0.02	0.01	0.04
dCr	-24	24	-118	-118	-56	-49	9	6	-24	-17	403	960
dZr	-39	38	133	-69	-127	-133	-105	-78	-117	-94	-202	-215
dY	-5	5	18	-11	-26	-26	-26	-7	-26	-5	-8	4
dCu	-9	9	0	1	-4	-9	-9	-9	-9	-9	1424	-11
dZn	ND	ND	ND	17	29	127	ND	ND	ND	5	25159	41
dNi	-5	0	1	-5	2	4	0	-1	-5	0	83	-5
dCo	3	-3	-8	-2	3	1	-2	-3	-3	-3	32	39
dNb	-20	0	-9	-14	-20	-20	-20	-20	-20	-20	6	-14
dV	-22	22	-74	-74	-12	-6	3	-28	-25	-33	137	20
dSc	-1	1	-2	-2	-2	-2	-2	-1	-3	-1	14	17
dBe	0	0	-4	-4	-1	-1	0	-1	-1	-5	-5	-5
dCO2	ND	ND	0	0	ND	ND	ND	ND	ND	ND	3	ND
dS	0	0	0	0	0	0	0	0	0	0	3	0

Appendix 3.2: Mass change data

sample	AU06724	AU04203	AU04237	23564	23568	AU04205	AU04218	AU04209	AU04216	AU06728	23557	AU04217
flag	VRC	VRS	VDF	VDA	VDA	VDA	VDA	VDC	VDC	VDC	VDS	VLF
SiO_2	69.48	84.20	69.84	63.47	61.02	70.28	62.47	62.09	60.26	59.97	68.63	79.03
Al_2O_3	12.84	8.41	14.32	17.08	15.69	14.21	14.46	14.25	14.52	16.89	13.88	13.08
Fe_2O_3	9.42	1.65	4.56	7.81	8.05	7.10	8.14	8.46	12.09	11.55	6.03	0.81
CaO	0.74	1.30	3.35	4.28	7.39	1.79	6.32	4.27	2.84	2.30	3.63	0.08
MgO	2.07	0.40	1.78	2.23	2.93	2.23	2.57	5.38	5.79	3.36	1.67	0.34
Na_2O	2.23	2.23	3.89	2.14	2.13	1.79	3.52	4.23	2.43	2.57	0.21	4.65
K_2O	2.68	1.59	1.30	1.85	1.52	1.67	1.40	0.25	0.92	2.06	4.75	1.87
TiO_2	0.35	0.18	0.73	0.89	0.82	0.75	0.77	0.72	0.78	0.93	0.76	0.10
MnO	0.07	0.02	0.07	0.11	0.21	0.08	0.14	0.20	0.17	0.24	0.07	0.01
P_2O_5	0.11	0.01	0.17	0.14	0.22	0.10	0.23	0.17	0.19	0.14	0.16	0.02
CO2	0.04	ND	ND	ND	ND	ND	ND	ND	ND	0.41	ND	ND
S	2.30	0.03	0.01	ND	ND	0.12	0.03	0.01	0.02	0.04	ND	0.01
loi	3.46	2.71	2.65	2.29	5.98	4.86	3.72	2.84	5.60	3.54	5.72	1.11
Cr	208	103	109	313	245	227	104	290	357	120	373	77
Zr	115	165	114	164	149	95	167	104	150	177	128	51
Y	11	31	10	21	21	11	10	10	21	10	16	15
Cu	255	3	26	10	3	37	16	16	32	125	11	3
Zn	633	ND	10	46	59	ND	ND	ND	ND	240	37	ND
Ni	26	ND	36	26	21	69	52	ND	ND	21	27	5
Co	26	5	26	21	21	26	26	31	53	26	16	ND
Nb	3	10	41	ND	ND	ND	5	ND	6	10	ND	ND
V	68	41	156	139	128	185	136	192	187	151	117	62
Sc	5	ND	10	15	11	19	13	21	17	16	11	5
Be	5	ND	10	5	5	11	10	5	11	5	5	5
mf (p/a)	0.96	1.46	1.00	0.84	0.91	1.01	0.99	1.00	0.99	0.85	1.03	1.00
Reconstituted Composition												
$rSiO_2$	66.43	122.67	69.84	53.20	55.66	70.82	61.85	62.37	59.41	50.83	70.81	79.27
rAl_2O_3	12.28	12.26	14.32	14.32	14.32	14.32	14.32	14.32	14.32	14.32	14.32	13.12
rFe_2O_3	9.01	2.41	4.56	6.54	7.35	7.15	8.06	8.50	11.92	9.79	6.22	0.81
rCaO	0.71	1.90	3.35	3.59	6.75	1.80	6.26	4.29	2.80	1.95	3.75	0.08
rMgO	1.98	0.59	1.78	1.87	2.67	2.25	2.54	5.40	5.71	2.84	1.92	0.34
rNa_2O	2.13	3.26	3.89	1.79	1.94	1.80	3.48	4.25	2.40	2.18	0.22	4.67
rK_2O	2.56	2.32	1.30	1.55	1.39	1.68	1.38	0.25	0.90	1.75	4.90	1.88
$rTiO_2$	0.34	0.26	0.73	0.75	0.75	0.76	0.76	0.72	0.77	0.79	0.78	0.10
rMnO	0.07	0.03	0.07	0.09	0.19	0.09	0.13	0.20	0.17	0.20	0.08	0.01
rP_2O_5	0.11	0.02	0.17	0.12	0.20	0.10	0.23	0.17	0.19	0.11	0.16	0.02
rCr	199	151	109	263	224	229	103	292	352	102	385	77
rZr	110	241	114	138	136	96	165	104	148	150	132	52
rY	11	45	10	17	19	11	10	10	20	9	16	15
rCu	244	4	26	8	2	37	15	16	32	106	11	3
rZn	605	ND	10	39	53	ND	ND	ND	ND	203	38	ND
rNi	25	ND	36	22	19	69	52	ND	ND	18	27	5
rCo	25	8	26	17	19	27	26	31	53	22	16	ND
rNb	3	15	41	ND	ND	ND	5	ND	6	9	ND	ND
rV	65	60	156	116	117	187	134	193	184	128	121	62
rSc	5	ND	10	13	10	19	12	21	17	13	11	5
rBe	5	ND	10	4	5	11	10	5	11	4	5	5
rCO2	0.04	ND	ND	ND	ND	ND	ND	ND	ND	0.34	ND	ND
rS	2.20	0.04	0.01	ND	ND	0.12	0.03	0.01	0.02	0.03	ND	0.01
Absolute Mass Change												
$dSiO_2$	-9.21	47.23	ND	-16.64	-14.18	0.97	-7.99	-7.47	-10.43	-19.01	0.97	0.73
dAl_2O_3	ND	ND	ND	ND	ND	ND	ND	ND	ND	ND	ND	ND
dFe_2O_3	5.26	-1.33	ND	1.98	2.79	2.59	3.50	3.93	7.36	5.22	1.66	-0.12
dCaO	-0.69	0.50	ND	0.24	3.40	-1.55	2.91	0.94	-0.55	-1.40	0.40	-0.20
dMgO	1.06	-0.33	ND	0.09	0.89	0.47	0.76	3.62	3.93	1.06	0.14	-0.02
dNa_2O	-1.80	-0.67	ND	-2.10	-1.94	-2.09	-0.41	0.36	-1.49	-1.71	-3.67	-0.46
dK_2O	0.87	0.63	ND	0.25	0.09	0.39	0.09	-1.05	-0.39	0.45	3.61	0.36
$dTiO_2$	0.04	-0.05	ND	0.02	0.02	0.03	0.04	-0.01	0.04	0.06	0.06	0.02
dMnO	0.02	-0.02	ND	0.02	0.12	0.01	0.06	0.13	0.10	0.13	0.00	0.00
dP_2O_5	0.06	-0.03	ND	-0.05	0.04	-0.07	0.06	0.00	0.02	-0.05	0.00	0.00
dCr	82	33	ND	154	115	120	-6	183	244	-7	276	-27
dZr	-105	27	ND	24	22	-18	51	-10	33	36	18	1
dY	-15	20	ND	7	9	0	0	0	10	-2	6	3
dCu	232	-8	ND	-18	-24	11	-10	-10	6	80	-15	-87
dZn	605	ND	ND	28	43	-10	-10	-10	-10	193	28	ND
dNi	20	-5	ND	-15	-17	33	15	-36	-36	-19	-9	-5
dCo	17	0	ND	-9	-6	1	0	5	27	-4	-9	ND
dNb	-18	-5	ND	-41	-41	-41	-36	-41	-35	-33	-41	ND
dV	-9	-14	ND	-39	-39	31	-21	37	29	-27	-35	21
dSc	-1	-6	ND	3	-1	9	2	10	6	3	1	0
dBe	0	-5	ND	-6	-6	0	0	-5	0	-6	-5	0
dCO2	0	ND	ND	ND	ND	ND	ND	ND	ND	0	ND	ND
dS	2	0	ND	0	0	0	0	0	0	0	0	0

Appendix 3.2: Mass change data

sample	AU04227	4377	4415	4389	AU04232	AU04233
flag	VLF	VBF	VBF	VBA	VBE	VBE
SiO_2	78.03	50.99	52.32	57.23	51.37	52.75
Al_2O_3	13.16	16.13	16.01	18.03	14.90	13.48
Fe_2O_3	1.06	12.22	10.84	8.67	11.69	14.37
CaO	0.49	9.29	8.52	6.91	10.44	9.79
MgO	0.38	6.50	5.90	3.36	6.76	5.55
Na_2O	5.60	2.98	2.41	3.61	3.09	2.45
K_2O	1.16	0.32	0.21	0.76	0.30	0.17
TiO_2	0.06	1.34	1.10	1.27	1.13	1.13
MnO	0.02	0.23	0.18	0.17	0.18	0.21
P_2O_5	0.03	0.01	0.10	ND	0.12	0.09
CO2	ND	0.19	2.41	4.04	ND	ND
S	0.01	0.01	ND	0.04	0.04	0.01
loi	0.61	2.00	6.40	6.00	0.95	1.74
Cr	132	ND	180	ND	208	82
Zr	51	ND	66	ND	61	49
Y	10	ND	25	ND	20	20
Cu	177	40	220	103	30	107
Zn	ND	124	66	103	ND	ND
Ni	15	41	110	ND	76	46
Co	ND	48	51	54	51	61
Nb	ND	ND	3	ND	5	1
V	20	ND	260	ND	339	403
Sc	ND	ND	34	ND	36	45
Be	ND	ND	1	ND	10	10
mf (p/a)	1.00	1.00	1.00	0.89	1.08	1.19
Reconstituted Composition						
$rSiO_2$	77.80	50.80	52.52	51.01	55.39	62.87
rAl_2O_3	13.12	16.07	16.07	16.07	16.07	16.07
rFe_2O_3	1.06	12.17	10.88	7.73	12.61	17.13
rCaO	0.48	9.25	8.55	6.16	11.26	11.66
rMgO	0.38	6.47	5.92	2.99	7.29	6.61
rNa_2O	5.58	2.97	2.42	3.21	3.33	2.92
rK_2O	1.16	0.32	0.21	0.68	0.33	0.21
$rTiO_2$	0.06	1.34	1.10	1.13	1.22	1.35
rMnO	0.02	0.23	0.18	0.15	0.20	0.26
rP_2O_5	0.03	0.01	0.11	ND	0.13	0.11
rCr	131	ND	181	ND	224	97
rZr	50	ND	66	ND	66	58
rY	10	ND	25	ND	22	24
rCu	177	40	221	92	33	128
rZn	ND	124	66	92	ND	ND
rNi	15	41	110	ND	82	55
rCo	ND	47	51	48	55	73
rNb	ND	ND	3	ND	5	1
rV	20	ND	261	ND	366	481
rSc	ND	ND	34	ND	41	54
rBe	ND	ND	1	ND	11	12
rCO2	ND	0.19	2.42	3.60	ND	ND
rS	0.00	0.01	ND	0.04	0.04	0.01
Absolute Mass Change						
$dSiO_2$	-0.73	-0.86	0.86	-0.65	3.74	11.21
dAl_2O_3	ND	ND	ND	ND	ND	ND
dFe_2O_3	0.12	0.64	-0.65	-3.80	1.08	5.60
dCaO	0.20	0.35	-0.35	-2.74	2.35	2.76
dMgO	0.02	0.27	-0.27	-3.20	1.09	0.41
dNa_2O	0.46	0.27	-0.28	0.52	0.64	0.23
dK_2O	-0.36	0.06	-0.06	0.41	0.06	-0.06
$dTiO_2$	-0.02	0.12	-0.12	-0.09	0.00	0.13
dMnO	0.00	0.02	-0.02	-0.05	-0.01	0.05
dP_2O_5	0.00	-0.05	0.05	-0.06	0.07	0.05
dCr	27	-180	1	-180	44	-83
dZr	-1	-66	0	-66	0	-8
dY	-3	-25	0	-25	-3	-1
dCu	87	-90	91	-38	-97	-2
dZn	ND	29	-29	-3	-95	-95
dNi	4	-35	35	-76	6	-21
dCo	ND	-2	2	-1	5	24
dNb	ND	-3	0	-3	2	-2
dV	-21	-260	1	-260	106	221
dSc	-5	-34	0	-34	7	20
dBe	-5	-1	0	-1	10	12
dCO2	ND	-1.11	1.12	2.30	-1.30	-1.30
dS	0	0.00	-0.01	0.03	0.04	0.01

Figure 3.1: A geological map of the Swayze greenstone belt. (Compiled by the author after Heather and Shore (1999) and unpublished Falconbridge Limited data.)

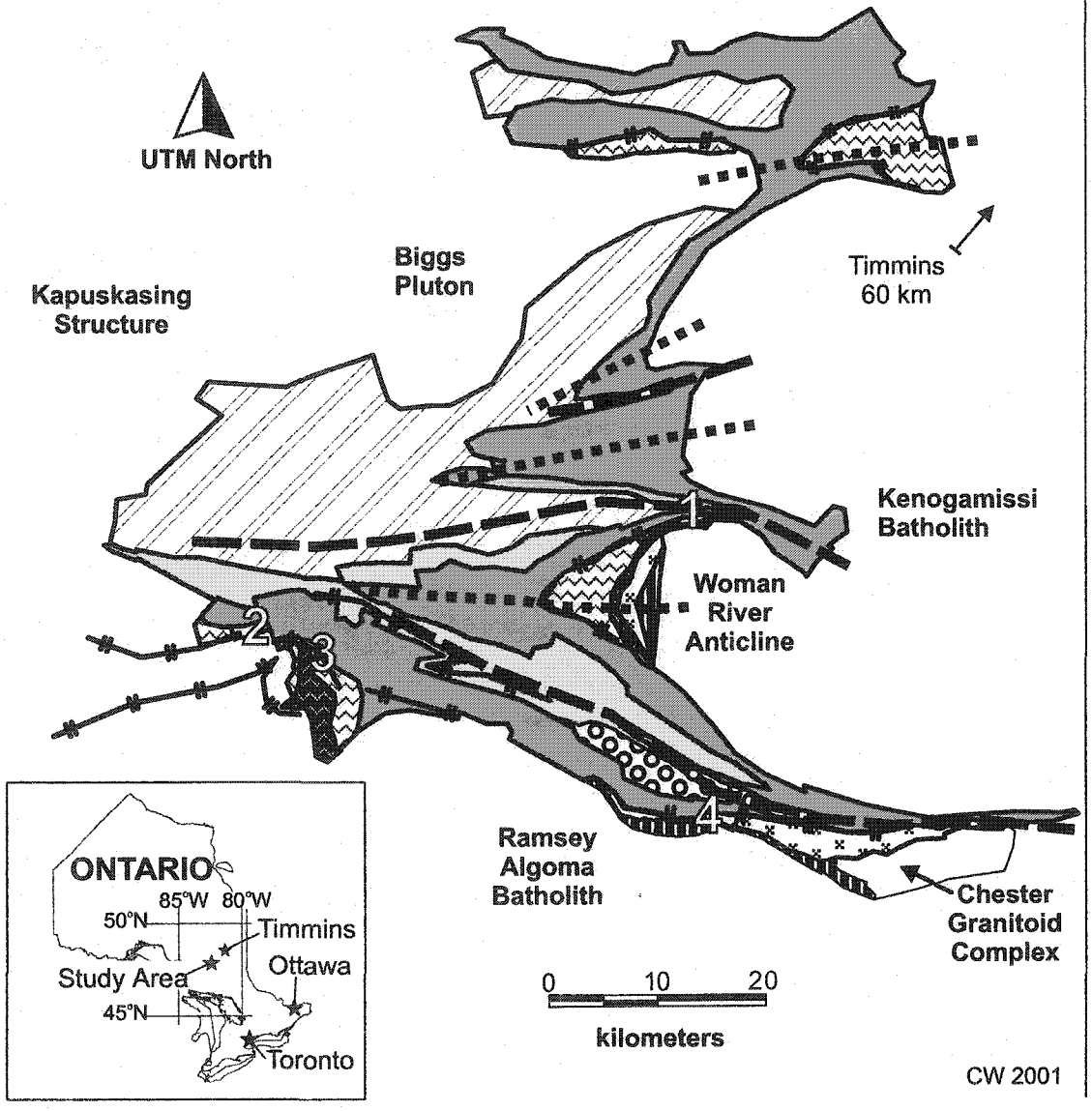

Swayze greenstone belt supracrustal stratigraphy

- Ridout Group sediment
- Swayze Group volcanic and sediment
- iron formation
- THi/THf (intermediate and felsic volcanic)
- TOm (mafic volcanic)
- iron formation
- MSf (felsic volcanic)
- MRm (mafic volcanic)
- iron formation
- CYf (dacite, rhyolite and low-Ti rhyolite)
- CAm (basalt)
- igneous / metamorphic complexes and undivided supracrustal rocks

Regional structural geology

- F_2 anticline axial-trace
- F_2 syncline axial-trace

Base-metal mineralization

1. Jefferson Zn-Pb deposit
2. Shunsby Zn-Cu deposits
3. Peter Lake Zn-Pb showing
4. Huffman Township Zn-Pb showing

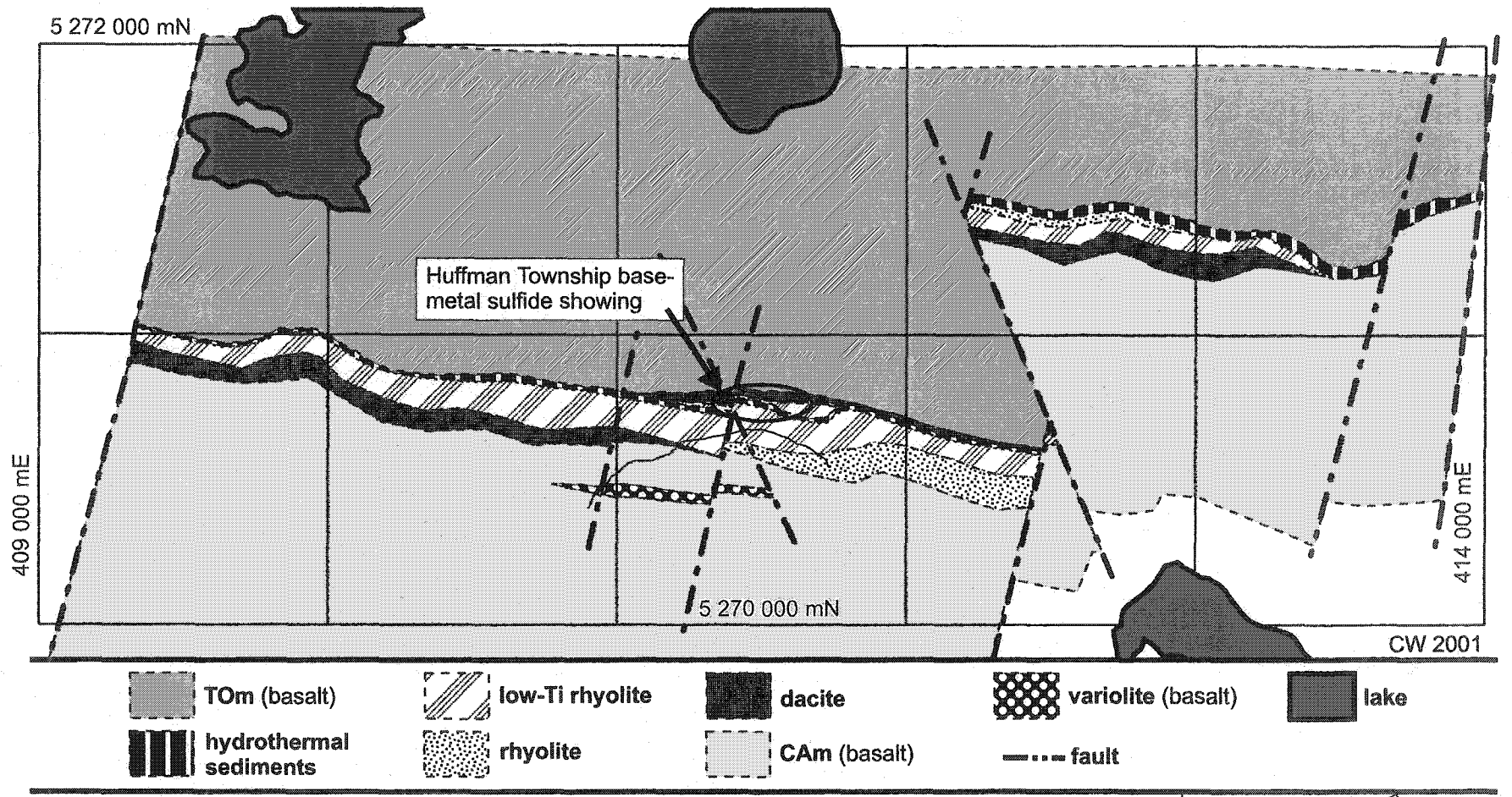

Figure 3.2: A plan view of the geology of the Huffman Township Zn-Pb showing drawn from outcrop and diamond-drill hole information and projected into UTM NAD 83, zone 17. The grid is aligned with UTM north (top), and grid lines are spaced 1 km apart. Northernmost mafic rocks belong to the Trailbreaker Group, while Chester Group rhyolite, dacite and basalt occur below the hydrothermal sediment horizon. Volcanic and sedimentary texturse indicate tops to the north for Chester and Trailbreaker group rocks.

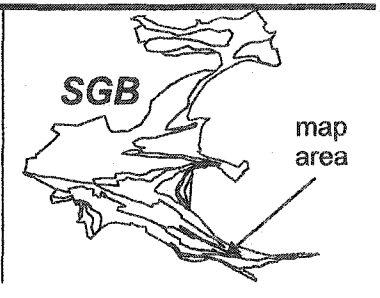

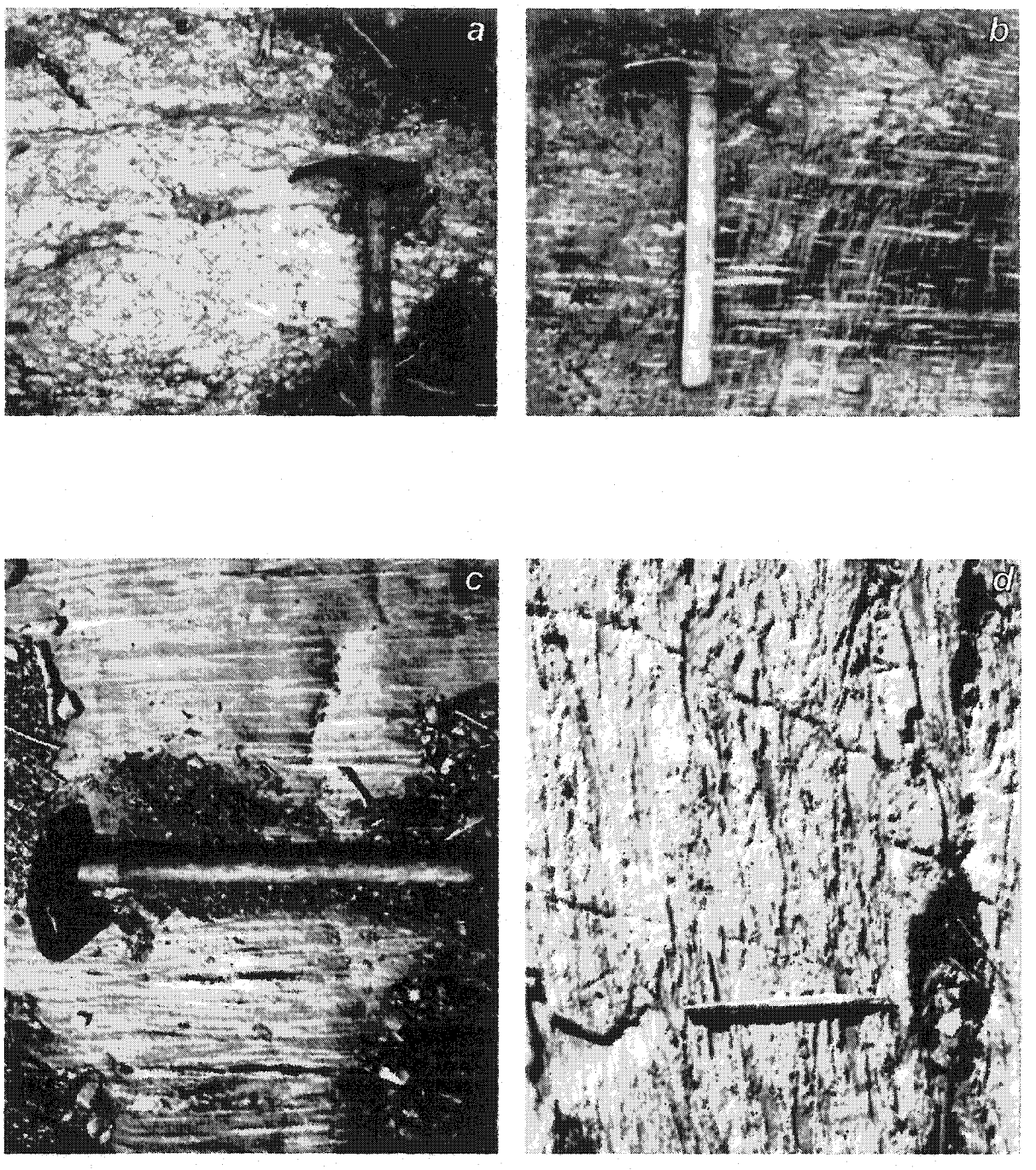

Figure 3.3: Photographs of Chester Group volcanic outcrops. The hammer handle is 40 cm long,, and the scribe is 15 cm long.
(a) A basalt flow with variolitic texture occurs in the upper 50 m of the CAm.
(b) Dacitic fragmental is exposed at upper contact with low-Ti rhyolite from the eastern end of the map area of Figure 3.1.
(c) Dacitic fragmental with quartz and feldspar crystal-rich matrix from the western end of the map area of Figure 3.1 has a dark gray, mud rich matrix indicative of mixing of volcaniclastic and epiclastic material in distal parts of the volcanic complex.
(d) Abraded fragments from the upper part of the rhyolite unit east of the eastern edge of the map area of Figure 3.1 indicating transportation away from the magmatic vent.

Figure 3.4: Schematic stratigraphic sections through the Huffman Township Zn-Pb showing and south-east SGB. Relative thicknesses of units in this figure are not representative of true stratigraphic thicknesses.

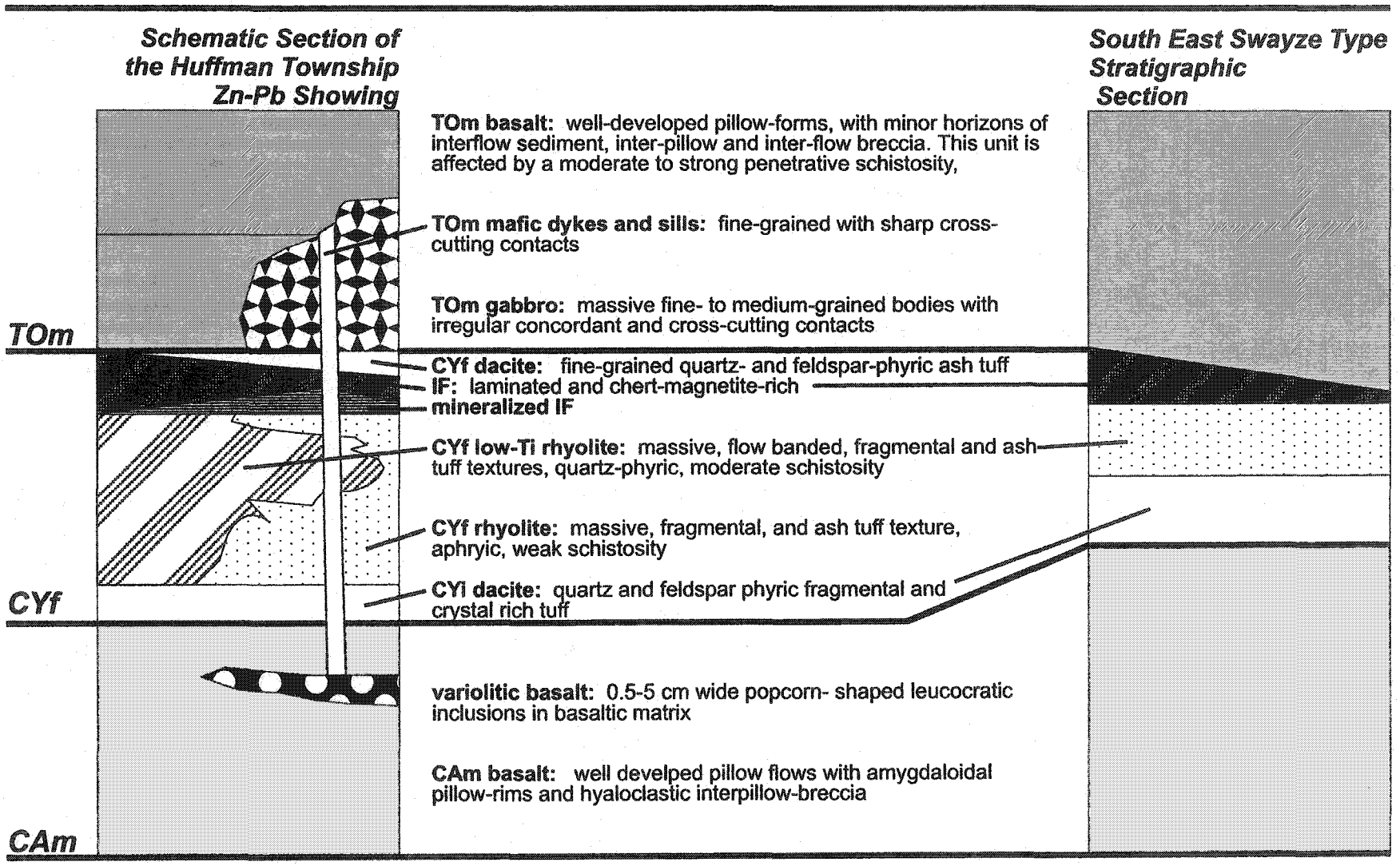

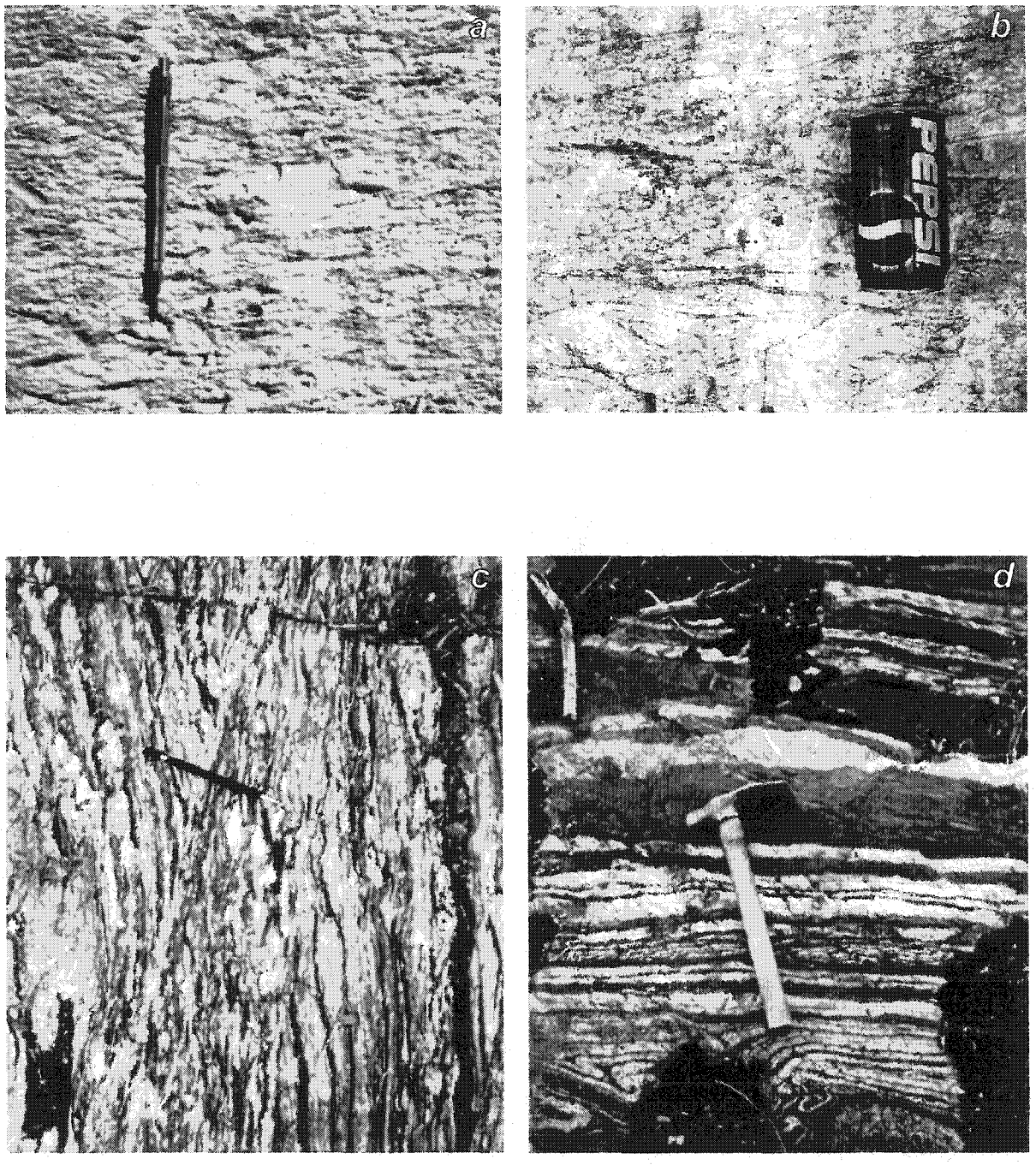

Figure 3.5: Photographs of Chester Group volcanic and hydrothermal sediment outcrops. The hammer and scribe used for scales are the same as in Figure 3.2.
(a) Rhyolite fragmental with a recessively weathering, sericite-quartz altered matrix and angular fragments outcrops from the centre of the map area of Figure 3.1.
(b) Flow-banded and weakly foliated low-Ti rhyolite from the dome exposed near the centre of the map area (Figure 3.1).
(b) Sheared rhyolite breccia 125 m north of the low-Ti rhyolite in figure 3.4b, occurs below the hydrothermal sediment horizon.
(d) Well-banded iron formation from the north east corner the map area of Figure 3.1.

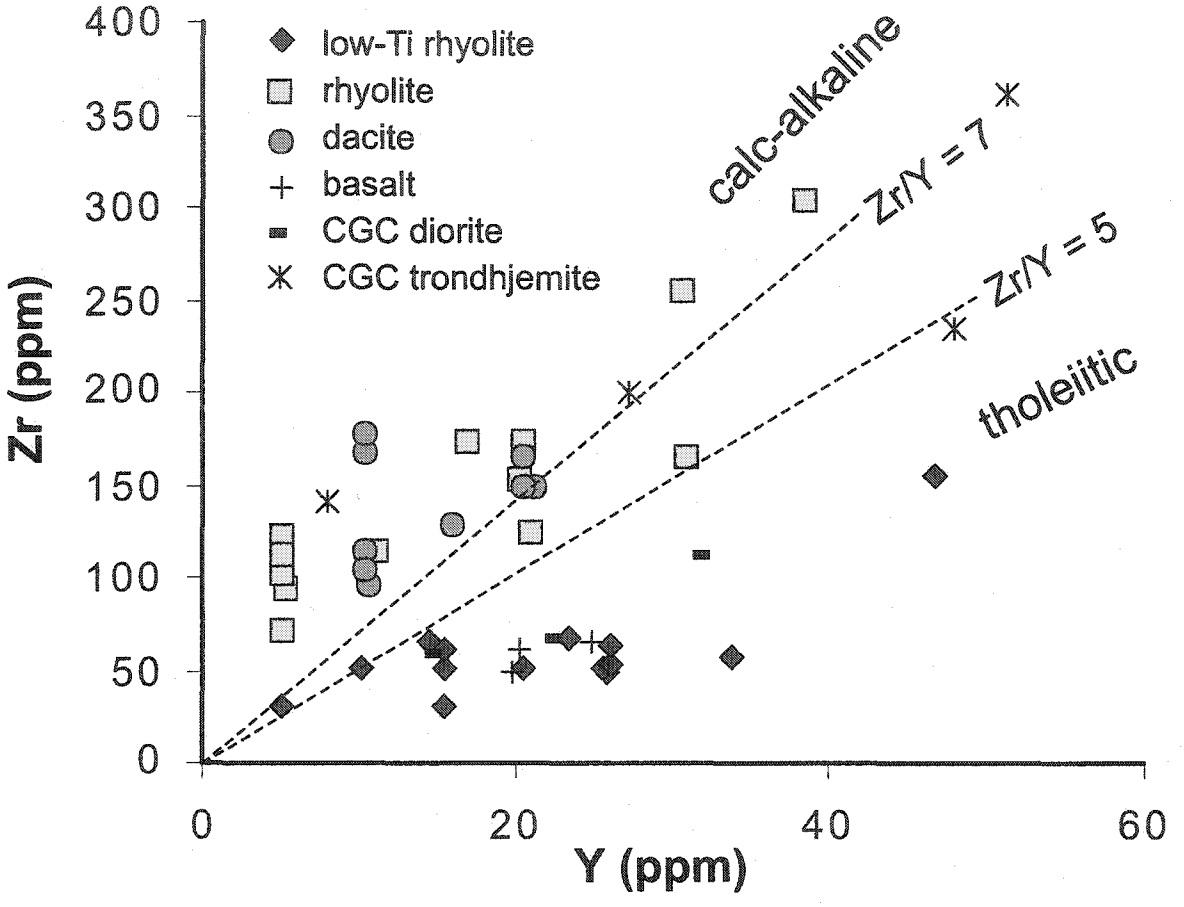

Figure 3.6: Bivariate plot of Zr versus Y for SESGB volcanics and CGC intrusives. Basalt (CAm), CGC diorite and low-Ti rhyolite have Zr/Y ratios <5, indicating a tholeiitic magmatic affinity. Rhyolite, dacite and CGC trondhjemite samples have Zr/Y ratios >5, which is common for rocks having transitional to calc-alkaline affinity. Tholeiitic and calc-alkaline affinity fields are defined by dotted lines based on the Zr/Y ratios in MacLean and Barrett (1993).

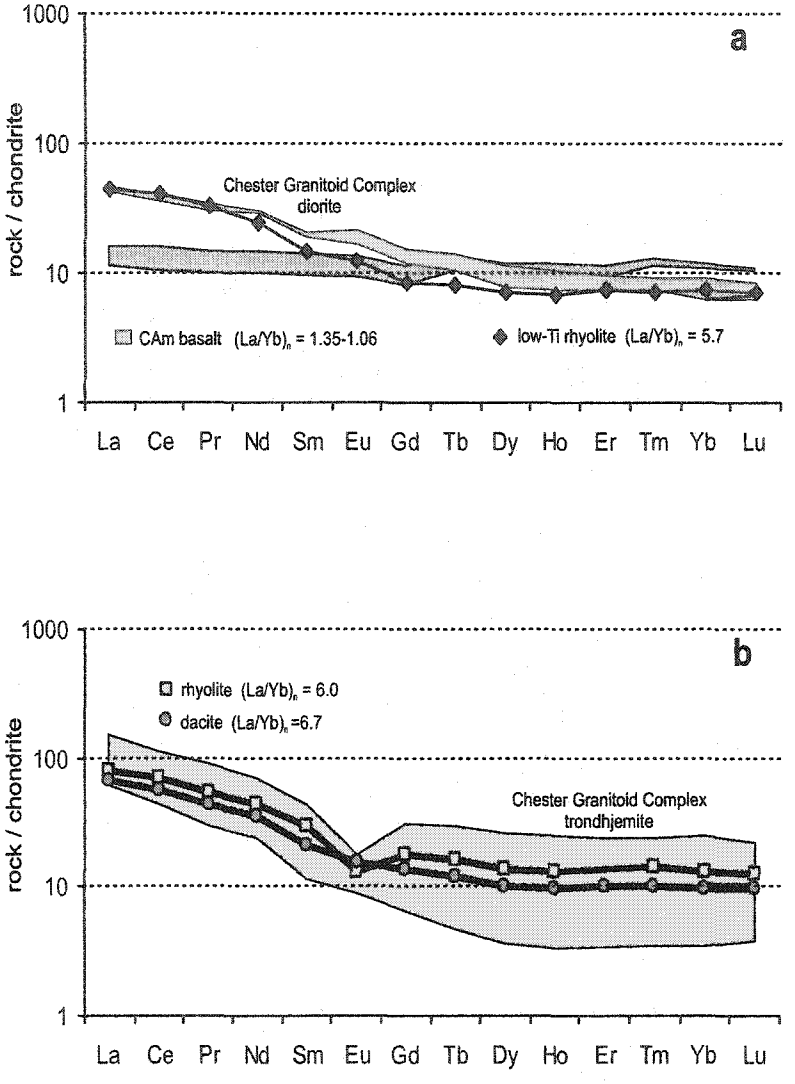

Figure 3.7: Chondrite-normalized REE profiles for the Chester Group volcanics and the Chester Granitoid complex of the SESGB.
(a) Low-Ti rhyolite (sample AU04242) has a $(La/Yb)_n$ ratio of 5.7, very similar to that of the CGC diorite and relatively depleted in LREE. Chester Group, Arbutus Formation basalt (CAm) is depleted in all REE and has a low La/Yb_n ratio (1.06 to 1.35; samples AU04322 and 4415).
(b) CYf rhyolite (average of samples 3469 and 3473) is enriched in all REE relative to dacite (sample 4216), but both fall within the range of REE concentrations of CGC trondhjemite. CGC trondhjemite, and CYf dacite and rhyolite are all relatively enriched in LREE, having $(La/Yb)_n$ >6.

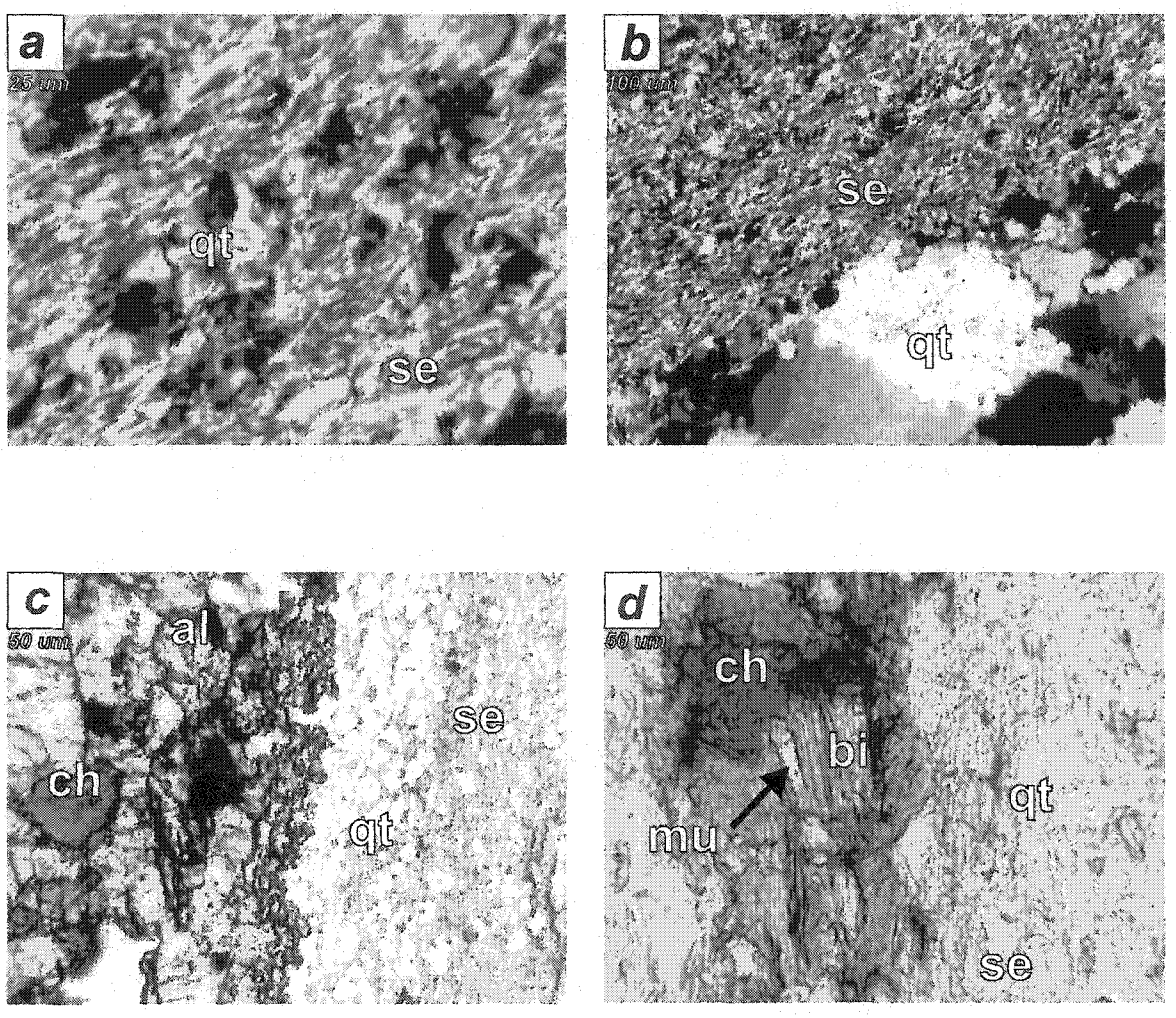

Figure 3.8: Photomicrographs of alteration minerals from type 1 (sericite-quartz) and type 2 (chlorite-sericite+/-biotite+/-garnet) alteration zones. The squares in the upper left corner of each photomicrograph are labeled to indicate scale.
(a) Sericite (se)-quartz (qt) assemblage typical of type 1 alteration (crossed-nicols) is well-developed in dacite, rhyolite and low-Ti rhyolite.
(b) Quartz veinlets and open-space fillings cause net mass-gains and decreased porosity in type 1 alteration (crossed-nicols).
(c) Sericite-quartz-altered rhyolite fragments and chloritic (ch) matrix, are overprinted by garnet (al) in type 2 alteration (plane light).
(d) Relatively coarse-grained muscovite (mu)-biotite (bi) assemblages overprint chloritic matrix in type 2 alteration (plane light).

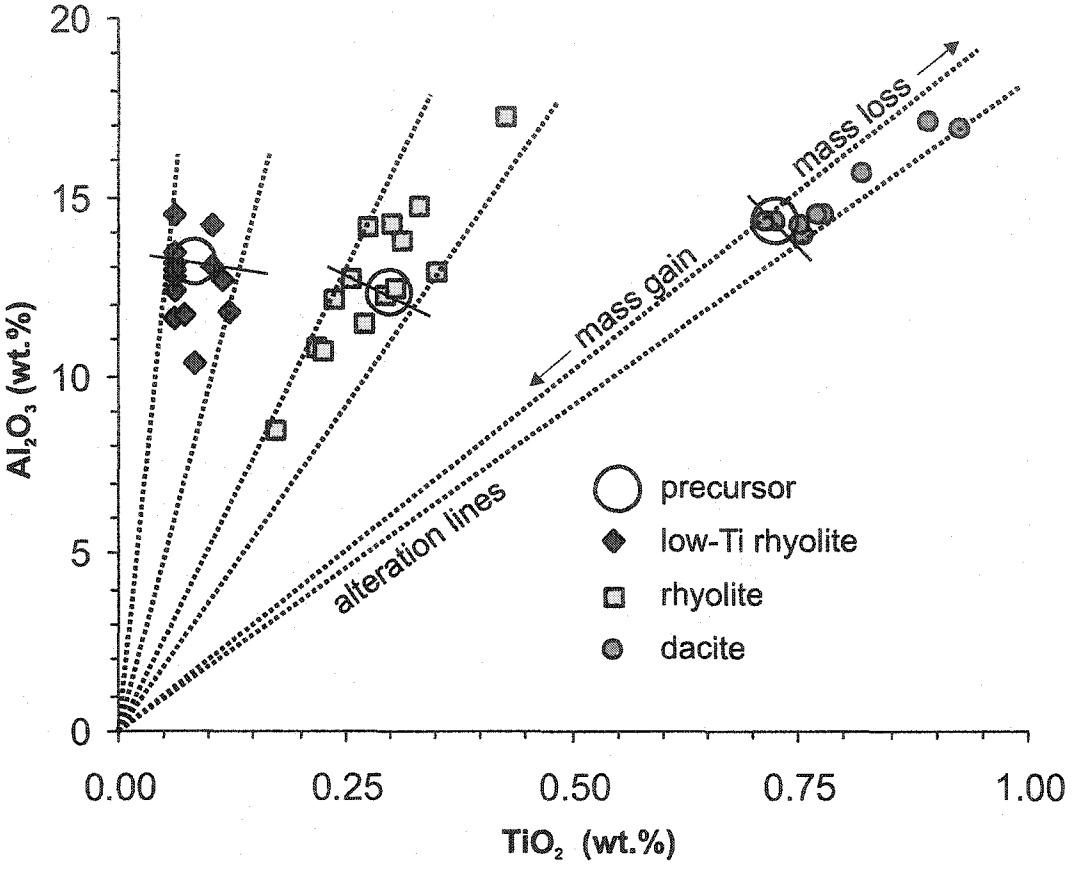

Figure 3.9: Bivariate plot of Al_2O_3 versus TiO_2 concentrations for Chester Group dacite, rhyolite and low-Ti rhyolite. The immobility of Al and Ti during mass-changes accompanying hydrothermal alteration is established by the displacement of altered sample compositions along discrete lines (dotted) trending through the origin. Rocks of similar type maintain near-constant Al/Ti ratios. Alteration involving net mass-gain of mobile components causes compositions to plot along alteration lines between the precursor composition and the origin. Rocks plotting above the precursor composition have undergone mass-loss of mobile components, enriching compositions in immobile elements such as Al and Ti.

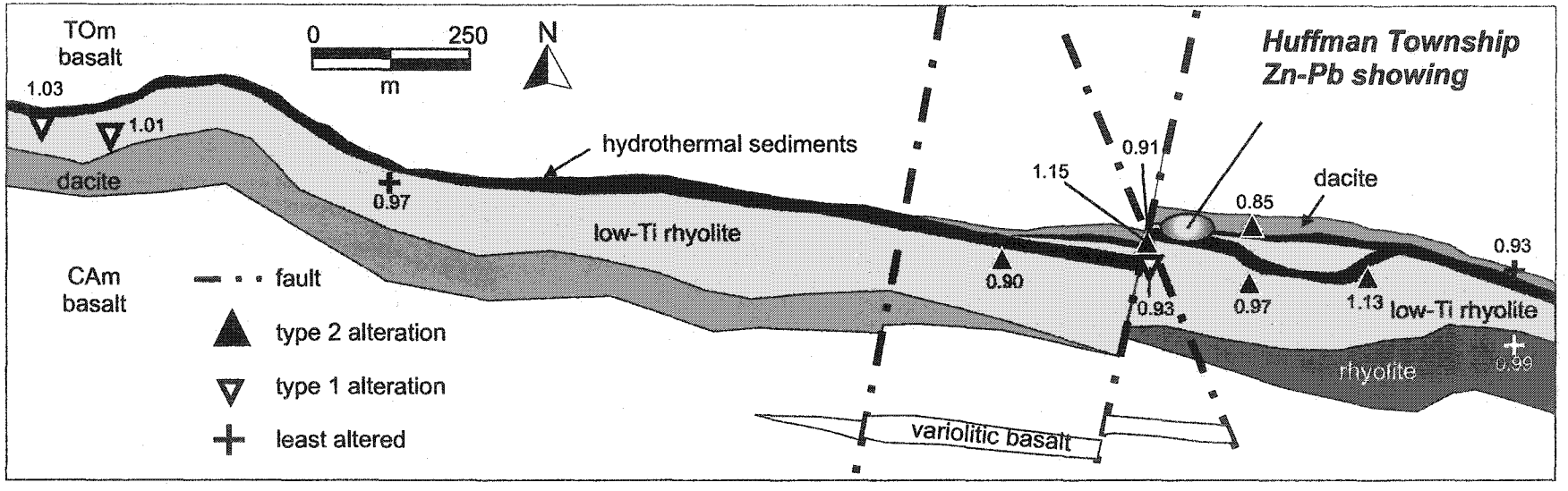

Figure 3.10: Map of the distribution of calculated net mass-changes associated with type 1 (sericite-quartz) and type 2 (chlorite-sericite+/-biotite+/-garnet) alteration of low-Ti rhyolite, rhyolite and dacite volcaniclastics at the Huffman Township Zn-Pb showing, SESGB. Values >1 correspond to net mass-gains during alteration, and values <1 correspond to net mass-losses. Type 1 alteration occurs distal to the mineralized hydrothermal sediments where mass-gain accompanies alteration. Type 2 alteration occurs in volcaniclastic rocks around base-metal sulphide mineralization and several synvolcanic faults. Pillow facing directions in both the CAm basalt and the TOm basalt indicate that stratigraphic top is to the north. Planar stratigraphic and structural features in the map area are subvertical in orientation. Not all samples in Appendix 3.1 occur in the map area.

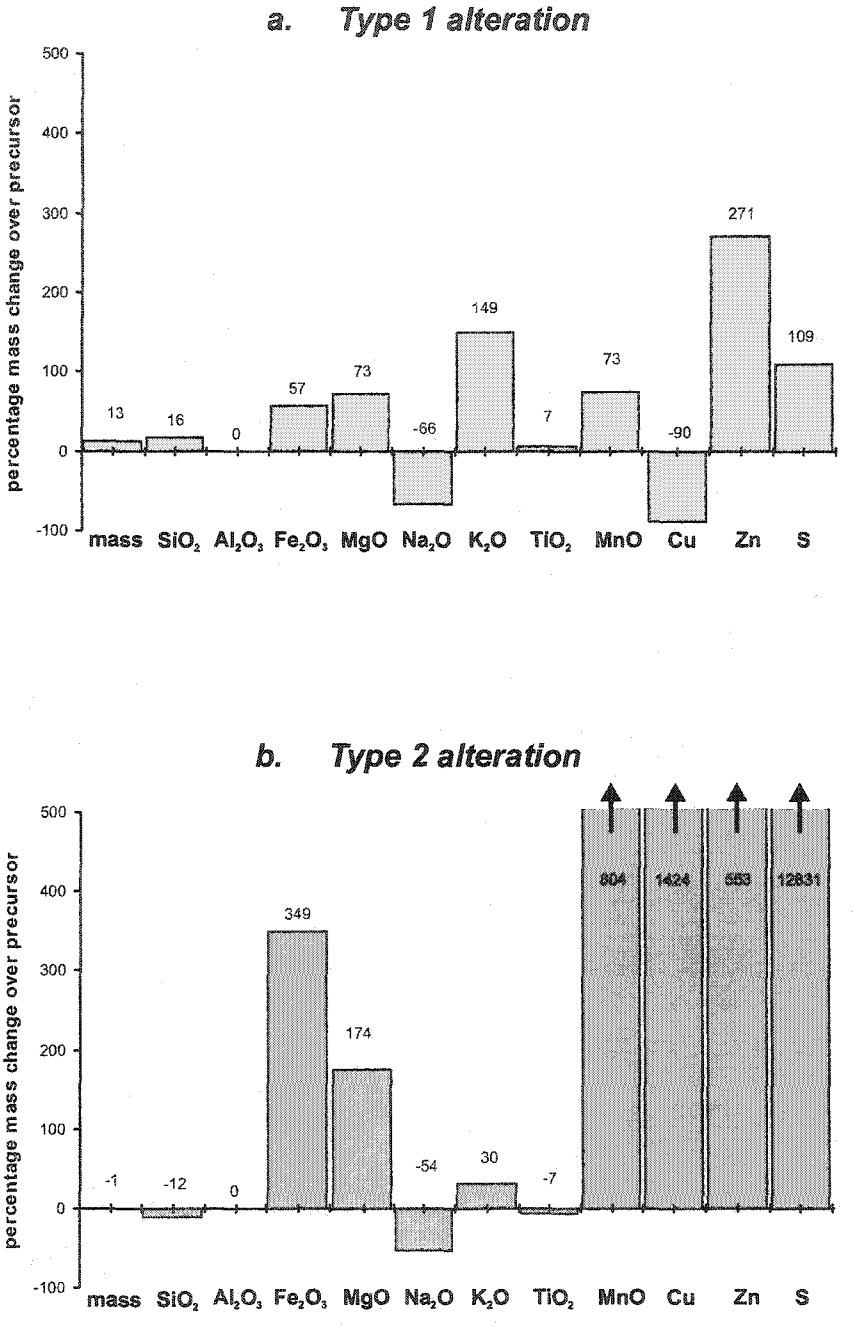

Figure 3.11: Bar-diagrams showing oxide and elemental mass-changes relative to precursor compositions for type 1 (sericite-quartz) and type 2 (chlorite-sericite+/-biotite+/-garnet) alteration facies. Type 1 alteration is characterized by minor additions of K, Si, Mg, Mn, Zn, S, loss of Na and Cu, and net-mass-gain of 13%. Large additions of Fe, Mg, Mn, Cu, Zn, and S and minor losses of Si and Na accompanied type 2 alteration which involved a net mass loss of 1%. The graphs are based on an average of 10 altered samples of each alteration type and include rocks of low-Ti rhyolite, rhyolite and dacite composition.

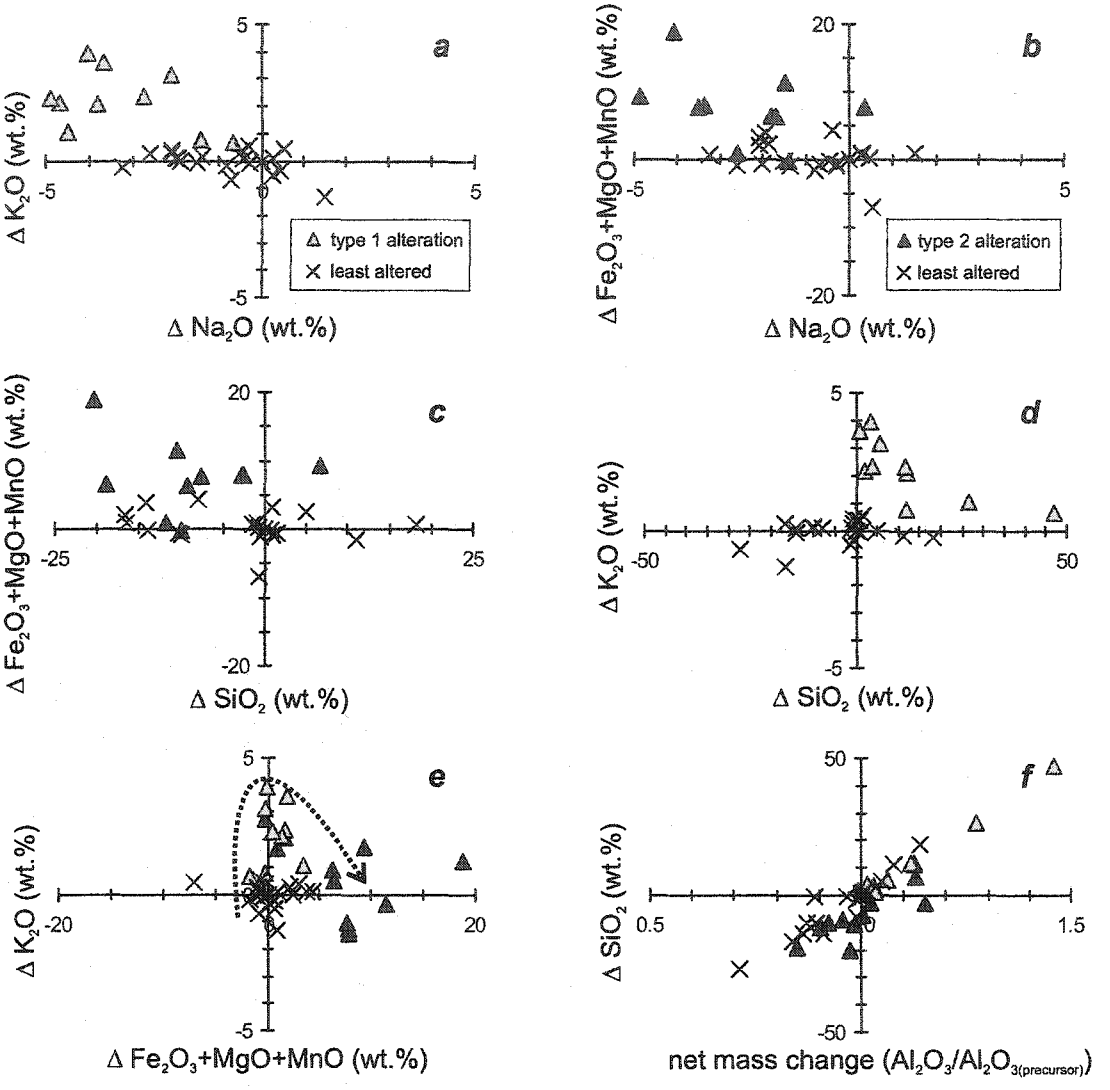

Figure 3.12: Calculated oxide and elemental mass-changes for CYf volcanics during type 1 (sericite-quartz) and type 2 (chlorite-sericite+/-biotite+/-garnet) alteration of low-Ti rhyolite, rhyolite and dacite.

(a) Na was depleted in low-Ti rhyolite, rhyolite and dacite and was replaced by K during type 1 alteration.

(b) Na_2O was depleted, and replaced by Fe, Mg and Mn during type 2 alteration.

(c) Type 2 alteration is associated with a loss of Si and an increase in Fe, Mg and Mn.

(d) Type 1 alteration is associated with an increase in Si.

(e) A path (dotted line) from K enrichment to K loss and gains in Fe, Mg and Mn occurred as type 1 alteration was overprinted by type 2 alteration.

(f) Net mass-change was accomplished by the addition or subtraction of Si.

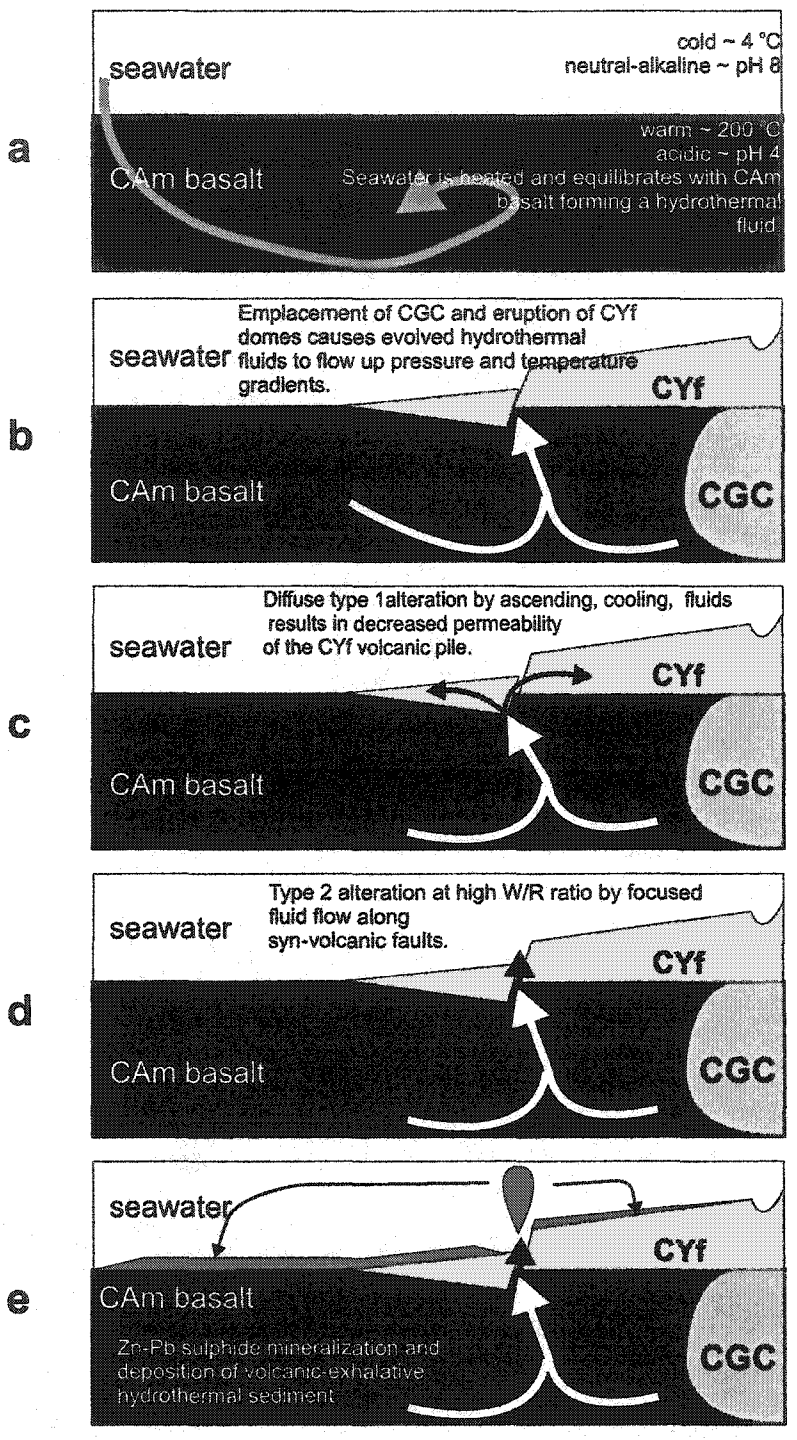

Figure 3.13: Diagram illustrating proposed model for alteration of Chester Group volcanics. (a) Seawater evolved to form a hydrothermal fluid within CAm basalt.
(b) Emplacement of CGC and CYf volcanics produced thermal and pressure gradients allowing circulation of evolved fluids.
(c) Type 1 alteration decreases the porosity of CYf volcaniclastics in initially porous volcaniclastic deposits.
(d) Hydrothermal fluid-flow and type 2 alteration was focused along syn-volcanic structures.
(e) Hydrothermal vents developed on the seafloor, leading to the formation of hydrothermal sediment and localized Zn-Pb sulphide mineralization.

	low-Ti rhyolite	rhyolite	dacite	basalt
	n=2	n=2	n=1	n=2
SiO_2	78.53	75.64	69.84	51.66
Al_2O_3	13.12	12.28	14.32	16.07
Fe_2O_3	0.94	3.75	4.56	11.53
CaO	0.28	1.40	3.35	8.90
MgO	0.36	0.92	1.78	6.20
Na_2O	5.13	3.93	3.89	2.69
K_2O	1.52	1.69	1.30	0.27
TiO_2	0.08	0.30	0.73	1.22
MnO	0.02	0.05	0.07	0.20
P_2O_5	0.03	0.05	0.17	0.06
S	0.01	0.01	0.01	0.01
L.O.I	0.86	0.89	2.65	4.20
V	41	74	156	260
Cr	104	118	109	180
Co	< 5	8	26	49
Ni	10	5	36	76
Cu	90	11	26	130
Zn	dl	dl	10	95
Sc	5	6	10	34
Y	13	26	10	25
Zr	51	215	114	66
Nb	< 5	20	41	3
Al_2O_3/TiO_2	160	41	20	13
Zr/Y	4.0	8.4	11.0	2.6

Table 3.1: Precursor compositions of Chester Group low-Ti rhyolite, rhyolite, dacite and basalt. Precursor compositions are averages (except dacite, n=1) based on least-altered samples for each rock type. Samples are judged as being least-altered on the basis of having the lowest content of secondary alteration minerals during macroscopic and microscopic examinations, and having low loss-on-ignition (LOI) values. Major-element compositions are listed as wt.%, and trace-elements are listed in ppm. Compositions have been normalized to volatile free such that major element concentrations sum to 100 wt.% for each sample.

	type 1 alteration	*type 2 alteration*
n =	10	10
SiO_2	12.48	-8.69
Al_2O_3	0.00	0.00
Fe_2O_3	0.57	5.90
CaO	0.44	1.97
MgO	0.26	1.57
Na_2O	-3.25	-2.44
K_2O	2.20	0.45
TiO_2	0.01	0.00
MnO	0.01	0.16
P_2O_5	-0.01	0.01
S	0.01	0.64
Cr	23	225
Co	0	14
Ni	-15	3
Cu	-72	131
Zn	28	2887
Y	8	4
Zr	20	-47
MF	1.13	0.99

Table 3.2: Average oxide and elemental mass changes for type 1 (sericite-quartz) and type 2 (chlorite-sericite+/-biotite+/-garnet) altered dacite, rhyolite and low-Ti rhyolite. Mass changes are expressed as wt.% for major elements, and as ppm for trace elements. Averages were calculated for 10 samples undergoing alteration of each type. The mass-factor was calculated as the ratio of Al_2O_3 of the altered rock to Al_2O_3 of the appropriate precursor. Type 1 alteration is characterized by significant net mass-gain, and addition of Si and K, and Na loss. Type 2 alteration is characterized by losses of Si and Na, and gains of Fe, Mg, Mn and K.

	seawater	back-arc basin vent fluids	mid-ocean ridge vent fluids	Kuroko fluid-inclusions
T °C	2	238-334	224-380	200-400
pH	7.8	4.7	3.2-5.0	4.5
mmol/kg				
Cl-	541	544-769	467, 544	490-1100
H2S	0	2.6-12.5	6.5, 7.1	-
SO42-	28.6			
CO2	2.3	**200**	41, 85	50-350
SiO2	0.16	12.5-14.2	15.1, 18.6	-
Ca	10.2	22.2, 39.4	28.4, 39.9	10-110
K	9.8	31-**73.7**	23.6	30-140
Na	464	425, 586	438	420-740
µmol/kg				
Mn	<0.001	370.0, **6800**	543, 1064	-
Fe	<0.001	21.0, 1710	51, 964	100
Zn	0.01	7.6, **2400**	118	32
Cu	0.007	0.003, 24	8	69
nmol/kg				
Pb	0.01	36-**4900**	302	12066

Table 3.3: Compilation of seawater, submarine hydrothermal vent-fluid and Kuroko fluid-inclusion compositions. Seawater and vent fluids are from Scott (1997) and references therein, and Kuroko data are from Pisthua-Arnond and Ohmoto (1985). Vent fluid compositions are calculated for end-member compositions. Seawater contributions to hydrothermal fluid compositions are made by estimating the amount of seawater mixing and normalizing end-member hydrothermal fluids to 0 mmol/kg Mg,. Numbers in bold for the back-arc basin fluid composition represent anomalous concentrations.

In the previous chapter, the high field-strength element geochemistry and alteration zone mass-changes of Chester Group Volcanic rocks of the SESGB placed constraints on the architecture and fluid compositions of the fossilized, submarine volcanic exhalative system that developed within the Chester Group volcanic-arc. In the following chapter, hydrothermal sedimentation associated with the emplacement and alteration of the Chester Group volcanic-arc will be investigated from the perspective of distribution, mineralogy, geochemistry and potential for economic base-metal mineralization.

Geology and lithogeochemistry of hydrothermal sediments, Swayze greenstone belt, Ontario

Christopher Wright[1] and A.E. Williams-Jones[2]

[1]Falconbridge Ltd., Timmins Exploration
P.O. Box 1140, Timmins, Ontario, Canada
P4N 7H9

[2]Department of Earth and Planetary Sciences
McGill University
3450 University St., Montréal, Québec, Canada
H3A 2A7

March 21, 2002

4.1 Abstract

Hydrothermal sediments or iron formation (IF) in the Swayze greenstone belt (SGB) are composed largely of Si and Fe. Base-metal mineralization in the south-east SGB and other localities in the SGB is hosted by brecciated hydrothermal sediments, overlain and flanked by more broadly distributed pelitic IF enriched in large ion lithophile elements (LILE), Al, Ti, and high field-strength elements (HFSE), with distinct Fe_2O_3/TiO_2 versus $Al_2O_3/(Al_2O_3+Fe_2O_3+MnO)$ ratios indicative of mixing with locally derived volcanic material. Well-laminated, banded IF-type hydrothermal sediments are widely distributed in the SGB and are enriched in Mn, depleted in LILE, HFSE and transition elements, and have a wide range of Ce/Ce* values, reflecting diverse redox conditions in depositional environments distal to hydrothermal venting. Thermodynamic calculations suggest that the fluids responsible for generation of the hydrothermal sediments have lower temperatures (250-300 °C) than volcanogenic massive-sulphide ore-forming fluids, but similar pH (~4).

4.2 Introduction

Polymetallic volcanogenic massive-sulphide (VMS) deposits are commonly associated with an ore-equivalent horizon consisting of hydrothermal sediments that are the distal products of the seafloor hydrothermal systems responsible for the production of the massive-sulphide deposits (e.g., Davidson, 1977; Large, 1992; Kalogeropoulos and Scott, 1989; Liaghat and MacLean, 1992; Peter and Goodfellow, 1996, 2000). This horizon is typically an Algoma-type iron formation (IF) from the point of view of its geological setting and its interpreted genesis. Iron formations are conspicuous in greenstone belts because they weather dominantly compared to their host volcanic rocks, frequently forming large, gossanous outcrops along ridge crests and lake shores, and because they produce extremely well-defined magnetic and electro-magnetic anomalies easily detectable by airborne and ground geophysical surveys.

The genesis of IF and metalliferous sediments has been studied extensively since the seventeenth century and the history of genetic concepts for IF has been reviewed by Gross (1991). The volcanogenic exhalative or hot-spring origin of some IFs was first suggested early in the 20th century by Collins *et al.* (1926), who described a mechanism by which ascending fluids first replaced volcanic strata with carbonate and sulphide minerals and then, upon meeting the surface, deposited silica and iron compounds during oxidation and cooling. These concepts were applied by James (1954) in his development of the facies concept of IF, in which oxide, sulphide, carbonate and silicate facies were distinguished on the basis of predominant iron-bearing minerals.

Gross (1965) distinguished two types of Precambrian IF on the basis of depositional environments and geological settings. In his model, Superior-type IFs, associated with

thick turbidite and minor volcanic sequences in rifted margin settings, were distinguished from volcanic-associated, Algoma-type IF, thought to be deposited from submarine hot springs. More recently, Kimberly (1989) summarized genetic models for many types of IF, and for the cherty Algoma-type IF, favours the exhalation of hydrothermal fluids that, upon mixing with seawater in the ocean water column, deposit a combination of fine, iron oxyhydroxide particles including glacuonite, greenalite and silica-gel. The precipitation of hydrous solid phases is interpreted to result from mixing between hydrothermal fluids and seawater. Klein (1973) demonstrated that diagenetic and later greenschist facies metamorphic processes transform various primary precipitates into chert, magnetite, grunerite, stilpnomelane, siderite, garnet, pyrite, pyrrhotite and chlorite. In addition, contamination of Algoma-type metalliferous sediments is common, and microscopic-, metre- or even hundred metre-thick intercalations of volcaniclastic or epiclastic detritus greatly affect bulk compositions (Liaghat and MacLean, 1992; Peter and Goodfellow, 1996, 2000).

IF was first identified in the Swayze greenstone belt (SGB) in 1906 when prospectors in search of iron-ore were drawn to the area by the expansion of railways westward from Sudbury, Ontario (Fulmerton *et al.*, 1993). Unfortunately, exploration for iron-ore has been fruitless to date because the iron ranges identified by early prospecting have proven to be too low in grade, high in sulphur content, and too narrow to be economic. However, during the late 1920s base-metal occurrences associated with iron formation were discovered at the Shunsby and Jefferson properties in Cunningham and Marion townships (Fulmerton *et al.*, 1993), and Algoma-type IF in the SGB became an important target for base-metal sulphide exploration. Recent work by Heather and Shore (1999) identified a single upward facing type-section consisting of five

stratigraphic groups, three of which (Chester, Marion, and Trailbreaker) are capped by regionally extensive IF horizons.

In this study, we use a combination of geological mapping, lithogeochemical and geochemical methods to interpret paleoenvironmental controls on hydrothermal sediment composition in the SGB. These data are used in conjunction with thermodynamic modelling to evaluate the potential of IF to represent a VMS ore-equivalent horizon in the SGB, and to refine exploration models for polymetallic massive-sulphide deposits in other greenstone belts.

4.3 Field and analytical methodology

Hydrothermal sediments throughout the SGB were sampled by the first author in order to generate a representative suite for petrographic and lithogeochemical analyses. A total of 88 samples were taken from outcrop and 39 from archived drill-core. Samples were collected such that the proportion of chert and iron-rich bands reflected the modal mineralogy of the exposure as a whole. A 2 to 4 kilogram sample was taken from each outcrop in the field, and a 1 kg portion was removed from the original sample block for analyses. Drill core samples are composites reflecting entire IF intersections, with two 2 cm-long pieces taken from each metre of IF.

Samples were sent to TSL Assayers in Swastika, Ontario where they were crushed to a minus 10 mesh and a 200 g split was taken. The 200 g sample was then pulverized to 70-90% minus 150 mesh with a ring pulverizer. To measure the loss on ignition (LOI) a 1 gram split was roasted for 2 hours at 1000 ° C, weighed, and the LOI was calculated by dividing this weight by the original weight of the sample. A 5 g split was taken and analyzed for Au using standard fire assay procedures. An additional 5 g split was taken

and analyzed for Zn, Pb and Cu, by flame atomic absorption (FAA) spectroscopy. The remaining pulverized sample was then sent to the TSL Assayers laboratory in Vancouver where C and S were determined by infrared methods and the remaining pulverized sample was roasted for 2 hours at 1000 °C to oxidize the sulphide component of the sample. A 5 g split of the roasted, pulverized sample was fused with a lithium metaborate flux, dissolved in HNO_3 and analyzed for major elements and Cr, Zr, Y, Cu, Zn, Ni, Co, Nb, V, Sc, Be, Ba and Sr by ion-coupled plasma atomic emission spectroscopy (ICP-AES). Major element data quoted in oxide wt.% have been normalized to total to 100%, inorganic carbon is reported as TIC, and all iron is reported as Fe_2O_3. Zinc and Cu values used in this study are from analysis by ICP-AES unless > 500 ppm, in which case FAA analyses are reported. Selected pulps were also analyzed for trace elements and REE by ion-coupled plasma mass spectroscopy (ICP-MS) from a solution derived from a fused sample.

All samples from outcrop and archived drill core were examined macroscopically to estimate modal mineralogy. Polished thin sections were prepared of representative samples and examined under a petrographic microscope to assess mineralogical and textural details in the hydrothermal sediments.

4.4 Geology of the Swayze greenstone belt

The SGB is considered the western-most extension of the Abitibi subprovince of the Superior province in northern Ontario (c.f., Ayer *et al.,* 1999; and Heather and Shore, 1999). The SGB is connected to the Abitibi subprovince by a thin band of supracrustal rocks in the north-east and to the Shining Tree greenstone belt by a sinew of volcanic and sedimentary rocks in the south-east. The SGB is bound to the south by the Ramsey-Algoma batholith and the Chester Granitoid Complex, to the east by the

Kenogamissi batholith, to the north by the Biggs pluton, and to the west by the Kapuskasing structure (Figure 4.1). On the basis of field observations and regional geological mapping, radiometric age determinations, and compilation of previous work, Heather *et al.* (1995) defined a stratigraphic type-section through the relatively undeformed Woman River anticline (Figure 4.1). The type-section correlates well with stratigraphic relationships throughout the SGB. Four cycles of mafic to felsic volcanic rocks (Chester, Marion, Trailbreaker and Swayze groups), each with minor intercalations of clastic sediment, occur at the base of the SGB stratigraphic section. All, except the Swayze Group, are capped by regionally extensive iron formation. The uppermost group in the type-section is the Ridout Group, which unconformably overlies the Trailbreaker and Swayze groups in various parts of the SGB. The Ridout Group consists of clastic sediments and quartz-pebble conglomerates, with minor quartz- and feldspar-porphyritic felsic dykes (QFP), felsic volcaniclastics and tuffaceous beds. These rocks correspond to the Timiskaming assemblage sediments described by previous workers (cf. Ayer *et al.*, 1999; Thurston *et al.*, 1977) and exhibit stratigraphic, temporal, textural and petrographic similarities to other Timiskaming sequences in the Abitibi subprovince.

Ayer *et al.* (1999), suggests that the ages published by Heather *et al.* (1995, 1996) and Heather and Shore (1999) for the Chester, Marion and Trailbreaker groups, are correlative with those of other volcanic assemblages elsewhere in the western Abitibi, such as the ca. 2745-2740 Ma Pacaud assemblage south of Kirkland Lake, and the ca. 2730-2725 Ma Deloro and 2710-2702 Ma Tisdale assemblages in the Timmins area.

All supracrustal rocks in the SGB have been metamorphosed to at least greenschist facies. Amphibolite to pyroxene hornfels facies contact-metamorphism has affected

rafts of supracrustal material within encompassing batholiths and is also manifested by narrow (~1 km) aureoles around syn- to post-tectonic batholiths. Contact-metamorphic aureoles are folded about F_2 axes.

Four major base-metal occurrences are known in the SGB, but there has been no significant production from the belt to date (Figure 4.1). The Jefferson Zn-Pb deposit (Figure 4.1) was discovered in the 1930s and underwent extensive, though sporadic exploration until the 1990s. Mineralization occurs as several small lenses of semi-massive- and stringer-type pyrite-sphalerite-galena with very minor chalcopyrite. The mineralization is hosted by brecciated IF above the Marion Formation, Strata Lake Group felsic volcanics (MSf) and below mafic flows of the Trailbreaker Group, October Lake Formation (TOm). A resource of 100 200 metric tonnes (t) grading 4.6% Zn and 3.3% Pb has been calculated for the deposit (Fulmerton, 1995).

Mineralization at the Shunsby Zn-Cu deposits (Figure 4.1) occurs at the same stratigraphic level as the Jefferson deposit; however, at the Shunsby deposits it comprises stringers of pyrite-chalcopyrite mineralization in a muddy rhyolite breccia below a discontinuous horizon of brecciated, laminated hydrothermal sediments (pyrite-sphalerite-chert±galena) below the base of the TOm. Five separate deposits have been outlined on the Shunsby property, with higher Zn and lower Cu grades in the larger lenses. A total resource of 3.98 Mt grading 2.51% Zn and 0.61% Cu has been calculated for the Shunsby deposits (Fulmerton, 1995).

The Peter Lake Zn-Pb showing has been intersected in three drill holes and lies along the same stratigraphic horizon as the Shunsby and Jefferson deposits, about 3 km west-north-west of the Shunsby property (Figure 4.1). This prospect consists of a brecciated,

discontinuous 5-10 m thick, laminated pyrite-sphalerite-chert horizon containing minor amounts of galena.

Base-metal mineralization at the Huffman Township Zn-Pb showing has been exposed over a strike length of 250 m in three small pits at surface and intersected in three drill holes. Mineralization consists of a single 2 m thick pod of massive pyrite, pyrrhotite and sphalerite, and several discontinuous 5-10 m thick pyrite-chert-sphalerite-chlorite-argillite horizons with thin laminations and cross-cutting veinlets of sphalerite and galena. The mineralized horizon occurs at the top of the Yeo Formation felsic volcanic pile within hydrothermal sediments overlain by Trailbreaker Group mafic volcanics. The most economically important drill hole intersection cut 12.3 m of argillaceous breccia-type IF with 1.5% Zn, 0.65% Pb and 1.5 ppm Ag, and 4 m of breccia-type IF with 2.8% Zn, 0.85 % Pb and 3.6 ppm Ag (calculated from data supplied by L. Bonhomme).

4.5 Petrography of SGB hydrothermal sediments

Hydrothermal sediments from the SGB consist dominantly of banded iron formation (BIF), less common phyllosilicate-rich IF (pelitic IF) and the localized breccia-type IF.

Exposures of well-banded hydrothermal sediments in the SGB are mainly composed of quartz and magnetite (Figure 4.2a,b), with subordinate hematite, pyrite, stilpnomelane, siderite, ankerite, grunerite, pyrrhotite, almandine and local traces of hornblende, albite and anorthite (Table 4.1). The majority of the BIF-type hydrothermal sediment in the area can be characterized as oxide-facies as they are composed almost entirely of quartz, magnetite and hematite. However, BIF in the SGB frequently contains significant quantities of carbonate, silicate and sulphide minerals, commonly intercalated with quartz and magnetite. The magnetite content of BIF varies from 20 to 100% in

layers from 0.1 mm to 0.5 m thick, with grain sizes from 0.01 mm to 1-2 mm. Quartz-rich beds are intercalated with the magnetite-rich beds, vary in colour from white, blue, black to jasperoidal (red) due to minor (<10%) contamination by magnetite, chlorite, graphite, siderite or hematite. The colour and composition of quartz-rich beds vary intricately from layer to layer. Substantial amounts of chlorite, amphibole, garnet (almandine) and stilpnomelane occur interbedded with quartz at several localities across the SGB (Table 4.1). These minerals are most abundant in well-laminated IF and create pelitic parting surfaces (Figure 4.2c,d).

Breccia-type iron formation occurs mainly at the base of, and within thick sequences of BIF and pelitic IF. Breccia-type IF features sub-angular tablets of fine-grained quartz, with a fine-grained matrix composed of quartz, magnetite, pyrite, sphalerite, chalcopyrite, chlorite, grunerite and ankerite (Table 4.1, Figure 4.2e). Breccia-type IF is clast-supported, and displays solution-breccia textures. Tablets are commonly laminated internally, rounded, bent and poorly sorted, ranging in size from 1-5 cm thick and 5-30 cm long. In rare cases, the chert-rich clasts occur with rhyolitic fragments that can be distinguished by the presence of quartz and albite phenocrysts.

Carbonate minerals in hydrothermal sediments can constitute 2 to 50% of the modal mineralogy, and consist primarily of ankerite, though siderite may be present locally (Table 4.1). Petrographic analysis of Mn-rich hydrothermal sediments from the Huffman Township showing indicates several percent rhodocrosite. Siderite weathers to bright orange limonite and the weathered surfaces of the carbonate-facies IF are very distinctive in outcrop.

Sulphide-bearing IF can be distinguished from altered, sulphidized IF by the presence of laminated pyrite, pyrrhotite, sphalerite, chalcopyrite and galena in the former that can be traced laterally in stratigraphic layers over several metres in outcrop. Pyrite, magnetite and pyrrhotite are commonly intergrown in sulphide-rich hydrothermal sediments (Figure 4.3a). Fine banding, of the type usually seen in quartz-magnetite IF is rarely duplicated in sulphide-rich sediments; sulphide-rich IF occurs usually as cherty breccia with colloform textures, and as brecciated, laminated sulphide-rich sediment at the Shunsby Cu-Zn deposit and Huffman Zn-Pb occurrence. Sulphide-rich BIF is laterally discontinuous, and is seldom traceable for more than 20 m along strike. Five examples of nearly massive, laminated Fe-sulphide (Figure 4.3a) were found in the southern SGB, occurring in close proximity to, or intercalated with graphitic argillite. Three of these localities are devoid of base-metal sulphides, but outcrops and drill intersections of nearly massive pyrite and argillaceous, breccia-type hydrothermal sediments are present at the Huffman Zn-Pb showing (Figure 4.3b) and the Shunsby Zn-Cu deposits, where sphalerite and chalcopyrite (Figure 4.3c) occur over intervals of 2 to 10 m.

4.6 Geochemistry of SGB hydrothermal sediments

Table 4.2 lists average compositions of 27 breccia-type IF, 32 pelitic IF, and 67 BIF samples from the SGB. The average whole rock compositions illustrate the dominance of Si and Fe in SGB hydrothermal sediments. S and TIC are also important anionic components of Fe-bearing phases in many sulphide- and carbonate-rich rocks. The three hydrothermal sediment types have roughly similar Si, Mg and P contents. The average BIF contains less than 1.5 wt.% combined Al_2O_3, TiO_2, Na_2O and K_2O, and ~6 wt.% more Fe_2O_3, 0.60 wt.% more TIC, and is significantly enriched in Mn relative to other types of hydrothermal sediments. The average pelitic IF has the highest average

alkali, Al and Ti contents and the lowest inorganic carbon content of the three hydrothermal sediment types. Breccia-type hydrothermal sediments have similar, but slightly lower alkali, Al and Ti concentrations than pelitic and BIF-type sediments and contain nearly 6 wt.% S.

Inter-element correlations (Table 4.3) show statistically significant positive r-values (Pearson coefficients) in the following three groupings:

Group 1: Si

Group 2: Fe, Mg, Mn, TIC and S

Group 3: Na, K, Ti and Al

Silicon displays strong negative coefficients of correlation with the Group 2 elements Fe (Figure 4.4a), Mn, TIC and S, whereas there are only weak negative coefficients of correlation between Si and the Group 3 elements Na, K, Ti and Al. Group 2 elements correlate positively among themselves (Figure 4.4b,c) but have ambiguous correlations with Group 3 elements. Calcum has moderately strong positive correlations with Mg and TIC but a plot of Mg+Ca versus TIC (Figure 4.4d) indicates that bulk-compositions of hydrothermal sediments reflect a mixture of carbonate phases including calcite, ankerite and siderite. Phosphorous has a moderately strong positive correlation with Al and Fe, but not with Ti or Mn, making its association somewhat ambiguous.

Figures 4.4e and 4.4f show positive correlations between pairs of Ti and Al and Na+K and Al suggesting that the concentration of the Group 3 elements have a mineralogical control in SGB hydrothermal sediments. Stilpnomelane has a quite variable composition (Table 4.1) but is the only commonly occurring mineral in SGB hydrothermal sediments that is capable of incorporating all of the Group 3 elements.

4.7 Trace element geochemistry of SGB hydrothermal sediments

The average compositions of the three types of metalliferous sediments found in the SGB are listed in Table 4.2 and show systematic differences in trace element compositions. BIF typically contains a lower concentration of most transition elements (except Ge, As, Mo, In, Sn, Sb, W and Bi), large ion lithophile elements (LILE) and high field strength elements (HFSE) than breccia and pelitic IF. Pelitic IF contains higher concentrations of LILE and HFSE, while breccia-type hydrothermal sediments are richer in base- and precious-metals and other transition elements (except Ge, As, Mo, In, Sn, Sb, W and Bi).

Correlations among the three groups of major elements developed above and trace elements are generally poor, and spurious high coefficients occur for many trace elements present at or near the lower detection limits. Standard and log-normalized bivariate plots were used to assess the correlation coefficients (Figure 4.4).

The HFSE, Y, Nb, Th and U are present in concentrations near the lower detection limits of the ICP-MS procedure used for this study, so correlation coefficients for these elements are unreliable. Zirconium is present in slightly greater quantities than the other HFSE in SGB hydrothermal sediments, and correlates positively with Th (Figure 4.5a). Yttrium and Zr show moderate negative correlations with Si ($r = -0.335$ and -0.350, respectively) and positive correlations with Group 3 elements Al (Figure 4.5b), Ti, Na and K ($r = 0.84, 0.70, 0.51, 0.40$, respectively).

Correlation coefficients between K and the minor-LILE, for example K and Ba (Figure 4.5c), are also positive. None of the LILE show strong correlations, positive or negative, with Si, but generally have strong positive correlations with the Group 3 elements; Ba,

has coefficients of 0.53, 0.42, 0.32 and 0.82 with Al, Ti, Na and K, respectively (Figure 4.5c).

There are no significant positive correlations occur the Group 2 elements, Fe and Mn, and any of the trace elements listed in Table 4.2, however, S shows moderate positive correlations with Ni (r = 0.564), Co (r = 0.391), and Ag (r = 0.356), and weak positive correlations with the transition elements Cu, Zn and Pb (r = 0.218, 0.160, and 0.128, respectively). The latter form important sulphide minerals such as sphalerite, galena and chalcopyrite, and occur as trace elements in iron sulphides. Many of the transition elements, especially Pb, Zn, Cu and Ag, display significant positive inter-element correlations (Figure 4.5e,f). No significant correlations were noted between the transition elements and the Group 3 major elements.

Cr shows a statistically significant positive correlation with Si (r = 0.366) and a negative correlation with Fe (r = -0.398) (Table 4.3, Figure 4.5g), making it the only element that is positively correlative with Si. It is likely that the Si-Cr correlation is an artefact of the sample preparation process, small quantities of Cr being contributed to the sample from steel in the grinding apparatus during pulverization of extremely hard, chert-rich samples.

4.8 Rare-earth element geochemistry of SGB hydrothermal sediments

The analysis of the rare-earth element (REE) content of hydrothermal sediments normalized to chondritic or shale REE abundances can be used to determine the physio-chemical conditions and origin of fluids from which the rocks were formed (Barrett *et al.*, 1988; and Peter and Goodfellow, 1996, 2000). In general, the behaviour of the REEs is a function of their high valence states and their differing atomic radii. The

REE content of natural hydrothermal solutions has an inverse relationship with pH (Michard, 1989). The REEs typically exist as trivalent cations and are commonly incompatible during igneous fractionation and immobile during hydrothermal alteration. However, under oxidizing conditions, Ce is a tetravalent cation (Ce^{4+}) and under reducing conditions Eu is a divalent cation (Eu^{2+}) making the behaviour of these elements different from the rest of the trivalent REEs. In oxidized aqueous fluids, Ce^{4+} is preferentially adsorbed to the surfaces of suspended particulates resulting in fluids with negative Ce anomalies. In reduced solutions, Eu^{2+} has greater solubility than other REE, resulting in fluids with REE patterns featuring a positive Eu anomaly (Michard, 1989).

Cerium and Eu anomalies are conventionally expressed as Ce/Ce* and Eu/Eu* and have been calculated herein using the methods of Toyoda and Masuda (1991) and McLennan (1989):

$$[4.1] \quad Ce/Ce^* = (5 \times Ce_n)/(4 \times La_n + Sm_n)$$

$$[4.2] \quad Eu/Eu^* = Eu_n/(Sm_n \times Gd_n)^{0.5}$$

where Ce_n, La_n, Sm_n, Eu_n and Gd_n are the REE abundances of a given sample normalized to the North American Shale Composite (NASC; McLennan, 1989). A Ce/Ce* value less than 0.9 corresponds to a negative Ce anomaly (Peter and Goodfellow, 1996).

Chondrite-normalized REE patterns for the BIF, pelitic IF and breccia-type hydrothermal sediments from the SGB are shown in Figures 4.6a-c. BIF-type hydrothermal sediments are weakly light REE- (LREE-) enriched (average $(La/Yb)_n = 3.9$), have positive Eu/Eu* anomalies (average Eu/Eu* = 3.51) and overall REE concentrations enriched 2 to 10

times relative to chondrite (Figure 4.6a). The average pelitic IF is strongly LREE-enriched ($(La/Yb)_n$ = 7.5), has a negligible Eu/Eu* anomaly (Eu/Eu* = 1.74) (Figure 4.6b), and has overall REE abundances slightly less than average Archean shale values (Taylor and McLennan,1985) (Figure 4.6d). The chondrite-normalized La/Yb ratios of breccia-type hydrothermal sediments are not enriched with respect to C1 chondrite (average $(La/Yb)_n$ = 3.8) and Eu/Eu* anomalies are intermediate between those of BIF and pelitic-type IF (Figure 4.6c). Average Ce/Ce* values for the three hydrothermal sediment types are listed in Table 4.4 and show Ce/Ce* values slightly <1.

4.9 Discussion

4.9.1 SGB hydrothermal sediment provenance

Lithogeochemical studies of modern and ancient hydrothermal sediments indicate that compositions are controlled mainly by mixing hydrothermal precipitates with clastic or volcaniclastic detritus (c.f., Liaghat and MacLean, 1993; Peter and Goodfellow, 1996, 2000). Iron is readily soluble in warm, mildly saline solutions, and can be used as a proxy to measure hydrothermal contributions to hydrothermal sediments (c.f., Bonström and Peterson, 1969). By contrast, Ti is virtually insoluble in such hydrothermal solutions by virtue of its relatively high valence to cationic radius ratio (c.f., Finlow-Bates and Stumpfl, 1981), and can be used as a proxy for the detrital input to hydrothermal sediments. Because Fe shows a strong positive correlation with Mn, TIC and S in the SGB hydrothermal sediments, the source of Group 2 major elements is likely the hydrothermal solutions. The Group 3 elements, Al, Na and K have a similar distribution to Ti in SGB hydrothermal sediments. Ratios of Fe/Ti and Al/(Al+Fe+Mn) have been used in previous studies to evaluate relative contribution of hydrothermal and detrital components to modern metalliferous sediments (Boström and Peterson, 1969). Here,

hyperbolic mixing equations (c.f., Langmuir *et al.*, 1978) define curves between end-member hydrothermal sediments and least-altered compositions for Chester Group volcanic rocks (Figure 4.7a), and indicate that the detrital component in SGB pelitic IF and breccia-type hydrothermal sediments is probably derived from local volcanic sources.

BIF and breccia-type hydrothermal sediments are characterized by strong positive Eu/Eu* anomalies and lack negative Ce/Ce* anomalies, consistent with precipitation from a reduced hydrothermal fluid similar to those produced at ocean-floor spreading centres (Michard, 1989; Figure 4.7b,c). Volcaniclastic and epiclastic material derived from SGB volcanic rocks and incorporated into hydrothermal sediments have Eu/Eu* values of zero or lower that overprint the strong positive Eu/Eu* values of the hydrothermal component in pelitic IF (Figure 4.7b). All types of hydrothermal sediment have positive Eu anomalies when normalized to Archean shale (Figure 4.7d), demonstrating the contribution of reduced hydrothermal fluids to the bulk chemistry of the SGB hydrothermal sediments. The wide range of Ce/Ce* values for BIF sediments reflects variable fO_2 conditions in depositional environments distal to major hydrothermal vent fields, whereas the relatively high Ce/Ce* values (0.9 to 1.1) of most breccia-type and pelitic IF sediments reflect the reduced nature of the vent-proximal environment (Figure 4.7c).

4.9.2 Compositional relationships between SGB IF and ore-equivalent horizons

The mineralized breccia-type and pelitic IF samples enriched in base-metals have Fe/Ti ratios intermediate between Chester Group volcanic rocks and pure hydrothermal end-member BIF (Figure 4.7d). By contrast, similar studies of hydrothermal sediments in

younger (e.g. Phanerozoic) settings such as that of the Bathurst District VMS deposits indicate that Al and Ti concentrations decrease systematically with increasing base-metal content and proximity to known orebodies (Peter and Goodfellow, 1996, 2000). This difference can be reconciled by considering the contrast between the ensialic-rift environment active during the formation of the Bathurst district VMS deposits (van Staal *et al.*, 1991), and the volcanic-arc environment interpreted for the SESGB hydrothermal sediments. In the continental-rift environment, hydrothermal sediment accumulation out-paced the input of clastic sediments to the juvenile ocean-basin proximal to hydrothermal vents and massive-sulphide accumulation, causing Fe/Ti ratios, or other hydrothermal/clastic element ratios, to decrease toward more ore-proximal environments. By contrast, in the submarine volcanic-arc environment, volcaniclastic input to hydrothermal sediments was greatest in areas of active hydrothermal and volcanic activity, and relatively minor in distal parts of the ocean basin. Consequently decreasing hydrothermal/clastic element ratios provide a vector toward felsic volcanic centres and more hydrothermal vent-proximal environments.

Several important observations can be made from comparisons of the composition of hydrothermal sediments within ore-equivalent horizons in the Noranda, Matagami, Bathurst and Kuroko VMS districts (Table 4.4), with the that of the SGB hydrothermal sediment types (Table 4.2). Samples from Archean hydrothermal sediments that are stratigraphically equivalent to massive-sulphide orebodies at Matagami Lake and Noranda contain 5.0 to 13.4 wt.% Al_2O_3, while BIF, pelitic IF and breccia-type hydrothermal sediments in the SGB contain only 0.4 to 4.5 wt.% Al_2O_3. This indicates that the input of Al from volcaniclastic material is significantly greater along the ore equivalent horizons of Archean Cu-Zn sulphide deposits than in sediments not

associated with major Cu-Zn sulphide deposits. The implication of this observation is that Archean hydrothermal sediments marking ore-equivalent horizons record more intense volcanic activity during periods of hydrothermal sedimentation than the BIF-type hydrothermal sediments of the SGB, which are contemporaneous with periods of relatively quiescent volcanism.

Hydrothermal sediments of the Key Tuffite at Matagami, the hydrothermal component of the Contact Tuff at Noranda and the chlorite-sulphide IF of the Brunswick Horizon, in the Bathurst district, and the Tetsusekiei Horizon of the Kuroko VMS district contain between 7.96 and 18.20 wt.% S. By contrast, the BIF, pelitic sediments and breccia-type IF of the SGB contain 3.70, 4.50 and 5.96 wt.% S, respectively. The relatively low S content of SGB hydrothermal sediments suggests that the hydrothermal fluids responsible for the transport of Fe and base-metals to the paleo-seafloor, and/or the ambient seawater, may have lacked sufficient reduced sulphur to deposit economically significant quantities of base-metal sulphide minerals.

4.9.3 Thermodynamic constraints on the chemistry of fluids responsible for SGB hydrothermal sediments

The predicted solubility of Fe, Pb, Zn, and Cu as chloride and sulphide complexes in a 0.5 mol/kg ΣCl^- solution in equilibrium with the assemblage magnetite-pyrite-pyrrhotite-sphalerite-galena-chalcopyrite at 300 bar pressure was calculated as a function of temperature and pH. The mineral assemblage was chosen to buffer fO_2, and maintain Fe-, Zn-, Pb- and Cu-sulphide mineral saturation during model runs. The 0.5 mol/kg ΣCl^- solution reflected mixing between a warm (150 to 400 °C), saline, low-pH (~4) submarine hot spring-type hydrothermal fluid and seawater. The pressure of 300 bar

was chosen to simulate reaction on the seafloor at a seawater depth of approximately 3000 m.

The HCh program of Shvarov (1999), supplemented with thermodynamic data for metal-mono- and -di-chloride complexes, metal-mono- and bi-sulphide complexes (Sverjensky *et al.,* 1997) and sulphide and oxide minerals (Helgeson *et al.,* 1978), were used to construct Figure 4.8. Reduced sulphur species (H_2S, HS^-) do not form strong complexes with base-metals at the conditions modelled here, so sulphur-bearing complexes were not considered during these calculations. The pH of each run was varied by making minor changes to the total concentration of Na in the system.

Copper solubility is strongly dependent on temperature with temperatures >350 °C being necessary to leach and transport significant quantities of Cu at pH >4 (Figure 4.8). The solubility of Zn and Pb is greatest in acidic, higher temperature fluids, but more Zn and Pb than Cu can be transported at lower temperatures at these conditions (Figure 4.8). Fe is readily soluble in acidic and higher temperature fluids, but can also be dissolved in appreciable quantities in fluids at temperatures <200 °C and near-neutral pH. Low pH (~4) and ~300 °C hydrothermal fluids were required to transport Fe, Cu and Zn to hydrothermal vents that formed the Shunsby Cu-Zn deposit. The Zn-Pb mineralization at the Jefferson, Peter Lake and Huffman Township Zn-Pb showings were likely formed by fluids that did not attain temperatures as high as those responsible for the Cu-rich mineralization at the Shunsby deposit; low-pH (~4), moderately high-temperature (~250 °C) hydrothermal fluids were capable of transporting moderate concentrations of Fe and Zn and Pb, with virtually no Cu at the Zn-Pb showings.

The thermodynamic model utilized here demonstrates that base-metal-sulphide and Fe saturation in hydrothermal fluids is reached by a combination of increasing pH and decreasing temperature (Figure 4.8). Mixing of metal-charged hydrothermal fluids with seawater of near-neutral pH, and low temperature at, or near the paleoseafloor is likely the cause of base-metal and Fe saturation. The concentration of total dissolved Cu drops two orders of magnitude with a decrease in temperature of 100 °C or an increase of two pH units upon mixing with cold, mildly alkaline seawater (Figure 4.8). Zn and Pb solubility are especially sensitive to pH, with solubilities dropping two orders of magnitude with a one-unit increase in pH. A 200 °C drop in temperature, or a combination of increasing pH, and decreasing temperature, caused by mixing with seawater will cause rapid Zn- and Pb-sulphide saturation (Figure 4.8). Iron solubility also decreases rapidly when hot, acidic hydrothermal fluid is mixed with seawater, as is shown in Figure 4.8, however, equilibrium calculations indicate that Fe exhibits retrograde solubility below temperatures of approximately 250 °C, and becomes much more soluble than base-metals at temperatures below 200 °C. Typical VMS ore-forming fluids mix with seawater, causing a rapid decrease in temperature, while pH is partially buffered by the production of H^+ during sulphide mineral precipitation, for example the precipitation of sphalerite from the di-chloride complex:

$$[4.1] \quad ZnCl_2^0 + H_2S = ZnS + 2Cl^- 2H^+$$

Ore-fluids thus evolve along a path from A to D (Figure 4.8), reaching Cu, then Zn, Pb and finally Fe saturation during mixing with seawater, and leading to the typical pattern of metal-zonation within VMS deposits (c.f. Franklin, 1996). The composition of SGB hydrothermal sediments indicates that the fluids responsible for their genesis must have had a limited capability to transport Cu, Zn and Pb, whereas they were able to transport

vast quantities of Fe. A 250-300 °C, low pH (~4) hot-spring fluid mixing with seawater at the paleo-seafloor likely followed a path between BD and CD in Figure 4.8. Fluid evolution along this path would allow the deposition of minor Cu, Zn and Pb proximal to the hydrothermal fluid-seawater mixing interface (e.g., within breccia-type hydrothermal sediments), and the transport of Fe long distances from the vent field, forming regionally continuous, but barren, BIF. Warmer fluids (BD) can transport greater quantities of Cu, and gave rise to hydrothermal sediments richer in Cu, such as those at the Shunsby deposit, while cooler fluids were responsible for the production of the Zn-Pb-rich (Cu-poor) hydrothermal sediments at the Jefferson Deposit and the Peter Lake and Huffman Township Zn-Pb showings of the SGB.

In short, the fluids responsible for the generation of SGB hydrothermal sediments may have reached pH values similar to typical VMS systems, but end-member hydrothermal fluids failed to attain the temperatures required to transport quantities of Cu, Zn and Pb sufficient to produce economic base-metal sulphide orebodies.

4.9.4 A model for the generation of breccia-, pelitic- and BIF-type hydrothermal sediments in the SGB

The petrographic and lithogeochemical characteristics of the three types of hydrothermal sediments in the SGB are a result of the geological environment in which they were deposited (Figure 4.9).

Moderately hot (250-300 °C), acidic (pH ~ 4) hydrothermal fluids rich in Fe and base-metals were discharged onto the seafloor at hydrothermal vents. Base-metal sulphide deposition upon mixing with seawater at or near the seafloor lead to the formation of breccia-type hydrothermal sediments proximal to hydrothermal vents. This type of hydrothermal sediment contains sub-economic Cu-Zn and Zn-Pb mineralization at the

Shunsby and Peter Lake deposits and the Jefferson and Huffman Township base-metal sulphide occurrences. In general, the exhalative systems responsible for the generation of hydrothermal sediments throughout the SGB lacked the high temperatures and the reduced sulphur necessary to form significant polymetallic massive-sulphide deposits.

Because Fe solubility remains high at higher pH and lower temperature than base-metal sulphides, a significant quantity of Fe was transported away from the vent field in hydrothermal plumes. Pelitic-type IF was deposited in an environment where end-member precipitates from hydrothermal plumes were mixed with volcaniclastic and epiclastic material from active volcanic centres. These sediments are an order of magnitude more distal to hydrothermal vents than the breccia-type hydrothermal sediment.

BIF-type hydrothermal sediments were deposited by precipitation from several hydrothermal plumes in the SGB, distal to explosive volcanic centres and during periods of volcanic quiescence. These sediments are the most extensive in distribution in the SGB, contain very little epiclastic and volcaniclastic detritus and were formed in the most hydrothermal vent-distal environment of the three hydrothermal sediment types.

4.10 Conclusions

1. BIF in the SGB is composed almost entirely of Si and Fe, has a relatively high CO_2 content and is depleted in LILE, HFSE and transition elements compared to pelitic IF and breccia-type hydrothermal sediments. BIF-type hydrothermal sediments have a wide range of Ce/Ce* values reflecting variable fO_2 conditions in hydrothermal vent-distal depositional environments. BIF can be found throughout the SGB, and overlies breccia-type and pelitic IF.

2. Pelitic IF is enriched in Al, Ti, Na, K, HFSE and LILE and is characterized by flat, slightly depleted REE profiles when normalized to average Archean shales. Pelitic IF compositions display a continuum of mixing between end-member BIF hydrothermal sediments and local Chester Group volcanic rocks, indicating deposition proximal to active SGB volcanic edifices.

3. Breccia-type hydrothermal sediments of the SGB are enriched in S, Zn, Pb, Cu, Ag, Au, Ni, and Co compared to BIF and pelitic IF. These elements were precipitated as sulphides from a hydrothermal solution that mixed with seawater in a vent-proximal environment. Zn, Cu and Pb mineralized breccias include the Jefferson, Shunsby, Peter Lake and Huffman Township base-metal showings of the SGB, and offer the most prospective geological environments for base-metal sulphide mineralization.

4. Hydrothermal sediments that occupy ore-equivalent stratigraphic positions in productive Archean VMS districts have higher S and Al concentrations than SGB hydrothermal sediments because of greater availability of S and greater volcanic activity during massive sulphide deposition. These observations can be used to gauge the potential of other IFs in similar tectonic settings to mark stratigraphic horizons containing economic massive sulphide deposits.

5. Thermodynamic calculations indicate that SGB hydrothermal sediments precipitated from a cooler (250-300 °C) fluid than those responsible for the generation of typical polymetallic massive-sulphide deposits.

4.11 References

Barrett, T.J., Fralick, P.W., and Jarvis, I., 1988. Rare-earth-element geochemistry of some Archean iron formations north of Lake Superior, Ontario. Canadian Journal of Earth Sciences, 25, p. 570-580.

Boström, K. and Peterson, M.N.A., 1969. The origin of aluminum-poor feromanganoan sediments in areas of high heat flow on the East Pacific Rise. Marine Geology, 7, p. 427-447.

Boynton, W.V., 1984. Geochemistry of the rare-earth elements: meteorite studies. *In*, P. Henderson (ed.), Rare-Earth Element Geochemistry, Elsevier, New York, p. 63-114.

Collins, W.H., Quirke, T.T. and Thomson, E., 1926. Michipicoten Iron Ranges. Canada Geological Survey Memoir, 147, 161 p.

Davidson, A.J., 1977. Petrography and chemistry of the Key Tuffite at Bell Allard, Matagami, Quebec. M.Sc. thesis, McGill University, Montreal, Québec, 131 p.

Finlow-Bates, T. and Stumpfl, E.F., 1981. The behavior of the so-called immobile elements in hydrothermally altered rocks associated with volcanogenic submarine exhalative ore deposits. Mineralium Deposita, 16, p. 319-328.

Franklin, J.M., 1996. Volcanic-associated massive-sulphide base-metals. *In,* O.R. Eckstrand, W.D. Sinclair, and R.I. Thorpe (eds.), Geology of Canadian Mineral Deposit Types. Geological Survey of Canada, Geology of Canada, 8, p. 158-183.

Fulmerton, S., Houle, K., and Archibald, G., 1993. Mineral showings, occurrences, deposits and mines of the Swayze greenstone belt, interim report, 1 and 2. Ontario Geological Survey Open File Report 5871, p. 1-763.

Fulmerton, S., 1995. Summary tables on mineral prospects in the Swayze greenstone belt. Ontario Geological Survey Open File Report 5913. p. 1-105.

Gross, G.A., 1965. Geology of iron deposits in Canada. Canada Geological Survey Economic Geology Report, 22, 181 p.

Gross, G.A., 1991. Genetic concepts for iron-formation and associated metalliferous sediments. Economic Geology Monograph 8, p. 51-81.

Heather, K.B. and Shore, G.T., 1999. Geology, Swayze Greenstone Belt, Ontario. Geological Survey of Canada, Open File 3384a-i.

Helgeson, H.C., Delany, J.M, Nesbitt, H.W., and Bird, D.K., 1978. Summary and Critique of the Thermodynamic Properties of Rock-Forming Minerals. American. Journal of Science, 278A, 229 p.

James, H.L., 1954. Sedimentary facies of iron-formation. Economic Geology, 49, p. 235-293.

Kalogeropoulos, S.I., and Scott, S.D., 1983. Mineralogy and geochemistry of tuffaceous exhalites (Tetsusekiei) of the Fukazawa mine, Hokuroku District, Japan. Economic Geology Monograph 5, p. 412-432.

Kalogeropoulos, S.I., and Scott, S.D., 1989. Mineralogy and geochemistry of an Archean tuffaceous exhalite: The Main Contact Tuff, Millenbach mine area, Noranda, Quebec. Canadian Journal of Earth Science, 26, p.88-105.

Kimberly, M.M., 1989. Exhalative origins of iron formations. Ore Geology Reviews, 5, p. 13-145.

Klein, C.K., Jr., 1973. Changes in mineral assemblages with metamorphism of some banded Precambrian iron-formations. Economic Geology, 68, p. 1075-1088.

Langmuir, C.H., Vocke, R.D. Jr., Hanson, G.N., and Hart, S.R., 1978. A general mixing equation with applications to Icelandic basalts. Earth and Planetary Science Letters, 37, p. 380-392.

Large, R.C., 1992. Australian volcanic-hosted massive sulfide deposits: features, styles, and genetic models. Economic Geology, 87, p. 471-510.

Liaghat, S. and MacLean, W.H., 1992. The Key Tuffite, Matagami mining district: Origin of the tuff components and mass-changes. Exploration and Mining Geology, 1, 2, p.197-207.

McLennan, S.M., 1989. Rare-earth elements in sedimentary rocks: influence of provenance and sedimentary processes. *In*, B.R. Lipin and G.A. McKay (eds.), Reviews in Mineralogy 21, Mineralogical Society of America, Washington, D.C., p. 169-200.

Michard, A., 1989. Rare-earth element systematics in hydrothermal fluids. Geochimica et Cosmochimica Acta, 53, p. 745-750.

Peter, J.M., and Goodfellow, W.D., 1996. Mineralogy, bulk and rare-earth element geochemistry of massive-sulphide associated hydrothermal sediments of the Brunswick Horizon, Bathurst Mining Camp, New Brunswick. Canadian Journal of Earth Sciences, 33, 2, p.252-283.

Peter, J.M. and Goodfellow, W.D., 2000. Hydrothermal sedimentary rocks of the Heath Steele Belt, Bathurst Mining Camp, New Brunswick-3: Application of mineralogy, and mineral and bulk compositions to massive-sulphide exploration. *In* W.D. Goodfellow, S.R. McCutcheon and Jan M. Peter (eds.), Economic Geology Monograph 11: Massive Sulfide Deposits of the Bathurst Mining Camp and Northern Maine. *in press.*

Shvarov, Y.V., 1999. Algorithnization of the numeric equilibrium modelling of dynamic geochemical processes. Geochemistry International, 37, 6, p. 571-576.

Sverjensky, D.A., Shock, E.L., and Helgeson, H.C., 1997. Prediction of the thermodynamic properties of aqueous metal complexes to 1000 C and 5 kb: Geochimica et Cosmochimica Acta, 61, 7, p. 1359-1412.

Toyoda, K. and Masuda, A., 1990. Chemical leaching of pelagic sediments: Identification of the carrier of Ce anomaly. Geochemical Journal, 25, p. 1093-1103.

van Staal, C.R., Winchester, J.A. and Bédard, J.H., 1991. Geochemical variations in Middle Ordovician volcanic rocks of the northern Miramichi Highlands and their tectonic significance. Canadian Journal of Earth Sciences, 28, p. 1031-1049.

Appendix 4.1: Lithogeochemical data

Appendix 4.1: Lithogeochemical data

sample	8474	8476	8478	8479	8480	AU01753	AU04212	AU04219	AU04234	AU04236
flag	IBH	IBH	IBH	IBH	IBH	IBH	IBH	IBH	IBH	IBH
SiO_2	74.64	49.78	59.69	71.21	73.53	56.46	64.36	83.41	81.07	61.12
Al_2O_3	0.54	1.03	0.55	0.60	0.25	0.46	0.69	0.21	0.05	0.25
Fe_2O_3	14.84	42.08	26.13	15.94	15.66	41.31	31.27	14.22	17.65	34.29
CaO	5.75	2.38	7.14	7.65	8.26	0.22	1.64	0.20	0.07	0.24
MgO	2.66	4.29	5.55	3.77	1.85	1.23	1.38	0.70	0.91	3.80
Na_2O	0.01	0.02	0.01	0.01	0.01	0.01	0.06	0.01	0.01	0.01
K_2O	0.02	0.05	0.01	0.01	0.01	0.02	0.12	1.04	0.02	0.03
TiO_2	0.02	0.04	0.01	0.02	0.01	0.03	0.03	0.02	0.01	0.02
MnO	0.45	0.19	0.75	0.41	0.38	0.03	0.23	0.11	0.10	0.06
P_2O_5	0.06	0.14	0.17	0.37	0.04	0.23	0.20	0.08	0.11	0.17
TIC	3.38	0.88	3.52	3.62	1.98	0.15	0.03	0.57	0.01	0.14
S	1.62	0.87	4.81	0.90	3.63	0.14	0.14	0.51	0.03	0.29
LOI	7.74	2.30	5.03	9.10	3.55	1.30	1.45	3.53	0.41	0.98
V*	44.1	82.3	73.9	55.1	52.1	81.4	61.3	36.4	40.4	66.0
Cr*	297.5	98.2	253.3	488.6	369.9	67.8	93.2	104.2	131.1	65.5
Co*	5.5	10.3	52.8	5.5	15.6	10.2	2.9	8.6	2.5	20.3
Ni*	41.9	26.8	61.2	32.0	26.0	16.3	2.6	2.6	2.5	2.5
Cu*	16.5	10.3	168.9	33.1	198.0	117.0	153.1	36.4	5.0	121.9
Zn*	2.8	406.4	221.7	55.1	104.2	2.5	2.6	2.6	33.3	35.6
Ga^3	1.9	4.3	2.6	1.7	1.3	2.8	5.3	1.4	1.3	2.6
Ge^3	3.80	3.92	2.57	3.24	3.06	12.45	4.58	4.21	4.01	8.56
As^3	51.6	2.6	2.6	2.8	2.6	2.5	2.6	7.5	2.5	2.5
Mo^3	2.9	4.6	1.1	2.8	1.0	1.0	1.0	2.2	1.0	2.7
Ag^2	0.3	0.1	0.7	0.1	0.5	0.1	0.1	0.1	0.1	0.1
In^3	0.055	0.206	0.053	0.055	0.052	0.103	0.256	0.052	0.050	0.111
Sn^3	0.6	0.5	0.5	0.6	0.5	0.5	3.9	0.5	0.5	0.5
Sb^3	0.110	0.103	0.106	0.250	0.104	0.884	0.102	0.104	0.101	0.751
W^3	0.3	1.1	0.3	0.3	0.3	0.3	0.3	1.4	0.3	0.3
Au^2	1.1	212.0	43.3	18.7	7.3	34.6	17.4	7.3	7.1	3.0
Tl^3	0.028	0.026	0.026	0.028	0.026	0.025	0.026	0.026	0.025	0.025
Pb^2	1.1	1.0	61.2	259.1	8.3	1.0	1.0	1.0	1.0	1.0
Bi^3	0.06	0.05	0.05	0.06	0.18	1.05	1.03	0.29	0.05	0.20
Be	2.8	2.6	2.6	2.8	2.6	2.5	2.6	2.6	2.5	2.5
Rb^3	0.6	0.5	0.5	0.6	0.5	0.5	0.5	0.5	0.5	0.5
Sr*	33.1	61.7	137.2	44.1	41.7	20.3	10.2	5.2	7.8	10.2
Cs^3	0.1	0.1	0.1	0.1	0.1	0.1	0.1	0.1	0.1	0.1
Ba*	19.4	15.2	1.6	1.7	10.3	5.5	114.5	7.0	16.7	22.8
Sc	2.8	2.6	5.3	2.8	2.6	2.5	2.6	2.6	2.5	2.5
Y*	6.6	6.9	7.6	17.7	5.9	7.2	7.5	2.6	3.6	6.6
Zr*	9.9	9.1	7.8	9.2	6.2	6.8	11.7	4.3	5.6	7.2
Nb*	0.1	0.1	0.1	0.1	0.1	0.1	0.1	0.1	0.1	0.1
Hf^3	0.23	0.33	0.16	0.26	0.15	0.20	0.30	0.05	0.05	0.18
Ta^3	0.01	0.02	0.01	0.01	0.01	0.01	0.11	0.01	0.01	0.01
Th^3	0.2	0.4	0.1	0.1	0.1	0.2	0.2	0.1	0.0	0.2
U^3	0.1	0.1	0.0	0.1	0.0	0.1	0.0	0.0	0.0	0.1
La^3	3.2	4.1	1.5	3.4	3.0	4.2	4.0	1.2	2.0	4.3
Ce^3	6.1	8.5	3.1	6.4	5.6	8.7	7.4	2.4	3.7	10.3
Pr^3	0.7	1.0	0.4	0.8	0.7	1.0	0.8	0.3	0.4	1.3
Nd^3	3.158	4.066	1.770	3.997	2.963	4.297	3.279	1.120	1.808	5.064
Sm^3	0.717	0.865	0.500	1.117	0.748	0.916	0.720	0.250	0.351	1.113
Eu^3	0.690	0.746	0.447	0.984	0.609	0.569	0.611	0.228	0.370	0.757
Gd^3	0.773	0.815	0.682	1.651	0.807	0.907	0.770	0.283	0.356	1.028
Tb^3	0.142	0.161	0.154	0.323	0.144	0.165	0.139	0.054	0.071	0.183
Dy^3	0.862	0.993	1.019	2.056	0.839	1.019	0.938	0.366	0.442	1.102
Ho^3	0.192	0.220	0.222	0.426	0.181	0.226	0.223	0.087	0.109	0.235
Er^3	0.587	0.706	0.662	1.150	0.550	0.723	0.729	0.264	0.337	0.744
Tm^3	0.082	0.108	0.088	0.136	0.081	0.106	0.110	0.040	0.051	0.111
Yb^3	0.515	0.727	0.568	0.700	0.525	0.694	0.682	0.270	0.323	0.750
Lu^3	0.081	0.111	0.086	0.104	0.078	0.106	0.103	0.040	0.046	0.117
UTM E	410563	410173	410401	410401	410401	415325	416170	411060	411769	412147
UTM N	5270758	5270756	5270735	5270759	5270771	5271245	5270340	5270668	5271443	5271340

-All data have been normalized to a volatile free basis such that major oxides total 100%.
-Major oxides, S, total inorganic carbon (TIC) and loss on ignition (LOI) are expressed as weight percent, Au is expressed in parts per billion, and all other trace elements as parts per million. The letters ND indicate that no data are available.

-analysis key ^{3} indicates analysis by ICP-MS
* indicates analysis by ICP-AES or AA

-flag key *first letter - sample type:* I=hydrothermal sediment sample
second letter - lithology type: B=BIF, S=pelitic IF, X=breccia
third letter: -iron formation: T=Trailbreaker Group, H=Huffman Township, W=Woman River, S=Shunsby, N=Northern SGB

-sample locations are given in NAD83 projection for UTM zone 17

Appendix 4.1: Lithogeochemical data

sample	AU04240	AU04242	AU04245	AU06673	AU06680	AU06684	AU06685	AU06542	AU06544	AU06545
flag	IBH	IBH	IBH	IBH	IBH	IBH	IBH	IBN	IBN	IBN
SiO_2	68.10	69.29	87.05	57.26	56.49	20.49	65.34	69.65	73.03	55.60
Al_2O_3	0.07	0.04	0.24	0.59	0.82	0.61	1.59	0.16	0.30	0.09
Fe_2O_3	27.37	24.72	12.20	41.24	41.45	75.46	30.43	27.09	22.99	37.32
CaO	1.59	1.49	0.03	0.14	0.43	0.30	0.54	0.21	0.49	1.80
MgO	2.67	3.91	0.18	0.29	0.30	2.45	1.75	2.59	2.22	3.37
Na_2O	0.01	0.01	0.05	0.04	0.17	0.01	0.01	0.01	0.01	0.01
K_2O	0.01	0.01	0.02	0.06	0.04	0.09	0.01	0.08	0.04	0.01
TiO_2	0.01	0.01	0.01	0.02	0.02	0.02	0.06	0.01	0.01	0.01
MnO	0.06	0.41	0.17	0.08	0.05	0.40	0.10	0.05	0.85	1.69
P_2O_5	0.12	0.11	0.04	0.27	0.23	0.17	0.18	0.12	0.06	0.10
TIC	3.57	0.47	0.06	0.05	0.06	0.05	2.48	0.11	0.06	0.24
S	0.56	0.17	0.21	0.14	0.11	20.60	1.05	0.41	0.20	0.11
LOI	11.08	1.26	2.14	3.75	0.06	19.49	10.15	1.24	0.37	0.01
V*	56.3	50.9	30.8	23.0	32.0	31.2	43.9	15.2	15.1	15.1
Cr*	111.4	295.4	126.7	130.3	175.3	87.3	172.9	137.1	267.3	135.5
Co*	5.6	10.2	2.7	8.8	5.0	25.0	15.7	5.1	5.0	5.0
Ni*	2.8	56.0	2.6	26.1	45.1	56.1	39.0	20.3	40.3	25.1
Cu*	56.3	2.5	2.6	344.0	50.1	243.3	334.6	5.1	45.4	30.1
Zn*	185.9	2.5	57.5	78.2	20.0	143.5	524.2	2.5	2.5	2.5
Ga^3	1.5	1.8	1.1	3.3	2.8	ND	5.1	1.4	ND	2.6
Ge^3	6.22	6.55	5.17	6.89	14.52	ND	3.11	1.92	ND	1.38
As^3	14.9	2.5	8.0	14.3	2.5	ND	52.2	15.5	ND	2.5
Mo^3	1.1	1.0	1.0	1.0	1.0	ND	1.1	1.0	ND	1.0
Ag^2	0.1	0.1	0.1	0.5	0.4	1.9	1.0	0.1	0.1	0.2
In^3	0.056	0.051	0.051	0.052	0.050	ND	0.146	0.051	ND	0.050
Sn^3	0.6	0.5	0.5	0.5	1.2	ND	0.6	0.5	ND	0.5
Sb^3	0.113	0.245	0.103	0.528	1.592	ND	1.031	0.587	ND	0.374
W^3	0.3	0.3	0.3	1.7	1.4	ND	1.7	0.9	ND	1.0
Au^2	7.9	7.1	17.5	7.3	1.0	183.4	23.4	1.0	1.0	1.0
Tl^3	0.028	0.025	0.026	0.026	0.025	ND	0.028	0.025	ND	0.025
Pb^2	1.1	1.0	1.0	1.0	8.0	143.5	7.8	1.0	1.0	1.0
Bi^3	0.06	0.05	0.05	0.15	0.12	ND	0.13	0.13	ND	0.14
Be	2.8	2.5	2.6	2.6	2.5	3.1	2.8	2.5	2.5	2.5
Rb^2	0.6	0.5	0.5	4.5	4.6	ND	1.7	3.7	ND	4.7
Sr*	56.3	8.5	5.1	10.4	30.0	12.5	22.3	20.3	20.2	30.1
Cs^3	0.1	0.1	0.1	0.2	0.3	ND	0.2	0.2	ND	0.4
Ba*	4.4	22.0	17.7	165.8	38.7	74.9	11.2	4.2	30.3	12.2
Sc	2.8	2.5	2.6	2.6	2.5	3.1	2.8	2.5	2.5	2.5
Y*	4.8	4.0	4.0	6.0	6.7	3.1	7.4	6.2	2.5	4.4
Zr*	6.3	5.1	4.6	8.4	7.1	37.4	14.8	6.1	20.2	6.9
Nb*	0.1	0.1	0.1	0.1	0.2	6.2	0.5	0.1	5.0	0.1
Hf^3	0.16	0.05	0.05	0.19	0.20	ND	0.40	0.11	ND	0.21
Ta^3	0.02	0.01	0.01	0.02	0.03	ND	0.05	0.01	ND	0.01
Th^3	0.2	0.1	0.1	0.3	0.3	ND	0.6	0.3	ND	0.4
U^3	0.1	0.0	0.0	0.1	0.2	ND	0.2	0.2	ND	0.1
La^3	1.9	2.1	2.1	3.1	7.8	ND	6.1	1.9	ND	1.0
Ce^3	3.3	4.0	3.5	6.4	14.7	ND	13.4	3.6	ND	1.6
Pr^3	0.4	0.5	0.4	0.7	1.5	ND	1.5	0.4	ND	0.2
Nd^3	1.664	1.996	1.555	2.890	6.293	ND	6.143	2.099	ND	0.799
Sm^3	0.342	0.413	0.307	0.656	1.284	ND	1.358	0.566	ND	0.214
Eu^3	0.384	0.321	0.272	0.750	0.956	ND	0.917	0.588	ND	0.187
Gd^3	0.406	0.465	0.321	0.729	1.157	ND	1.256	0.750	ND	0.292
Tb^3	0.082	0.086	0.055	0.121	0.178	ND	0.198	0.127	ND	0.060
Dy^3	0.550	0.548	0.381	0.764	1.037	ND	1.198	0.767	ND	0.396
Ho^3	0.124	0.114	0.093	0.172	0.202	ND	0.252	0.163	ND	0.102
Er^3	0.422	0.366	0.313	0.512	0.581	ND	0.748	0.480	ND	0.354
Tm^3	0.062	0.053	0.047	0.071	0.077	ND	0.101	0.069	ND	0.055
Yb^3	0.392	0.345	0.304	0.533	0.548	ND	0.684	0.446	ND	0.341
Lu^3	0.055	0.054	0.049	0.083	0.080	ND	0.106	0.066	ND	0.060
UTM E	412292	410867	412925	415784	417093	419150	419150	412600	426175	428283
UTM N	5271327	5270771	5271486	5271121	5270699	5269575	5269570	5334210	5335790	5336075

Appendix 4.1: Lithogeochemical data

sample	AU06547	AU06550	AU06747	AU06748	AU06750	AU06503	AU06709	AU06535	AU06669	AU06671
flag	IBN	IBN	IBN	IBN	IBN	IBS	IBS	IBT	IBT	IBT
SiO_2	64.76	75.19	36.51	50.43	45.25	82.46	82.40	44.08	75.33	50.59
Al_2O_3	0.12	0.14	0.01	0.01	0.01	0.22	0.14	1.99	0.28	0.64
Fe_2O_3	29.31	19.34	62.34	45.17	48.32	12.69	14.85	51.30	19.94	41.85
CaO	1.46	2.02	0.31	1.09	1.53	3.31	0.36	0.44	1.92	4.51
MgO	2.83	2.53	0.43	2.95	4.49	1.01	1.85	1.54	1.92	2.01
Na_2O	0.01	0.01	0.03	0.06	0.08	0.04	0.01	0.01	0.02	0.01
K_2O	0.01	0.01	0.11	0.05	0.06	0.07	0.09	0.13	0.02	0.01
TiO_2	0.01	0.01	0.01	0.01	0.01	0.01	0.01	0.08	0.01	0.02
MnO	1.42	0.65	0.04	0.05	0.11	0.13	0.24	0.10	0.41	0.08
P_2O_5	0.08	0.08	0.22	0.18	0.14	0.05	0.05	0.32	0.14	0.27
TIC	0.03	0.04	0.02	5.33	8.55	0.59	0.05	0.43	0.05	4.53
S	0.08	1.69	0.13	0.24	0.04	1.43	0.33	2.76	1.99	0.23
LOI	0.01	1.83	0.01	16.32	20.79	2.76	2.47	3.37	0.63	11.25
V*	15.1	5.1	44.6	60.0	63.2	36.1	25.7	26.0	20.2	29.2
Cr*	185.7	265.4	87.4	162.0	164.4	299.5	215.7	124.6	232.4	214.6
Co*	2.5	5.1	3.5	6.0	3.2	5.2	15.4	15.6	2.5	2.8
Ni*	15.1	25.5	14.9	18.0	12.6	15.5	41.1	26.0	25.3	33.9
Cu*	15.1	97.0	129.0	102.0	82.2	2.6	113.0	207.6	106.1	33.9
Zn*	2.5	25.5	34.7	78.0	69.6	2.6	82.2	26.0	2.5	2.8
Ga[3]	ND	ND	1.9	ND	ND	1.8	ND	ND	ND	ND
Ge[5]	ND	ND	5.61	ND	ND	0.26	ND	ND	ND	ND
As[3]	ND	ND	2.5	ND	ND	2.6	ND	ND	ND	ND
Mo[5]	ND	ND	1.0	ND	ND	2.9	ND	ND	ND	ND
Ag[2]	0.1	0.3	0.1	0.1	0.1	0.9	0.2	0.4	0.4	0.2
In[3]	ND	ND	0.050	ND	ND	0.052	ND	ND	ND	ND
Sn[3]	ND	ND	0.5	ND	ND	0.5	ND	ND	ND	ND
Sb[3]	ND	ND	0.099	ND	ND	0.411	ND	ND	ND	ND
W[2]	ND	ND	0.6	ND	ND	3.1	ND	ND	ND	ND
Au[2]	1.0	1.0	20.8	1.2	8.9	10.3	7.2	1.0	1.0	1.1
Tl[3]	ND	ND	0.025	ND	ND	0.026	ND	ND	ND	ND
Pb[2]	1.0	1.0	1.0	1.2	1.3	3.1	1.0	1.0	1.0	1.1
Bi[3]	ND	ND	0.10	ND	ND	0.11	ND	ND	ND	ND
Be	2.5	2.6	2.5	3.0	3.2	2.6	2.6	2.6	2.5	2.8
Rb[3]	ND	ND	3.2	ND	ND	3.4	ND	ND	ND	ND
Sr*	10.0	20.4	69.4	96.0	88.5	16.7	71.9	20.8	20.2	90.4
Cs[3]	ND	ND	0.2	ND	ND	0.3	ND	ND	ND	ND
Ba*	10.0	10.2	6.4	12.0	12.6	5.8	10.3	10.4	10.1	22.6
Sc	2.5	2.6	2.5	3.0	3.2	2.6	2.6	2.6	2.5	2.8
Y*	2.5	2.6	6.0	3.0	3.2	5.1	2.6	5.2	5.1	2.8
Zr*	10.0	10.2	5.7	24.0	25.3	7.7	10.3	41.5	10.1	22.6
Nb*	5.0	5.1	0.1	6.0	6.3	0.1	5.1	5.2	5.1	5.6
Hf[3]	ND	ND	0.10	ND	ND	0.17	ND	ND	ND	ND
Ta[3]	ND	ND	0.00	ND	ND	0.01	ND	ND	ND	ND
Th[3]	ND	ND	0.1	ND	ND	0.2	ND	ND	ND	ND
U[3]	ND	ND	0.1	ND	ND	0.2	ND	ND	ND	ND
La[3]	ND	ND	4.3	ND	ND	2.2	ND	ND	ND	ND
Ce[3]	ND	ND	8.5	ND	ND	5.2	ND	ND	ND	ND
Pr[2]	ND	ND	0.8	ND	ND	0.6	ND	ND	ND	ND
Nd[3]	ND	ND	3.455	ND	ND	2.687	ND	ND	ND	ND
Sm[3]	ND	ND	0.652	ND	ND	0.684	ND	ND	ND	ND
Eu[3]	ND	ND	0.377	ND	ND	0.545	ND	ND	ND	ND
Gd[3]	ND	ND	0.628	ND	ND	0.794	ND	ND	ND	ND
Tb[3]	ND	ND	0.101	ND	ND	0.139	ND	ND	ND	ND
Dy[3]	ND	ND	0.676	ND	ND	0.790	ND	ND	ND	ND
Ho[3]	ND	ND	0.155	ND	ND	0.162	ND	ND	ND	ND
Er[3]	ND	ND	0.523	ND	ND	0.488	ND	ND	ND	ND
Tm[3]	ND	ND	0.079	ND	ND	0.065	ND	ND	ND	ND
Yb[3]	ND	ND	0.562	ND	ND	0.423	ND	ND	ND	ND
Lu[3]	ND	ND	0.088	ND	ND	0.063	ND	ND	ND	ND
UTM E	429423	431750	401780	404166	407070	371200	374495	383242	352502	377415
UTM N	5335940	5337083	5333620	5333753	5333760	5285560	5285600	5288732	5278888	5291475

Appendix 4.1: Lithogeochemical data

sample	AU06672	AU06687	AU06690	AU06691	AU06704	AU06705	AU06710	AU06736	AU06737	AU06740
flag	IBT	IBT	IBT	IBT	IBT	IBT	IBT	IBT	IBT	IBT
SiO_2	53.02	64.33	71.05	66.24	59.79	69.83	57.13	55.61	74.56	70.35
Al_2O_3	0.65	0.17	0.76	0.16	0.01	0.01	1.09	0.35	0.01	0.19
Fe_2O_3	41.45	31.38	19.32	19.95	38.09	28.13	35.80	39.86	23.00	24.54
CaO	2.05	1.05	6.16	8.72	1.49	0.15	4.76	2.65	0.35	1.66
MgO	2.29	2.09	2.16	4.12	0.36	1.61	0.88	0.88	1.26	1.84
Na_2O	0.01	0.01	0.01	0.02	0.01	0.01	0.01	0.13	0.10	0.11
K_2O	0.01	0.01	0.02	0.03	0.08	0.14	0.12	0.12	0.16	0.08
TiO_2	0.02	0.01	0.02	0.01	0.01	0.01	0.03	0.02	0.01	0.02
MnO	0.23	0.74	0.42	0.61	0.07	0.05	0.13	0.19	0.43	1.10
P_2O_5	0.28	0.21	0.09	0.11	0.09	0.05	0.05	0.19	0.11	0.11
TIC	5.10	4.44	1.40	5.14	0.35	0.02	2.91	0.02	0.04	2.24
S	3.88	0.06	2.36	0.51	0.12	0.18	1.13	0.28	0.01	0.50
LOI	16.42	13.19	5.78	11.41	0.38	0.40	6.00	0.01	0.47	7.15
V*	36.0	17.3	21.3	11.3	55.3	35.3	48.1	70.0	30.2	54.0
Cr*	197.8	201.8	234.4	186.4	221.0	141.1	224.3	149.9	131.0	275.6
Co*	3.0	2.9	21.3	2.8	30.1	10.1	26.7	5.0	2.5	2.7
Ni*	18.0	28.8	42.6	22.6	35.2	20.2	42.7	10.0	25.2	21.6
Cu*	125.9	51.9	1395.8	56.5	2.5	40.3	170.9	104.9	125.9	145.9
Zn*	113.9	161.4	175.8	2.8	20.1	146.1	240.3	70.0	45.3	108.1
Ga^3	ND	ND	ND	1.5	3.9	1.1	4.3	2.9	ND	2.7
Ge^3	ND	ND	ND	0.28	7.28	2.59	0.27	5.77	ND	0.27
As^3	ND	ND	ND	2.8	33.3	2.5	7.2	2.5	1.9	22.1
Mo^3	ND	ND	ND	1.1	2.7	1.0	2.6	2.3	ND	1.1
Ag^2	0.5	0.3	1.1	0.5	0.1	0.1	0.1	0.2	0.1	0.1
In^3	ND	ND	ND	0.056	0.050	0.050	0.053	0.050	ND	0.054
Sn^3	ND	ND	ND	0.6	1.8	0.5	0.5	0.5	ND	0.5
Sb^3	ND	ND	ND	2.480	1.562	0.326	0.583	0.577	ND	1.108
W^3	ND	ND	ND	0.6	1.8	0.6	2.4	1.2	ND	1.4
Au^2	1.2	16.1	1.1	1.1	3.0	10.1	1.1	10.0	10.1	3.2
Tl^3	ND	ND	ND	0.028	0.025	0.025	0.027	0.025	ND	0.027
Pb^2	7.2	1.2	25.6	4.5	1.0	1.0	1.1	1.0	1.0	1.1
Bi^3	ND	ND	ND	0.12	0.11	0.05	0.05	0.10	ND	0.05
Be	3.0	2.9	2.7	2.8	5.0	2.5	2.7	2.5	2.5	2.7
Rb^3	ND	ND	ND	1.4	7.5	1.2	1.5	4.8	ND	5.0
Sr*	24.0	11.5	32.0	45.2	50.2	60.5	117.5	70.0	ND	118.9
Cs^3	ND	ND	ND	0.1	1.6	0.1	0.1	3.3	ND	0.1
Ba*	12.0	23.1	10.7	3.4	15.3	4.4	5.9	15.0	10.1	9.7
Sc	3.0	2.9	2.7	2.8	2.5	2.5	2.7	2.5		2.7
Y*	6.0	5.8	5.3	2.6	5.7	3.6	4.0	5.2	2.5	4.5
Zr*	24.0	23.1	21.3	6.3	5.6	5.1	14.8	8.6	10.1	6.7
Nb*	6.0	5.8	5.3	0.1	1.8	0.1	0.4	0.2	ND	0.1
Hf^2	ND	ND	ND	0.12	0.17	0.10	0.30	0.21	ND	0.16
Ta^3	ND	ND	ND	0.01	0.02	0.01	0.03	0.02	ND	0.01
Th^3	ND	ND	ND	0.1	0.5	0.1	0.2	0.3	ND	0.2
U^3	ND	ND	ND	0.0	0.4	0.0	0.1	0.2	ND	0.1
La^3	ND	ND	ND	1.3	7.0	2.2	1.6	2.7	ND	2.5
Ce^3	ND	ND	ND	2.3	16.6	4.8	3.6	5.5	ND	4.7
Pr^3	ND	ND	ND	0.2	1.7	0.5	0.4	0.6	ND	0.5
Nd^3	ND	ND	ND	1.008	7.135	2.109	2.002	2.639	ND	2.013
Sm^3	ND	ND	ND	0.250	1.184	0.453	0.502	0.575	ND	0.432
Eu^3	ND	ND	ND	0.378	0.451	0.416	0.265	0.351	ND	0.479
Gd^3	ND	ND	ND	0.302	0.920	0.448	0.547	0.609	ND	0.444
Tb^3	ND	ND	ND	0.052	0.129	0.081	0.105	0.103	ND	0.076
Dy^3	ND	ND	ND	0.343	0.774	0.508	0.627	0.655	ND	0.537
Ho^3	ND	ND	ND	0.074	0.157	0.108	0.133	0.144	ND	0.121
Er^3	ND	ND	ND	0.232	0.456	0.350	0.436	0.432	ND	0.386
Tm^3	ND	ND	ND	0.034	0.062	0.051	0.068	0.057	ND	0.055
Yb^3	ND	ND	ND	0.239	0.406	0.347	0.437	0.394	ND	0.381
Lu^3	ND	ND	ND	0.039	0.054	0.053	0.069	0.061	ND	0.062
UTM E	377415	377665	378113	378113	387050	386190	375539	379267	379600	390130
UTM N	5291475	5283230	5282872	5282872	5287075	5281720	5291515	5288757	5289215	5284580

Appendix 4.1: Lithogeochemical data

sample	AU06741	AU06744	AU06504	AU06507	AU06509	AU06514	AU06516	AU06517	AU06519	AU06522
flag	IBT	IBT	IBW	IBW	IBW	IBW	IBW	IBW	IBW	IBW
SiO_2	69.95	56.01	45.33	19.04	13.93	6.68	23.19	69.56	8.76	55.51
Al_2O_3	0.07	0.45	0.81	0.50	0.71	0.32	0.34	0.70	1.72	0.29
Fe_2O_3	25.44	36.15	45.41	69.51	77.33	76.07	64.64	21.29	78.89	35.52
CaO	2.37	2.94	0.57	0.63	0.19	5.64	3.39	3.65	0.49	2.56
MgO	1.17	3.89	4.94	7.02	6.16	8.34	6.23	3.69	7.75	4.33
Na_2O	0.09	0.22	0.12	0.21	0.27	0.14	0.18	0.16	0.10	0.18
K_2O	0.02	0.13	0.07	0.06	0.12	0.04	0.09	0.15	0.09	0.14
TiO_2	0.01	0.03	0.05	0.02	0.04	0.01	0.03	0.02	0.08	0.01
MnO	0.75	0.26	2.57	2.85	1.09	2.59	1.78	0.62	1.87	1.33
P_2O_5	0.13	0.12	0.13	0.17	0.16	0.17	0.14	0.15	0.25	0.13
TIC	2.60	0.02	1.33	4.16	4.10	6.67	6.69	3.00	2.71	0.68
S	2.81	0.14	10.60	18.70	20.50	18.90	18.10	3.46	17.80	2.12
LOI	9.22	0.01	5.35	9.67	10.61	21.25	20.54	8.60	11.26	2.81
V*	33.2	55.2	42.5	27.7	45.0	57.2	58.3	16.5	50.8	22.6
Cr*	254.2	90.3	207.1	88.7	73.1	139.8	189.1	247.3	129.9	405.2
Co*	2.8	5.0	31.9	38.8	33.7	50.8	50.4	27.5	33.9	10.3
Ni*	22.1	75.3	74.3	85.4	106.8	95.3	107.1	44.0	107.3	31.0
Cu*	77.4	165.6	21.2	11.1	56.2	76.2	37.8	567.0	118.6	113.6
Zn*	171.3	80.3	276.1	419.1	472.1	165.2	499.2	307.7	460.0	353.2
Ga*	ND	ND	ND	ND	ND	3.4	3.2	ND	ND	2.6
Ge*	ND	ND	ND	ND	ND	0.32	0.32	ND	ND	0.79
As*	ND	ND	ND	ND	ND	3.2	18.2	ND	ND	6.7
Mo*	ND	ND	ND	ND	ND	1.3	1.3	ND	ND	4.1
Ag*	0.4	0.1	0.4	0.1	0.6	0.9	0.6	0.4	0.5	0.5
In*	ND	ND	ND	ND	ND	0.064	0.063	ND	ND	0.135
Sn*	ND	ND	ND	ND	ND	0.6	0.6	ND	ND	0.5
Sb*	ND	ND	ND	ND	ND	0.127	0.126	ND	ND	0.881
W*	ND	ND	ND	ND	ND	2.0	2.1	ND	ND	10.4
Au*	34.3	7.0	40.3	61.0	1.1	125.8	30.3	3.3	62.1	1.0
Tl*	ND	ND	ND	ND	ND	0.032	0.032	ND	ND	0.026
Pb*	1.1	1.0	1.1	37.7	1.1	6.4	6.3	1.1	1.1	96.0
Bi*	ND	ND	ND	ND	ND	0.21	0.17	ND	ND	1.41
Be	2.8	2.5	2.7	2.8	2.8	3.2	3.2	2.7	2.8	2.6
Rb*	ND	ND	ND	ND	ND	0.6	2.8	ND	ND	5.9
Sr*	132.6	110.4	10.6	11.1	5.6	25.4	37.8	33.0	11.3	31.0
Cs*	ND	ND	ND	ND	ND	0.1	0.2	ND	ND	2.0
Ba*	11.1	10.0	10.6	11.1	22.5	5.9	6.4	11.0	11.3	113.2
Sc	2.8	2.5	5.3	2.8	2.8	6.4	6.3	2.7	5.6	2.6
Y*	2.8	2.5	5.3	5.5	2.8	15.2	9.4	11.0	16.9	6.4
Zr*	11.1	20.1	31.9	44.4	45.0	13.6	14.0	22.0	79.1	9.4
Nb*	5.5	5.0	5.3	5.5	5.6	0.1	0.3	5.5	5.6	0.3
Hf*	ND	ND	ND	ND	ND	0.28	0.33	ND	ND	0.19
Ta*	ND	ND	ND	ND	ND	0.01	0.03	ND	ND	0.01
Th*	ND	ND	ND	ND	ND	0.3	0.4	ND	ND	0.2
U*	ND	ND	ND	ND	ND	0.5	0.6	ND	ND	0.3
La*	ND	ND	ND	ND	ND	5.8	4.6	ND	ND	2.7
Ce*	ND	ND	ND	ND	ND	8.6	7.5	ND	ND	7.0
Pr*	ND	ND	ND	ND	ND	0.9	0.7	ND	ND	0.5
Nd*	ND	ND	ND	ND	ND	3.859	3.087	ND	ND	2.274
Sm*	ND	ND	ND	ND	ND	0.883	0.785	ND	ND	0.529
Eu*	ND	ND	ND	ND	ND	0.698	0.494	ND	ND	0.505
Gd*	ND	ND	ND	ND	ND	1.201	0.890	ND	ND	0.623
Tb*	ND	ND	ND	ND	ND	0.229	0.170	ND	ND	0.114
Dy*	ND	ND	ND	ND	ND	1.531	1.243	ND	ND	0.680
Ho*	ND	ND	ND	ND	ND	0.361	0.281	ND	ND	0.147
Er*	ND	ND	ND	ND	ND	1.232	0.901	ND	ND	0.464
Tm*	ND	ND	ND	ND	ND	0.195	0.154	ND	ND	0.067
Yb*	ND	ND	ND	ND	ND	1.269	1.056	ND	ND	0.437
Lu*	ND	ND	ND	ND	ND	0.230	0.181	ND	ND	0.067
UTM E	390130	378956	409830	409980	410186	408565	408015	408015	410470	398528
UTM N	5284580	5289200	5298432	5298487	5298460	5298227	5297925	5297925	5296576	5293083

Appendix 4.1: Lithogeochemical data

sample	AU06523	AU06524	AU06526	AU06527	AU06528	AU06529	AU06532	AU06533	AU06534	AU06715
flag	IBW	IBW	IBW	IBW	IBW	IBW	IBW	IBW	IBW	IBW
SiO_2	52.09	51.63	70.38	74.02	71.65	54.96	66.66	46.95	60.36	64.24
Al_2O_3	2.48	0.17	0.16	0.20	0.24	0.38	0.20	0.20	0.14	0.01
Fe_2O_3	38.29	39.22	21.92	24.26	23.23	35.21	29.08	44.10	32.36	31.16
CaO	0.38	2.42	3.09	0.11	0.75	4.17	0.92	2.89	2.05	0.54
MgO	4.60	5.42	3.73	0.93	3.02	3.99	1.97	3.82	3.32	3.27
Na_2O	0.09	0.08	0.01	0.01	0.04	0.01	0.01	0.01	0.04	0.01
K_2O	0.54	0.16	0.03	0.01	0.05	0.07	0.02	0.01	0.06	0.03
TiO_2	0.07	0.01	0.01	0.01	0.02	0.02	0.01	0.01	0.01	0.01
MnO	1.31	0.77	0.60	0.39	0.94	1.07	1.04	1.90	1.55	0.68
P_2O_5	0.13	0.12	0.07	0.06	0.06	0.10	0.06	0.11	0.09	0.05
TIC	0.48	1.03	1.20	0.90	0.63	4.25	2.22	6.20	4.67	0.02
S	4.83	3.96	1.83	9.89	2.42	2.76	6.89	3.86	2.82	0.18
LOI	6.19	5.22	4.44	9.78	3.76	13.62	11.14	18.57	14.90	0.82
V*	42.7	21.2	31.5	11.1	15.6	29.1	28.2	37.0	29.4	45.4
Cr*	261.8	253.9	336.3	510.7	359.6	166.6	315.7	185.0	294.3	80.8
Co*	10.7	5.3	5.3	22.2	5.2	5.8	11.3	12.3	5.9	10.1
Ni*	42.7	26.4	31.5	61.1	31.3	40.7	50.7	37.0	35.3	20.2
Cu*	149.6	42.3	189.2	161.0	140.7	104.6	67.7	67.6	70.6	50.5
Zn*	154.9	2.6	157.7	5.6	2.6	139.5	2.8	3.1	2.9	141.3
Ga*	ND	ND	ND	ND	ND	ND	ND	ND	ND	ND
Ge*	ND	ND	ND	ND	ND	ND	ND	ND	ND	ND
As*	ND	ND	ND	ND	ND	ND	ND	ND	ND	ND
Mo*	ND	ND	ND	ND	ND	ND	ND	ND	ND	ND
Ag*	1.0	0.5	1.1	0.7	0.5	0.6	0.8	0.6	0.6	0.1
In*	ND	ND	ND	ND	ND	ND	ND	ND	ND	ND
Sn*	ND	ND	ND	ND	ND	ND	ND	ND	ND	ND
Sb*	ND	ND	ND	ND	ND	ND	ND	ND	ND	ND
W*	ND	ND	ND	ND	ND	ND	ND	ND	ND	ND
Au*	28.8	32.8	35.7	53.3	7.3	1.2	343.9	55.5	153.0	128.2
Tl*	ND	ND	ND	ND	ND	ND	ND	ND	ND	ND
Pb*	27.8	11.6	22.1	21.1	8.3	8.1	11.3	7.4	2.4	1.0
Bi*	ND	ND	ND	ND	ND	ND	ND	ND	ND	ND
Be	2.7	2.6	2.6	2.8	2.6	2.9	2.8	3.1	2.9	2.5
Rb*	ND	ND	ND	ND	ND	ND	ND	ND	ND	ND
Sr*	10.7	31.7	84.1	22.2	62.5	93.0	33.8	74.0	82.4	70.7
Cs*	ND	ND	ND	ND	ND	ND	ND	ND	ND	ND
Ba*	21.4	31.7	21.0	11.1	41.7	34.9	11.3	12.3	11.8	10.1
Sc	2.7	2.6	2.6	2.8	2.6	2.9	2.8	3.1	2.9	2.5
Y*	5.3	2.6	5.3	5.6	5.2	5.8	5.6	12.3	11.8	2.5
Zr*	32.1	21.2	10.5	11.1	10.4	23.3	11.3	24.7	11.8	10.1
Nb*	5.3	5.3	5.3	5.6	5.2	5.8	5.6	6.2	5.9	5.0
Hf*	ND	ND	ND	ND	ND	ND	ND	ND	ND	ND
Ta*	ND	ND	ND	ND	ND	ND	ND	ND	ND	ND
Th*	ND	ND	ND	ND	ND	ND	ND	ND	ND	ND
U*	ND	ND	ND	ND	ND	ND	ND	ND	ND	ND
La*	ND	ND	ND	ND	ND	ND	ND	ND	ND	ND
Ce*	ND	ND	ND	ND	ND	ND	ND	ND	ND	ND
Pr*	ND	ND	ND	ND	ND	ND	ND	ND	ND	ND
Nd*	ND	ND	ND	ND	ND	ND	ND	ND	ND	ND
Sm*	ND	ND	ND	ND	ND	ND	ND	ND	ND	ND
Eu*	ND	ND	ND	ND	ND	ND	ND	ND	ND	ND
Gd*	ND	ND	ND	ND	ND	ND	ND	ND	ND	ND
Tb*	ND	ND	ND	ND	ND	ND	ND	ND	ND	ND
Dy*	ND	ND	ND	ND	ND	ND	ND	ND	ND	ND
Ho*	ND	ND	ND	ND	ND	ND	ND	ND	ND	ND
Er*	ND	ND	ND	ND	ND	ND	ND	ND	ND	ND
Tm*	ND	ND	ND	ND	ND	ND	ND	ND	ND	ND
Yb*	ND	ND	ND	ND	ND	ND	ND	ND	ND	ND
Lu*	ND	ND	ND	ND	ND	ND	ND	ND	ND	ND
UTM E	398766	398737	398822	399140	399140	400953	399631	399502	399502	398220
UTM N	5293301	5293330	5293722	5294206	5294173	5294070	5294101	5294122	5294131	5291822

Appendix 4.1: Lithogeochemical data

sample	AU06717	AU06718	AU06719	AU06731	AU06732	AU06733	AU06745	8470	8481	AU04221
flag	IBW	IBW	IBW	IBW	IBW	IBW	IBW	ISH	ISH	ISH
SiO_2	41.65	73.11	70.03	88.44	90.27	68.27	16.06	52.48	72.83	51.91
Al_2O_3	0.01	0.01	0.70	0.39	0.03	0.01	0.01	3.19	6.44	13.90
Fe_2O_3	51.33	23.26	25.14	10.12	9.28	29.74	75.45	37.68	13.41	22.87
CaO	1.25	0.31	1.84	0.26	0.03	0.37	0.51	2.21	1.61	3.42
MgO	4.31	2.35	0.89	0.21	0.03	0.89	4.58	3.53	2.90	3.01
Na_2O	0.01	0.16	0.12	0.19	0.18	0.14	0.09	0.06	1.90	2.27
K_2O	0.01	0.08	0.81	0.20	0.11	0.14	0.05	0.32	0.27	0.70
TiO_2	0.01	0.01	0.05	0.01	0.01	0.01	0.01	0.11	0.43	1.04
MnO	1.36	0.64	0.32	0.12	0.03	0.32	3.13	0.18	0.13	0.76
P_2O_5	0.05	0.07	0.11	0.05	0.03	0.13	0.09	0.24	0.08	0.11
TIC	0.18	0.08	0.43	0.06	0.01	0.53	0.77	0.37	0.31	2.04
S	0.13	0.18	11.60	1.56	0.32	1.24	25.50	0.48	4.06	0.16
LOI	1.14	0.51	10.78	1.80	0.63	3.86	17.75	2.24	4.62	1.71
V*	76.1	25.2	56.3	35.7	30.2	62.7	110.0	82.0	136.9	173.6
Cr*	20.3	272.5	315.2	464.7	528.8	298.0	85.5	51.1	315.9	68.8
Co*	10.2	2.5	11.3	2.6	2.5	2.6	42.8	10.2	36.8	30.6
Ni*	15.2	15.1	16.9	35.7	20.1	15.7	97.8	22.5	64.2	15.3
Cu*	2.5	60.7	202.7	188.9	141.0	130.7	126.3	30.7	184.2	20.4
Zn*	137.1	60.5	90.1	148.1	85.6	449.6	305.5	2.6	352.7	108.3
Ga[2]	1.4	ND	ND	ND	1.4	2.2	3.8	7.7	7.8	20.0
Ge[3]	0.25	ND	ND	ND	0.25	2.37	0.31	4.16	1.57	1.71
As[3]	2.5	ND	ND	ND	16.3	20.7	3.1	2.6	2.6	2.6
Mo[3]	1.0	ND	ND	ND	4.0	4.6	1.2	1.0	1.1	2.5
Ag[2]	0.1	0.1	3.3	0.5	0.2	0.2	0.2	0.2	0.4	0.1
In[3]	0.051	ND	ND	ND	0.050	0.052	0.061	0.103	0.053	0.051
Sn[3]	0.5	ND	ND	ND	0.5	0.5	0.6	2.7	0.5	1.8
Sb[3]	0.102	ND	ND	ND	0.523	1.222	0.122	0.879	0.105	0.102
W[3]	0.7	ND	ND	ND	3.7	13.4	3.0	0.7	0.8	0.5
Au[2]	177.7	21.2	1548.1	176.7	3.0	286.5	29.3	76.9	22.1	31.7
Tl[3]	0.025	ND	ND	ND	0.025	0.026	0.031	0.026	0.026	0.026
Pb[2]	1.0	1.0	10.1	94.0	10.1	32.4	1.2	22.5	47.4	1.0
Bi[3]	0.05	ND	ND	ND	0.15	0.05	0.16	0.05	0.05	0.28
Be	2.5	2.5	2.8	2.6	2.5	2.6	3.1	2.6	2.6	5.1
Rb[3]	6.6	ND	ND	ND	1.3	4.4	5.0	0.5	0.5	9.3
Sr*	60.9	60.7	90.1	91.9	100.7	115.0	134.4	30.7	84.2	367.7
Cs[3]	1.1	ND	ND	ND	0.1	0.2	0.1	2.2	0.1	0.1
Ba*	15.8	20.2	45.0	40.9	4.7	11.0	10.4	45.2	109.4	259.7
Sc	2.5	2.5	2.8	2.6	2.5	2.6	3.1	2.6	15.8	15.3
Y*	8.2	2.5	2.8	2.6	1.9	6.4	9.5	9.3	8.0	32.2
Zr*	5.1	10.1	11.3	10.2	7.7	3.7	9.7	27.8	39.6	165.0
Nb*	0.1	5.0	5.6	5.1	0.1	0.1	0.1	0.4	0.5	6.9
Hf[3]	0.12	ND	ND	ND	0.16	0.05	0.20	0.90	1.09	5.37
Ta[2]	0.01	ND	ND	ND	0.01	0.01	0.01	0.09	0.17	0.70
Th[3]	0.1	ND	ND	ND	0.2	0.2	0.1	0.8	0.6	3.8
U[3]	0.1	ND	ND	ND	0.0	0.1	0.2	0.2	0.2	0.8
La[3]	2.6	ND	ND	ND	1.2	3.4	1.6	8.2	4.2	19.8
Ce[3]	5.7	ND	ND	ND	2.5	6.7	2.6	15.8	9.5	42.9
Pr[3]	0.6	ND	ND	ND	0.3	0.7	0.3	1.8	1.2	5.1
Nd[3]	3.000	ND	ND	ND	1.016	3.208	1.228	6.924	5.131	20.369
Sm[3]	0.807	ND	ND	ND	0.214	0.798	0.346	1.371	1.259	4.545
Eu[3]	0.704	ND	ND	ND	0.173	0.816	0.228	0.927	0.445	1.172
Gd[3]	0.936	ND	ND	ND	0.234	0.885	0.559	1.243	1.201	4.429
Tb[3]	0.171	ND	ND	ND	0.038	0.151	0.143	0.215	0.229	0.840
Dy[3]	1.056	ND	ND	ND	0.231	0.880	1.064	1.337	1.408	5.287
Ho[3]	0.233	ND	ND	ND	0.051	0.188	0.270	0.288	0.286	1.131
Er[3]	0.729	ND	ND	ND	0.166	0.556	0.908	0.907	0.883	3.708
Tm[3]	0.104	ND	ND	ND	0.023	0.076	0.150	0.126	0.133	0.610
Yb[3]	0.684	ND	ND	ND	0.157	0.470	1.006	0.832	0.850	3.897
Lu[3]	0.104	ND	ND	ND	0.027	0.069	0.177	0.128	0.122	0.581
UTM E	397650	397948	398180	395612	395510	395700	410170	410563	410401	410959
UTM N	5291950	5292380	5292954	5290828	5290925	5290550	5298640	5270720	5270775	5270696

Appendix 4.1: Lithogeochemical data

sample	AU04238	AU06679	AU06683	AU06703	AU06725	AU06727	AU06543	AU06549	AU06502	AU06521
flag	ISH	ISH	ISH	ISH	ISH	ISH	ISN	ISN	ISS	ISS
SiO_2	51.37	82.21	59.24	28.49	89.36	89.75	51.06	36.23	65.99	65.89
Al_2O_3	12.05	1.48	4.51	1.13	2.08	0.29	12.91	8.13	2.89	5.34
Fe_2O_3	32.10	14.86	33.80	68.97	6.56	3.20	24.73	49.02	24.67	23.00
CaO	0.12	0.10	0.11	0.11	0.35	5.70	4.97	1.33	2.48	2.22
MgO	3.52	1.00	0.95	0.87	0.95	0.70	2.35	2.26	2.62	2.12
Na_2O	0.01	0.01	0.17	0.01	0.23	0.19	1.54	0.04	0.02	0.16
K_2O	0.09	0.01	0.78	0.12	0.18	0.05	0.61	1.92	0.07	0.79
TiO_2	0.44	0.05	0.29	0.16	0.07	0.01	0.43	0.45	0.09	0.14
MnO	0.03	0.18	0.06	0.07	0.04	0.09	1.19	0.31	0.90	0.17
P_2O_5	0.27	0.09	0.10	0.05	0.18	0.02	0.22	0.30	0.07	0.18
TIC	ND	0.66	0.02	0.01	0.26	1.11	0.07	0.01	0.60	0.66
S	0.18	1.74	19.60	34.80	3.55	0.25	2.75	0.77	1.84	6.27
LOI	9.25	4.47	16.50	26.38	3.36	2.34	2.48	10.45	2.96	6.20
V*	155.1	15.7	60.3	102.5	26.2	10.3	87.3	118.0	31.0	38.9
Cr*	51.8	199.5	283.3	239.1	374.6	350.3	159.8	191.0	154.8	183.2
Co*	22.2	21.0	114.5	61.5	16.8	2.6	17.4	5.6	10.3	44.4
Ni*	16.6	31.5	108.5	82.0	39.1	30.9	98.0	33.7	15.5	72.2
Cu*	2.8	189.0	444.9	321.1	2806.4	231.8	98.0	174.1	2.6	589.7
Zn*	2.8	503.9	577.5	82.0	50648.5	1050.9	2.6	390.9	2.6	17879.0
Ga^3	25.6	ND	ND	ND	3.4	ND	16.4	18.8	ND	ND
Ge^3	10.27	ND	ND	ND	0.28	ND	0.26	1.32	ND	ND
As^3	123.0	ND	ND	ND	6.7	ND	2.6	2.8	ND	ND
Mo^3	4.6	ND	ND	ND	2.6	ND	1.0	1.1	ND	ND
Ag^2	0.1	0.4	2.4	2.6	4.1	0.2	0.6	0.4	0.3	5.8
In^3	0.280	ND	ND	ND	0.056	ND	0.052	0.056	ND	ND
Sn^3	3.7	ND	ND	ND	0.6	ND	0.5	0.6	ND	ND
Sb^3	0.263	ND	ND	ND	0.056	ND	0.103	0.601	ND	ND
W^3	0.8	ND	ND	ND	1.0	ND	1.9	0.3	ND	ND
Au^2	1.1	3.1	41.0	154.4	7.8	10.3	7.2	165.1	27.9	30.0
Tl^3	0.028	ND	ND	ND	0.031	ND	0.176	0.028	ND	ND
Pb^2	ND	1.0	130.2	266.5	17330.1	323.5	1.0	1.1	1.0	3842.3
Bi^3	0.06	ND	ND	ND	0.06	ND	0.11	0.06	ND	ND
Be	5.5	2.6	3.0	3.4	2.8	2.6	2.6	5.6	2.6	2.8
Rb^3	0.6	ND	ND	ND	3.1	ND	20.8	35.3	ND	ND
Sr*	15.5	21.0	36.2	54.7	111.8	123.6	381.6	150.5	10.3	22.2
Cs^3	0.1	ND	ND	ND	0.1	ND	2.5	0.1	ND	ND
Ba*	14.5	5.2	132.6	41.0	26.9	5.2	123.2	386.8	10.3	33.3
Sc	10.0	2.6	12.1	3.4	2.8	2.6	5.2	11.2	2.6	5.6
Y*	24.4	5.2	6.0	3.4	2.7	2.6	11.2	27.5	5.2	11.1
Zr*	122.5	21.0	72.3	82.0	22.5	10.3	70.0	174.9	31.0	55.5
Nb*	4.9	5.2	6.0	6.8	0.5	5.2	3.5	10.9	5.2	5.6
Hf^3	3.92	ND	ND	ND	0.48	ND	2.42	5.35	ND	ND
Ta^3	0.55	ND	ND	ND	0.06	ND	0.28	1.00	ND	ND
Th^3	4.2	ND	ND	ND	0.6	ND	1.6	8.9	ND	ND
U^3	1.0	ND	ND	ND	0.2	ND	0.5	1.1	ND	ND
La^3	15.9	ND	ND	ND	4.2	ND	13.0	70.6	ND	ND
Ce^3	33.5	ND	ND	ND	9.4	ND	28.4	152.4	ND	ND
Pr^3	4.0	ND	ND	ND	1.0	ND	3.0	17.6	ND	ND
Nd^3	16.314	ND	ND	ND	4.180	ND	12.955	65.194	ND	ND
Sm^3	3.577	ND	ND	ND	0.769	ND	2.553	9.771	ND	ND
Eu^3	2.130	ND	ND	ND	0.305	ND	0.967	2.035	ND	ND
Gd^3	3.143	ND	ND	ND	0.582	ND	2.192	6.966	ND	ND
Tb^3	0.604	ND	ND	ND	0.091	ND	0.327	0.971	ND	ND
Dy^3	3.884	ND	ND	ND	0.509	ND	1.753	4.978	ND	ND
Ho^3	0.824	ND	ND	ND	0.097	ND	0.345	0.941	ND	ND
Er^3	2.567	ND	ND	ND	0.295	ND	0.975	2.813	ND	ND
Tm^3	0.370	ND	ND	ND	0.047	ND	0.129	0.415	ND	ND
Yb^3	2.377	ND	ND	ND	0.338	ND	0.809	2.667	ND	ND
Lu^3	0.358	ND	ND	ND	0.053	ND	0.112	0.369	ND	ND
UTM E	412143	416558	413800	419150	410572	410572	425320	429640	371400	372950
UTM N	5271338	5270993	5271450	5269570	5270770	5270772	5335690	5336065	5285180	5287314

Appendix 4.1: Lithogeochemical data

sample	AU06699	AU06536	AU06537	AU06538	AU06539	AU06540	AU06670	AU06735	AU06743	AU06505
flag	ISS	IST	IST	IST	IST	IST	IST	IST	IST	ISW
SiO_2	97.32	56.49	48.74	64.29	58.35	45.75	55.89	45.24	44.11	62.39
Al_2O_3	0.34	4.71	5.92	1.87	3.48	3.05	13.28	2.08	2.05	1.84
Fe_2O_3	1.30	30.14	37.88	28.47	31.05	46.32	17.46	42.44	40.84	31.49
CaO	0.77	3.84	1.57	3.06	3.33	0.90	7.08	4.72	6.06	0.90
MgO	0.15	2.91	4.88	1.81	2.24	2.90	2.16	3.52	5.34	2.39
Na_2O	0.01	0.15	0.09	0.01	0.01	0.24	1.95	0.32	0.22	0.15
K_2O	0.02	1.23	0.40	0.06	1.00	0.33	0.85	0.18	0.87	0.14
TiO_2	0.01	0.18	0.21	0.09	0.18	0.15	0.29	0.11	0.12	0.07
MnO	0.03	0.12	0.13	0.20	0.17	0.12	0.91	1.30	0.24	0.49
P_2O_5	0.05	0.23	0.19	0.16	0.20	0.25	0.12	0.09	0.15	0.12
TIC	0.08	0.32	0.22	2.71	2.03	4.63	0.10	0.01	0.53	0.12
S	0.07	1.65	8.71	1.27	3.41	6.76	0.97	3.70	3.64	6.37
LOI	0.30	3.02	8.98	9.02	10.27	16.79	0.94	2.60	5.35	2.61
V*	5.0	36.3	38.5	27.7	39.2	48.5	50.6	82.6	85.0	41.2
Cr*	396.9	119.2	93.5	210.4	185.0	418.1	197.2	98.1	63.8	200.7
Co*	35.2	20.7	22.0	11.1	16.8	54.5	10.1	15.5	159.5	56.6
Ni*	40.2	41.5	55.0	38.8	39.2	54.5	30.3	56.8	31.9	94.7
Cu*	361.7	171.0	544.4	177.2	140.2	513.8	75.9	129.1	895.1	733.0
Zn*	361.7	10.4	110.0	1882.6	2.8	649.5	2.5	77.4	95.7	238.8
Ga[3]	ND	ND	ND	ND	ND	ND	ND	7.0	ND	ND
Ge[3]	ND	ND	ND	ND	ND	ND	ND	0.26	ND	ND
As[3]	ND	ND	ND	ND	ND	ND	ND	2.6	ND	ND
Mo[3]	ND	ND	ND	ND	ND	ND	ND	1.0	ND	ND
Ag[2]	0.3	0.1	0.3	0.9	0.4	0.5	0.3	0.2	0.2	1.2
In[3]	ND	ND	ND	ND	ND	ND	ND	0.052	ND	ND
Sn[3]	ND	ND	ND	ND	ND	ND	ND	0.5	ND	ND
Sb[3]	ND	ND	ND	ND	ND	ND	ND	0.103	ND	ND
W[3]	ND	ND	ND	ND	ND	ND	ND	1.1	ND	ND
Au[2]	1.0	10.4	1.1	1.1	1.1	1.2	1.0	7.2	1.1	42.2
Tl[3]	ND	ND	ND	ND	ND	ND	ND	0.026	ND	ND
Pb[2]	63.3	5.2	1.1	2.2	1.1	1.2	3.0	1.0	2.1	1.0
Bi[3]	ND	ND	ND	ND	ND	ND	ND	0.12	ND	ND
Be	2.5	2.6	2.7	2.8	2.8	3.0	2.5	2.6	5.3	2.6
Rb[3]	ND	ND	ND	ND	ND	ND	ND	4.8	ND	ND
Sr*	100.5	31.1	11.0	33.2	44.8	24.2	131.5	82.6	138.2	10.3
Cs[3]	ND	ND	ND	ND	ND	ND	ND	3.6	ND	ND
Ba*	5.0	238.4	55.0	11.1	100.9	48.5	80.9	18.0	21.3	10.3
Sc	2.5	5.2	5.5	2.8	5.6	6.1	5.1	5.2	2.7	5.1
Y*	2.5	10.4	11.0	5.5	5.6	6.1	10.1	7.9	2.7	5.1
Zr*	10.0	51.8	77.0	33.2	44.8	48.5	91.0	23.9	42.5	30.9
Nb*	10.0	5.2	5.5	5.5	5.6	6.1	5.1	0.7	5.3	5.1
Hf[3]	ND	ND	ND	ND	ND	ND	ND	0.58	ND	ND
Ta[3]	ND	ND	ND	ND	ND	ND	ND	0.08	ND	ND
Th[3]	ND	ND	ND	ND	ND	ND	ND	0.4	ND	ND
U[3]	ND	ND	ND	ND	ND	ND	ND	0.3	ND	ND
La[3]	ND	ND	ND	ND	ND	ND	ND	4.0	ND	ND
Ce[3]	ND	ND	ND	ND	ND	ND	ND	7.9	ND	ND
Pr[3]	ND	ND	ND	ND	ND	ND	ND	0.8	ND	ND
Nd[3]	ND	ND	ND	ND	ND	ND	ND	3.420	ND	ND
Sm[3]	ND	ND	ND	ND	ND	ND	ND	0.744	ND	ND
Eu[3]	ND	ND	ND	ND	ND	ND	ND	0.312	ND	ND
Gd[3]	ND	ND	ND	ND	ND	ND	ND	0.820	ND	ND
Tb[3]	ND	ND	ND	ND	ND	ND	ND	0.157	ND	ND
Dy[3]	ND	ND	ND	ND	ND	ND	ND	1.016	ND	ND
Ho[3]	ND	ND	ND	ND	ND	ND	ND	0.224	ND	ND
Er[3]	ND	ND	ND	ND	ND	ND	ND	0.691	ND	ND
Tm[3]	ND	ND	ND	ND	ND	ND	ND	0.106	ND	ND
Yb[3]	ND	ND	ND	ND	ND	ND	ND	0.675	ND	ND
Lu[3]	ND	ND	ND	ND	ND	ND	ND	0.104	ND	ND
UTM E	375835	384271	383796	388075	388784	362821	354825	379362	386576	409830
UTM N	5286172	5288044	5288187	5286394	5286188	5288110	5279629	5288857	5287350	5298432

Appendix 4.1: Lithogeochemical data

sample	AU06508	AU06515	AU06518	AU06525	AU06530	AU06531	AU06720	AU06722	AU06734	8471
flag	ISW	ISW	ISW	ISW	ISW	ISW	ISW	ISW	ISW	IXH
SiO_2	60.08	53.44	43.55	63.97	64.82	36.81	69.12	73.24	91.75	36.98
Al_2O_3	6.67	1.68	6.84	3.72	2.45	2.59	5.09	1.24	1.38	1.05
Fe_2O_3	26.65	34.64	35.23	24.52	25.20	50.02	23.08	22.03	5.27	38.75
CaO	0.56	4.73	5.61	1.16	1.86	3.23	0.06	1.09	0.23	12.62
MgO	2.96	4.38	5.86	2.90	4.62	4.41	1.82	0.89	0.63	9.71
Na_2O	0.60	0.16	0.88	0.61	0.09	0.05	0.13	0.16	0.22	0.01
K_2O	1.50	0.08	0.19	2.07	0.09	0.85	0.13	0.54	0.17	0.03
TiO_2	0.17	0.07	0.74	0.11	0.13	0.16	0.19	0.14	0.04	0.05
MnO	0.72	0.63	0.81	0.84	0.57	1.72	0.29	0.58	0.05	0.70
P_2O_5	0.08	0.21	0.28	0.09	0.16	0.16	0.09	0.10	0.05	0.10
TIC	0.05	1.20	0.09	0.03	0.26	1.56	0.02	0.76	0.02	5.43
S	2.42	2.89	1.35	9.04	0.63	5.11	6.40	2.32	0.76	1.75
LOI	1.69	3.13	1.34	8.49	1.43	2.88	6.30	5.96	0.91	11.99
V*	25.5	93.4	193.8	112.3	45.8	77.7	48.2	64.2	20.2	85.7
Cr*	183.7	129.7	321.2	329.1	320.4	82.9	267.8	406.8	454.8	2.9
Co*	5.1	36.3	45.9	11.0	10.8	25.9	16.1	21.4	10.1	11.4
Ni*	40.8	72.6	111.2	38.4	76.3	62.2	32.1	107.0	30.3	34.3
Cu*	107.2	531.1	326.3	197.5	117.0	243.5	85.7	224.8	313.3	22.9
Zn*	698.0	513.5	398.7	87.8	213.6	350.2	176.7	460.3	121.3	479.9
Ga*	ND	ND	ND	9.1	5.8	ND	ND	ND	ND	3.0
Ge*	ND	ND	ND	0.27	0.89	ND	ND	ND	ND	4.91
As*	ND	ND	ND	2.7	2.5	ND	ND	ND	ND	7.2
Mo*	ND	ND	ND	1.1	1.0	ND	ND	ND	ND	1.1
Ag*	0.2	0.5	0.3	4.4	0.3	1.0	0.9	0.2	0.1	0.2
In*	ND	ND	ND	0.055	0.051	ND	ND	ND	ND	0.057
Sn*	ND	ND	ND	0.5	0.5	ND	ND	ND	ND	0.6
Sb*	ND	ND	ND	0.110	0.259	ND	ND	ND	ND	0.114
W*	ND	ND	ND	8.1	1.3	ND	ND	ND	ND	0.3
Au*	17.3	1.0	1.0	1226.5	3.1	14.5	28.9	18.2	1.0	85.7
Tl*	ND	ND	ND	0.085	0.025	ND	ND	ND	ND	0.029
Pb*	68.4	1.0	1.0	19.7	1.0	6.2	9.6	1.1	3.0	1.1
Bi*	ND	ND	ND	0.13	0.22	ND	ND	ND	ND	0.06
Be	2.6	2.6	2.5	2.7	2.5	2.6	2.7	2.7	2.5	2.9
Rb*	ND	ND	ND	73.4	5.8	ND	ND	ND	ND	0.6
Sr*	61.2	20.7	132.6	32.9	50.9	93.3	53.6	85.6	121.3	34.3
Cs*	ND	ND	ND	12.9	1.7	ND	ND	ND	ND	0.1
Ba*	265.3	10.4	40.8	208.8	21.8	124.3	53.6	64.2	10.1	7.9
Sc	5.1	15.6	25.5	2.7	5.1	5.2	2.7	2.7	2.5	5.7
Y*	5.1	15.6	20.4	5.2	9.2	10.4	2.7	2.7	2.5	11.7
Zr*	51.0	31.1	40.8	49.2	34.3	31.1	64.3	21.4	30.3	8.9
Nb*	5.1	5.2	5.1	1.1	1.0	5.2	5.4	5.4	5.1	3.5
Hf*	ND	ND	ND	1.20	0.82	ND	ND	ND	ND	0.25
Ta*	ND	ND	ND	0.09	0.07	ND	ND	ND	ND	0.01
Th*	ND	ND	ND	0.7	1.1	ND	ND	ND	ND	0.3
U*	ND	ND	ND	0.3	0.3	ND	ND	ND	ND	0.2
La*	ND	ND	ND	4.9	7.4	ND	ND	ND	ND	5.5
Ce*	ND	ND	ND	10.0	16.1	ND	ND	ND	ND	11.9
Pr*	ND	ND	ND	1.0	1.7	ND	ND	ND	ND	1.5
Nd*	ND	ND	ND	4.040	6.030	ND	ND	ND	ND	6.441
Sm*	ND	ND	ND	0.884	1.871	ND	ND	ND	ND	1.440
Eu*	ND	ND	ND	0.374	0.864	ND	ND	ND	ND	0.866
Gd*	ND	ND	ND	0.805	1.679	ND	ND	ND	ND	1.422
Tb*	ND	ND	ND	0.122	0.265	ND	ND	ND	ND	0.270
Dy*	ND	ND	ND	0.752	1.498	ND	ND	ND	ND	1.728
Ho*	ND	ND	ND	0.149	0.298	ND	ND	ND	ND	0.389
Er*	ND	ND	ND	0.460	0.871	ND	ND	ND	ND	1.188
Tm*	ND	ND	ND	0.066	0.119	ND	ND	ND	ND	0.171
Yb*	ND	ND	ND	0.472	0.806	ND	ND	ND	ND	1.108
Lu*	ND	ND	ND	0.080	0.119	ND	ND	ND	ND	0.173
UTM E	410186	408565	410470	398699	402127	402127	398180	396280	396094	410563
UTM N	5298460	5298227	5298576	5293683	5295330	5295405	5292935	5290991	5290446	5270739

Appendix 4.1: Lithogeochemical data

sample	8472	8473	AU04225	AU04226	AU06681	AU06726	AU06541	AU06548	AU06510	AU06511
flag	IXH	IXH	IXH	IXH	IXH	IXH	IXN	IXN	IXS	IXS
SiO_2	79.32	67.16	74.18	92.85	53.50	57.28	47.39	6.30	64.90	58.89
Al_2O_3	0.08	0.03	1.11	0.24	0.82	3.40	13.55	0.73	5.98	6.62
Fe_2O_3	14.23	24.98	23.84	3.36	41.69	34.48	19.74	80.57	20.01	29.75
CaO	3.44	3.98	0.05	2.68	0.42	2.22	7.65	5.03	5.15	1.10
MgO	2.64	3.28	0.52	0.76	2.80	2.06	4.64	4.39	2.48	1.94
Na_2O	0.01	0.01	0.01	0.01	0.01	0.12	4.92	0.01	0.22	0.31
K_2O	0.01	0.01	0.04	0.01	0.23	0.07	0.14	0.02	0.46	0.80
TiO_2	0.01	0.01	0.06	0.01	0.02	0.12	1.44	0.05	0.19	0.37
MnO	0.22	0.37	0.06	0.06	0.16	0.09	0.35	2.73	0.52	0.13
P_2O_5	0.04	0.16	0.13	0.02	0.34	0.15	0.16	0.17	0.08	0.09
TIC	1.43	4.77	0.01	0.63	2.86	0.86	3.13	2.15	0.62	0.25
S	0.50	0.21	0.48	0.20	9.50	18.10	5.17	9.89	3.76	14.00
LOI	4.32	12.88	4.32	2.14	16.67	14.07	13.63	18.48	4.15	11.92
V*	37.0	46.2	63.2	15.6	24.2	73.7	344.3	36.9	41.9	97.5
Cr*	322.5	90.3	147.2	187.4	163.0	276.3	180.4	18.4	199.1	699.6
Co*	2.6	5.8	10.5	2.6	12.1	116.7	75.7	12.3	26.2	126.2
Ni*	39.1	43.9	2.6	2.6	48.3	132.6	146.7	86.1	36.7	211.0
Cu*	15.9	5.8	347.8	26.1	690.8	798.1	157.2	129.1	172.9	498.9
Zn*	2.6	43.9	2.6	570.7	6.0	41748.5	5.8	3.1	397.1	3016.4
Ga*	-1.1	-1.2	4.8	1.4	ND	6.5	20.4	ND	ND	ND
Ge*	6.03	4.03	4.36	4.81	ND	0.31	0.29	ND	ND	ND
As*	2.6	2.9	2.6	2.6	ND	23.1	14.8	ND	ND	ND
Mo*	3.5	1.2	3.0	2.6	ND	1.2	1.2	ND	ND	ND
Ag*	0.1	0.1	0.1	0.1	1.1	3.9	2.0	0.9	0.4	3.2
In*	0.053	0.058	0.053	0.052	ND	0.061	0.058	ND	ND	ND
Sn*	0.5	0.6	0.5	0.5	ND	0.6	0.6	ND	ND	ND
Sb*	0.106	0.116	0.105	0.104	ND	0.485	0.472	ND	ND	ND
W*	0.3	0.3	0.3	0.3	ND	1.9	41.1	ND	ND	ND
Au*	18.0	31.2	7.4	3.1	443.2	17.2	12832.4	130.4	5.2	1.1
Tl*	0.026	0.029	0.026	0.026	ND	0.031	0.029	ND	ND	ND
Pb*	4.2	1.2	1.1	214.9	12.1	10633.6	1.2	1.2	3.1	141.1
Bi*	0.05	0.06	0.36	0.05	ND	0.18	0.15	ND	ND	ND
Be	2.6	2.9	2.6	2.6	3.0	3.1	2.9	3.1	2.6	2.9
Rb*	0.5	0.6	0.5	0.5	ND	3.6	3.7	ND	ND	ND
Sr*	21.1	23.1	5.3	9.1	24.2	73.7	151.3	61.5	10.5	11.5
Cs*	0.1	0.1	0.1	0.1	ND	0.2	0.1	ND	ND	ND
Ba*	3.5	7.4	40.4	1.6	72.5	36.7	62.0	12.3	41.9	57.3
Sc	2.6	2.9	2.6	2.6	3.0	3.1	40.7	3.1	5.2	17.2
Y*	3.5	5.4	7.0	2.7	6.0	8.1	46.6	3.1	5.2	5.7
Zr*	10.3	7.5	28.2	15.1	24.2	35.4	103.7	36.9	62.9	57.3
Nb*	0.1	0.1	0.1	0.1	6.0	1.2	3.3	6.1	5.2	5.7
Hf*	0.16	0.14	0.53	0.24	ND	0.78	2.87	ND	ND	ND
Ta*	0.01	0.01	0.04	0.01	ND	0.14	0.19	ND	ND	ND
Th*	0.0	0.0	0.5	0.1	ND	0.9	0.5	ND	ND	ND
U*	0.0	0.0	0.1	0.0	ND	0.3	0.2	ND	ND	ND
La*	1.1	2.0	5.3	1.6	ND	9.6	6.1	ND	ND	ND
Ce*	2.3	3.9	10.8	3.3	ND	21.0	16.0	ND	ND	ND
Pr*	0.3	0.5	1.3	0.4	ND	2.3	2.1	ND	ND	ND
Nd*	1.280	2.087	5.226	1.727	ND	9.706	11.357	ND	ND	ND
Sm*	0.335	0.475	1.032	0.363	ND	1.867	3.823	ND	ND	ND
Eu*	0.357	0.471	0.617	0.211	ND	0.779	1.345	ND	ND	ND
Gd*	0.380	0.517	1.014	0.371	ND	1.588	5.182	ND	ND	ND
Tb*	0.080	0.100	0.172	0.064	ND	0.248	1.080	ND	ND	ND
Dy*	0.528	0.655	1.022	0.372	ND	1.391	7.400	ND	ND	ND
Ho*	0.125	0.144	0.225	0.079	ND	0.254	1.644	ND	ND	ND
Er*	0.389	0.433	0.710	0.245	ND	0.777	5.117	ND	ND	ND
Tm*	0.059	0.063	0.100	0.035	ND	0.110	0.766	ND	ND	ND
Yb*	0.395	0.381	0.633	0.239	ND	0.736	4.749	ND	ND	ND
Lu*	0.065	0.057	0.093	0.036	ND	0.111	0.712	ND	ND	ND
UTM E	410563	410563	410586	410606	414250	410572	406680	428283	373056	373056
UTM N	5270742	5270754	5270782	5270770	5271650	5270767	5333880	5336055	5287166	5287166

Appendix 4.1: Lithogeochemical data

sample	AU06512	AU06513	AU06520	AU06692	AU06693	AU06694	AU06695
flag	IXS	IXS	IXS	IXS	IXS	IXS	IXS
SiO_2	62.08	45.77	63.58	50.79	60.81	95.59	35.22
Al_2O_3	3.48	5.85	5.60	6.18	6.95	0.48	15.59
Fe_2O_3	25.35	34.92	21.80	40.67	27.26	1.65	42.41
CaO	4.66	7.71	5.03	0.22	3.03	1.90	0.33
MgO	3.36	4.77	2.83	1.59	1.37	0.20	4.53
Na_2O	0.13	0.10	0.13	0.01	0.01	0.01	0.01
K_2O	0.25	0.12	0.37	0.01	0.01	0.07	0.62
TiO_2	0.24	0.44	0.30	0.19	0.25	0.01	0.49
MnO	0.32	0.20	0.18	0.07	0.13	0.03	0.12
P_2O_5	0.12	0.13	0.17	0.27	0.17	0.05	0.67
TIC	0.75	3.13	1.15	0.02	0.64	0.23	0.02
S	5.74	11.70	7.97	17.50	7.10	0.06	9.11
LOI	8.08	14.72	9.72	12.28	6.47	0.62	10.01
V*	78.8	136.8	78.0	61.0	44.2	2.5	136.0
Cr*	567.8	1201.2	726.0	186.8	221.1	425.4	79.3
Co*	32.8	101.1	66.0	590.6	121.6	10.1	453.3
Ni*	148.5	331.8	90.0	203.7	60.8	20.3	222.1
Cu*	196.5	2021.9	1476.1	50379.7	3747.9	335.3	12577.9
Zn*	1212.1	3270.7	38401.5	1687.4	16915.4	317.1	2017.0
Ga[3]	7.4	ND	ND	15.4	ND	ND	ND
Ge[3]	1.88	ND	ND	0.30	ND	ND	ND
As[3]	6.7	ND	ND	19.2	ND	ND	ND
Mo[3]	1.1	ND	ND	1.2	ND	ND	ND
Ag[2]	1.0	5.1	5.2	29.3	4.5	0.3	9.6
In[3]	0.055	ND	ND	0.060	ND	ND	ND
Sn[3]	0.5	ND	ND	0.6	ND	ND	ND
Sb[3]	0.055	ND	ND	0.121	ND	ND	ND
W[3]	1.1	ND	ND	10.3	ND	ND	ND
Au[2]	5.5	3.6	20.4	78.3	1.1	1.0	57.8
Tl[3]	0.142	ND	ND	0.030	ND	ND	ND
Pb[2]	115.7	113.0	13920.6	272.4	3040.4	12.2	192.6
Bi[3]	0.05	ND	ND	0.13	ND	ND	ND
Be	2.7	3.0	3.0	3.0	2.8	2.5	5.7
Rb[3]	8.5	ND	ND	0.6	ND	ND	ND
Sr*	25.7	23.8	24.0	12.1	22.1	60.8	56.7
Cs[3]	1.5	ND	ND	0.1	ND	ND	ND
Ba*	29.7	11.9	36.0	3.7	5.5	10.1	79.3
Sc	10.9	23.8	12.0	6.0	5.5	2.5	11.3
Y*	9.3	11.9	6.0	8.0	11.1	2.5	5.7
Zr*	28.9	47.6	48.0	62.3	66.3	10.1	158.6
Nb*	1.0	5.9	6.0	2.0	5.5	30.4	5.7
Hf[3]	0.75	ND	ND	1.54	ND	ND	ND
Ta[3]	0.06	ND	ND	0.17	ND	ND	ND
Th[3]	0.6	ND	ND	1.6	ND	ND	ND
U[3]	0.1	ND	ND	0.9	ND	ND	ND
La[3]	4.1	ND	ND	3.4	ND	ND	ND
Ce[3]	9.1	ND	ND	7.2	ND	ND	ND
Pr[3]	1.0	ND	ND	0.8	ND	ND	ND
Nd[3]	4.573	ND	ND	3.580	ND	ND	ND
Sm[3]	1.315	ND	ND	0.946	ND	ND	ND
Eu[3]	0.788	ND	ND	0.433	ND	ND	ND
Gd[3]	1.416	ND	ND	1.066	ND	ND	ND
Tb[3]	0.258	ND	ND	0.187	ND	ND	ND
Dy[3]	1.465	ND	ND	1.089	ND	ND	ND
Ho[3]	0.298	ND	ND	0.241	ND	ND	ND
Er[3]	0.870	ND	ND	0.805	ND	ND	ND
Tm[3]	0.115	ND	ND	0.132	ND	ND	ND
Yb[3]	0.725	ND	ND	0.957	ND	ND	ND
Lu[3]	0.104	ND	ND	0.174	ND	ND	ND
UTM E	372911	372911	372950	375650	375640	375660	375650
UTM N	5287296	5287296	5287307	5286115	5286115	5286115	5286120

Appendix 4.1: Lithogeochemical data

sample	AU06697	AU06700	AU06706	AU06708	AU06738	AU06712	AU06506	AU06716	AU06721	AU06746
flag	IXS	IXS	IXS	IXS	IXS	IXT	IXW	IXW	IXW	IXW
SiO_2	84.04	58.18	62.40	64.69	85.27	72.06	50.50	52.07	55.85	78.77
Al_2O_3	0.55	0.01	12.29	0.50	1.92	0.53	9.66	0.01	0.01	0.03
Fe_2O_3	15.00	36.00	16.32	30.81	11.35	26.19	32.37	40.83	37.15	18.42
CaO	0.10	2.20	3.43	0.31	0.15	0.10	0.31	0.82	0.40	0.28
MgO	0.16	2.20	1.56	2.39	0.87	0.78	5.25	4.44	3.69	1.76
Na_2O	0.01	0.01	1.26	0.01	0.14	0.01	0.19	0.01	2.03	0.09
K_2O	0.05	0.07	2.15	0.10	0.04	0.09	0.08	0.08	0.20	0.04
TiO_2	0.02	0.01	0.33	0.02	0.10	0.03	0.19	0.01	0.01	0.01
MnO	0.02	1.30	0.21	1.11	0.08	0.15	1.29	1.68	0.59	0.58
P_2O_5	0.05	0.01	0.05	0.05	0.06	0.06	0.18	0.05	0.07	0.02
TIC	0.01	2.76	0.11	0.03	0.14	1.66	0.03	0.14	0.01	0.20
S	6.61	7.50	5.06	3.06	1.83	9.34	6.45	0.03	0.17	4.15
LOI	4.50	11.27	5.05	3.86	2.29	11.04	6.43	0.23	0.58	2.52
V*	31.4	79.1	63.5	41.7	36.0	33.8	49.3	45.3	50.5	46.3
Cr*	492.7	175.2	174.6	135.6	575.7	445.5	136.8	30.2	111.2	318.6
Co*	21.0	79.1	52.9	20.9	15.4	39.5	54.7	10.1	5.1	5.1
Ni*	73.4	28.3	79.3	36.5	72.0	67.7	49.3	20.1	10.1	46.3
Cu*	508.4	322.1	645.4	229.5	349.5	124.1	186.1	2.5	126.3	169.6
Zn*	199.2	67.8	1311.9	240.0	107.9	107.2	10288.2	85.6	288.0	257.0
Ga[3]	1.9	16.8	ND	ND	3.8	ND	12.0	ND	ND	ND
Ge[3]	4.60	4.72	ND	ND	0.26	ND	0.55	ND	ND	ND
As[3]	22.3	12.5	ND	ND	2.6	ND	2.7	ND	ND	ND
Mo[3]	1.0	3.9	ND	ND	1.0	ND	1.1	ND	ND	ND
Ag[2]	0.5	1.2	0.6	0.2	0.3	0.1	0.9	0.1	0.2	0.1
In[3]	0.052	0.057	ND	ND	0.051	ND	0.055	ND	ND	ND
Sn[3]	0.5	1.2	ND	ND	0.5	ND	0.5	ND	ND	ND
Sb[3]	0.462	0.938	ND	ND	0.412	ND	0.109	ND	ND	ND
W[3]	0.8	1.9	ND	ND	0.8	ND	0.7	ND	ND	ND
Au[2]	1.0	159.3	1.1	7.3	7.2	84.6	15.3	7.0	3.0	34.9
Tl[3]	0.026	0.259	ND	ND	0.026	ND	0.027	ND	ND	ND
Pb[2]	145.7	27.1	1.1	1.0	1.0	1.1	4663.4	1.0	1.0	1.0
Bi[3]	0.05	0.14	ND	ND	0.17	ND	0.05	ND	ND	ND
Be	2.6	2.8	2.6	2.6	2.6	2.8	2.7	2.5	2.5	2.6
Rb[3]	1.2	27.7	ND	ND	2.8	ND	2.4	ND	ND	ND
Sr*	73.4	67.8	243.3	62.6	113.1	79.0	12.1	60.4	60.6	102.8
Cs[3]	0.1	0.4	ND	ND	0.2	ND	0.3	ND	ND	ND
Ba*	4.4	54.3	412.6	20.9	16.2	11.3	1.6	20.1	20.2	10.3
Sc	2.6	2.8	10.6	2.6	5.1	2.8	5.5	2.5	2.5	2.6
Y*	3.6	10.3	2.6	2.6	2.7	2.8	11.8	2.5	2.5	2.6
Zr*	11.1	111.0	116.4	20.9	10.6	22.6	123.0	20.1	20.2	10.3
Nb*	0.1	4.0	5.3	5.2	0.3	5.6	3.6	5.0	5.1	5.1
Hf[3]	0.19	2.91	ND	ND	0.26	ND	3.11	ND	ND	ND
Ta[3]	0.01	0.39	ND	ND	0.02	ND	0.39	ND	ND	ND
Th[3]	0.2	3.7	ND	ND	0.1	ND	3.0	ND	ND	ND
U[3]	0.1	0.9	ND	ND	0.0	ND	1.0	ND	ND	ND
La[3]	2.0	6.0	ND	ND	1.4	ND	22.3	ND	ND	ND
Ce[3]	4.5	14.3	ND	ND	3.1	ND	41.6	ND	ND	ND
Pr[3]	0.5	1.4	ND	ND	0.3	ND	4.0	ND	ND	ND
Nd[3]	1.993	5.975	ND	ND	1.433	ND	15.864	ND	ND	ND
Sm[3]	0.493	1.567	ND	ND	0.369	ND	3.089	ND	ND	ND
Eu[3]	0.323	0.734	ND	ND	0.205	ND	1.066	ND	ND	ND
Gd[3]	0.529	1.431	ND	ND	0.389	ND	2.560	ND	ND	ND
Tb[3]	0.096	0.273	ND	ND	0.070	ND	0.339	ND	ND	ND
Dy[3]	0.543	1.747	ND	ND	0.435	ND	1.796	ND	ND	ND
Ho[3]	0.120	0.359	ND	ND	0.096	ND	0.354	ND	ND	ND
Er[3]	0.363	1.080	ND	ND	0.297	ND	1.023	ND	ND	ND
Tm[3]	0.055	0.155	ND	ND	0.043	ND	0.144	ND	ND	ND
Yb[3]	0.359	1.082	ND	ND	0.283	ND	1.003	ND	ND	ND
Lu[3]	0.060	0.171	ND	ND	0.044	ND	0.152	ND	ND	ND
UTM E	375880	375807	373713	374820	370775	375422	409980	397450	396899	410350
UTM N	5286145	5285957	5286245	5286890	5283850	5291580	5298487	5292050	5291466	5298700

Figure 4.1: A geological map of the Swayze greenstone belt. (Compiled by the author after Heather and Shore (1999) and unpublished Falconbridge Limited data.)

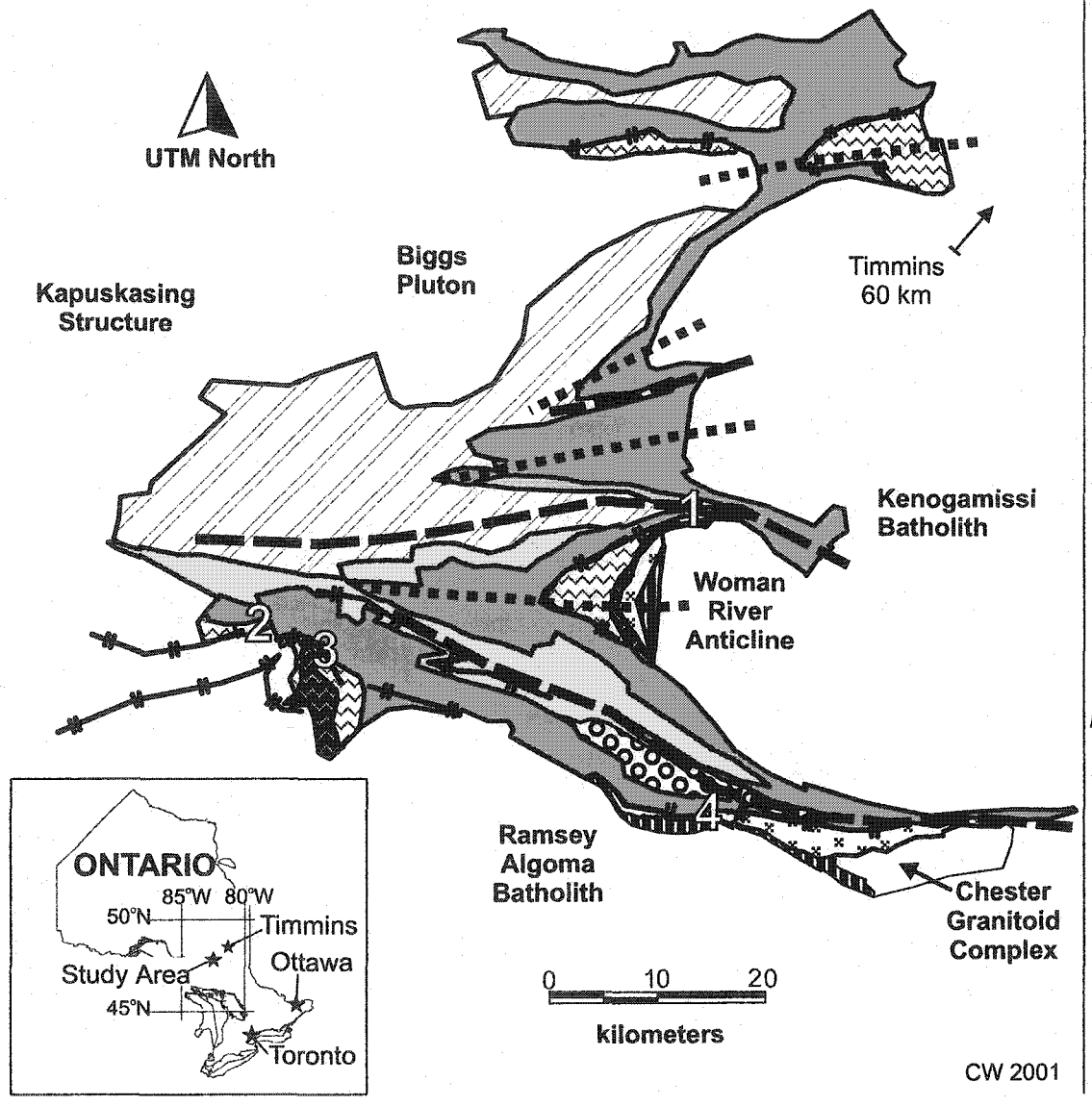

Swayze greenstone belt supracrustal stratigraphy

- Ridout Group sediment
- Swayze Group volcanic and sediment
- iron formation
- THi/THf (intermediate and felsic volcanic)
- TOm (mafic volcanic)
- iron formation
- MSf (felsic volcanic)
- MRm (mafic volcanic)
- iron formation
- CYf (dacite, rhyolite and low-Ti rhyolite)
- CAm (basalt)
- igneous / metamorphic complexes and undivided supracrustal rocks

Regional structural geology

- F_2 anticline axial-trace
- F_2 syncline axial-trace

Base-metal mineralization

1. Jefferson Zn-Pb deposit
2. Shunsby Zn-Cu deposits
3. Peter Lake Zn-Pb showing
4. Huffman Township Zn-Pb showing

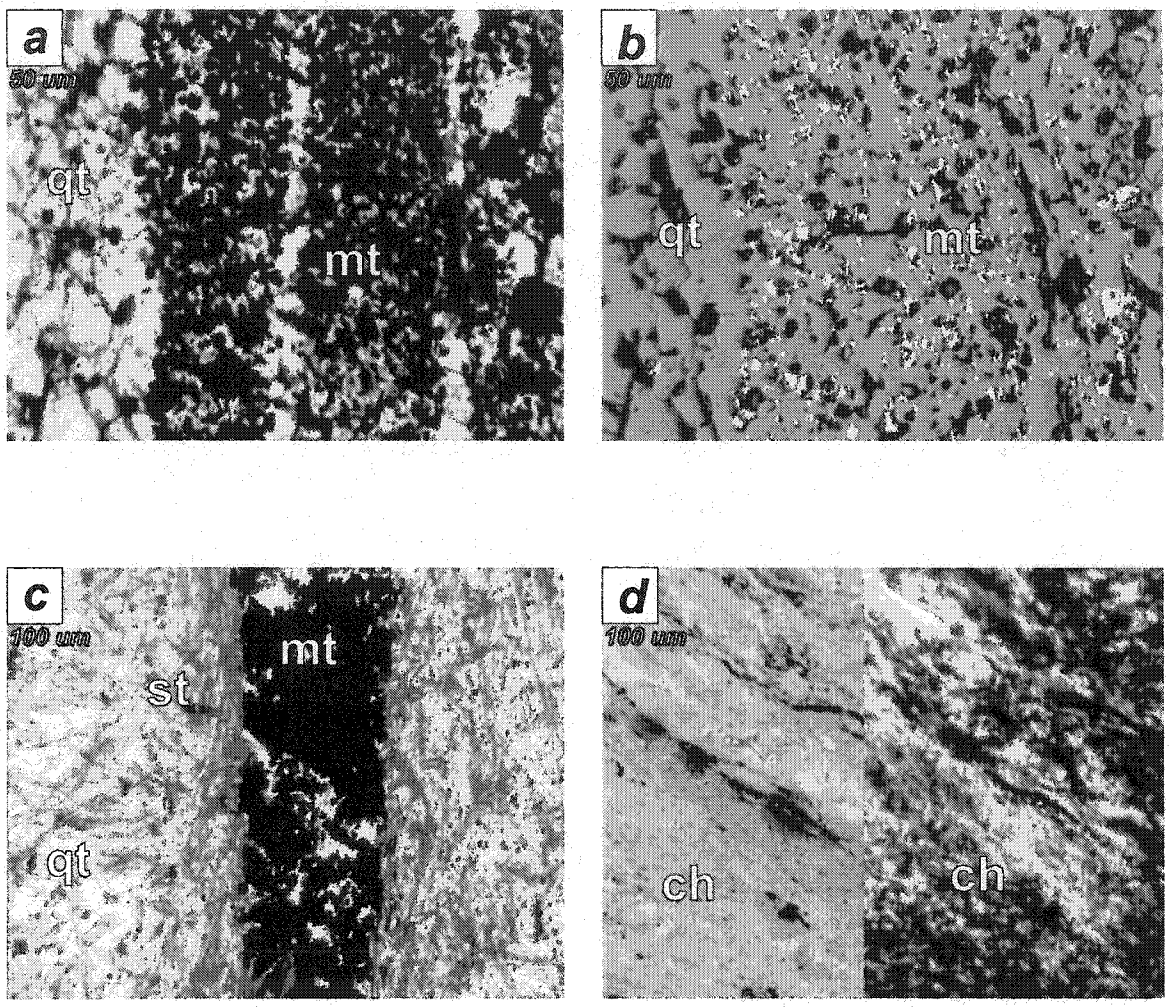

Figure 4.2: Photomicrographs of Fe-oxide and Fe-silicate minerals from SGB hydrothermal sediments. The white squares in the upper left corner of each photomicrograph are labeled for scale.
(a) Very finely laminated magnetite (mt) and quartz (qt) from BIF in plane light.
(b) The same image as 4.1a, viewed in reflected light.
(c) A thin, magnetite-rich band enveloped by stipnomelane (st) fibres from pelitic IF, in plane light.
(d) Fe-rich chlorite (ch) in plane light (left), and with characteristic berlin-blue birefringence under transmitted light with crossed nicols (right).
(e) Coarse (gr) grunerite and quartz inbreccia-type IF under transmitted light with crossed nicols.

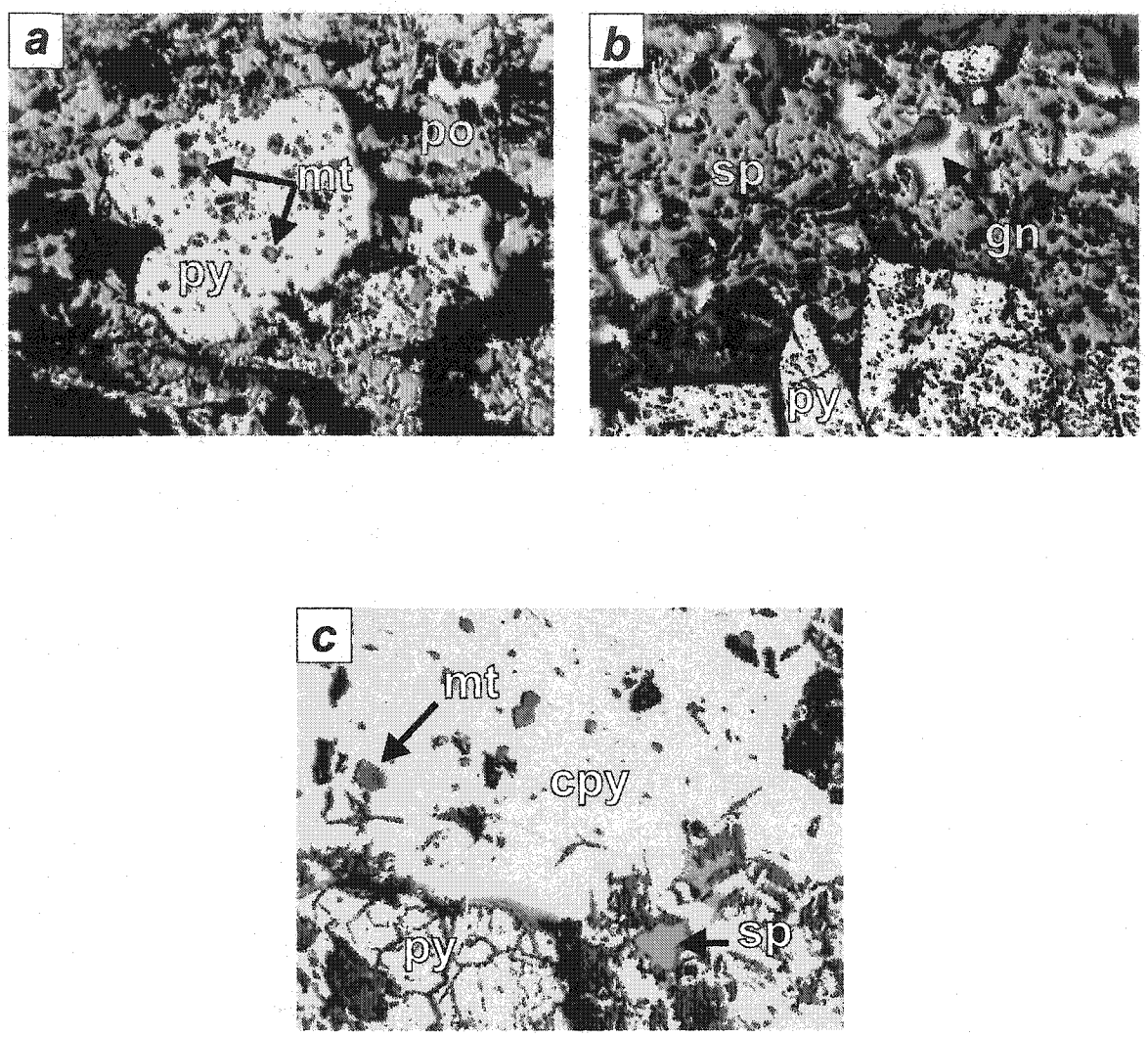

Figure 4.3: Photomicrographs of sulphide minerals from SGB hydrothermal sediments in reflected light. White squares in the upper left corner of each photomicrograph have sides 50 μm long.
(a) Magnetite (mt) and pyrite (py) with pyrrhotite (po) from sulphide-rich IF.
(b) A band of galena (gn) and sphalerite (sp) within pyritic IF from the Huffman Township Zn-Pb occurrence.
(c) Chalcopyrite (cpy) and sphalerite mineralization with pyrite from the Shunsby Cu-Zn deposit.

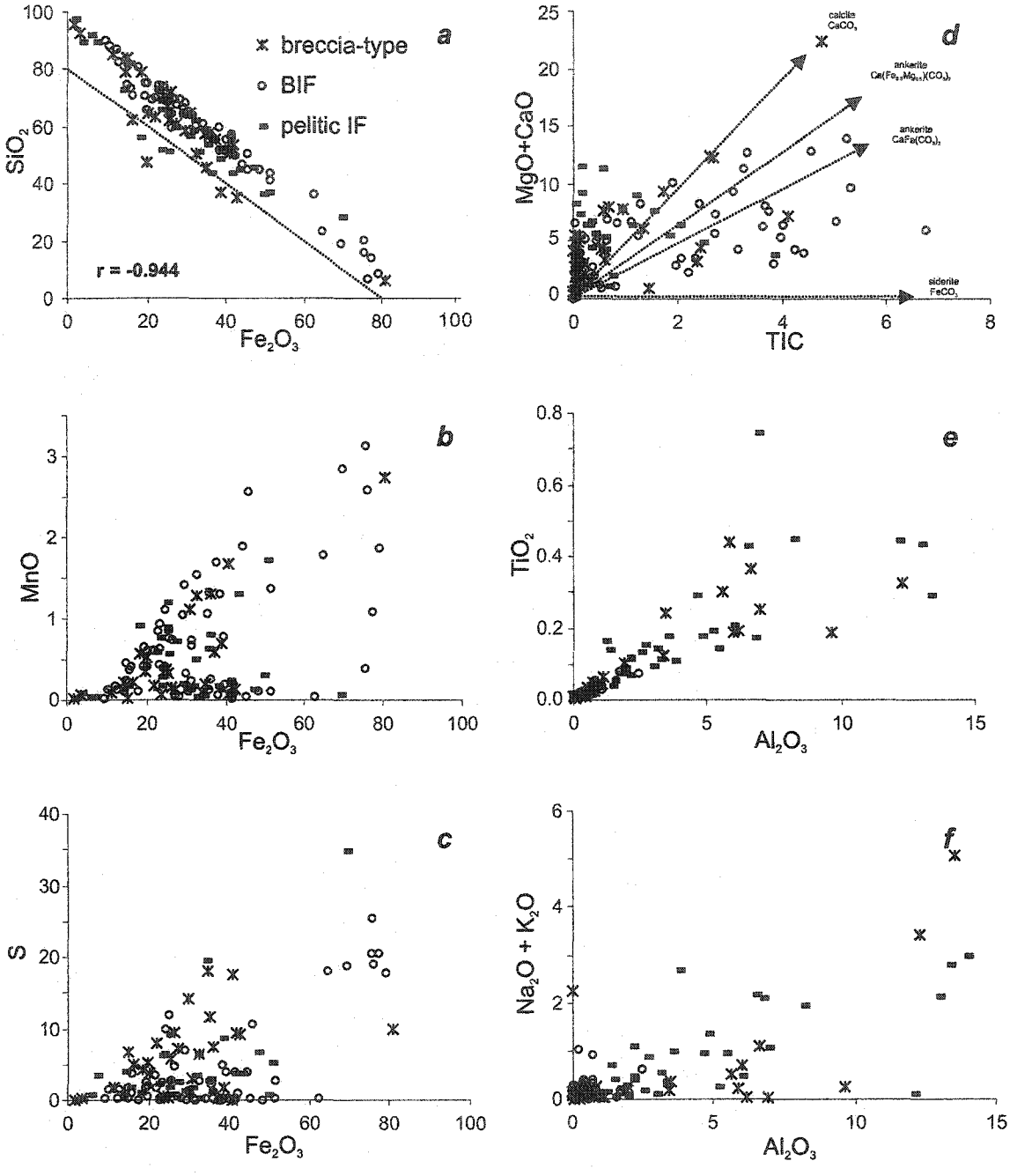

Figure 4.4: Bivariate plots of whole rock compositions for SGB metalliferous sediments..
(a) Most rocks are composed of >80% SiO_2+Fe_2O_3. The dotted line marks compositions of 80% SiO_2+Fe_2O_3.
(b) and (c) There are strong positive correlations between Fe and Mn and Fe and S.
(d) Bulk-rock C and MgO+CaO content correspond to a mixture of calcite, ankerite and siderite.
(e) Ti and Al show strong positive correlations SGB hydrothermal sediments.
(f) Na + K concentrations show moderately strong positive correlations with Al in SGB hydrothermal sediments.

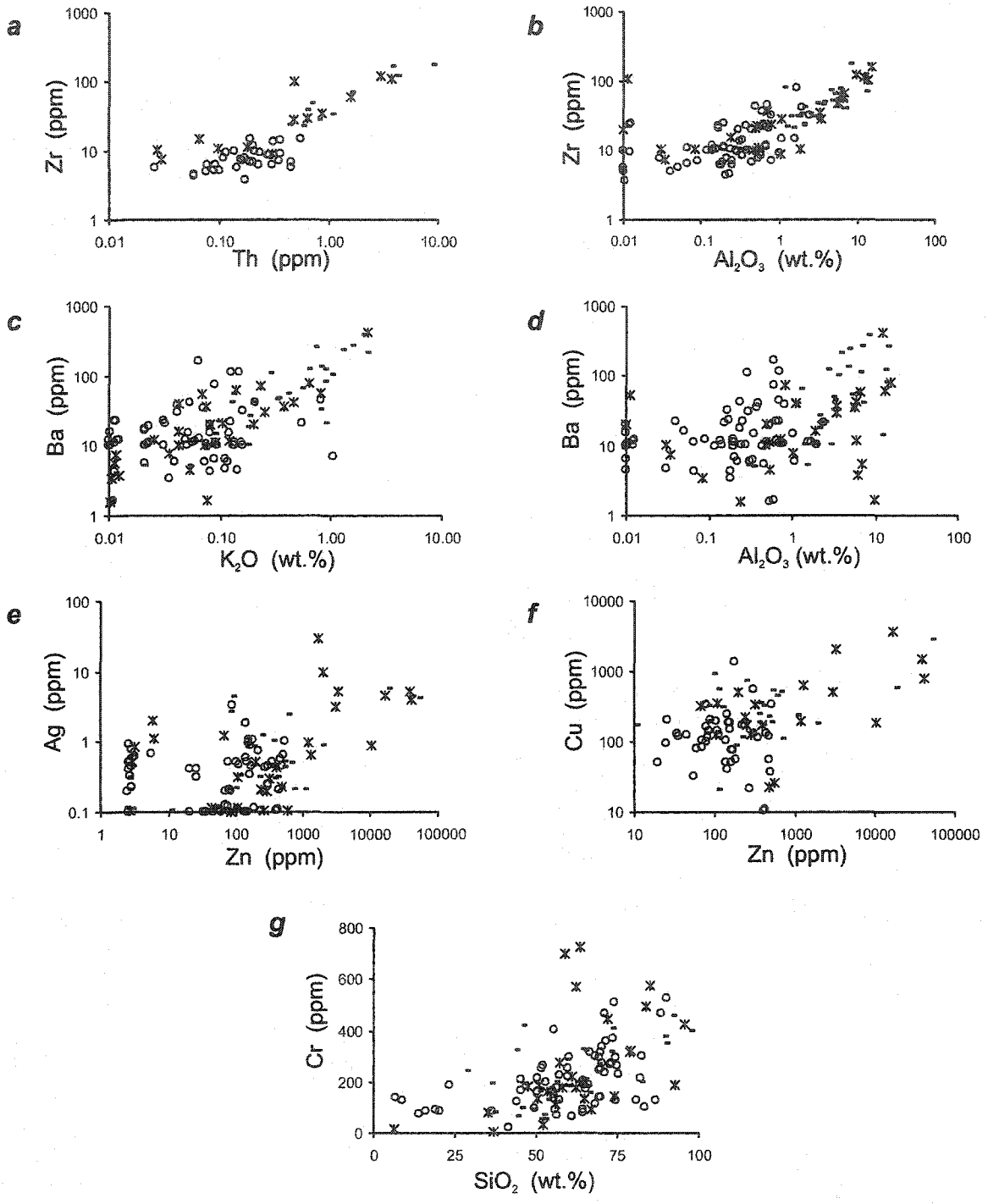

Figure 4.5: Bivariate plots of major- and trace-elements of SGB hydrothermal sediments. Open circles represent compositions of BIF- type sediment, filled rectangles represent pelitic IF, and asterisks represent breccia-type IF.
(a) and (b) HFSE such as Zr and Th have strong positive inter-element correlations and strong positive correlations with Group 3 elements.
(c) and (d) LILE such as Ba have moderate positive correlations with K_2O and Group 3 elements..
(e) and (f) Transition elements such as Ag, Zn and Cu show significant inter-element correlations
(g) Cr shows a moderately strong positive correlation with SiO_2.

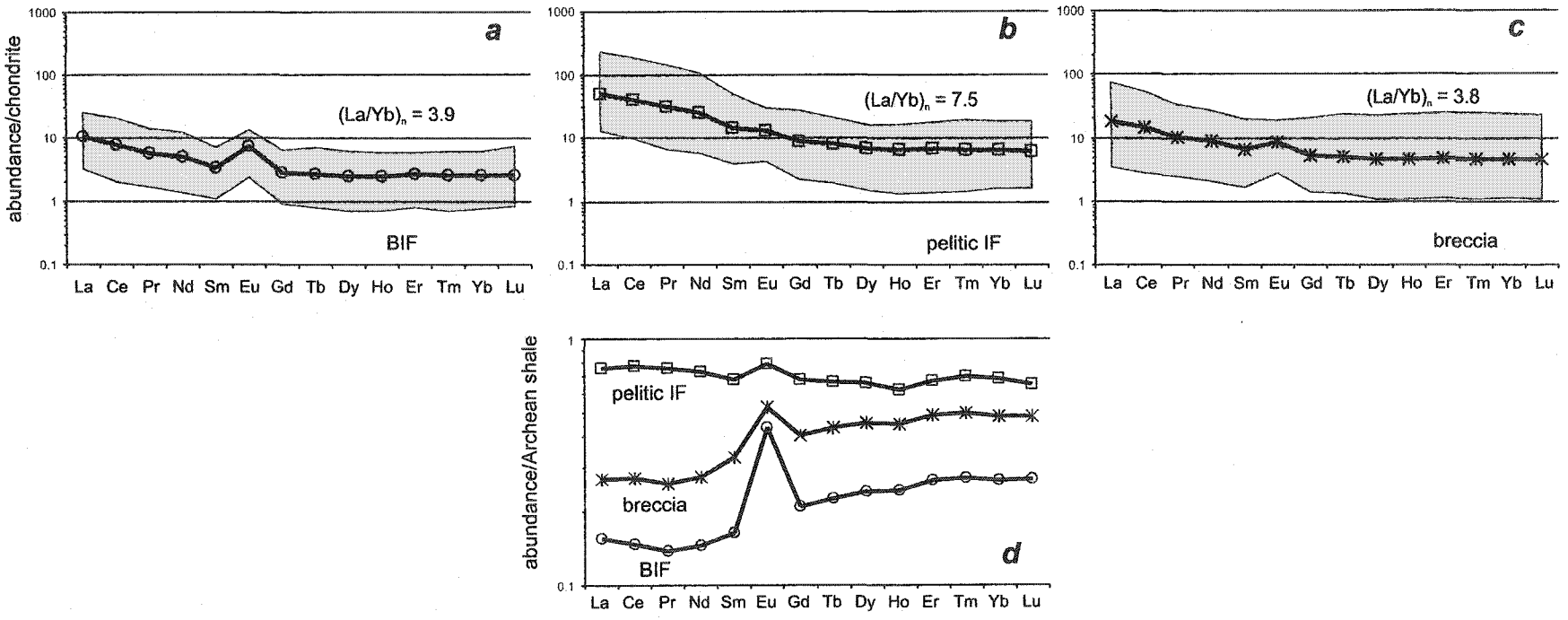

Figure 4.6: Diagram showing REE patterns for BIF, pelitic IF, and breccia-type hydrothermal sediments from the SGB. REE have been normalized to the C1 chondrite of Boynton (1984), and show average and ranges (grey) of normalized concentrations of REE in the three hydrothermal sediment types.

(a) BIF samples have low overall abundances of REE's, lack negative Ce anomalies, and have positive Eu/Eu* values. Chondrite-normalized La/Yb ratios are low (average $(La/Yb)_n = 3.9$) for BIF-type hydrothermal sediment.

(b) Pelitic IF has high overall REE abundances and shows strong LREE enrichment (average $(La/Yb)_n = 7.5$). Pelitic IF samples lack Ce and Eu anomalies.

(c) Breccia-type hydrothermal sediments have weak LREE enrichment (average $(La/Yb)_n = 3.8$), and a small, positive Eu anomaly.

(d) Average REE abundances for BIF, pelitic and breccia-type hydrothermal sediments normalized to the average Archean shale value of Taylor and McLennan (1985), showing the shale-like REE pattern for pelitic IF, and the LREE-depleted hydrothermal end-member BIF pattern.

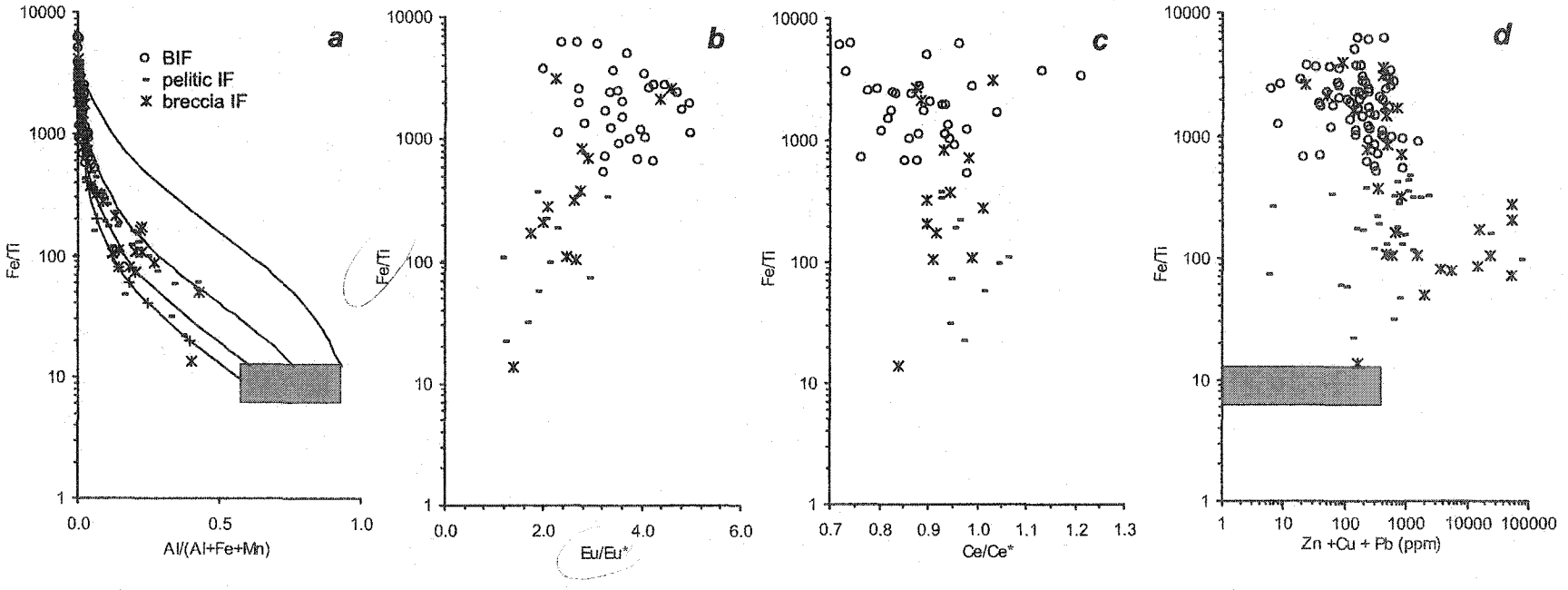

Figure 4.7: Bivariate plots illustrating clastic sediment and hydrothermal fluid contributions to SGB hydrothermal sediments. Gray boxes define the composition of least-altered Chester Group basalt, dacite, rhyolite and low-Ti rhyolite from the SGB.
(a) Hyperbolic mixing lines were calculated between end-member hydrothermal sediment and CAm basalt (cross), CYf dacite (circle), CYf rhyolite (square), and CYf low-Ti rhyolite (diamond). Compositions of pelitic- and breccia-type hydrothermal sediment can be explained by mixtures between end-member hydrothermal sediment and rhyolite, dacite or basalt.
(b) There is a strong correlation between Fe/Ti ratios and Eu/Eu*, reflecting the contrasting REE signatures of seafloor hydrothermal fluids, with a strong positive Eu anomaly, and clastic sediment derived from volcanic material having Eu/Eu* values =<0.
(c) The greatest range of Ce anomalies are present in BIF type sediment indicating a wide range of redox conditions of vent-distal depositional environments. No Ce anomalies exist for breccia and pelitic-type hydrothermal sediment reflecting the reducing conditions of depositional environments proximal to hydrothermal vents.
(d) Base-metal rich hydrothermal sediments have Fe/Ti ratios between least-altered SGB volcanics and BIF-type hydrothermal sediments.

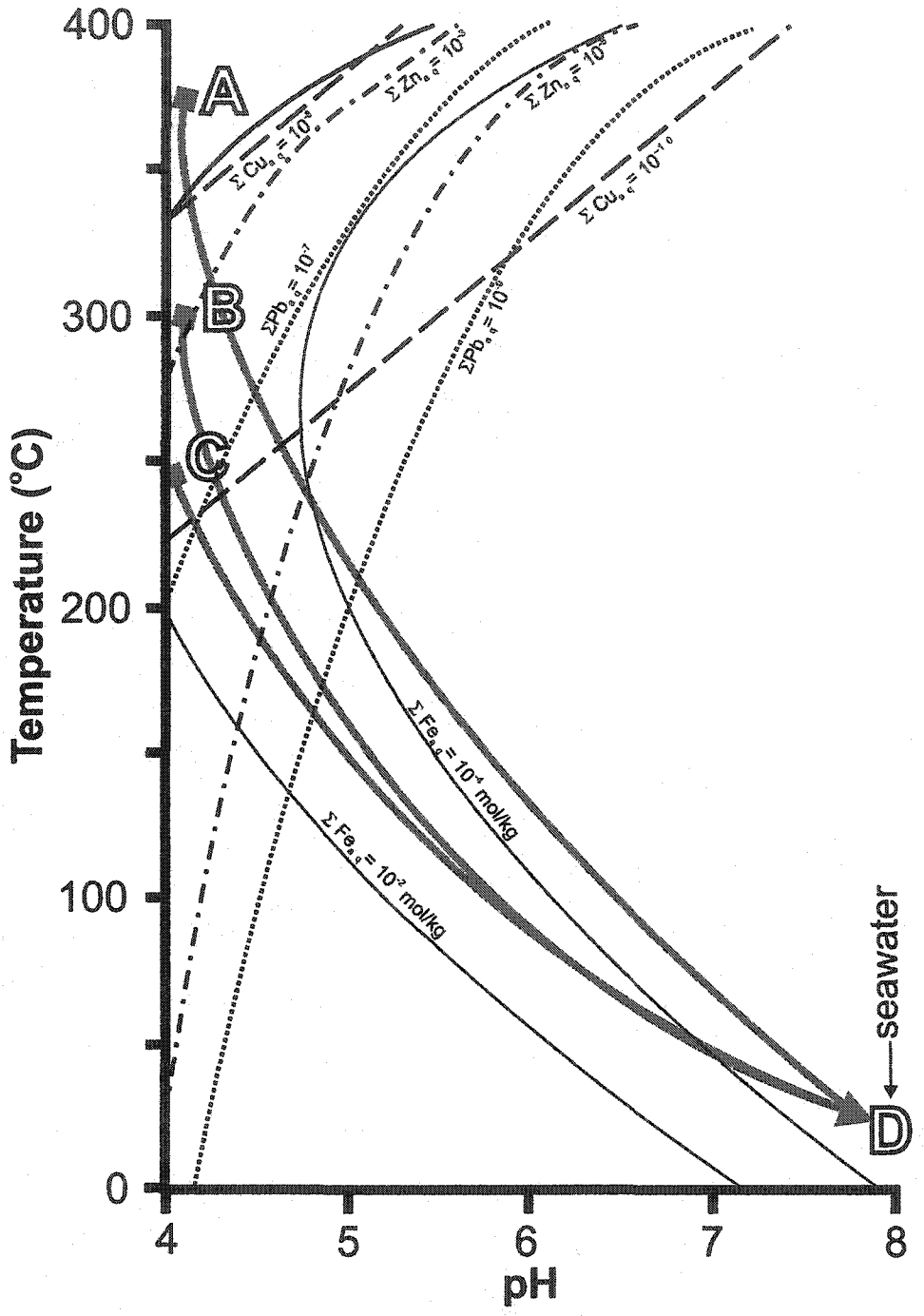

Figure 4.8: Diagram showing the predicted solubilities of Fe, Pb, Zn and Cu as chloride complexes as a function of temperature and pH. A 0.5 mol/kg ΣCl^- solution in equilibrium with the assemblage magnetite-pyrite-pyrrhotite-galena-sphalerite-chalcopyrite at 300 bar pressure was used to calculate Fe and base-metal solubilities (see text for details). Cu (dashed lines), Zn (dashed and dotted lines) and Pb (dotted lines) solubility decreases with decreasing temperature and increasing pH. Fe solubility (solid lines) decreases with decreasing temperature and pH at high temperatures but is retrograde below approximately 250 °C. The solid lines AD, BD and CD reflect the effects of mixing between end-member hydrothermal fluids and seawater. Mixing lines are curved to account for the production of H^+ ions as a result of sulphide mineral precipitation and cooling (see text for details).

Figure 4.9 Schematic illustration of the distribution and genesis of BIF, breccia-type and pelitic IF in the SGB.

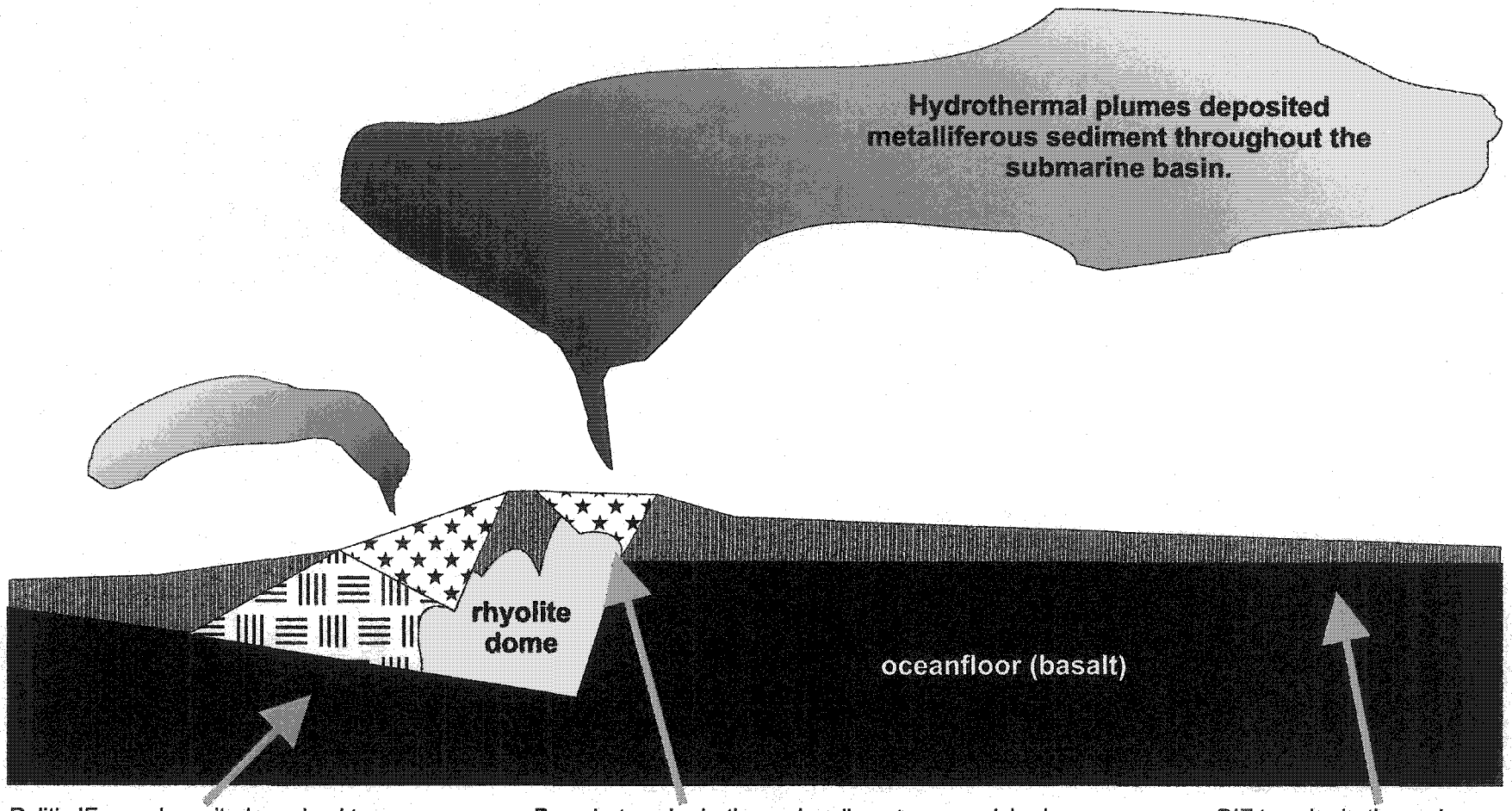

Pelitic IF was deposited proximal to felsic volcanic centers where volcaniclastic and epiclastic material were mixed with the hydrothermal sediments.

Breccia-type hydrothermal sediments are enriched in base metals, and developed solution-breccia textures as warm hydrothermal fluids penetrated BIF and pelitic IF overlying the felsic volcanic complex.

BIF type hydrothermal sediment was deposited in distal parts of the basin and during periods of volcanic quiescence.

mineral	composition	abundance	occurrence
quartz	SiO_2	ubiquitous	Found as relatively pure quartz bands, and as groundmass to iron-bearing minerals in iron-rich bands within BIF and pelitic IF, and as brecciated cherty quartz, rhyolite clasts, and in the matrix of breccia-type IF.
magnetite	Fe_3O_4	ubiquitous	Common as quartz-magnetite bands and as a breccia matrix constituent.
stipnomelane	$(K,Ca)_{0\text{-}1.4}(Fe,Mg,Al)_{5.9\text{-}8.2}\ Si_8O_{20}(OH)_4$	common	Developed as fibrous aggregates within pelitic IF and BIF.
ankerite	$Ca(Mg,Fe,Mn)(CO_3)_2$	common	Dominantly as laminations in BIF or with quartz, magnetite and pyrite as a constituent of breccia matrices.
grunerite	$(Mg,Fe)_7Si_8O_{22}(OH)_2$	minor	Crystallographically continuous mats with fine opaque inclusions, or as indivdual laths in breccia and pelitic IF.
pyrite	FeS_2	minor	Interlayered with quartz and in semi-massive to massive bands in close proximity to argilliaceous material.
hematite	Fe_2O_3	minor	Present as fine inclusions within quartz-rich bands.
pyrrhotite	$Fe_{1-x}S$	rare	Rare wisps in pyrite-rich samples.
chlorite	$(Mg,Mn,Fe,Al)_{12}(Si,Al)_8O_{20}(OH)_{16}$	rare	Constituent of breccia matrix.
almandine	$Fe_3Al_2Si_3O_{12}$	rare	Most common in pelitic IF from the western and southern parts of the SGB where metamorphic grade is relatively high.

Table 4.1: Mineral abundances and modes of occurrence in SGB hydrothermal sediments.

Table 4.2: Average whole rock compositions of BIF, pelitic IF, and breccia-type hydrothermal sediments from the SGB. Major elements, S, TIC, and LOI are expressed as wt.%, Au in parts per billion, and all other trace-elements in parts per million. BIF is rich in Fe, and total inorganic carbon (TIC) and poor in most transition elements, large ion lithophile elements (LILE), and high field strength elements (HFSE). Pelitic IF is richest in Al, Ti, LILE and HFSE, while breccia-type hydrothermal sediments are richest in TIC, S, and LOI and most transition elements. Data for individual samples is given in Appendix 4.1.

	BIF	*pelitic IF*	*breccia*
	n=67	*n=32*	*n=28*
SiO_2	59.33	60.38	61.30
Al_2O_3	0.41	4.52	3.69
Fe_2O_3	34.53	28.40	28.21
CaO	1.97	2.36	2.69
MgO	2.77	2.62	2.75
Na_2O	0.06	0.40	0.35
K_2O	0.10	0.52	0.22
TiO_2	0.02	0.22	0.18
MnO	0.68	0.44	0.48
P_2O_5	0.13	0.15	0.13
TIC	1.77	0.65	1.18
S	3.70	4.50	5.96
LOI	6.42	5.78	8.01
V	40	68	67
Cr	210	222	296
Co	13	31	74
Ni	35	53	82
Cu	123	343	2724
Zn	126	2439	4394
Ga	1.2	3.8	3.3
Ge	1.8	0.7	1.3
As	5.1	4.7	4.4
Mo	0.9	0.5	0.8
Ag	0.4	0.9	2.6
In	0.036	0.025	0.026
Sn	0.3	0.4	0.3
Sb	0.260	0.081	0.129
W	0.9	0.5	2.1
Au	62	61	502
Tl	0.013	0.015	0.025
Pb	15	692	1197
Bi	0.10	0.04	0.05
Rb	1.2	4.8	1.9
Sr	49	83	54
Cs	0.2	0.7	0.1
Ba	21	81	39
Sc	2.9	6.4	7.2
Y	5.7	9.0	7.3
Zr	15	53	46
Nb	2.8	4.8	4.6
Hf	0.09	0.69	0.49
Ta	0.01	0.10	0.05
Th	0.1	0.7	0.4
U	0.1	0.2	0.1

	SiO_2	Al_2O_3	Fe_2O_3	CaO	MgO	Na_2O	K_2O	TiO_2	MnO	P_2O_5	TIC	S	LOI
SiO_2	**1.000**												
Al_2O_3	-0.190	**1.000**											
Fe_2O_3	**-0.944**	-0.074	**1.000**										
CaO	-0.141	0.170	-0.081	**1.000**									
MgO	**-0.674**	0.110	**0.527**	**0.406**	**1.000**								
Na_2O	-0.084	**0.579**	-0.121	0.232	0.106	**1.000**							
K_2O	-0.080	**0.508**	-0.049	0.016	-0.036	0.240	**1.000**						
TiO_2	-0.195	**0.827**	-0.050	0.240	0.150	**0.765**	**0.333**	**1.000**					
MnO	**-0.554**	-0.102	**0.521**	0.094	**0.590**	0.012	-0.078	-0.090	**1.000**				
P_2O_5	**-0.439**	**0.376**	**0.374**	0.022	0.234	-0.014	0.104	0.259	-0.089	**1.000**			
TIC	**-0.342**	-0.188	**0.307**	**0.409**	**0.450**	-0.027	-0.217	-0.076	0.265	0.134	**1.000**		
S	**-0.566**	0.100	**0.576**	-0.094	0.262	-0.021	0.062	0.095	**0.331**	0.082	0.124	**1.000**	
LOI	**-0.528**	0.041	**0.515**	0.142	**0.303**	-0.040	-0.010	0.094	0.214	0.230	**0.668**	**0.662**	**1.000**

Table 4.3: Pearson inter-element correlation coefficients (r) for SGB hydrothermal sediments. The high positive coefficients between Na, K, Ti, and Al indicate positive correlations between this group of elements. High positive coefficients for Fe, Mn and S suggest that these elements were deposited together and constitute important elements in hydrothermal sediments in the SGB . Large negative coefficients of correlation between Si and Fe, Mg, Mn, P, TIC and S demonstrate the effect of dilution of metalliferous components by quartz.

Ore-equivalent horizon	Locality	Age	Lateral extent	Sample	SiO_2 (wt.%)	Al_2O_3 (wt.%)	Fe_2O_3 (wt.%)	S (wt.%)	CO_2 (wt.%)	Cu (ppm)	Zn (ppm)	Pb (ppm)	reference*
Contact-tuff (clastic)	Noranda Camp	Archean	0-20m x ~2.6 km	average n=16	58.29	13.40	25.73	1.61	ND	402	1075	40	1
Contact-tuff (chemical)	Noranda Camp	Archean		average n=12	53.02	10.16	22.84	8.34	ND	648	3730	90	1
Key Tuffite (calc-alkaline)	Mattagami Lake	Archean	0.3-6m x 10 km	average n=5	48.49	11.15	18.62	8.80	ND	1372	17500	258	2
Key Tuffite (tholeiite)	Mattagami Lake	Archean		average n=5	43.21	4.96	17.97	7.96	ND	485	6620	141	2
Brunswick Horizon-siderite IF	Brunswick Belt	Ordovician	1-10m x ~12 km	POA026	25.20	2.50	32.60	0.85	25.40	35	490	1000	3
Brunswick Horizon-chlorite IF	Brunswick Belt	Ordovician		POA060	54.90	9.40	18.39	0.36	4.00	35	220	190	3
Brunswick Horizon-magnetite IF	Brunswick Belt	Ordovician		POA063	19.30	1.20	69.21	0.11	2.60	100	2100	5000	3
Brunswick Horizon-chlorite-sulphide IF	Brunswick Belt	Ordovician		POA093	26.20	8.40	40.20	18.20	1.40	67	32000	4800	3
Tetsusekiei (clastic)	Kuroko District	Miocene		T1	59.22	10.67	15.00	6.01	ND	59	191	99	4
Tetsusekiei (chemical)	Kuroko District	Miocene		T3	47.05	5.45	25.31	14.48	ND	16	181	282	4

*references: (1) Kalogeropoulos and Scott (1989), (2) Liaghat and MacLean (1992), (3) Peter and Goodfellow (1996), (4) Kalogeropoulos and Scott, (1983)
ND indicates no data is available

Table 4.4: Compositions of hydrothermal sediments occupying ore-equivalent horizons in major VMS districts.

Conclusions

This thesis presents interpretations of the geological and lithogeochemical characteristics of variably altered rock in the southeast Swayze Greenstone Belt (SESGB), and of the hydrothermal sediments associated with base-metal sulphide mineralization in the Swayze Greenstone Belt (SGB). The conclusions of chapters 3 and 4 represent a significant contribution to the scientific understanding of the SGB and of hydrothermal sedimentation and base-metal mineralization in Archean greenstone belts. The 14 conclusions of this study are:

1. Chester Group volcanic rocks within the SESGB comprise pillowed amygdaloidal and variolitic basalt of the Chester Group Arbutus Formation (CAm), and quartz- and feldspar-phyric dacite and rhyolite with massive, laminated pyroclastic, and fragmental textures of the Yeo Formation (CYf). The Chester Group volcanic rocks are overlain by 5-20 m of hydrothermal sediments, containing sub-economic Zn-Pb-sulphide mineralization. These geological features are indicative of submarine volcanism and volcanic-exhalative activity.

2. Macro-scale textural characteristics combined with HFSE analyses of CYf dacite, rhyolite and low-Ti rhyolite indicate deposition in a submarine volcanic-arc setting.

3. A magma of calc-alkaline affinity produced the CYf dacite and rhyolite, and the CGC trondhjemite. The CYf dacite and rhyolite are geochemically similar to rhyolites that are not known to host VMS deposits elsewhere in the Superior province.

4. A second batch of magma assimilated large quantities of HFSE-depleted mafic crust (CAm) during fractionation to felsic composition in a shallow sub-volcanic magma chamber. This magma was the source of the CYf low-Ti rhyolite, which has low overall abundances of HFSE and low Zr/Y and $(La/Yb)_n$ ratios. Such uniformly HFSE depleted rhyolite magmas have not been documented in other parts of the Superior Province.

5. CYf volcanics underwent regionally extensive, porosity-occluding, sericite-quartz (type 1) alteration, characterized by loss of Na, addition of Si and K, and net mass-gain, with a minimum estimated water/rock ratio of 6.

6. Chlorite-sericite±biotite±garnet (type 2) alteration occurred at paleo-hydrothermal vent sites localized along synvolcanic fault structures. Alteration was associated with a loss of Na, addition of Si, and K, and minor net mass-loss, requiring water/rock ratios in excess of 400.

7. The fluids responsible for Type 1 and type 2 alteration in the SESGB were both quartz-undersaturated and initially equilibrated with basalt. During type 1 alteration, fluids became saturated in quartz through a combination of extensive interaction with felsic volcaniclastics and cooling, while fluids became quartz-undersaturated during type 2 alteration because interaction with the volcaniclastics was localized and cooling was minimal.

8. From the perspective of alteration mass changes, alteration intensity, alteration zone architecture and hydrothermal products, hydrothermal sediments and base-metal sulphide mineralization from the SESGB can be placed in a continuum

between polymetallic massive-sulphide deposit such as the Horne Mine, and siderite-pyrite iron deposits such as the Helen Mine.

9. SGB hydrothermal sediments are predominantly fine-grained, chemical precipitates that accumulated in submarine basins during breaks in regional volcanic activity of 10-40 Ma in duration.

10. BIF in the SGB is composed almost entirely of Si and Fe, has a relatively high CO_2 content and is depleted in LILE, HFSE and transition elements compared to pelitic IF and breccia-type hydrothermal sediments. BIF-type hydrothermal sediments have a wide range of Ce/Ce* values reflecting variable fO_2 conditions in hydrothermal vent-distal depositional environments. BIF can be found throughout the SGB, and overlies breccia-type and pelitic IF.

11. Pelitic IF is enriched in Al, Ti, Na, K, HFSE and LILE and is characterized by flat, slightly depleted REE profiles when normalized to average Archean shales. Pelitic IF compositions display a continuum of mixing between end-member BIF hydrothermal sediments and local Chester Group volcanic rocks, indicating deposition proximal to active SGB volcanic edifices.

12. Breccia-type hydrothermal sediments of the SGB are enriched in S, Zn, Pb, Cu, Ag, Au, Ni, and Co compared to BIF and pelitic IF. These elements were precipitated as sulphides from a hydrothermal solution that mixed with seawater in a vent-proximal environment. Zn, Cu and Pb mineralized breccias include the Jefferson, Shunsby, Peter Lake and Huffman Township base-metal showings of the SGB, and offer the most prospective geological environments for base-metal sulphide mineralization.

13. Hydrothermal sediments that occupy ore-equivalent stratigraphic positions in productive Archean VMS districts have higher S and Al concentrations than SGB hydrothermal sediments because of greater availability of reduced S and greater volcanic activity during massive sulphide deposition. These observations can be used to gauge the potential of other IFs in similar tectonic settings to mark stratigraphic horizons containing economic massive sulphide deposits.

14. Thermodynamic calculations indicate that SGB hydrothermal sediments precipitated from a cooler (250-300 °C) fluid than those responsible for the generation of typical polymetallic massive-sulphide deposits.

It is hoped that the data and interpretations of the geology and lithogeochemistry of the Chester Group volcanics presented in this thesis will guide future base-metal exploration in the SESGB. The conclusions about the geological controls on hydrothermal sediment composition in the SGB can be used to help understand the geology and depositional environments of other IFs in the Superior province that can be used by the explorationist to assess the potential productivity of a particular hydrothermal sedimentary horizon. Conclusions pertaining to the alteration associated with the formation of iron formation and sub-economic base-metal deposits, and the thermodynamic modelling of fluids responsible for the mobilization, transportation and deposition of Fe and base-metals can be integrated with existing petrogenetic models of VMS ore-formation. These refinements can be used to increase the success of mineral exploration efforts in ancient submarine volcanic environments.